ULB Faculté des Sciences

Deep Learning in the Face of Time: Exploring the Impact of Aging on Pierre Auger Observatory Measurements

Thesis presented by Orazio Zapparrata
in fulfilment of the requirements of the PhD Degree in Physics
("Doctorat en Physique")
Année académique 2022-2023

Supervisor: Professor Ioana Codrina Mariş

Inter-University Institute For High Energies (IIHE)

Thesis jury:

Prof. Petr Tinyakov (Université libre de Bruxelles, Chair)
Prof. Juan Antonio Aguilar Sánchez (Université libre de Bruxelles, Secretary)
Prof. Dr. Ralph Engel (Karlsruher Institut für Technologie)
Dr. Mariangela Settimo (Centre national de la recherche scientifique Subatech - Nantes)
Prof. Antonio Bueno Villar (Universidad de Granada)

fnrs LA LIBERTÉ DE CHERCHER

Ascoltatore: *"Forse gli anni passano, ma i mesi...ritornano!"*
Mario: *"MA CHE ***** VUOL DIRE?!?"*

Corrado Guzzanti - Il caso Scafroglia

Acknowledgements

It is not easy for me to write the acknowledgements since every person I met during these four years impacted me and my choices, leading me to this point: Writing these pages just three days before the public defence. Of course, some people had a more significant influence on me than others, and that's why I will try to name everyone on this piece of paper, hopefully not forgetting anybody (and if that is the case, please forgive me and do not add my name on your black-list).

First, I must thank my supervisor, Ioana, with whom I navigated these years and who guided me on this journey that I could not have done alone. I learned a lot from her, both professionally (with the desire to deliver meaningful and high-quality work, striving for the best) and in life, such as how to approach problems from different points of view and overcome difficulties that looked too big to handle. I hope I also taught her something, probably how to handle a difficult student who always has something to complain about!

I want to thank also the jury members for putting time and effort into reading this thesis carefully and improving the final result with interesting comments on the manuscript and during the private defence. In particular, Peter and Juanan, who were part of the PhD Committee that accompanied my research work at ULB.

The IIHE will have a special place in my heart for all my life, and I want to thank all the people who are the foundations of this place: the secretaries (Audrey, Sofie and Nina), the IT team and the directors, Jorgen and Barbara. A special mention and thanks to the ULB Science Faculty's secretary, Iustina, who has always been available and kind, helping me with all the bureaucracy, and to Mohamed, the cleaning staff, with whom I exchanged only "Bonjours" for four years because I don't speak French, but who supported me silently during these years, especially when he met me at 6 a.m. in the office while writing my thesis. The thumbs-up was a sign of encouragement.

Then there is the Auger group at the IIHE, a fantastic group of people who supported me in every way, always ready to help and encourage me. Thanks to Daniela, Nico, Mauricio, Katka, and Vincent: these years would have been much more difficult and less fun without you. It would take me an entire page to describe each of you and our great moments together! I'll write a separate book for that.

Some say that what is more important is the friends that you make during the journey rather than the journey itself. I am glad I found great people at the IIHE that I feel proud to call friends, starting from my office mate Rose (thanks for all the support, the conversations and the laughs!), and then Quique, always ready to cheer me up with a joke or introducing me to some obscured topic I had no clue about, Simon, always ready with unexpected jokes that almost broke me in the IIHE kitchen, Yarno Giacomo Massimo Manfredi (it's a full name), being as supportive as annoying while trying to speak in Italian and with whom I shared some of the most mature and most immature conversations ever (surprisingly most of the time in parallel), Jethro (the IIHE chef), Godwin (my buddy), Mitja (my Italian buddy), Dieder (fratello ritrovato), Felix (Felicino), Nhan, Denise and the newcommer Abby. With most of them we shared happiness, sadness, joy, frustration and, most importantly, memes. I am proud to be part of the "Howtie" group. There are so many people who made staying at IIHE much better and a place that felt like home, and I want to thank them: Simona, Nick, Krijn and Laurent (and I am probably forgetting someone).

And I will not forget the people who have been here at IIHE but already left, like Pablo (my bro, thanks for all the nice talks and the laughs, get well soon and we are going to celebrate again!), Paul, Nadège, Giovanni, Chris, Uzair and AR.

I want to thank the Auger Collaboration for the fruitful discussions and all the nice people I met during the meetings. With some of them, during the social dinners, we laughed until we cried. Il Maestro rimane sempre il migliore.

All of you had an important role, and I want to thank you all.

Besides the new people I met during my PhD, some people in my life have always been there, and I would not be here without them. I will start with the friends who are like my brothers: Toti, Peppe, Gianluca, Salvo and Andrea. We grew up together, and we will be there for each other in all the moments of our lives, and I could not be happier. These were difficult years, and you know that better than anyone else, but I knew I could always count on you. I want to thank all my friends in Sicily (Gianpaolo, Alessio la Madonna, Bakita, Manfredi, Peppe Salieri, Serena, Monica and all the others), in Milano (Alberto, Fabio, Giulia, Eliana, Rosy, Marco and many more) and all over the world. Even receiving a small message, a call, or a meme improved my day and, consequently, my life.

None of this would have been possible without my family. My parents have always been supportive, even when explaining what I was actually doing was difficult. They believed in me more than I did myself, so this achievement, in some sense, is theirs the same as it is mine. I want to thank my sister Valentina and my brother Totò for being so understanding, even when I am annoying or distant, and always caring for me, checking that I am okay and everything is going well. And their sons and daughters, Giuseppe (not so small anymore, almost as tall as me), Ginevra and Andrea, and their partners, Alessandra and Mattia, bringing joy during our family reunions. A big thank to my Nonna QuoQua, always checking on me and spoiling me whenever she could. Talking about grandparents, I cannot forget Nonna Biagia and Nonno Dad, that are not here anymore but still presents in our hearts.

Last but not least, the person who has been the most important for me in the last year and a half: Agatha. I would never have imagined finding someone as amazing as you. Just the simple thing of you being next to me made my life so much better. And on top of that, you have been so caring, kind and understanding during this stressful period and organized everything that otherwise would have overwhelmed me (for the readers, consider, for example, that she helped me prepare the thesis cover). I cannot find enough words to express all my feelings for you. But I can say that Ti Amo. Thank you for being the amazing person you are (and being with me, of course, shows that you also have good taste), and thanks also to your great family, who welcomed me and gave me huge support. She introduced me to amazing people (Jan, Asia, Mahault, Pieter, Paulina, Manu) that cheered for me in these months and I want to thank them for this.

Thanks to all the people I forgot to mention and those I did not want to mention. I am at this point in my life because of you (good or bad), and considering the great people surrounding me, I feel lucky. The last thing I want to say is better said in this video: https://youtu.be/GvpZ2mcUJWc?t=219

Now, let's move on to a new adventure!

Contents

Alla mia famiglia

Introduction

Cosmic rays were discovered over a century ago, and since then, they inspired the pursuit of knowledge regarding their origin and production mechanisms. They provided physicists with a natural laboratory in which particles are accelerated to the highest energies ever recorded. Indeed, these extraterrestrial particles, most of which are charged nuclei, arrive at Earth with energies up to 10^{20} eV, several orders of magnitude larger than the one produced at particle colliders, like the Large Hadron Collider at CERN, raising the question of which type of astrophysical objects can accelerate them at such high energies. Many questions remain open even if they have been studied for over a century. In particular, for cosmic rays at the highest energies ($E > 10^{18}$ eV), most of the mysteries are still unsolved, such as the type of nuclei arriving at Earth. These particles are called ultra-high energy cosmic rays (UHECRs), and one of the difficulties in answering the questions resides in their small number on Earth: Their flux steeply decreases as a function of their energy, reaching even a level of 1 particle per century per km^2 for energies above $10^{19.5}$ eV. Due to the low flux, the detection with experiments in orbit around the Earth is not feasible (as done for low-energy cosmic rays), and a vast area is needed to collect a statistically significant amount of data.

For this reason, more than 20 years ago, the idea of a vast cosmic ray observatory was conceived and brought to life. The Pierre Auger Observatory started to be built in 2002 and was completed after six years of deployment of its ground detectors, covering a total area of 3000 km^2. The Observatory exploits the characteristic feature of high energy cosmic rays that, upon their arrival at Earth, they interact with the atmosphere, producing a cascade of secondary particles that reach the ground, called extensive air shower. The Observatory was built in order to perform two independent measurements of the shower: The first consists of sampling the signals of shower particles at the ground with an array of water-Cherenkov particle detectors (exploiting the Cherenkov light produced in water by ultra-relativistic particles) called Surface Detector (SD), and the second technique measures the fluorescence light produce by the de-excitation of nitrogen molecules after the passage of the particles, using fluorescence telescopes (FD). The SD, with its 1660 water-Cherenkov tanks (WCD), possesses a 100% duty cycle, while the FD only a 15% one since it can be operated only during clear and dark nights. The latter is a strong constraint since the best estimator for the mass of the primary particle X_{max} is obtained with FD measurements. The other observable linked to the nature of the primary, the number of muons at the ground N_μ, is not directly accessible in the SD, which measures the convolution of all the secondary particles at the ground. The FD and SD measurements allow for calibration, crosschecks and combined studies, thanks to those events being simultaneously observed by both detectors. Employing these techniques, the Observatory has performed several studies on the origin of UHECRs (finding, for example, strong indications for an extragalactic origin), their possible sources (identifying Starburst Galaxies and Active Galactic Nuclei as possible candidates), the mass composition of these particles (with indications of heavier nuclei at the highest energies) and, at the same time, fundamental hadronic interactions, with the discovery of a discrepancy between data and simulations in which less muons

are observed in the simulated shower, thus called the *muon deficit*. Indeed, simulations of showers (based on hadronic interaction models) and the detector itself are employed as a comparison with data.

After almost 20 years of operations, signs of aging started to appear in the WCDs, showing a decreasing signal over time. This adds another discrepancy between data and simulations, since the array simulation does not contain the temporal dependency. In this work, the long-term performances of the SD have been studied, and the effect of aging in the number of triggered WCDs and the shape of the signals (through an observable called risetime) have been assessed. The next step consisted of understanding what is causing the aging in the WCDs and modelling the observed behaviour over time using dedicated detector simulations. The reflectivity of the internal walls of the tanks has been found to be the main contributor to the aging, and a model has been built to describe each WCD independently over almost 20 years of operations.

Having been able to describe the signal evolution over time for each WCD, a new and more realistic simulations library of reconstructed air showers has been produced and then validated with data, verifying that the decrease in time of the previously mentioned observables in data is reproduced in simulations and assessing the change in other high-level observables. The use of this new library also allowed for a deeper study of the aging effects in the reconstruction of air showers, in particular, the reconstructed energy and its resolution. Based on these simulations, the energy resolution was assessed. Measuring the air showers at one stage of their development on the ground leads to significant shower-to-shower fluctuations. They are described in Chapter 5. The total and the detector resolution have also been compared with data.

A more realistic, time-dependent description of the detector is also helpful in the studies of the properties of the shower, such as the muon number, since new techniques employing Deep Learning models have been used to extract mass-sensitive observables from the SD signals, such as N_μ from the raw traces of the WCDs. However, these models heavily rely on simulations for their training. The new simulations library has been used to train a Deep Neural Network designed to extract the muon time trace in the WCDs. This enabled the removal of time dependencies of the detector response in the network, which then was applied to data. With this information about the muons on the ground, preliminary studies have been carried out to understand the discrepancy between data and simulations due to incorrect hadronic interaction models.

Chapter 1

Ultra-high energy cosmic rays

Ultra-high energy cosmic rays (UHECRs) are charged particles coming from space and arriving at Earth with energies above 10^{18} eV, with the most energetic ones exceeding 10^{20} eV [1], more than three orders of magnitude larger than the energy reached at the Large Hadron Collider at CERN [2]. Besides being the most energetic particles known today, UHECRs are messengers of extreme and violent processes in the Universe, in which they are assumed to be created and accelerated.

UHECRs, however, are very rare: at energies above $10^{19.5}$ eV the flux of these particles on Earth is equal to 1 particle per century per km^2. A very large detection surface is thus needed to study them with sufficient statistics.

The Pierre Auger Observatory, located in Argentina, is the largest Observatory for cosmic rays and has been design to collect a significant amount of data to study the origin and the characteristics of UHECRs. The Observatory exploits the fragmentation process happening in the atmosphere when a very energetic cosmic ray arrives at Earth and, thanks to two different techniques employed, can infer the properties of the original particle that collided high in the atmosphere.

In this chapter, UHECRs and their features will be described and then the operation and some of the main findings of the Auger Observatory will be presented.

1.1 Cosmic rays

Cosmic rays (CR) are high-energy particles originating from sources beyond our solar system, such as supernovae and active galactic nuclei. They are ionized nuclei, mostly protons, with relativistic energies. The discovery of cosmic rays dates back over a century ago. Henri Becquerel's discovery of natural radioactivity in 1896 [3] opened the door for the study of this phenomenon, with the hypothesis that the origin of this radiation was to be attributed to elements at Earth. Pacini's underwater tests challenged the notion of Earth as the sole radiation source [4], but it was with Victor Hess's balloon flights in 1912 [5] that the extraterrestrial origin of cosmic rays was solidified and accepted, earning him a Nobel Prize. Pierre Auger's 1939 observations of coincident triggers in distant Geiger counters led to the discovery of extensive air showers [6], with Heitler's cascade model describing the electromagnetic shower component [7], proposed a few years later. The first ultra-high energy cosmic ray shower, exceeding 10^{20} eV, was identified by the M.I.T (Massachusetts Institute of Technology) group at Volcano Ranch in 1963 [8], marking the start of the UHECR study. Cosmic rays' exploration formed the basis of modern Particle Physics, thanks to critical findings such as antimatter, muons, and pions. For a more complete and historical overview of cosmic rays, see [9, 10].

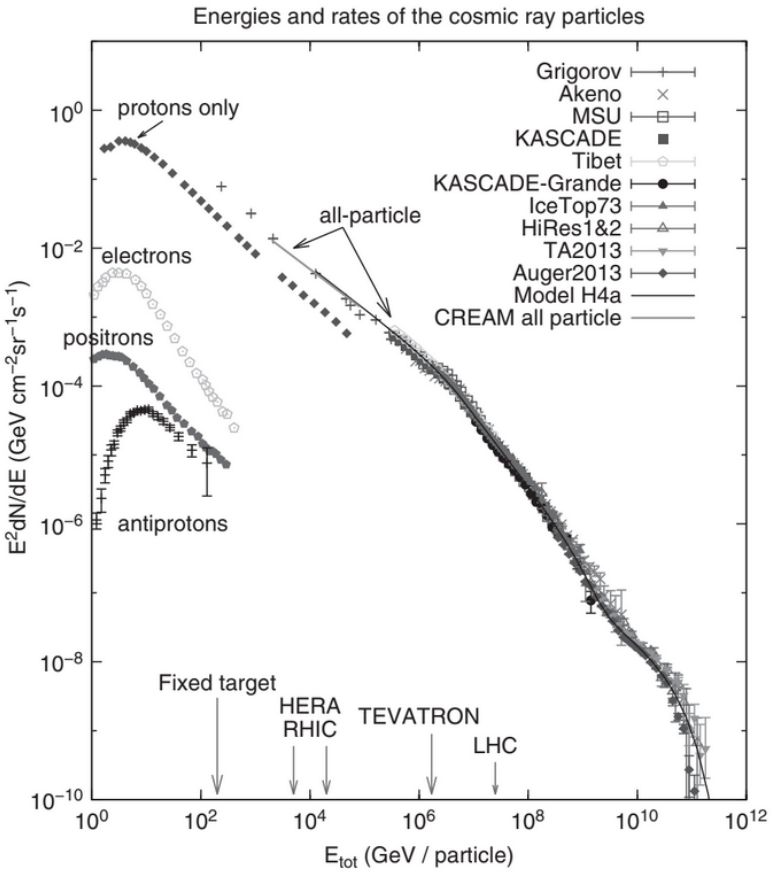

FIGURE 1.1: Cosmic rays differential flux for different experiments, spanning more than ten decades in energy [11]. The data are multiplied by E^2 to enhance the features of the spectrum. Comparisons with the center-of-mass energy of man-made accelerators are shown.

1.1.1 Spectrum

The energy spectrum of UHECRs stands as a fundamental window into the nature of these enigmatic particles. It represents the flux of UHECRs as a function of their energy, $J = \mathrm{d}N/\mathrm{d}E$, a parameter essential for understanding the mysteries of their origin, acceleration, and propagation. It covers more than ten decades, Fig. 1.1, in energy and decreases following a power-law $E^{-\gamma}$, in which E is the energy of the CR and γ is the spectral index, being ≈ 2.7. It can also be noticed that the number of CRs decreases rapidly with the energy, with only a few particles per km^2 per day above 10^{14} eV, becoming 1 particle per century per km^2 at energies above $10^{19.5}$ eV. A very large detection surface is thus needed to study them with sufficient statistics.

This spectrum is far from a simple power-law distribution; it contains features that enclose a complex mix of various physical processes.

The spectrum takes a significant turn at an energy around 10^{15} eV, with γ changing from 2.7 to 3.1. This transition point is known as "the knee" and holds clues about the acceleration and propagation mechanisms of cosmic rays within our galaxy. Indeed, at energies below the knee, it is assumed that the dominant contribution is of galactic origin, with supernovae remnants and binary systems as possible sources. The knee is thought to correspond to the energy beyond which the efficiency of the accelerators of the bulk of galactic CRs is steadily exhausted, providing insights into

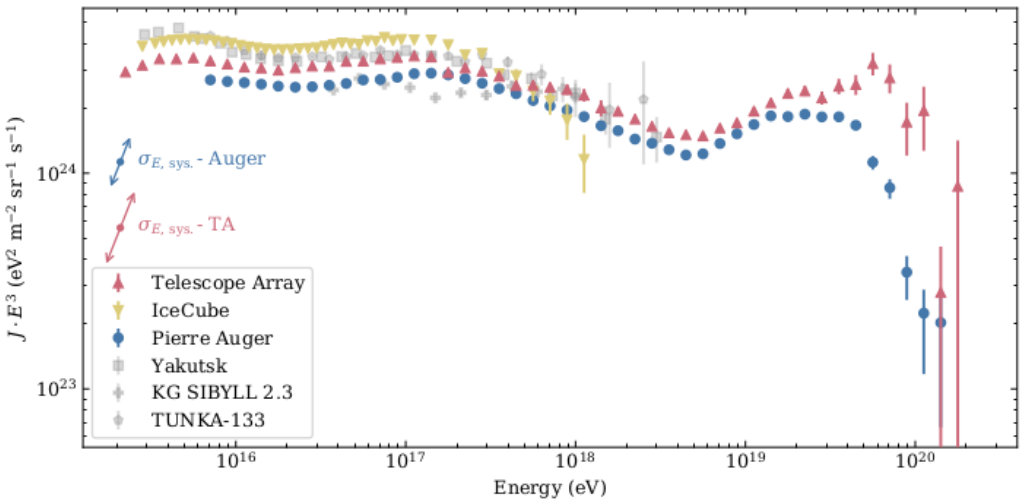

FIGURE 1.2: Measured spectrum from different experiments. Zoom on the high energies to emphasize the spectral features. From [12].

the limits of cosmic particle acceleration within our Milky Way. Around 10^{17} eV, a "second knee" emerges in the UHECR energy spectrum, characterized by a slight steepening of the flux, as visible in Fig. 1.2, where the flux has been multiplied by E^3 to heighten the different features of the spectrum. This feature is connected to changes in the composition of cosmic rays [13], with a transition from lighter cosmic ray nuclei to heavier ones; Thus, the "second knee" is also referred to as "iron knee", suggesting that havier nuclei are accelerated to higher energies. This can be explained as a consequence of a *Peters cycle*, in which the steepening happens at the same rigidity (E/Z, where Z indicates the atomic charge and E the energy of the particle), and thus at different energies for different particles [14].

At 5×10^{18} eV, the spectrum presents another feature called "the ankle." At this energy, the spectrum exhibits a flattening, with the spectral index assuming a value of ≈ 2.6. Cosmic rays at these energies are supposed to have an extragalactic origin, with a possible transition from galactic to extragalactic cosmic rays taking place between the second knee and the ankle. The extragalactic origin is supported by the presence of a dipole measurement with an amplitude of $6.0^{+1.0}_{-0.9}\%$ [15], which is inconsistent with isotropy and points in the opposite direction of the Galactic center [15, 16]. Potential extragalactic candidates include active galactic nuclei and gamma-ray bursts, which possess the capacity to accelerate particles to the energies associated with the ankle feature. Recently, a new feature called "instep" has been observed at $\approx 10^{19}$ eV [1] that can be described by an energy-dependent mass composition model [17].

At energies above approximately 5×10^{19} eV, a drastic reduction in the observed cosmic ray flux is observed, a phenomenon referred to as "suppression" or "cut-off" [18, 19]. This region holds critical information about the nature of cosmic ray sources and the fundamental interactions that govern their propagation. The origin of this suppression is still unknown, with two possible scenarios. The main one is related to the propagation of these highly energetic particles through the Universe to the Earth. The suppression arises from the interaction between UHECRs and cosmic microwave background radiation (CMB) or the infrared background (IRB) [20], producing resonances. In the case of protons with energy larger than 5×10^{19} eV [21],

the Greisen-Zatsepin-Kuzmin (GZK) effect [21, 22] takes place, in which pion production occurs through one of the following processes:

$$\begin{aligned} \gamma_{CMB} + \mathrm{p} \rightarrow \Delta^{+} \rightarrow \mathrm{p} + \pi^{0}, \\ \gamma_{CMB} + \mathrm{p} \rightarrow \Delta^{+} \rightarrow \mathrm{n} + \pi^{+} \end{aligned} \tag{1.1}$$

This initiates energy losses (around 20% for protons) that reduce their propagation distances up to 200 Mpc (assuming a uniform distribution of sources [23]), the so-called *GZK-horizon*. Heavier nuclei are affected in a similar way, through photodissociation processes [24]. In this case, the photon absorption cross section is mainly due to the giant dipole resonance, causing the excited nucleus to disintegrate in lighter nuclei and typically one or two nucleons. Other processes, such as photopion production and pair production, contribute to the total cross section.

The second possibility behind the presence of the cut-off in CRs flux could be attributed to the maximum energy attainable within cosmic sources' acceleration mechanisms. This upper limit varies among different nuclei, correlating with their atomic charge, Z. Consequently, the observed suppression emerges as an outcome of the intricate interplay of distinct energy cut-offs corresponding to various nuclei.

The suppresion is likely due to the concurrence of these two scenarios: maximum energy reached at the sources and energy losses during propagation. This is suggested by a combined fit of an astrophysical model where identical sources are uniformly distributed, and nuclei are accelerated through a rigidity-dependent mechanism to both the energy spectrum and mass composition data measured by the Pierre Auger Observatory [25].

1.1.2 Sources and anisotropies in the arrival direction

The origin and acceleration mechanisms of UHECRs remain enigmatic. While cosmic rays up to the GeV range are predominantly of solar origin, higher-energy cosmic rays must arise from different types of sources, given that solar processes lack the capacity to produce such energies. The maximum energy attainable by a charged particle depends on the characteristics of the source, more specifically on its radius R and magnetic field B, since particles are accelerated and confined in the source environment until $r_{\mathrm{L}} \leq R$, where $r_{\mathrm{L}} = E/ZeB$ is the Larmor radius of the particle. Charged particles are accelerated through a diffusive shock acceleration mechanism [26, 27], in which they gradually gain energy at each passing through a shock front, moving with a velocity $\beta = v/c$, due to the strong turbolent magnetic fields present in these regions. After being scattered multiple times, the energy E of a particle with charge Z is $E \approx \beta ZBR$. This relation, also known as the *Hillas criterion*, helps restrict the potential classes of sources that have the capability to accelerate particles to these extreme energies [28] . This classification can be seen in the so-called "Hillas plot" shown in Fig. 1.3, where the sources capable of accelerating protons (red) and irons (blue) up to 10^{20} eV are displayed.

Another difficulty in identifying the sources arises from the nature of these particles: Being charged particles, in their journey from these sources to Earth, they are deflected by galactic and extragalactic magnetic fields. Due to the deflections, tracing them back to the production site is not trivial, leaving the question of their origin open. Indeed, the deflection during propagation in the galactic magnetic field for a proton with energy 6×10^{19} eV is expected to be $\approx 5^{\circ}$ [31, 32]. Nonetheless, recent results have shown a large-scale anisotropy in the arrival directions of these

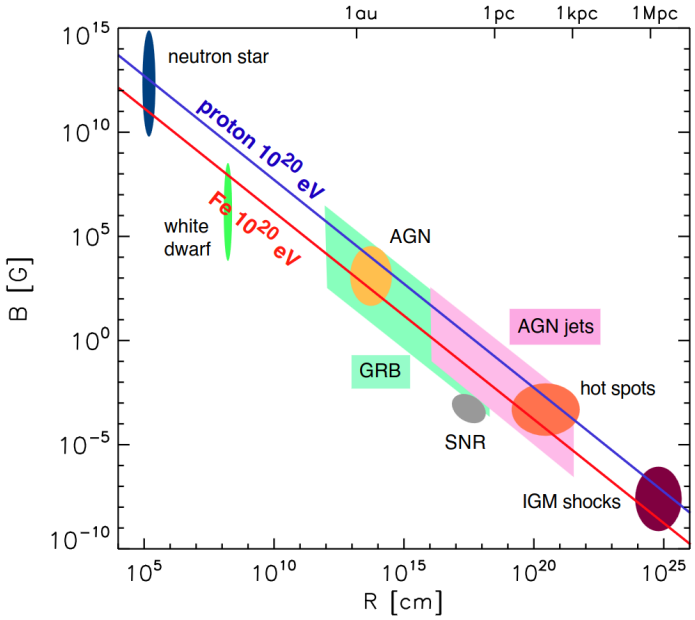

FIGURE 1.3: A Hillas-like plot for the potential sources for UHECRs according to their size and magnetic field strength. The lines correspond to proton (solid) and iron (broken) primaries accelerated up to 10^{20} eV, with $\beta = 1$. From [29].

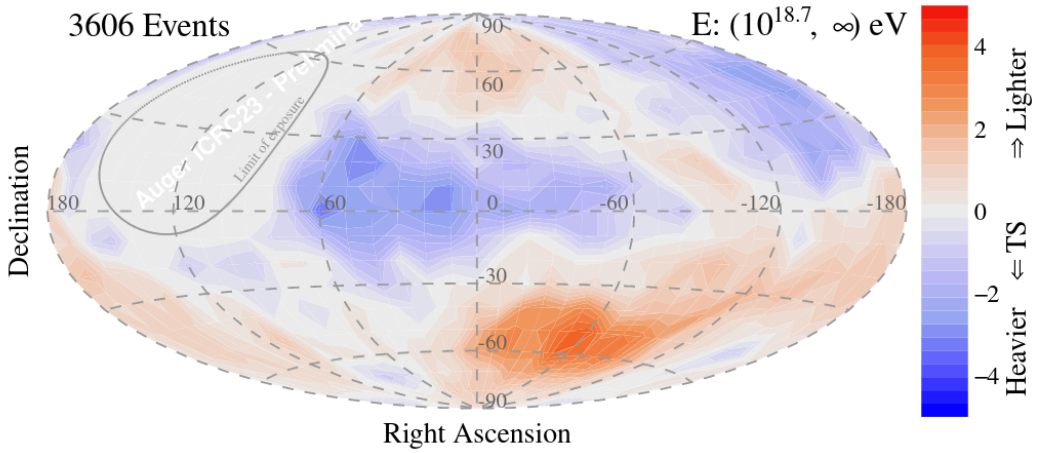

FIGURE 1.4: Sky composition map of cosmic rays in galactic coordinates for $E \geq 10^{18.7}$ eV. From [30].

particles for energies above 8×10^{18} eV with a 5.2σ level of significance, which is consistent with an extra-galactic origin [16]. Since the flux of UHECRs is suppressed due to the energy losses experienced during the propagation to the Earth, just the local Universe (at the *GZK horizon*) contributes to the observed flux and the anisotropies in the sky could offer essential clues towards the identification of nearby sources. Indeed, an excess from nearby sources has been found, suggesting that two classes of extragalactic sources, Starburst galaxies and Active Galactic Nuclei could be some of the plausible production sites of cosmic rays with energy above 39 EeV [33].

In addition, the deflection angle depends on the rigidity of the particle. Thank to their charge, heavier nuclei are thus deviated more than lighter ones with the same energy. Hints of mass-dependent anisotropies have been observed [34], for energies

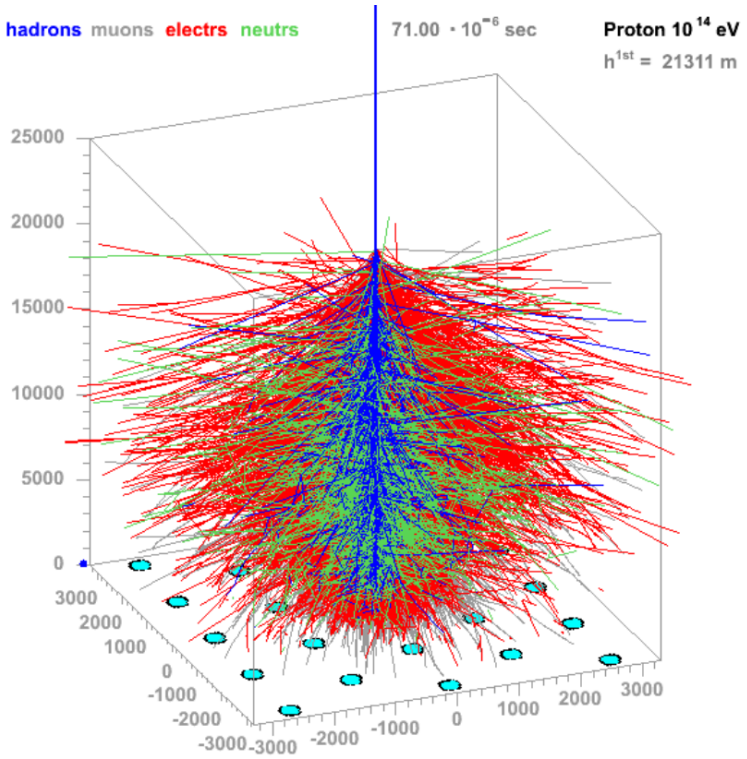

FIGURE 1.5: Simulated extensive air shower development for a vertical proton with energy 10^{14} eV. The different components are shown: hadrons (blue), muons (grey), electromagnetic components (red) and neutrons (green). From [35].

above $10^{18.7}$ eV, indicating that the mean mass of primary particles arriving from the galactic plane region (galactic latitude $|b| < 30°$) is larger than that of those coming from the off-plane region. This result provides an indication of the influence of the galactic magnetic field on the observed UHECRs sky. The latest results [30] show a presence of heavier elements along the plane again, displayed in Fig. 1.4 but a decrease in the correlation between them and the galactic plane. In order to confirm or not this anisotropy, more studies are planned, increasing the events in the sample by employing mass-sensitive observables estimated by the Surface Detector of the Pierre Auger Observatory, described later in the chapter.

1.1.3 Mass composition from Extensive Air Showers properties

A separation between cosmic rays with different masses can be achieved by exploiting the different features observed when these UHECRs reach Earth. A cosmic ray arriving on Earth (called a *primary*) interacts high in the atmosphere with an air nucleus, producing a cascade of secondary particles ($\approx 10^{10}$ at the sea level for a vertical proton with $E = 10^{19}$ eV), with the atmosphere acting like a calorimeter medium. This cascade is called an extensive air shower (EAS) and is made of three components: the electromagnetic one (γ, $e^{\pm}$) that accounts for the 99% of the secondary particles and the 85% of the total energy, the muonic ($\mu^{\pm}$) that represents the 10% of the energy, travelling through the atmosphere almost unaffected, and the hadronic one that is dominant at the start of the shower and feeds the other two components, reaching the ground with only $\approx$ 4% of the total energy. An example of a simulated EAS can be seen in Fig. 1.5, where the different components are displayed with a colour code. The shower footprint extends for a few km^2, becoming

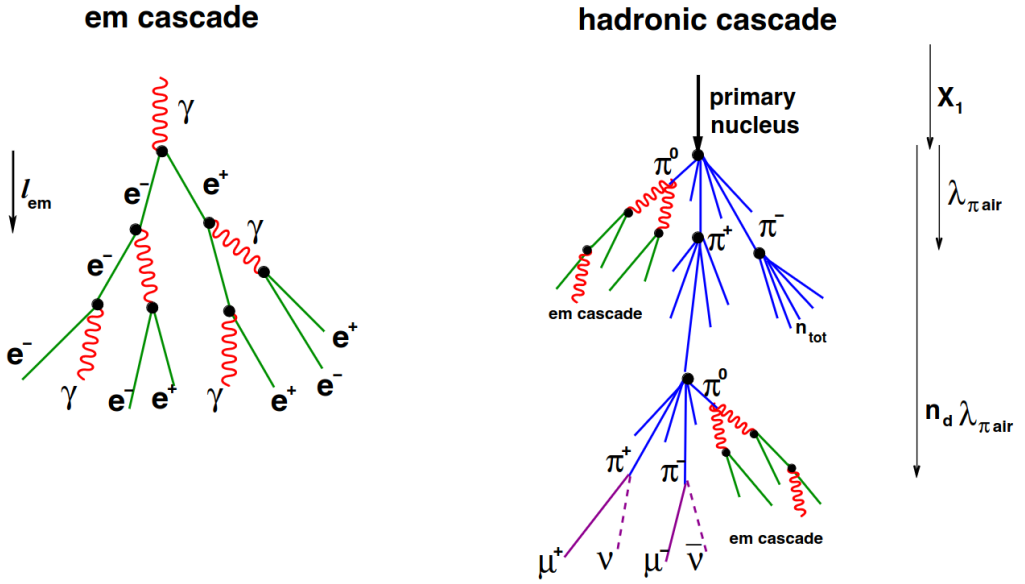

FIGURE 1.6: Schematic view of the development of the different types of cascades: Left, electromagnetic shower, right, hadronic shower. The black dots represent molecules of air. From [38].

larger as the energy increases. Air showers are simulated using detailed hadronic interaction models [36, 37]. However, a simple model for air showers, the Heitler model [7], can be employed to understand the basic features.

The Heitler model

The Heitler model describes the development of an electromagnetic cascade as a simple binary tree, left in Fig. 1.6, in which, at each step $l_{\rm em}$ of length $d = \lambda_r \ln 2$ (where $\lambda_r \approx 37\,\mathrm{g\,cm^{-2}}$ is the radiation length in air), a particle interacts with air nuclei, splitting into two particles, each with half of the initial energy. Specifically, electrons (or positrons) emit a γ via Bremsstrahlung, while for γ the relevant process is the electron-positron pair production. After n steps, $N_{\rm n}$ particles are produced and each one has an energy of $E_0/N_{\rm n}$. This chain of interactions continues until the particles' energy reaches a critical energy, $E_c^e \approx 80\,\mathrm{MeV}$, after which the losses due to ionization become dominant and particles start to be attenuated by the atmosphere. Thus, the maximum number of particles, $N_{\rm max}$ is reached at this stage and can be obtained as E_0/E_c^e. The atmospheric depth at which the EAS reaches the maximum number of particles is called $X_{\rm max}$ and is determined by the number of occurred steps, translated in a logarithmic dependency on the energy of the primary particle:

$$X_{\rm max} = X_0 + \lambda_r \ln(E_0/E_c^e) \tag{1.2}$$

where X_0 is the height in the atmosphere where the first interaction takes place.

Hadronic showers

The model developed for electromagnetic cascades can be generalized to hadronic showers by assuming that, in this case, when a hadron of energy E interacts with an air nucleus, $N_{\rm tot}$ pions are produced after each interaction, each one with energy $E/N_{\rm tot}$. Two-thirds of these particles, $N_{\rm ch}$, are charged pions ($\pi^{\pm}$) and one-third

are neutral pions (π^0). The latter decay almost immediately into 2γs, creating pure electromagnetic sub-showers, thus feeding the electromagnetic component.

Charged pions will continue to experience interactions, with the same distance between each step governed by the hadronic interaction length, λ_π, as $d = \lambda_\pi \ln 2$, until a critical energy ($E_c^\pi \approx 20\,\text{GeV}$ in air) is met, at which the decay length is comparable to the interaction length. Thus, pions are more likely to decay into muons and neutrinos than keep interacting. To reach this critical energy, n_d interactions are needed:

$$E_c^\pi = \frac{E_0}{(N_\text{tot})^{n_\text{d}}} \qquad \Rightarrow \qquad n_\text{d} = \frac{\ln(E_0/E_c^\pi)}{\ln N_\text{tot}} \tag{1.3}$$

The number of muons, N_μ, is then equal to the number of charged pions at the critical energy:

$$N_\mu = (N_\text{ch})^{n_\text{d}} \qquad \Rightarrow \qquad \ln N_\mu = n_\text{d} \ln N_\text{ch} = \ln(E_0/E_c^\pi)\frac{\ln N_\text{ch}}{\ln N_\text{tot}} \tag{1.4}$$

$$N_\mu = \left(\frac{E_0}{E_c^\pi}\right)^\beta, \qquad \text{with} \quad \beta = \frac{\ln N_\text{ch}}{\ln N_\text{tot}} \tag{1.5}$$

These results show that the number of muons grows as a function of the primary energy following a power-law, with an index, β, that depends on the pions multiplicity. In detailed simulations of the showers, this parameter has been found to range between 0.9 and 0.95 [39]. This parameter can also be studied by measuring the number of muons at the ground for different energies, Chapter 6. Air-shower simulations are performed with softwares, such as the `CORSIKA` software [40], in which the interactions are modelled using extrapolations at the highest energies of hadronic interactions measured at the LHC. Some of the most known post-LHC hadronic interaction models are EPOS-LHC [41], Sibyll [42] and QGSJET [43]. After particles are generated, their path in the atmosphere is followed until they interact again, decay or reach the ground.

The above-described model is for a shower initiated by a proton primary. However, the model can be easily extended to heavier primaries by considering a nucleus of mass A and energy E_0 as A independent nucleons with $E_\text{h} = E_0/A$. This approximation, called the *superposition model*, proves to be highly effective since the binding energy per nucleon (in the order of 5 MeV) is much smaller than the energies at which interactions occur. Due to this, Eq. (1.2) and Eq. (1.5) can be expressed for heavier elements as

$$X_\text{max}^A(E_0) = X_\text{max}(E_0/A) \tag{1.6}$$

$$N_\mu^A(E_0) = A^{1-\beta}\left(\frac{E_0}{E_c^\pi}\right)^\beta. \tag{1.7}$$

From Eq. (1.6), it can be noticed that showers induced by lighter elements develop deeper in the atmosphere compared to heavier ones, which instead reach their maximum at higher altitudes, allowing discrimination between primaries. Measuring the secondary particles that reach the ground, instead, can also provide information about the primary mass: the number of muons (N_μ) that reach the ground is larger as the mass of the primary particle increases, as obtained in Eq. (1.7). These two observables are highly correlated and can be used to discriminate between different primaries.

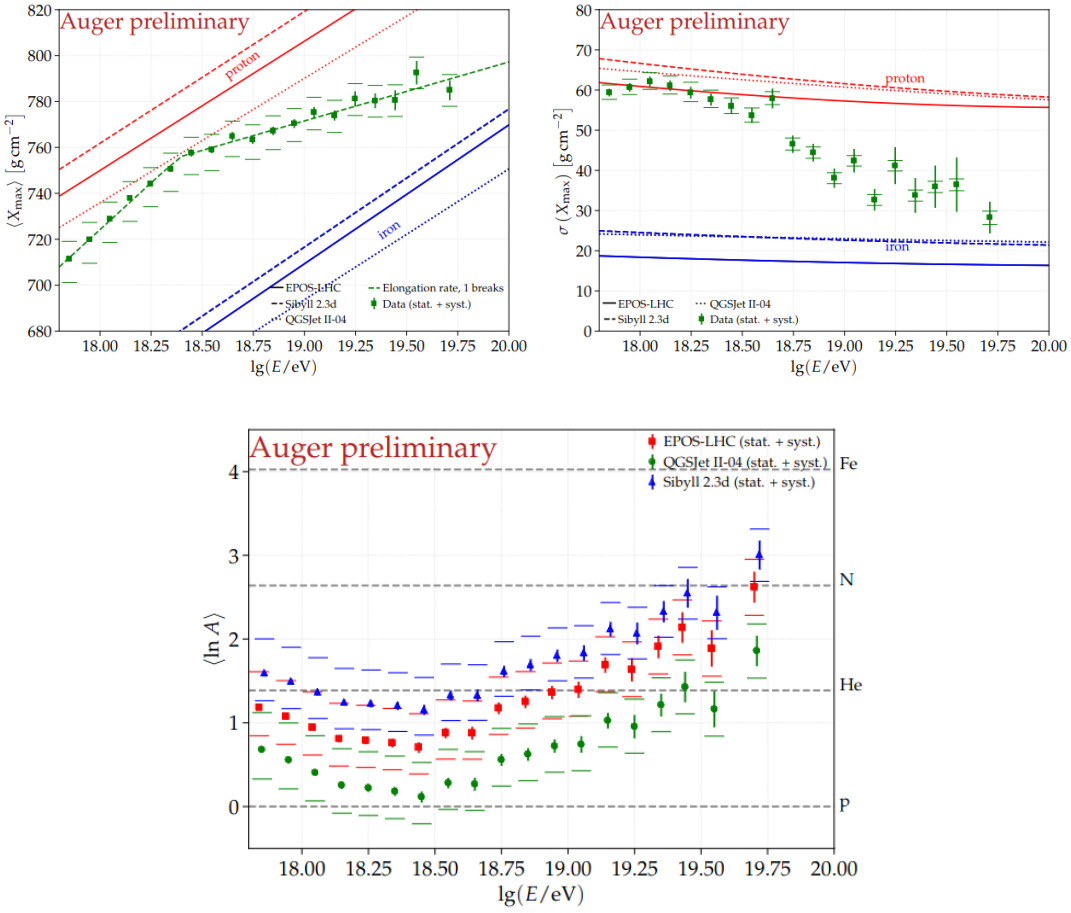

FIGURE 1.7: Top: Evolution as a function fo the energy of $\langle X_{\max} \rangle$ and $\sigma(X_{\max})$ obtained from $X_{\max}$ distributions. The dashed green line represents the elongation rate fitting. Bottom: $\langle \ln A \rangle$ versus energy, obtained from converting $\langle X_{\max} \rangle$. From [44].

$X_{\max}$ measurements

In order to unveil the mass composition of UHECRs, measurements of the longitudinal profile of showers have been performed by observing the fluorescence light emitted by the de-excitation of nitrogen molecules when charged particles of the shower pass through the atmosphere. Indeed, the amount of fluorescence light is proportional to the energy deposit [45, 46] and the depth where the energy deposit is maximum, $X_{\max}$, is obtained from a fit to the longitudinal profile. Unfortunately, due to fluctuations in the early stage of the shower development, an event-by-event mass determination cannot be obtained but the composition trend with energy must be inferred from the mean and standard deviation of $X_{\max}$ distributions.

The most recent results from the Pierre Auger Observatory [44], that include 60% more events compared to the previous work [47] (due to the addition of four more years of data and improved cuts) and improved aerosol attenuation measurements [48] as well as a new reconstruction of the longitudinal profiles [49], are shown in Fig. 1.7, top: The elongation rate, that refers to the change of $X_{\max}$ with $\ln E$ that can be observed on the left plot, has a fitted value of $\approx 81\,\mathrm{g/cm^2/decade}$ up to the break at $\approx 10^{18.4}\,\mathrm{eV}$ and after that is $\approx 28\,\mathrm{g/cm^2/decade}$. Since the elongation rate is expected to be the same for any primary [36], this behaviour points towards a composition becoming lighter from $10^{17.8}\,\mathrm{eV}$ to $10^{18.3}\,\mathrm{eV}$ and getting heavier after

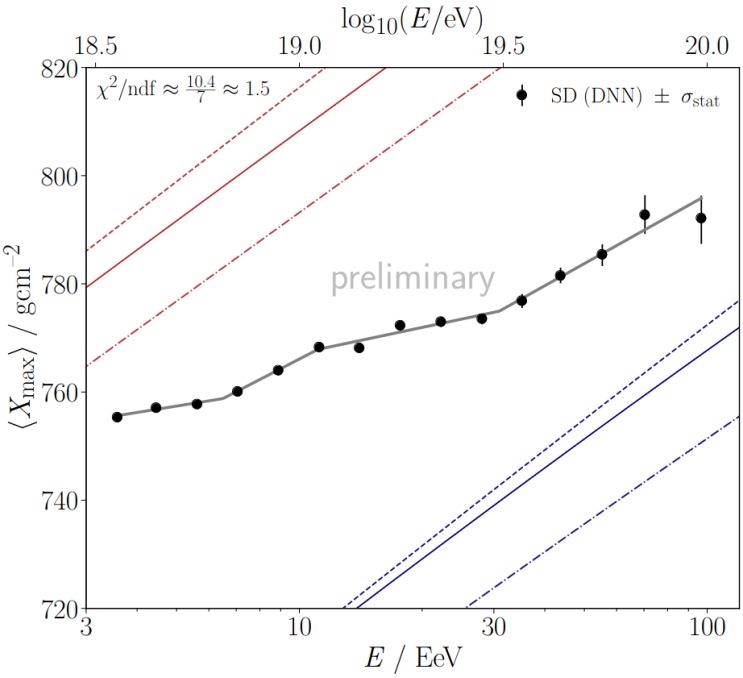

FIGURE 1.8: Fit of the mean X_{max} with a piece-wise linear function. From [54].

the break; the evolution of $\sigma(X_{\text{max}})$ suggests a mixed composition before the break and a purer one as the energy increases, as found in previous studies [50].

The same evolution of the composition is observed when converting the X_{max} values into the logarithm of the mass number A using simulations, shown in Fig. 1.7 for different post-LHC hadronic models. The equation to obtain $\langle \ln A \rangle$ [51], based on [52] assuming the validity of the *superposition model* and a linear relation between X_{max} and the logarithm of the primary energy, is

$$\langle \ln A \rangle = \ln 56 \cdot \frac{\langle X_{\text{max}} \rangle_p - \langle X_{\text{max}} \rangle_{\text{data}}}{\langle X_{\text{max}} \rangle_p - \langle X_{\text{max}} \rangle_{Fe}} \quad . \tag{1.8}$$

Recent studies employed Deep Learning algorithms to infer the X_{max} from the signal of secondary particles reaching the ground [53], increasing statistics significantly by a factor of 10 and extending the current measurement of X_{max} to the highest energies. A characteristic and more complex structure in the evolution of X_{max} over the energy has been identified [54], suggesting three breaks in the elongation rate, as shown in Fig. 1.8, where a piece-wise linear function is fitted to data. These breaks occur in positions where the ankle, the instep and the suppression are observed in the spectrum. More studies are being carried out to investigate these features. A description of the DNN studies can be found in Chapter 6.

N_μ and the *muon deficit*

The other mass-sensitive observable, as it was shown in Eq. (1.7), is the number of muons at the ground, N_μ. The two experiments at the highest energies that are able to collect the secondary particles at the ground, Auger and Telescope Array (TA), do not have, with their standard surface detectors, the capability to measure the muonic content in a direct way (while for the Auger upgrade, instead, an Underground Muon Detector was deployed to directly measure the muons [56, 57]). In

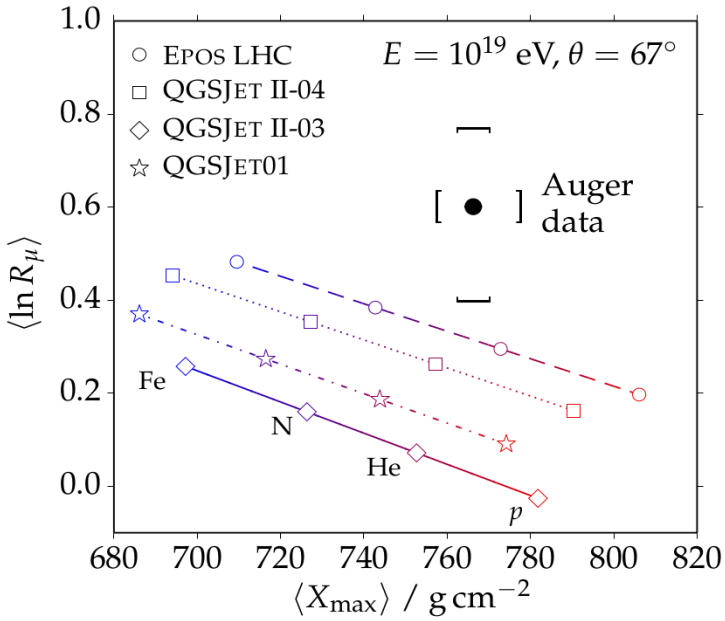

FIGURE 1.9: Average muon content $\langle \ln R_\mu \rangle$ as a function of the average shower depth $X_{\max}$ at 10^{19} eV. Simulated showers have a zenith angle of 68°. From [55].

Auger's case, for example, the recorded signal in each of the stations (used to sample the shower) of the ground array is the convolution of all the particles entering the station, thus it is not possible to directly obtain N_μ. A way to measure the muons in Auger can be achieved due to its design that allows to measure the signal deposited at the ground by showers with a large inclination, $\theta > 62°$ and up to 80°. Indeed, these showers travel a longer path in the atmosphere, which causes the attenuation of the electromagnetic component of the shower, leaving them as the main contribution of the recorded signal in the stations.

Measurements of these *inclined showers* have been performed by the Collaboration [55], and they revealed an interesting scenario: the number of muons in simulations appears to be lower than the one measured in data that is reconstructed by fitting a model of the lateral profile of the muon density at the ground to the observed signals. This discrepancy between data and simulations (called *muon deficit*), is in the order of 30% to 80^{+17}_{-20}%(sys.) at 10^{19} eV depending on the model. The disagreement can be seen in Fig. 1.9, where the lack of overlap between the data point measured by Auger and the prediction lines is clear. The observable R_μ shown in the plot is obtained as the ratio between the integrated number of muons at the ground and a reference given by the average number of muons in simulated proton showers at 10^{19} eV and given zenith angle, and, thus, it is proportional to N_μ. A deficit in the number of muons has been observed in other experiments and with other techniques [58, 59], as well. The origin of the lack of muons in simulations could to be related to a small deficit at every stage of the shower development that accumulates along the path rather than a discrepancy in the first interaction, as suggested by the agreement of the fluctuations in the number of muons in data and simulations [60]. These fluctuations are, indeed, dominated by the processes in the first interaction. Thus, models that, in order to increase the number of muons in simulations, modify the first interaction would directly change the fluctuations. Henceforth, no adjustments to the first interaction and, instead, a small deficit in every hadronic interaction during the shower development will increase the number of muons and keep

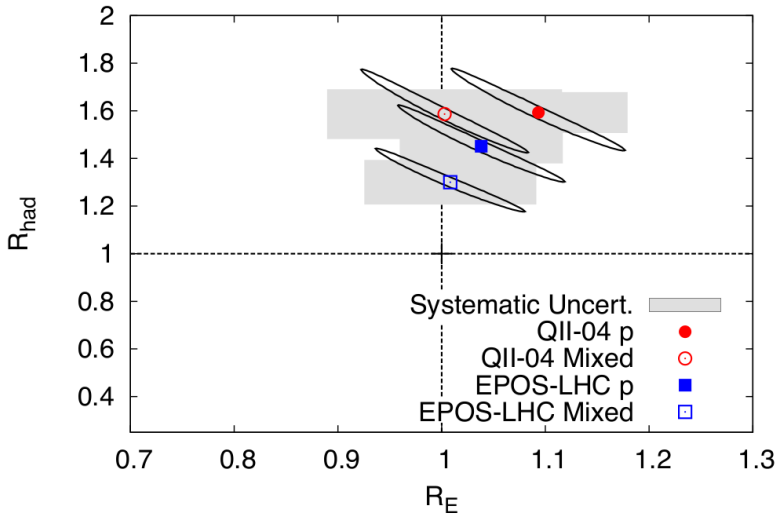

FIGURE 1.10: Values of the energy and hadronic rescaling obtained from the fit (see text) for QGSJet-II-04 and EPOS-LHC, for pure proton (solid circle/square) and mixed composition (open circle/square). From [61].

the fluctuations in agreement with data.

An overall energy rescaling, R_E as a cause of the deficit has also been studied and ruled out [61], while at the same time a rescaling of the hadronic shower signal, R_{had}, has been found to be quite large $\approx 1.3 - 1.6$, depending on the hadronic model, Fig. 1.10. This analysis was performed using showers that were measured both in the atmosphere and on the ground. For each shower, the measured longitudinal profile was matched to simulations and having characterized the shower in this way, the ground signal was simulated and compared with the measured one.

Since N_μ is sensitive to hadronic interactions, the observed discrepancy shows that the hadronic models in simulations are inaccurate, not being able to properly reproduce the data. What exactly is causing the mismatch is not yet clear, if incorrectly modelled features of hadron collisions or the the appearance of new phenomena in hadronic interactions at very high-energy, but the simultaneous comparison of independent air shower observables, such as X_{max} and N_μ can constrain the phase space of hadronic models. These studies are, however, limited in statistics due to the use of inclined events and fluorescence measurements ($\approx$ 15% duty cycle). The use of Deep Learning models can increase the statistics and provide a way to study the presence of the muon deficit also for vertical events, as it will be shown in Chapter 6. These models, in turn, are trained using simulations that require a detailed description of the detector over the years, Chapter 4.

1.2 The Pierre Auger Observatory

The Pierre Auger Observatory is located in Argentina, covering an area of 3000 km^2 in Pampa Amarilla [62], near the town of Malargüe in the Province of Mendoza. The area presents optimal characteristics for the measurement of EAS, with flat land and an average altitude of 1400 m, corresponding to an atmospheric overburden of $\approx$ 875 g/cm^{-2} and, thus, close to the shower maximum in the atmosphere. Auger is the largest experiment ever built to detect air showers and to infer the properties of primary cosmic rays with energies above 10^{17} eV. The Observatory operates in

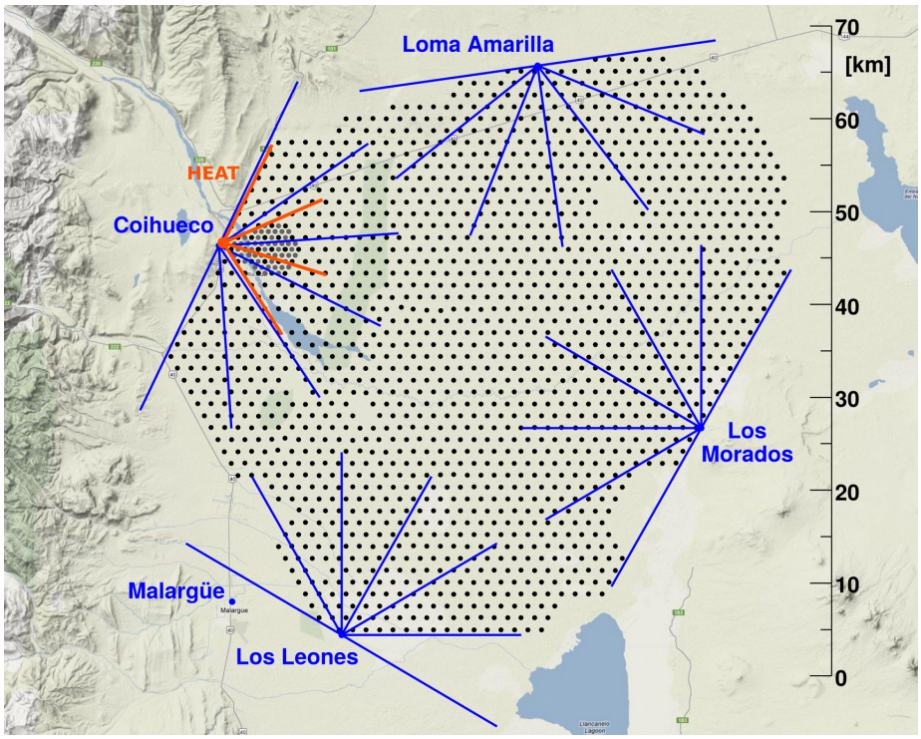

FIGURE 1.11: The Pierre Auger Observatory. Each black dot represents a water-Cherenkov station of the surface detector array, which is overlooked by the fluorescence telescopes with their view fields indicated in blue. Three extra high elevation (HEAT) telescopes are shown in red.

the so-called *hybrid mode*, combining a fluorescence detector (FD) composed of 27 fluorescence telescopes placed in four sites measuring the longitudinal profile of the air shower in the atmosphere and a surface array (SD) composed of 1660 water-Cherenkov detectors (WCD), spaced 1.5 km apart to sample secondary particles at the ground. The simultaneous use of these two complementary techniques provides cross-checks and measurement redundancy.

The map of the Observatory with its components can be seen in Fig. 1.11. The FD detects the fluorescent light produced by the excited nitrogen molecules during the shower development. Observing the air shower's longitudinal profile makes it possible to directly measure the $X_{\max}$ and energy of the primary due to a near-calorimetric measurement. This can be done only during clear and moonless nights, limiting the FD duty cycle to 15% of the time. The SD measures the lateral distribution of the air shower at the ground using the signals recorded by WCDs. Since the SD operates regardless of the weather conditions, it has a duty cycle of $\approx 100\%$. Thus, the amount of statistics gathered with the SD is much larger than that in hybrid mode.

The Observatory has also undergone a recent and almost complete upgrade [63], called AugerPrime, to enhance the sensitivity to the different components of extensive air showers (deploying new detectors such as radio antennas, buried muon detectors and scintillators) as well as increasing the data quality (using improved electronics and extending its dynamic range).

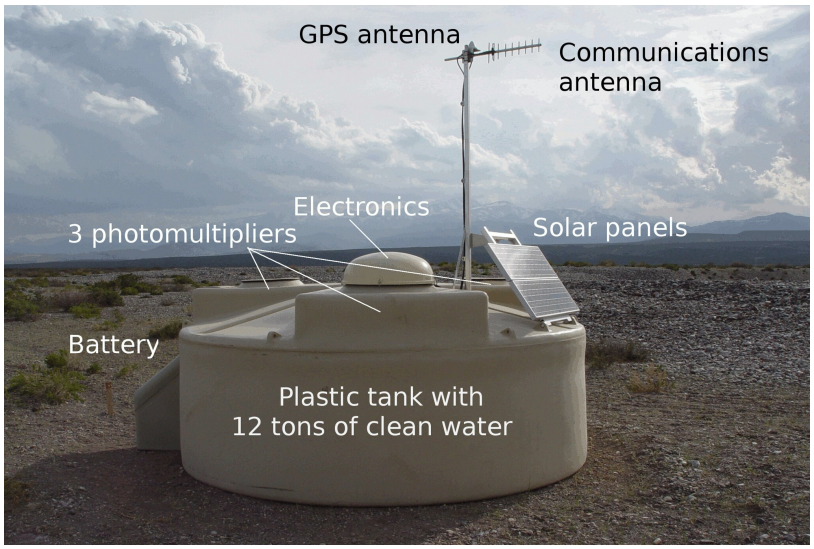

FIGURE 1.12: Picture of a Water Cherenkov Detector in the field with the description of its component. From [64].

1.2.1 Surface Detector

The deployment of the SD started in 2002 and was completed in 2008, while the data acquisition started in 2004 with an engineering array of 100 stations. The long-term perfomances of the detector during the years will be discussed in Chapter 2. The spacing of 1.5 km between the stations makes the array fully efficient for cosmic rays with energies above $10^{18.5}$ eV. Each WCD station, with an example shown in Fig. 1.12, is composed of tank with a height of 1.2 m and a diameter of 3.6 m, containing 12 t of ultra-pure water. This water is contained in a liner bag that has the internal walls covered with a reflective material called Tyvek^{TM}. Three 9-inch diameter photomultipliers (PMTs), symmetrically distributed at 1.2 m from the tank centre, are optically coupled using optical silicone to UV-transparent polyethylene dome windows fitted in the liner and facing the water. The PMTs look downwards into the station to collect the Cherenkov light, which is produced by relativistic charged particles when traversing the water and is multiply reflected by the internal walls.

Stations are equipped with a solar power system that provides 10 W for the PMTs, the electronics (contained in an aluminium dome on top of the tank) and the communication system, used to send the data to the Central Data Acquisition System (CDAS). Due to this power supply and batteries, stations are autonomous and independent, and for this reason, they require a reliable and robust self-calibration performed in situ. The calibration procedure is based on rescaling recorded raw signals to units of VEM, which is the signal released by a vertical muon in a tank. The station's calibration is explained in more detail in Section 2.1. A GPS receiver, installed in each station, serves as a synchronization between the stations and retrieves the events' timestamps.

During the years of operation, stations' signals have also shown a decrease over time, Chapter 2, which is necessary to understand and model (Chapter 3) to properly describe the detector (Chapter 4) and assess the induced effects on high-level variables.

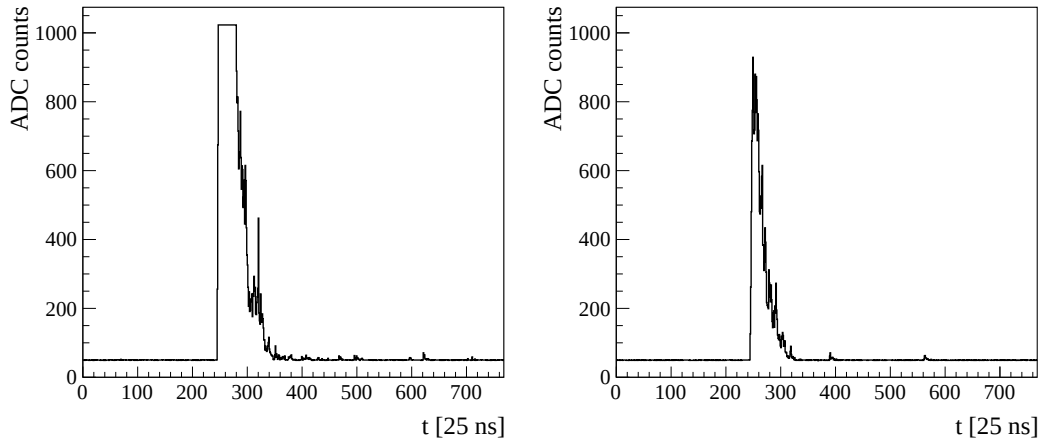

FIGURE 1.13: Two examples of dynode signals recorded in a station from a single PMT. Left: Saturated trace. Right: Non-saturated trace.

SD electronics

The high voltage (HG) necessary for the functioning of the PMTs is provided locally by a module integrated into the PMT base, with a nominal operating gain of 2×10^5, extendable to 10^6. For each PMT, two signals are read out: the signal at the anode and the signal at the last dynode, with the latter being inverted and amplified by a nominal factor of 32. This allows a dynamic range capable of measuring close to the shower core (down to a distance of about 500 m for a CR with 100 EeV [62]) and a large distance (due to the amplification performed to the last dynode signal). The signals in the tanks are filtered and digitized by a 40 MHz 10-bit Flash Analog Digital Converter (FADC). Signals are, thus, described in terms of FADC counts every 25 ns, and are read by a programmable logic device (PLD), that is in charge of trigger decisions, described later in the text, on the signal. The signal of the six FADCs traces (2 per PMT) is sampled in 768 points for a total time length of 19.2 μs.

Closer to the shower core, the high gain channel (dynode) can saturate, as shown in Fig. 1.13, and not be reliable for reconstructing the shower properties. In these cases, the low-gain channel (anode) is used. If both channels are saturated, methods have been studied and implemented to recover the signals [65, 66].

SD triggers

The triggers used to identify air showers are implemented in a hierarchical structure [67], with triggers at the station level (T1 and T2), at the array level (T3), physics triggers (T4) and, finally, quality triggers (T5). The last two triggers are off-line triggers and are associated more with the event-level selection than detector triggers, but they will be briefly discussed here.

The T1 trigger is the first one to be applied and it can be realized in four different modes: 1) Threshold trigger (Th), in which a 3-fold coincidence of the PMTs in a station having signals larger than 1.75 VEM is required, 2) time-over-threshold trigger (ToT), requiring a signal above 0.2 VEM for 13 FADC bins in a time window of 3 μs for at least 2 PMTs, 3) ToT-deconvoluted trigger (ToTd) [68], that improves the regular ToT by deconvoling the traces before applying the ToT condition,

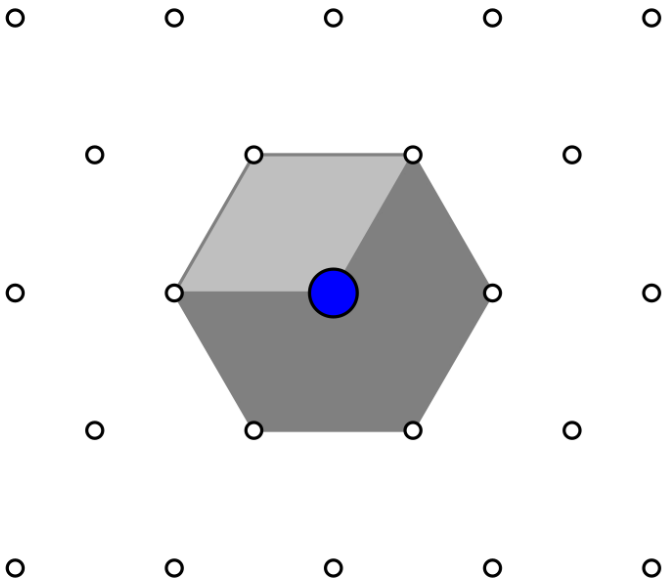

FIGURE 1.14: Schema of the 6T5 configuration, with the *hottest station* shown in blue and surrounded by 6 working stations. From [66].

4) multiplicity-of-positive-steps trigger (MoPs) [69] counts the number of positive-going signal steps above a certain threshold in two of three PMTs within a 3 μs sliding window. The last two triggers were implemented later (2013) than the first two and were designed to be less influenced by muons, increasing the trigger efficiency for photon and neutrino showers.

The second level trigger (T2) applies stricter conditions to reduce the trigger rate to about 23 Hz, to avoid saturating the bandwidth of the communication system. Th triggers can be promoted to T2 only if, in a 3-fold coincidence between the PMTs, the signals are above a threshold of 3.2 VEM, while all the other T1 triggers are directly promoted to T2. The data acquisition system of the station transmits the timestamps of the T2 events collected each second to CDAS.

At the CDAS level, then, the T2 signals are analyzed by looking at time coincidences to determine the stations that belong to a potential air shower. This trigger, called T3, has two different modes in order to improve the detection of vertical ($\theta < 60^\circ$) and inclined showers ($\theta < 60^\circ$).

The physics trigger, T4, is needed to discriminate between real showers from the set of stored T3 data and random coincidences of single atmospheric muons. To determine incompatibilities between adjacent stations and identify signals produced by random muon signals, a requirement for the stations has to be satisfied in order to be part of an event. This condition requires the difference between their timestamps to be lower than the distance between stations divided by the speed of light, allowing for a marginal limit of 200 ns. This condition comes from the assumption of the shower front as a planar front moving with the speed of light.

The last trigger, the quality trigger T5, is a fiducial cut designed to exclude events that are not fully contained in the array, which could lead to a possible missing signal and lack of accuracy in the reconstruction of the air shower. In practice, for a set of stations that are flagged as part of an event, the station with the highest signal (the *hottest station*), is required to have six nearest working neighbours (not necessarily

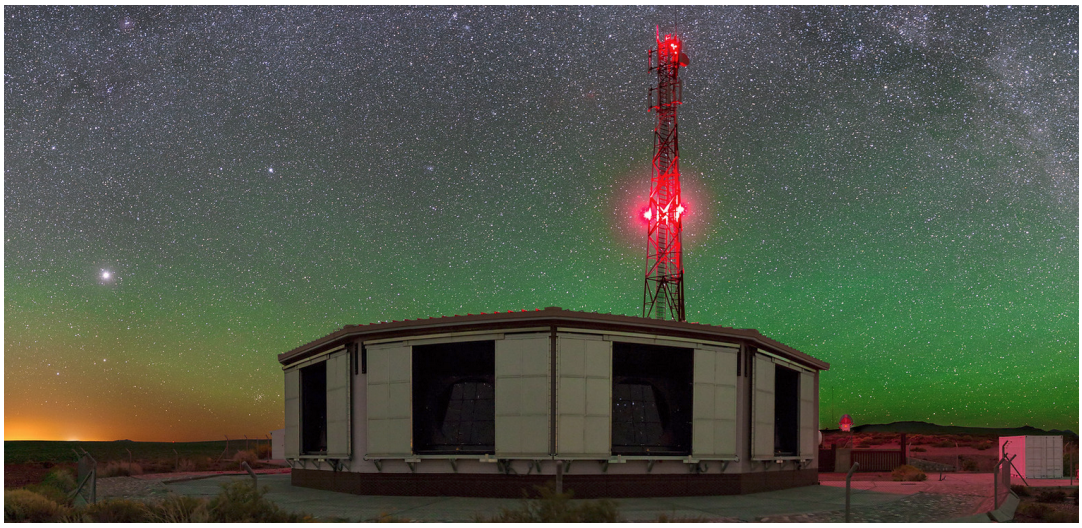

FIGURE 1.15: Picture of an FD site, where four of the six telescopes' apertures are visible. From [64].

triggered) at the time of the event. This criterion, a schema of which can be observed in Fig. 1.14 is also called 6T5 and assures an unbiased reconstruction of the shower. A less stringent version, called 5T5, requires only five active neighbours and can be used for arrival directions studies [15] in order to increase the statistics.

1.2.2 Fluorescence Detector

The standard FD conducts surveys in the SD area from four different sites: Los Leones, Los Morados, Loma Amarilla, and Coihueco [70]. Each site, as the one shown in Fig. 1.15, is equipped with six fluorescence telescopes that cover a field of view of 180° in azimuth and 30° in elevation together. These telescopes are inwardly pointed to observe the atmosphere above the SD and have a $30° \times 30°$ field of view in azimuth and elevation. An extension to measure lower energies has been obtained with the deployment of three other telescopes, HEAT (High Elevation Auger Telescope), at the Coihueco site that, additionally to the standard horizontal mode, can be tilted upward by 29° to observe showers that interact higher in the atmosphere.

The telescope's setup includes several components to enhance its performance, and it is shown in Fig. 1.16, left. The design is based on Schmidt optics to minimize coma aberration in large optical systems. The fluorescence light, produced by the air shower in the atmosphere, passes through a circular diaphragm having a 1.1 m radius aperture covered with a UV-transmitting filter glass that reduces the background light, thus improving the signal-to-noise ratio while at the same time, keeping the environment clean and climate-controlled. An annular lens is placed around the diaphragm, in the outer part, to correct for spherical aberration. The light is then collected by a spherical hexagonally segmented mirror, with an area of $\approx 13\text{m}^2$ and a curvature radius of 3.4 m, and focused on the camera. The camera is composed by 440 PMTs, arranged in a 22×20 matrix, each one representing a 1.5° field of view pixel of the spherical focal surface that has a radius of 1.7 m. For each PMT, the light is collected to the active cathode by simplified Winston cones, avoiding dead spaces between the PMT cathodes and separating them. A head electronic unit is connected to each PMT, sending the signals to an analog board for filtering and amplification.

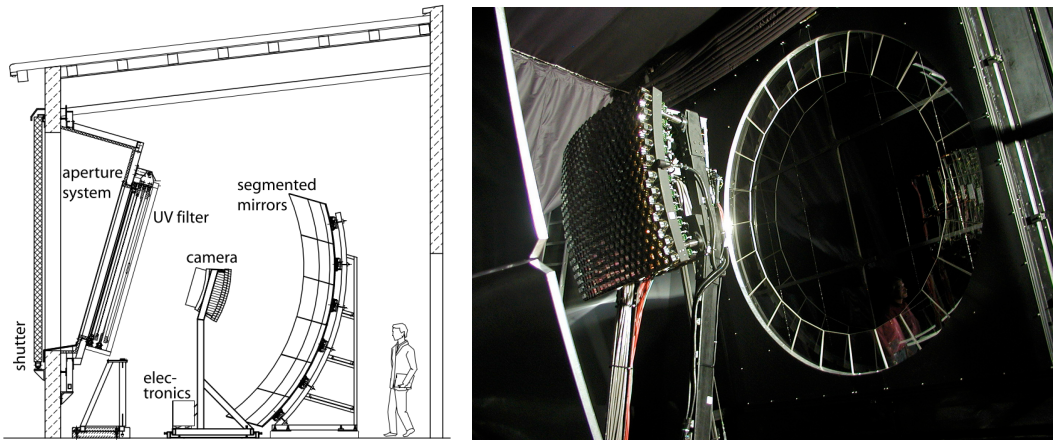

FIGURE 1.16: Left: Schematic view of the telescope setup. Right: A picture showing the camera and the diaphragm. From [64].

The board can handle 22 channels, controlling the gains of the PMTs, and is linked with the digital front-end board, which houses the trigger boards.

To protect the telescope, shutters are present to block daylight and automatically close in high wind or rain conditions. Furthermore, a fail-safe curtain is installed behind the diaphragm to prevent daylight exposure in case of shutter malfunctions or issues with the Slow Control System, which is responsible for remote operations of the FD system. Regular cleaning and maintenance are performed to ensure optimal detector operation. The external UV filter is cleaned multiple times a year to remove dust deposits, while equipment inside the building requires less frequent cleaning due to its protected environment. Different cleaning methods have been employed for the mirrors to improve their reflectivity, which is measured periodically and shows minimal changes over time, with less than a 1% variation per year.

1.3 Event reconstruction

From sampling the secondary particles at the ground with the SD, several properties of the shower, such as the arrival direction and the shower size (an estimator of the primary's energy), can be inferred. The shower reconstruction in Auger [71] is implemented and performed using in-house software developed by the Collaboration, Offline [72].

The event building, resulting in sets of stations (called "candidate stations") that are associated with events, has been described previously, together with the physics and quality cuts that these candidate showers have to pass in order to be reconstructed. Additionally, since the array is sensitive to lightning happening during thunderstorms, events that show oscillations (a sign of lightning has struck nearby) in at least a PMT trace of one of the candidate stations are discarded.

The total signal recorded in a station is obtained by identifying the relevant information in the FADC traces of all the PMTs in each station. The traces are scanned to find candidate signal *fragments*, consisting of consecutive bins with an amplitude of at least 3 ADC count above the baseline. Other conditions, such as distance in time and size of the integrated signals between consecutive fragments, are required for the candidate fragments before being merged in the final signal segment, which is then averaged between PMT to obtain the station-level segment. The final segment with the largest signal is used to obtain the start and stop times at the station level,

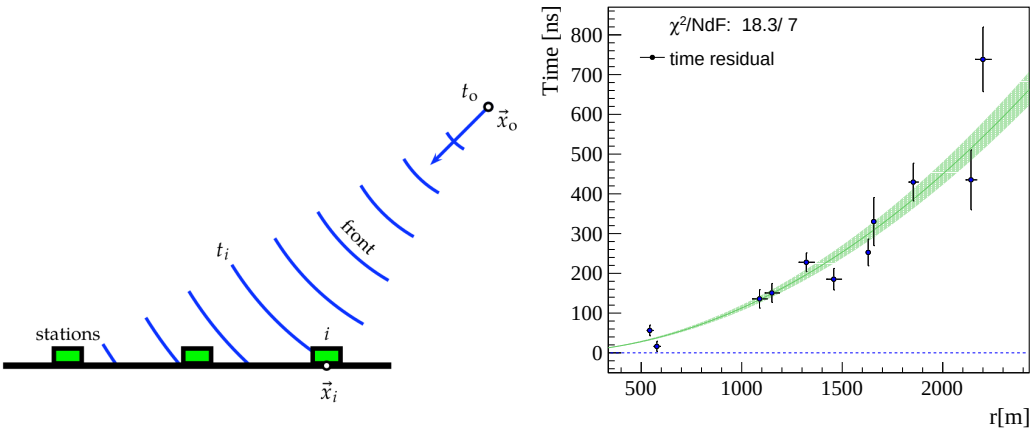

FIGURE 1.17: Left: Schematic view of the development of the shower front. Right: Time residuals of the stations with respect to the shower front as a function of the distance to the shower core.

defining the time window of interest where the traces are integrated to obtain the signal.

The start times are used to reconstruct the geometry of the shower, thus, the shower axis and the curvature of the shower front. These parameters are obtained from the minimization of the sum of the squares of the differences between the predicted and the measured start times:

$$\chi^2 = \sum_i \frac{[t_i - t_{sh}(\vec{x}_i)]^2}{\sigma_{t_i}^2} \tag{1.9}$$

where t_i and σ_{t_i} are the start time and its uncertainty of station i and $t_{sh}(\vec{x}_i)$ is the predicted start time at the distance $\vec{x}_i$ of station i, evaluated from the model of the evolution of the shower front, that in Auger is approximated with a speed-of-light concentrically inflating sphere with t_0 and $\vec{x}_0$ being the virtual start time and origin of the shower development, as follow:

$$ct_{sh}(\vec{x}_i) = ct_0 - |\vec{x} - \vec{x}_i| \tag{1.10}$$

The schematic view of the model and the dependency of the time residuals (with respect to the shower front) of the stations as a function of the distance to the shower core is shown in Fig. 1.17.

1.3.1 Lateral Distribution Function and energy reconstruction

The signal measured by the SD is only part of the total one of the shower at the ground, due to the sampling of the footprint, with an example of footprint shown in Fig. 1.18, left image. In order to obtain the shower size, a fit of the recorded signals in the stations as a function of their distance to the shower axis is performed. The lateral distribution function (LDF) used for this purpose is a modified Nishimura-Kamata-Greisen (NKG) function [73, 74]:

$$S_r = S_{r_{\text{opt}}} \left(\frac{r}{r_{\text{opt}}}\right)^{\beta} \left(\frac{r + r_{\text{scale}}}{r_{\text{scale}} + r_{\text{opt}}}\right)^{\beta+\gamma} \tag{1.11}$$

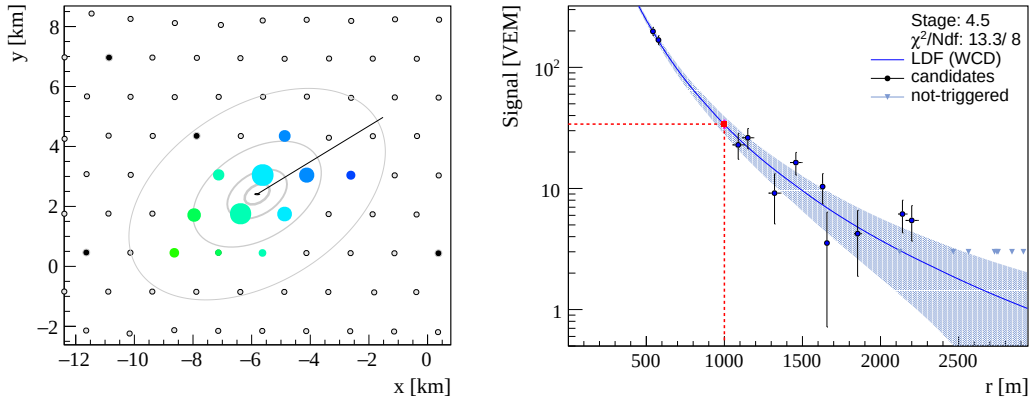

FIGURE 1.18: Left: Footprint at the ground for a shower with reconstructed energy equals to 10^{19} eV and zenith angle of $\approx 52°$. Right: Lateral distribution of the same shower shown on the left, with a fitted LDF; the shower size estimator is shown as a red dot. (Auger ID: 160041588500)

where r_{opt} is the optimal distance at which the signal is a good estimator of the shower energy, and in the case of Auger corresponds to 1000 m [66, 75], and thus the shower size is $S(1000)$, as can be seen in Fig. 1.18; the scale parameter, r_{scale}, is fixed at 700 m, while β and γ determine the slope of the function and are parametrized as a function of the zenith angle and $S(1000)$. The fit of the lateral distribution function (LDF) uses a maximum likelihood method, which also takes into account the probabilities for the stations that did not trigger and the stations close to the shower axis with saturated signal traces. The convergence of the fit is improved by using an iterative procedure. The statistical uncertainties of the reconstructed shower size, $\sigma(S(1000))$, are directly related to the number of triggered stations and the uncertainties in their signals, that are parametrized [76] as:

$$\sigma_S = 0.865(1 + 0.593(\sec\theta - 1.22))\sqrt{S} \tag{1.12}$$

The estimation of the shower size is a first important step in the determination of the energy of the primary particle. Other corrections and calibration with the almost-calorimetric energy estimation obtained by the FD are needed. In particular, the shower size has a dependence on the zenith angle, decreasing as θ increases. This effect is due to the fact that the more inclined the shower is, the more attenuated in the atmosphere is the electromagnetic component of the shower, reducing the signal at the ground. The attenuation curve is obtained using the constant intensity cut (CIC) method [77] and is parametrized with a 3rd degree polynomial in the form $f_{CIC}(\theta) = 1 + ax + bx^2 + cx^3$, where $x = cos\theta - cos38°$. In this way, it is possible to convert $S(1000)$ to an angle-independent shower size, called S_{38} and obtained as:

$$S_{38} = \frac{S(1000)}{f_{CIC}(\theta)} \tag{1.13}$$

S_{38} can be thought of as the signal that would have been measured if the shower would have arrived with a zenith angle of 38°. Since an energy dependence is observed in the attenuation curve, the polynomial coefficients (a, b and c) are parametrized with a 2nd degree polynomial in $\log_{10}(S_{38}/40\text{VEM})$ [1], and are shown in Appendix A.

The shower size can be converted into an energy estimation of the primary particle thanks to the hybrid design of the Observatory [1]. Indeed, the cross-calibration

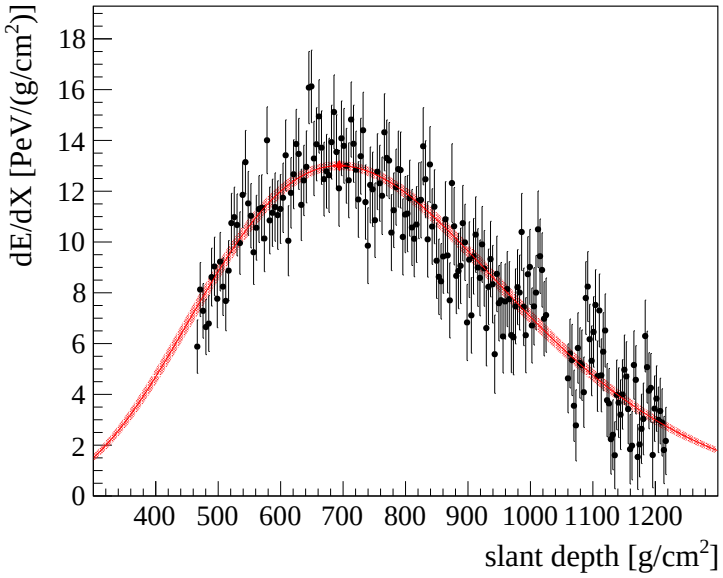

FIGURE 1.19: Example of a longitudinal profile fit for a shower with reconstructed energy $\approx 9.3 \times 10^{18}$, $\theta = 49^\circ$ and $X_{\max} \approx 700$ g/cm^2/decade. Telescope: Coihueco. Auger ID = 190906049400.

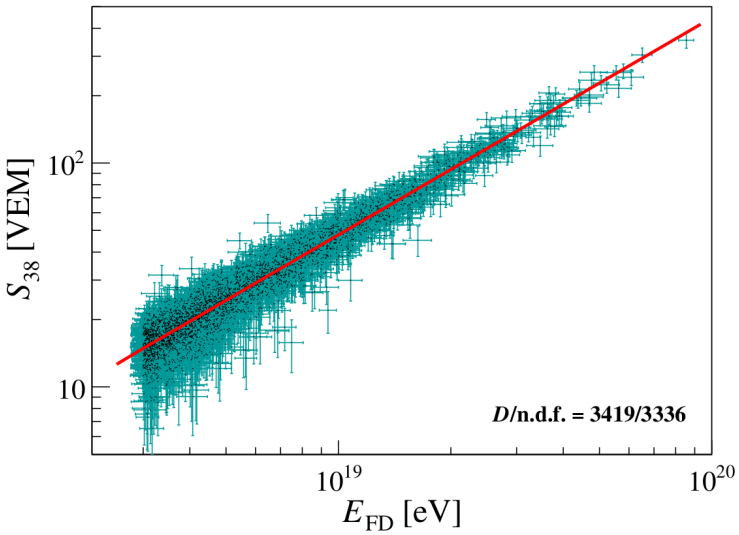

FIGURE 1.20: Correlation between the SD shower-size estimator, and the reconstructed FD energy for the selected 3 338 hybrid events used in the fit [1]. The line is the best fit of the power-law dependence on the data.

between the FD energy, $E_{\rm FD}$, and S_{38} is obtained by leveraging the combined information contained in events that were simultaneously observed and reconstructed by the two detectors; those events are called *golden hybrids*. The FD energy is obtained by fitting a Gaisser-Hillas function [77] to the full longitudinal profile of the light detected in the PMTs of the FD camera, as shown in Fig. 1.19, then integrating the results and correcting for the "invisible energy" carried away by neutral particles, such as neutrinos, and muons. The most recent published results [1] used 3 338 *golden hybrids* events to obtain the calibration curve, displayed in Fig. 1.20. The

correlation between S_{38} and E_{FD} is obtained using a maximum likelihood method allowing various effects of experimental origin to be taken into account [78], and S_{38} is well described by a single power-law function, being:

$$E_{FD} = A(S_{38}/\text{VEM})^B. \tag{1.14}$$

The best fit parameters are $A = (1.86 \pm 0.03) \times 10^{17}$ eV and $B = 1.031 \pm 0.004$ and the correlation coefficient between the parameters is $\rho = -0.98$ [1].

Having a closer look at Eq. (1.14), it can be noticed the similarity with Eq. (1.5) and Eq. (1.7), in which the number of muons is related to the energy of the primary and its mass. In Eq. (1.14), E_{FD} is the estimator of the energy of the primary, while S_{38} is the sum of the electromagnetic and muonic components of primaries, with $1/B \approx 0.97$ the slope of the signal as a function of the energy. The two signal components have different slopes as a function of the energy, with a larger one for the electromagnetic component, and thus B is a combination of the two and higher than the values listed for β in Section 1.1.3. For this reason, the parameter B can not be directly compared to β, but the extraction of the muonic component using Deep Learning Models can enable a study of β, as shown in Chapter 6, and can give insights about the mass composition.

The energy bias and resolution are obtained by looking at the mean and spread of the distributions of E_{SD}/E_{FD} as a function of E_{FD}. The bias is close to zero in the regime of full efficiency. The resolution has been parametrized from measurements as a function of the energy and ranges from 20% at 2×10^{18} eV and tends smoothly to 7% at 2×10^{19} eV. This results on the resolution will be checked in simulations in Chapter 5, and compared to data.

Chapter 2

Long-term performance of the Surface Detector

The Pierre Auger Observatory has been in operation for nearly 20 years, collecting data during this period with the Surface Detector in mostly stable conditions. Considering the large area covered by the SD and the high numbers of water Cherenkov tanks deployed, such an achievement has been obtained thanks to a robust, reliable, and automatic self-calibration procedure performed on each tank every minute. This calibration, exploiting the uniform flux of secondary particles produced by low energy showers, ensured good quality data taking over the years, along with continuous monitoring of the stations' conditions.

The constant evaluation and the measurement of several parameters at the station level, obtained during calibration, reveals changes in the detector's response. This phenomenon is related to the aging of the detector and long-term effects have an impact on high-level variables, such as risetime, curvature, and the mean number of triggered stations. Having data that now extends for more than 16 years, a quantification of these changes can be performed extensively.

In this chapter, the calibration of the tanks will be presented, and the relevant quantities will be explained. Based on the tank information obtained from single station calibration, the aging of the detector is defined as the measured change in these station-level observables. These changes over time will be studied and quantified, together with the effect on high-level variables such as the number of triggered stations over time and its implications on the reconstructed energy of the showers.

2.1 SD calibration

The calibration of the tanks is performed locally by the onboard electronics of each station since stations are very remote and the communication with the CDAS is limited to 1200 bits per second [79]. These conditions constrained the calibration design to be very simple and flexible to accommodate for possible and unpredictable failures of PMTs in the tanks. Since differences are present from tank to tank and even from PMT to PMT (i.e., different gains), the calibration needs to be performed against a common reference. This is also very important in order to be able to compare data and simulations. In this way, a uniform triggering condition is also maintained for the full array. The calibration exploits the flux of secondary particles reaching the ground as a calibration source, particularly atmospheric muons passing through the tanks at a rate of 2500 Hz.

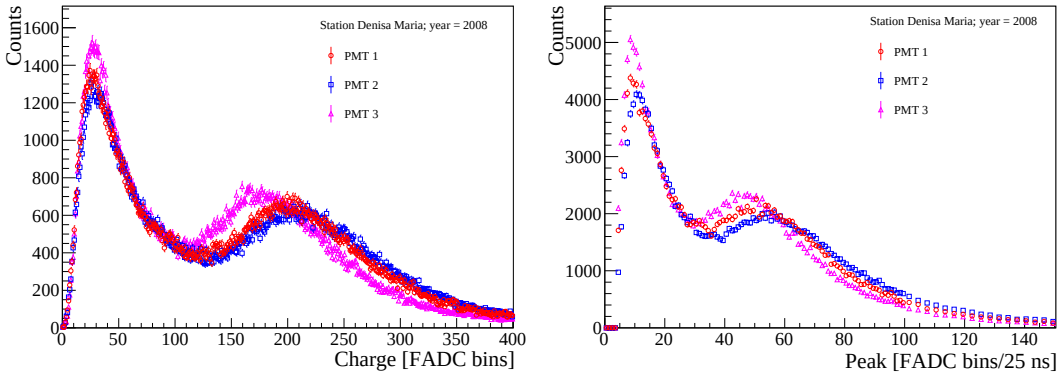

FIGURE 2.1: Charge and peak distributions of one event in 2008 (station Denisa Maria).

2.1.1 Calibration histograms

Since atmospheric muons produce a typical response in the detector [80], the signal released by vertical muons (VEM) passing through a station is used to calibrate each station independently. The goal of the calibration is to measure this quantity station by station to be able to convert from electronic units to units of VEM. More specifically, since stations cannot select particles from a specific direction, a station collects the amplitude and the charge of signals generated by atmospheric particles produced by low-energy showers, building the so-called calibration histograms for each PMT. An example of charge and peak histograms for all the PMTs of station Denisa Maria (ID = 1698) is shown in Fig. 2.1, where the two types of histograms are built with the total integrated signals of going-through particles (charge, left), measured as integrated FADC channels (also indicated as FADC bins), and the maximum value of their signal (peak, right, sometimes also referred to as the current I measured by the PMTs), with the number of FADC channels/25 ns as units.

Each station continuously collects information from signals with time windows of 60 s (recording ≈150.000 entries per histogram) and builds these histograms that are sent to CDAS whenever a shower event satisfies the trigger conditions. This means that when the event is sent to CDAS, the calibration information obtained 60 seconds before the event is sent together with the data. A charge histogram with the sum of all three PMTs is also produced and sent to CDAS with the other histograms. In this case, a condition is required to obtain the summed histogram: a 3-fold coincidence between the PMTs when the peak of the signal in the PMTs is larger than a threshold of five channels above the baseline. The choice of this threshold level is later explained in the text.

It can be seen that two different peaks are present in both charge and peak histograms: the first, on the left, is mainly produced by the electromagnetic particles ($e^{\pm}, \gamma$), while the second one comes from the muonic contribution ($\mu^{\pm}$). The charge produced by VEM (Q_{VEM}) is obtained for each station by scaling the peak in the charge histogram Q_{VEM}^{peak} produced by omnidirectional muons with a conversion factor obtained from a dedicated muon telescope on a reference WCD at the beginning of the operation of the Observatory [81], and more recently using an RPC hodoscope [82].

This conversion factor is defined as $f_Q = Q_{VEM}^{peak}/Q_{VEM}$ and for single PMT is equal to 1.03 ± 0.02 [81], while for a 3-fold coincidence is equal to 1.08 ± 0.01 [82].

The difference between the two values can be understood by considering that a single PMT can record only the part of the signal closest to itself, while the sum of the PMTs measures the total signal.

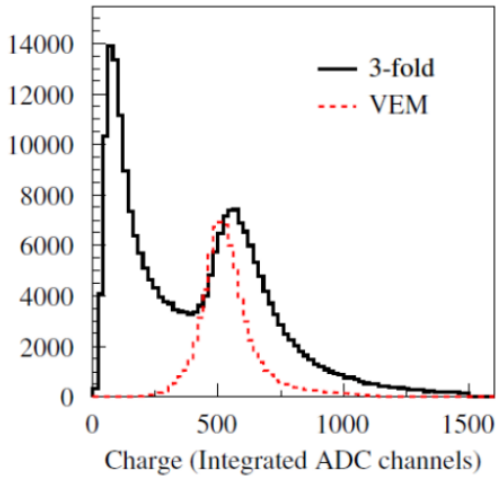

FIGURE 2.2: Example of a summed charge histogram for omnidirectional muon (black line) in a 3-fold condition and for vertically centered muons (red line). Taken from [83].

The need for the conversion factor f_Q arises from the fact that the distribution of signals for omnidirectional muons is shifted and broader compared to the one for vertical muons, as it can be seen from Fig. 2.2: in the first case, muons with different incident directions are entering the tank, and thus they will have a larger track length distribution, leading to a different total number of Cherenkov photons produced along the path. The measured values of f_Q over time in the two acquisition campaigns agree with each other, showing the reliability of the calibration method.

Another proof of the stability of this factor has been obtained from simulations that try to reproduce the aging of the detector, meaning a loss of the recorded signals, by changing the internal reflectivity of the water Cherenkov tanks, see Chapter 3 for more details. The evolution of f_Q as a function of the internal reflectivity s, shown in the bottom plot of Fig. 2.3, agrees with the measurements and is contained within its uncertainties. Simulated calibration histograms of omnidirectional and vertical centered muons (VCM) injected in the tank for different liner reflectivities are visible in Fig. 2.3, top plots: a Gaussian fit is performed around the muon peak of these histograms to obtain Q^{peak}_{VEM} and Q_{VEM}.

The peak histograms, and in particular the position of the muon peak I^{peak}_{VEM} obtained from them, are used to maintain stable and uniform triggers all over the array. When the electronics of a station are switched on the first time, the gains of the PMTs are adjusted to match a rate of 100 Hz at a point of 150 channels above the baseline: in this way PMTs have ≈ 50 channels$/I^{peak}_{VEM}$, creating a relative common reference between them. This point in the spectrum was chosen based on the measurement of the rate performed on a reference tank [81]. This procedure called *end-to-end gain setup*, balances the PMTs between them and, as a consequence, sets different high-voltage gains for each PMT, even in the same station, as it can be seen in Fig. 2.1: if a PMT has a worse optical coupling or a different quantum efficiency, thus recording fewer photons than the other PMTs, this setup will correct the gains to match the required conditions and ensure that the PMT signals will be similar in amplitude. The method also allows compensating between tanks that produce a different number of Cherenkov photons than the reference tank by adjusting their PMT gains.

During normal operations in the field, the value of I^{peak}_{VEM} changes due to a possible drift in the high-gain of PMTs, thus a continual on-line calibration is needed to re-evaluate I^{peak}_{VEM} and keep the triggers uniform. Extracting the value of I^{peak}_{VEM} is time-consuming for the local electronics, and for this reason, an estimate I^{est}_{VEM} is used. This variable is defined at the PMT level as the value obtained when requesting that the rate of events satisfying a "calibration trigger" is equal to 70 Hz. The "calibration trigger" conditions require that the signal of the event is above $2.5 I^{est}_{VEM}$

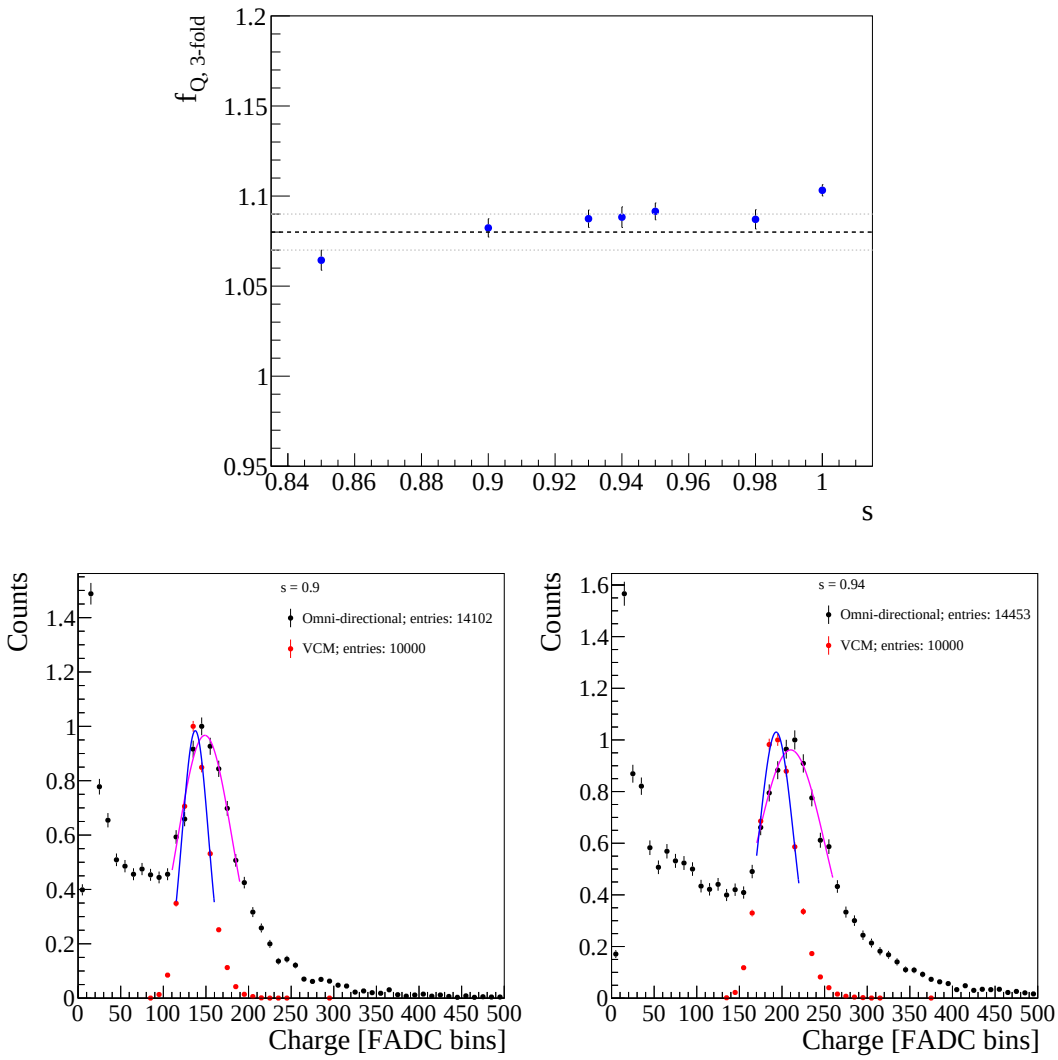

FIGURE 2.3: Top: Evolution of scaling factor f_Q for different internal reflectivities of the tank. Lines represent the value with its uncertainties obtained on the field using an RPC hodoscope [82]. Bottom: Simulated average charge histograms with a 3-fold condition for VCM (red) and omnidirectional muons (black) for two different tank conditions.

for the selected PMT and above $1.75 I^{est}_{VEM}$ for all the three PMTs. Following these requirements, I^{est}_{VEM} is obtained in an iterative way, in which a test value of I^{est}_{VEM} is modified by a certain adjustment, called δ, if the measured rate is outside of a defined bound, called σ. This procedure is called $\sigma - \delta$ convergence algorithm. Its accuracy is approximately 6%, a precision that is better than the 10% required considering the quantization of the channels and the ToT trigger, the lower target trigger threshold at the station level used to identify candidates described in the previous chapter, which is implemented as a threshold of $0.2 I^{est}_{VEM}$ (≈10 channels).

After the algorithm has been performed and the value of I^{est}_{VEM} has been obtained, a different trigger with a threshold of $0.1 I^{est}_{VEM}$ (5 channels) is used to collect the signals of low energy particles passing through the tank at a higher rate and consequently build the calibration histograms.

Since the trigger thresholds are based on the estimation of the maximum amplitude of omnidirectional muons measured by each tank in the field, this information

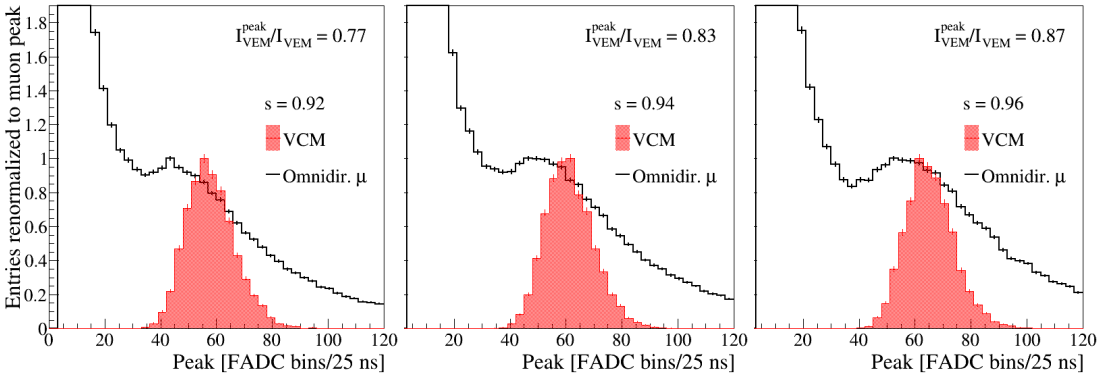

FIGURE 2.4: Simulated peak histograms for vertical centered muons, VCM, (red) and omnidirectional muons (black) for different liner reflectivities (0.92, 0.94, 0.96).

is not available in simulations that rely, instead, on values of I_{VEM} and Q_{VEM} obtained from the simulated injection of vertically centered muons in a tank. Another conversion factor f_I from I_{VEM} to I^{peak}_{VEM} for a single PMT is then needed in simulation to set the correct trigger threshold. Acquisition campaigns using muon telescopes have been performed in the past, providing $I^{peak}_{VEM}/I_{VEM} = 0.87$, used as a fixed value in simulations to set the trigger threshold. This variable, however, when reconstructed in calibration simulations performed in this study, shows a dependency on the internal properties of the tank (i.e., internal reflectivity). Thus it is affected by the aging of the detector, determining a difference between data and simulations. It can be seen in Fig. 2.4 that f_I changes for different tank conditions, with the muon peak for omnidirectional particles closer to the muon peak of vertical muons for higher reflectivities ($f_I = 0.87$ for $s = 0.96$) and an increased difference for tanks with a smaller reflected light in the water volume ($f_I = 0.77$ for $s = 0.92$).

2.1.2 Shape histograms

The on-line calibration of the station also provides an estimation of the average VEM charge, named Q^{est}_{VEM}, obtained by integrating the pulses with a peak equal to I^{est}_{VEM}. The comparison between this value and the one extracted directly from a fit performed from charge calibration histograms shows an accuracy of 4%, being their conversion $Q^{est}_{VEM} = (0.96 \pm 0.03) Q^{peak}_{VEM}$.

The calibration method exploits the estimated average charge to select pulses with an integrated charge in the range $(1.0 \pm 0.1) Q^{est}_{VEM}$: this choice allows to select signals from vertical muons among the secondary particles from low energy showers that enter the tank and are recorded in each PMT. These FADC traces are then summed to build the so-called *pulse shape histograms* or simply *shape histograms* since they represent the average shape of the light deposition in the PMT. An example of shape histograms recorded by the PMTs of station Denisa Maria in 2008 can be seen in Fig. 2.5, where a sharp rise is followed by an exponential decrease caused by the multiple reflections of photons inside the tank.

These histograms show the average time response of a tank to a vertical muon. They are beneficial for monitoring the tank conditions and studying the evolution over time of the tank response to secondary particles. This is achieved by analyzing the behavior of the time decay constant of the VEM signals over the years, as shown in the next section.

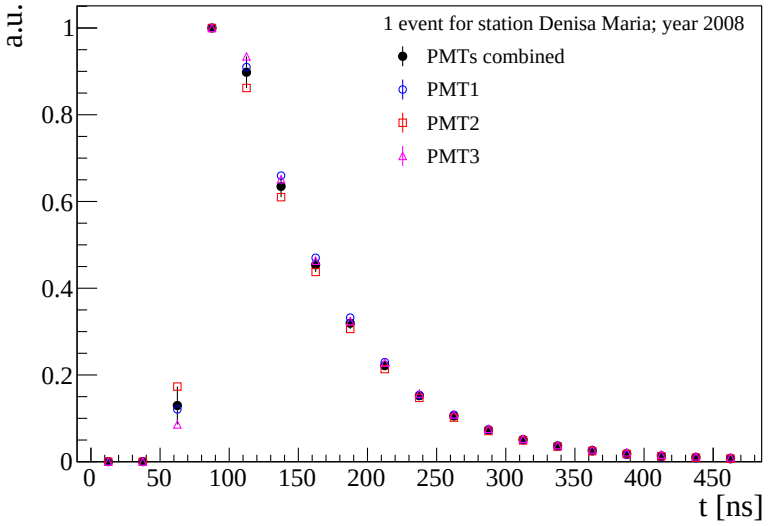

FIGURE 2.5: Shape histograms for one event in 2008 for station Denisa Maria, ID = 1698.

2.2 Aging

The surface detector experienced changes over the years, and signs of aging appeared in the recorded data. The aging is defined as a decrease in the response of the tanks to secondary particles with time, caused mainly by a loss of collected light in the tanks. This effect is visible in the change of shape of vertical muon pulses recorded during the calibration process, quantified by the slope change in the signal. This decrease, in turn, modifies the Area and Peak obtained from calibration histograms since the Area represents the total charge produced by a single vertical muon, and the Peak is the maximum value in FADC counts of its signal. The "Area over Peak" ratio, denoted here as A/P, is one of the observables at the station level that is well known to change over time in individual detectors. A general decrease over time of the time-decay constants and the Area over Peak is observed for all the stations in the field, with two different populations that share the same trend over the years, nonetheless having different absolute values.

2.2.1 Time-decay constant of VEM signals

Shape histograms are directly affected by decreased efficiency of the light collection. Since fewer photons will reach the PMTs, smaller signals are produced. In Fig. 2.5, an example of a shape histogram for station Denisa Maria (Id = 1698), chosen as a reference, is shown: Single PMTs, represented by open symbols, slightly differ between them due to effects induced by the electronics, most probably the filter applied during the digitalization of the signal. We combined these histograms by taking for each bin the mean value between the maximum and minimum values of the PMTs. In this way, the combined one can give us an overall picture of the tank conditions. As error bars, we used the distance between the maximum and the minimum from the middle point. The difference in the shape over time can be observed in Fig. 2.6, left plot, for events obtained from two different years. These histograms are normalized to their peak. An exponential fit is performed to extract the time decay constant of the signals (τ), as follows:

$$f(x) = A \cdot e^{-\frac{x}{\tau}} \tag{2.1}$$

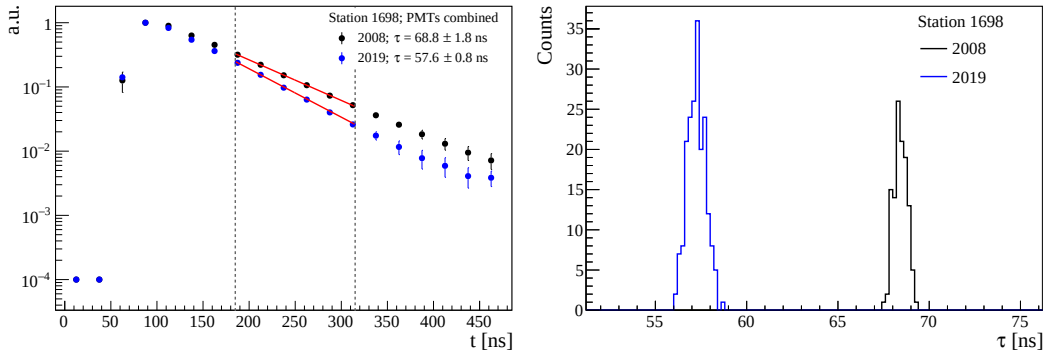

FIGURE 2.6: Left: Two events for station Denisa Maria, one in 2008 and one in 2019. Right: Distributions of τ for station Denisa Maria for two different years, 2008 and 2019.

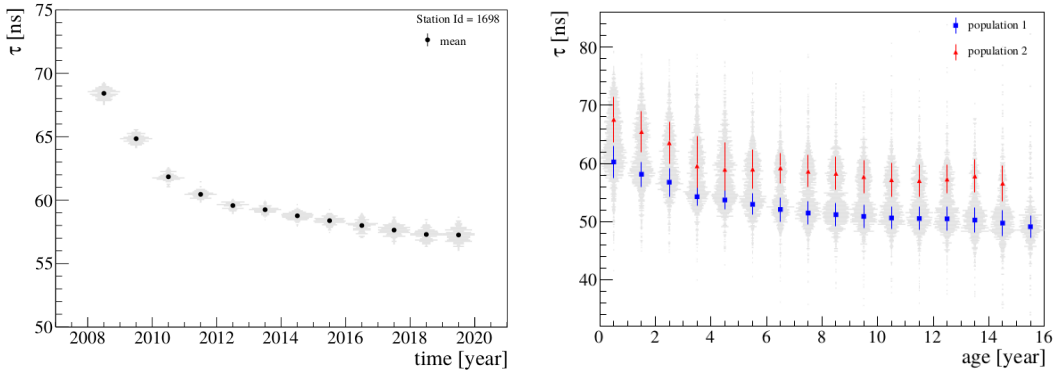

FIGURE 2.7: τ evolution over time for station Denisa Maria (left) and the full array (right). See text.

The fit range is fixed at [185, 315] ns, which corresponds to analyzing six time bins. The lower edge has been chosen to avoid the first reflections or the direct light that reaches the PMTs; thus, only the central part of the signal is considered, where we expect to have a cloud of randomized photons that went through multiple reflections inside the tank. In this way, the effect of the overall reflectivity is enhanced. The upper edge is chosen to avoid possible biases from low photoelectron statistics. It can be noticed in the same Fig. 2.6, how the shape of the signals has changed in 11 years, with a decrease of τ of 11 ns.

In order to study in more detail the evolution over time of τ, we selected good-quality shape histograms by requiring that for each event, the histogram of each PMT must have in its maximum more than 10^5 bin entries (a minimum number of entries at the peak for a standard non-normalized shape histogram), a converged fit and the difference between PMTs decay constant ($\Delta\tau$) must be less than 10%. This last choice is related to the assumption that each PMT in a station should record a signal that has experienced the same tank conditions; thus, those parameters should be similar. For station Denisa Maria, these quality cuts reduced the number of events from 1821 to 1807, a decrease of 0.8%. This low number of excluded events reflects the good behavior of this station during its lifetime in the field. The distributions of τ for events in 2008 and 2019 are displayed in Fig. 2.6, right plot. The two distributions are clearly separated, showing that the decrease cannot be attributed to some statistical fluctuation.

The τ evolution over time is shown in Fig. 2.7, left: over 11 years, the mean time

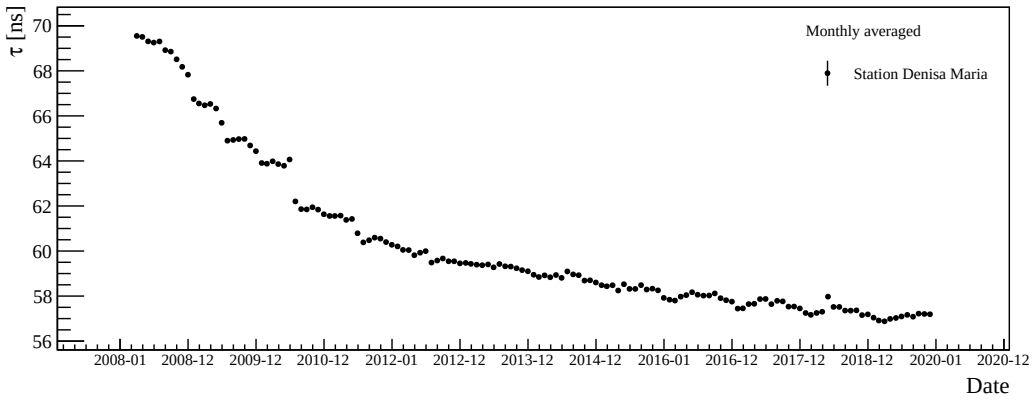

FIGURE 2.8: τ evolution over time station Denisa Maria, including data for other months.

decay constant decreased by 11 ns, faster during the first four years, reaching a level of decrease of 0.5 ns per year during the last years. As error bars, we considered the error of the mean, while the grey shadow in the plot represents each year's distribution.

We performed the same analysis described previously on 1640 stations. For just five stations, it was not possible to recover any information. Other few stations showed erratic behavior; thus, we applied an additional cut on the decay constant, requiring that $\tau < 100$ ns. The Ids of these stations are 1132, 1198, 151, 1520, 417, 497, 665, 666, 748, 847, 873, 902, and 967. The τ evolution over time and examples of shape histograms for station 1132 are visible in Appendix B. The evolution of τ as a function of time after deployment (denoted here as "age" of the tank) for all the selected stations is shown in Fig. 2.7, right plot: it can be noticed that the distribution is bimodal. The mean time decay constants for the two populations in each year are obtained by fitting a sum of two Gaussians for each year's distribution, as shown in Appendix C.1, Fig. C.1.

Even if the two populations show different values of τ, their decrease over time is the same. The population with the highest values (red points) exhibits a decrease of τ from 68 ns to 57 ns in 15 years, while for the other population τ starts at 60 ns and drops to 50 ns in the same time interval. The uncertainties represent the standard deviation of the fitted Gaussians, and the gray shadows show the distribution of the mean τ of the stations in a specific year. The map of the stations as a function of τ values and as a function of the year of deployment can be seen in Appendix C.2, Fig. C.4.

We also checked seasonal effects on τ by studying the evolution of the time decay constant during all months for station Denisa Maria. The overall trend can be seen in Fig. 2.8, where it is not possible to see a clear modulation, despite some hints starting from 2016. Despite an initial larger difference between months, probably due to the sharp decrease in the initial years, the fluctuation of τ is only ≈ 0.1 ns, suggesting that seasonal fluctuations do not strongly impact shape histograms. Considering two different months such as January and July, with January being usually the warmest month and July the coldest one according to the weather in Malargüe, the mean difference between these two months in a stable period (in this case after 2012) is ≈ 0.12 ns.

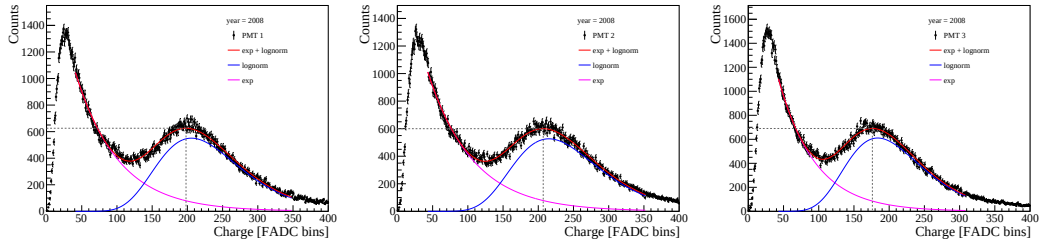

FIGURE 2.9: Charge distributions with fits to each PMT for an event in 2008 (station Denisa Maria).

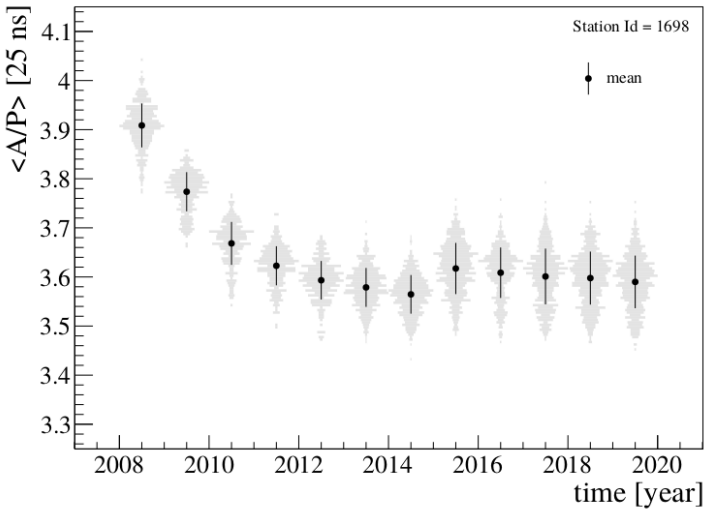

FIGURE 2.10: A/P for station Denisa Maria over time.

2.2.2 Area over Peak

The change in the signals recorded by WCDs of the SD has been studied during the years of operation of the Observatory by several analyses using the "Area over Peak ratio" [84, 85, 86, 87].

A recent study [88] shows that A/P is decreasing with time with almost 20% of PMTs that had a loss of A/P of more than 15% over 14 years. This decrease is present even when seasonal variations or abrupt changes due to earthquakes (in 2010 [88] and 2015 [89]) and freezing of the water in the tanks [90] are taken into account.

Since A/P from data shows a dependence with temperature [88], in order to avoid seasonal effects we selected events in CDAS for all stations in a fixed time window for each year (2004-2019), more specifically in the last week (23-30) of November. From all events, we extracted the calibration histograms to study the behavior of the tanks over the years.

An example of charge and peak histograms for the 3 PMTs is shown in Fig. 2.1 for an event in 2008 for station Denisa Maria. The difference in the PMT distributions is due to different PMT gains in the field that have been set up by the *end-to-end gain* procedure. As previously described, calibration histograms are composed of an electromagnetic contribution that is dominant for low signals (first peak) and a muonic contribution (second peak). The total distribution can be modeled as the sum of an exponential (used to describe the em contribution) and a lognormal (describing the

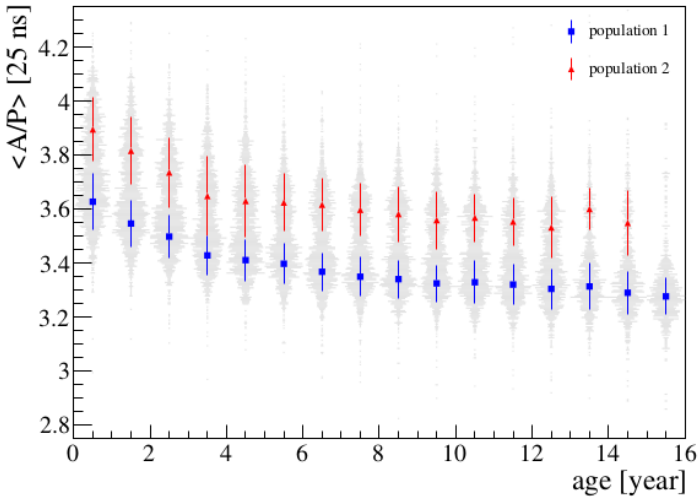

FIGURE 2.11: A/P evolution over time for the full array.

muonic contribution), as following:

$$f(x) = e^{\left(A - \frac{x}{\tau_{em}}\right)} + \frac{1}{x} \cdot e^{-\frac{B(\ln x - \ln \mu)^2}{2\sigma^2}} \quad , \tag{2.2}$$

where μ is the mean charge deposited by a vertical muon, σ is the spread of the lognormal and τ_{em} is the decay constant of the electromagnetic component.

Area and Peak are defined based on the second derivative of the fit function. Each calibration histogram is fitted with Eq. (2.2), as shown in Fig. 2.9 for charge histograms of an event in 2008 for station Denisa Maria: the charge histograms show muon peaks at $A_{PMT1} = 200$ FADC bins, $A_{PMT2} = 210$ FADC bins and $A_{PMT3} = 178$ FADC bins.

We applied quality cuts also on calibration histograms for each event: all six calibration histograms (charge and peak histograms for each PMT) must have non-zero entries, and for each histogram, we asked for a reduced $\chi^2 < 10$ to avoid bad fits of the histograms or bad-behaved PMTs. These cuts reject bad periods due to noisy PMTs or other effects in the tank that can interfere with the normal calibration procedure. Another cut is based on the fact that, for each event, PMTs are expected to show a similar A/P, removing any additional and unwanted effect caused by, for example, electronics or software. This is the same principle as used for τ.

Taking this into consideration, we also required $|\Delta A/P| < 0.5\,[25\text{ ns}]$ between PMTs in the same event. In the case of station Denisa Maria, all events passed the cuts, another proof that this station had good behavior during its lifetime in the field.

The evolution over time of A/P for the selected events (around 165 events per year) is shown in Fig. 2.10. A clear decreasing trend from $3.9 \pm 0.02\,[25\text{ ns}]$ to $3.6 \pm 0.02\,[25\text{ ns}]$ between 2008 and 2014 is visible before stabilizing around $3.6 \pm 0.03\,[25\text{ ns}]$. Uncertainties are defined as the standard deviation of the distribution. The jump observed in 2015 is caused by the freezing events [88]. One can note that this jump is not present in the τ distribution, Fig. 2.7.

At the same time, A/P has been obtained from calibration histograms for all the other stations, and an additional cut was applied to remove outlier values: we required that $A/P < 5\,[25\text{ ns}]$. The result is shown in Fig. 2.11 (right): a decrease of A/P over the years is visible and, as already seen for τ, A/P values seem to

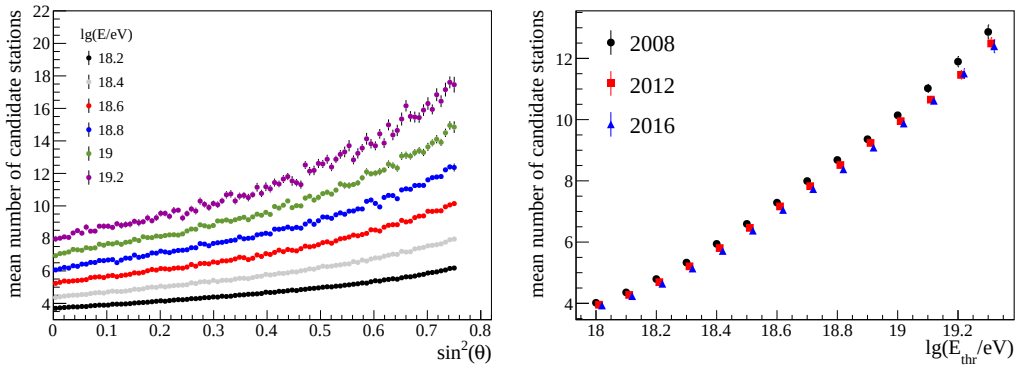

FIGURE 2.12: Mean number of stations as a function of zenith angle θ for different E_{thr} (left) and as a function of E_{thr} for different years (right).

cluster in 2 different populations, compatible with what was seen for all PMTs in the field [87, 88]. Both of them have a $\Delta A/P \approx 0.35\,[25\text{ ns}]$ over 15 years, starting from $A/P \approx 3.9\,[25\text{ ns}]$ and $A/P \approx 3.65\,[25\text{ ns}]$ respectively, with a steeper decrease in the first five years. As for τ, error bars are defined as the standard deviation of the fitted Gaussians and gray shadows represent the distribution of the average A/P of the stations in a certain year.

2.3 Number of triggered stations over time

The Area over Peak and τ are related to the T2 trigger rate, and its decrease should result in a decrease in the number of triggered stations. The average number of triggered stations depends on the primary particle's energy. The mean number of stations per event above a certain energy is illustrated in Fig. 2.12 for 6T5 events with a zenith angle smaller than 60°. The number of stations depends on the zenith angle; for example, above 10 EeV an air shower will trigger on average eight stations if it were vertical and 12 if it were inclined. The number of stations increases almost linearly with the logarithm of the threshold energy, having, on average, four stations per event above 1 EeV and about eight stations per event above 10 EeV. A decrease with time can already be observed in the same figure.

Two effects can cause the decrease: a decrease with time of the reconstructed energy (or in $S(1000)$) or, assuming that $S(1000)$ is constant, stations far from the shower axis are not triggered anymore. Preliminary studies [91] show that the average signal evolves with time, even for large signals. Thus the decrease in the number of stations is likely related to a combination of the two effects. In Chapter 3, we cannot disentangle the two effects. However, we come back to this in Chapter 5. Here, we investigated the required energy shifts to obtain the same distribution of the number of stations over time.

2.3.1 Data and test statistics

The underlying hypothesis is that the distribution of the number of candidate stations over the years (for fixed energy) should be similar, so comparable to a distribution of a year chosen as a reference.

We used the data set from 2004 until the end of 2018, Observer ICRC 2019 production [92]. Bad periods were rejected, and we selected events with zenith angles

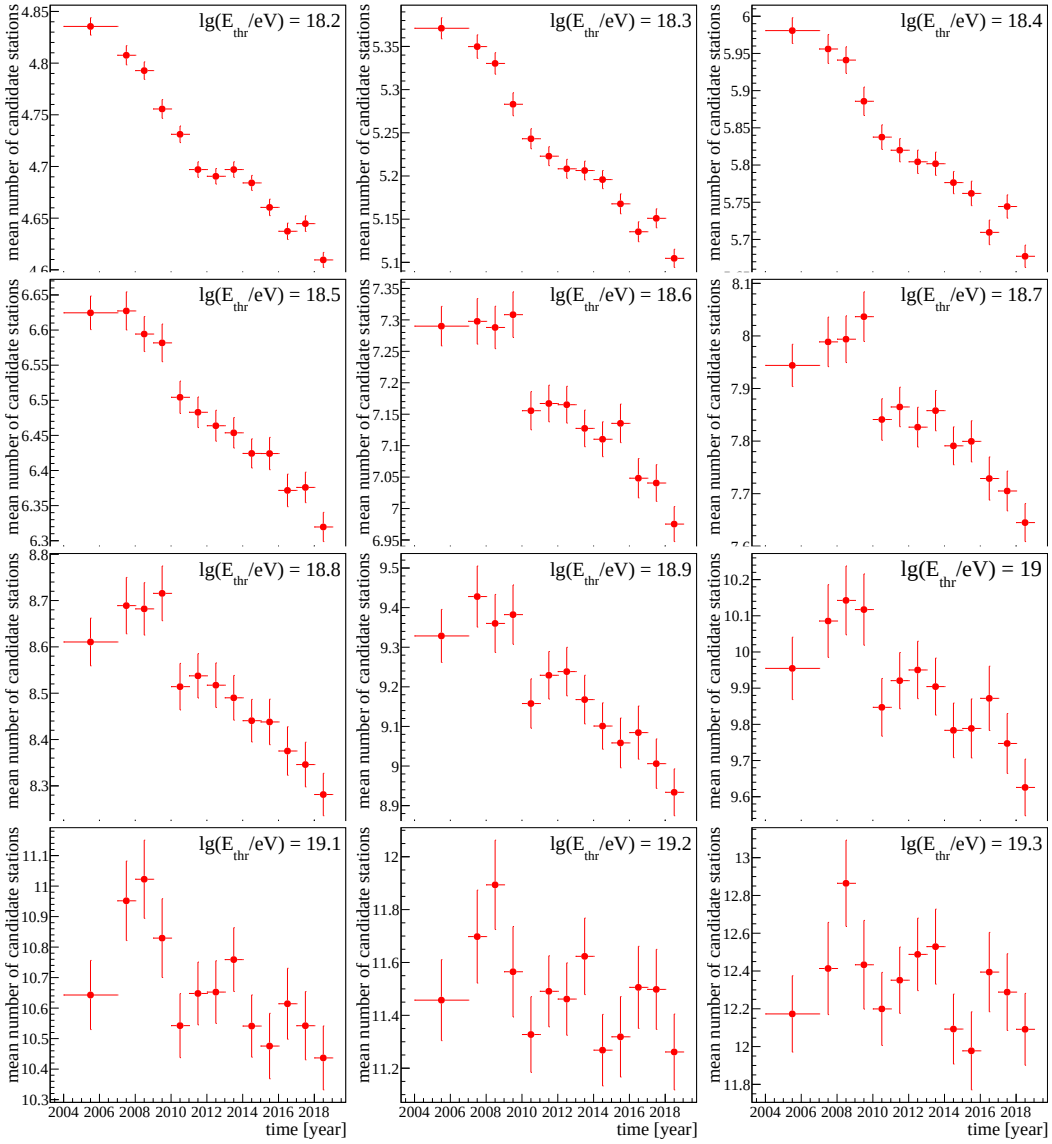

FIGURE 2.13: Mean number of candidate stations over time.

smaller than 60° and a 5T5/6T5 trigger. In Fig. 2.13, the mean number of candidate stations above different threshold energies, E_{thr} is shown, evolving during the years. Data from 2004, 2005, and 2006 are grouped together to increase statistics, considering the deployment of the array. A decrease in the mean number over the years is observed for all threshold energies until $\log_{10}(\mathrm{E_{thr}}/\mathrm{eV}) = 19.1$; for higher energies, there is not enough data to assert such implication directly.

The average number of stations also depends on the number of working stations at the time of the event. In the deployment years, the array was evolving and had many more borders than after completion. Therefore, the fraction of the number of air-shower footprints falling at the borders of the array, and thus not fully contained in the array, was larger than after completion. This can also be observed in Fig. 2.13. Therefore, the following study has only been performed for data after 2007.

In this study, we employed not only the first moment of the station distributions, but the entire distribution using a Kolmogorov-Smirnov test (KS test). The KS test is a statistical test that can be used to compare a sample with a reference probability

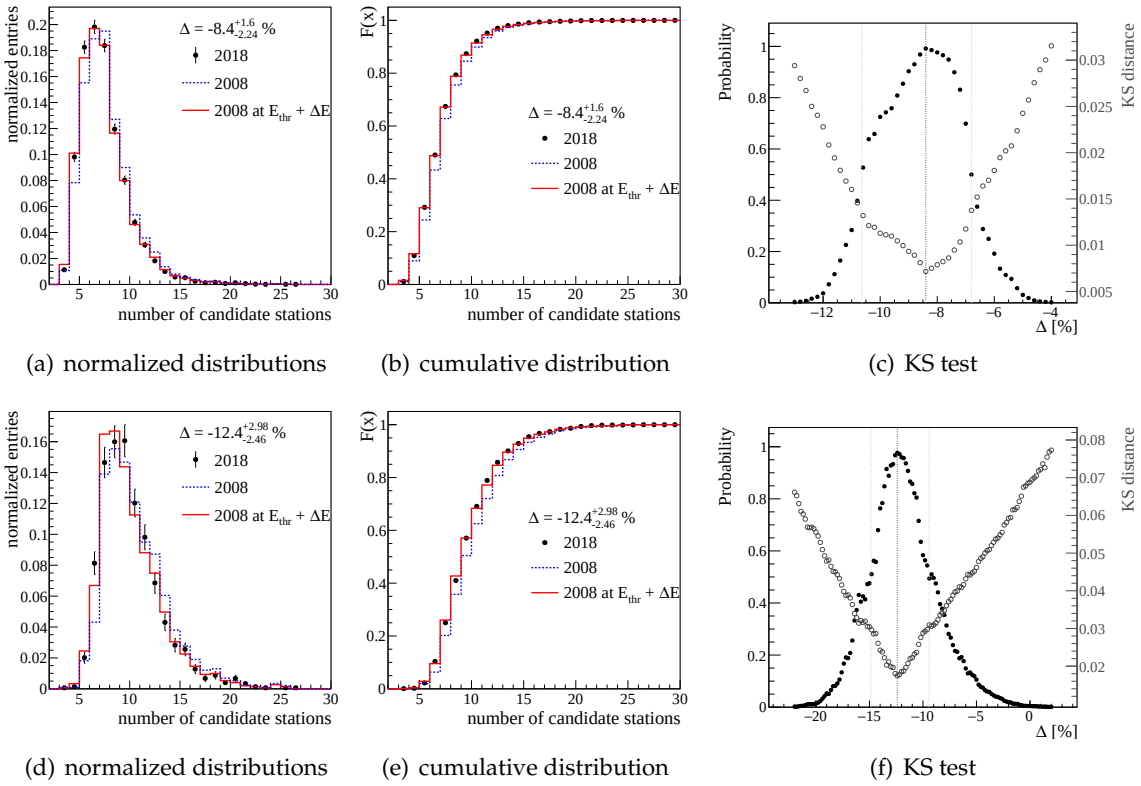

(a) normalized distributions (b) cumulative distribution (c) KS test

(d) normalized distributions (e) cumulative distribution (f) KS test

FIGURE 2.14: Components of the Kolmogorov-Smirnov test for $\lg(E/\mathrm{eV}) = 18.6$ (upper panels) and $\lg(E/\mathrm{eV}) = 19$ (lower panels). For more details, see the text.

distribution; it can also be used to compare two samples based on their shape and decide if they both come from a population with a specific distribution (this is referred to as the null hypothesis H_0). In the latter case, in which we are interested in, the test statistics use the absolute difference between the empirical cumulative distribution functions (CDF) of two samples to prove H_0 to a chosen level of significance. This difference is referred to as "KS distance" and is defined as:

$$D_{KS} = \max|F(x) - G(x)| \tag{2.3}$$

where $F(x)$ and $G(x)$ are the empirical CDF of the first and the second sample, respectively. *max* is the maximum value of the set of differences computed for each data point of the samples. This value represents the "maximum distance" between the CDFs of the distributions under comparison and is sensitive to differences in both location and shape of CDFs. The probability obtained with this method represents the confidence level for the null hypothesis.

Using this method, we checked the compatibility between the distribution of candidate stations for 2018 (used as reference year) and distributions of candidate stations for all other years. Data were selected using the same E_{thr}. For example, comparing the data sets from 2008 and 2018 above $\log_{10}(E_{\mathrm{thr}}/\mathrm{eV}) = 18.6$, we obtain a KS probability of $8.56 \cdot 10^{-10}$, corresponding to a KS distance of $5.67 \cdot 10^{-2}$. The two data sets are incompatible. This is illustrated in Fig. 2.14 where the black dots represent 2018 and the blue line, 2008, at $\log_{10}(E_{\mathrm{thr}}/\mathrm{eV}) = 18.6$. The disagreement is more visible in the upper middle plot of Fig. 2.14 where the CDFs of the samples are shown (black dots for 2018 and blue line for 2008).

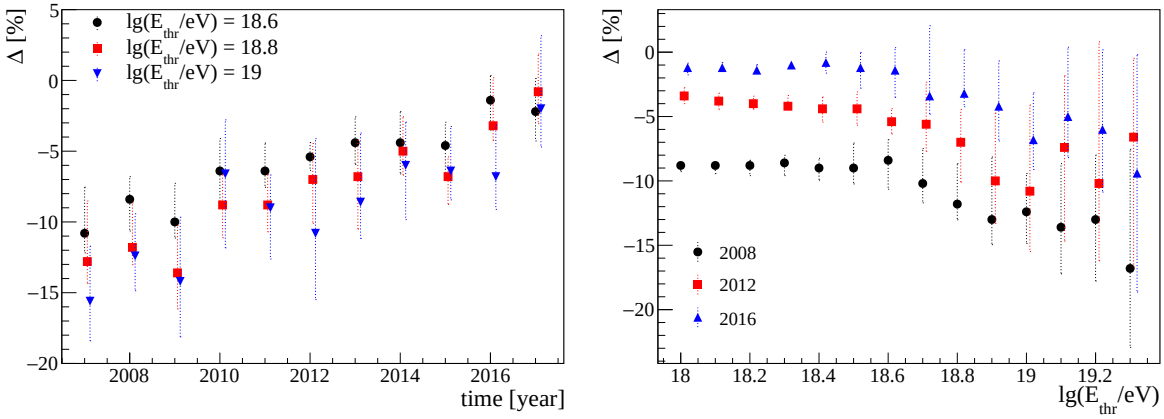

FIGURE 2.15: Left: Δ as a function of time for different threshold energies. Right: Δ as a function of threshold energy for different years.

We assume that there exists a threshold energy in 2008 above which the compatibility between the two histograms is very good. We scan over a relative shift in energy ($\Delta = (E/E_{\rm thr} - 1)$) with a step of 0.2% to find the best matching value of delta, called "equivalent energy shift". At each step, we evaluate the KS distance and KS probability for distributions obtained at those energies with respect to the reference distribution of 2008 candidate stations at that $E_{\rm thr}$. We decided to use $CL = 50\%$ as the limit for error bars, meaning values of Δ over that level are accepting the H_0 (hypothesis of compatibility) correctly at least 50% of the time.[1]

Values for the KS distance and compatibility probability are shown for 2008 in Fig. 2.14 (right). The error bars (shown in the figure with two vertical dotted lines) are computed at 50% probability around the best matching value, defined as the value of Δ for which the KS distance has a minimum. For instance, the best match for 2008 is found at $\Delta = (-8.4^{+1.60}_{-2.24})\%$, with $D_{KS} = 7.17 \cdot 10^{-3}$, which corresponds to $Prob_{KS} = 99.15\%$. The better agreement at the best matching value can be seen in the plots of the CDFs in Fig. 2.14 (upper middle one, red line for the best match). This agreement is also visible in the upper left plot, where the normalized distributions are drawn. In the lower panel, the same procedure is used for $\log_{10}(E_{\rm thr}/{\rm eV}) = 19$. In this case, the uncertainties on Δ are larger due to the decrease of the statistics by a factor of 5. This is reflected in the size of the confidence interval around the best match: $\Delta = (-12.4^{+2.98}_{-2.46})\%$. This method is employed to quantify the needed shift in energy for the threshold energy of the year under study to obtain a compatible distribution of candidate stations with the one of the reference year. This value is computed for each year and for each $E_{\rm thr}$ and presented in the next section.

2.3.2 Equivalent energies

Using 2018 as a reference year, we have computed Δ for each year and for various energy thresholds from $\log_{10}(E_{\rm thr}/{\rm eV}) = 18.1$ up to $\log_{10}(E_{\rm thr}/{\rm eV}) = 19.3$ in steps of 0.1. The results for different energy thresholds are illustrated in Fig. 2.15 (left) as a function of time. As can be seen, to obtain the same distribution of stations as in 2018, the energy threshold would need to be changed by about 10-15% in 2007. Similar behavior with time is observed for all energies shown.

The dependence of Δ on energy is illustrated in the same figure in the right panel for three different years. Data points are correlated as we used the same data set with

[1] A χ^2 test has been performed and led to similar results.

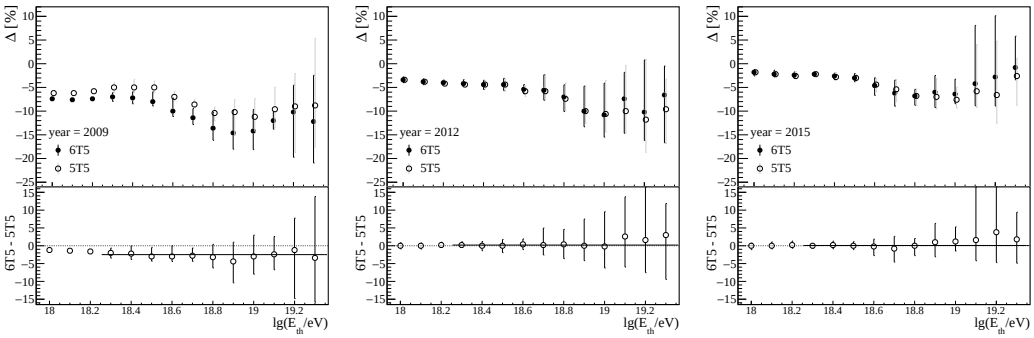

FIGURE 2.16: The evolution of the energy shift with threshold energy for 5T5 and 6T5 events and for three years:2009, 2012 and 2015. A linear fit above $\log_{10}(E_{\mathrm{thr}}/\mathrm{eV}) = 18.3$ is performed to assess the systematic uncertainty.

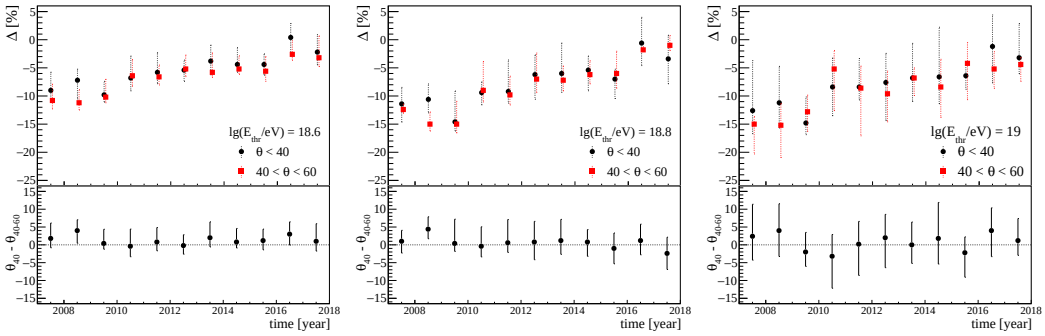

FIGURE 2.17: Δ as a function of time for different angles.

different threshold energies. Due to the steeply falling spectrum, the distributions are dominated by events with energies close to the threshold energy. Below the energy for full trigger efficiency (i.e. $\log_{10}(E_{\mathrm{thr}}/\mathrm{eV}) = 18.5$) Δ is constant. Above this energy, a decrease of Δ with energy is observed. The cause of a larger delta needed for larger energies has yet to be understood. In other words, the air-shower footprint on the array is smaller as time passes, and the change is larger for higher energies.

Systematic uncertainties The number of stations depends on the array's status: any event on the border will have fewer stations triggered. Therefore, if there is a time evolution in the array status, this would be reflected in a change in the average number of triggered stations and, thus, would directly affect Δ. The same analysis was performed on 5T5 events to investigate a possible systematic effect. The difference as a function of energy is illustrated in Fig. 2.16 for three different years. We performed a linear fit of the difference for each year. The result is illustrated in Fig. 2.18 with filled circles. As can be seen, the systematic uncertainty is lower than 2% for the time period 2007-2010, and afterward, it is compatible with zero.

The data have also been divided into two subsets: vertical events, with zenith angle smaller than 40°, and inclined events, with zenith angles between 40° and 60° (details in Fig. 2.17). The results of the linear fit above $\log_{10}(E_{\mathrm{thr}}/\mathrm{eV}) = 18.3$ are shown in Fig. 2.18 as a function of time. There is no hint that the required energy shifts depend on the zenith angle. This leads to the interpretation that the calculated delta is not only a loss of stations per event, but it might have an energy contribution.

As a crosscheck of the method, the reference year was changed to 2008 and computed the equivalent energy shift for 2018. The absolute values of Δ are depicted

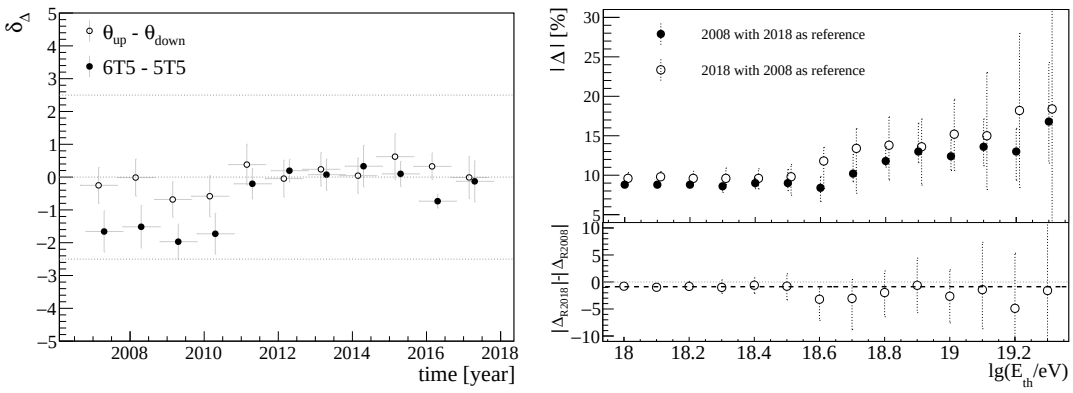

FIGURE 2.18: Left: Systematic uncertainties from the trigger and zenith angle. Right: Systematic uncertainties due to change of reference year.

in Fig. 2.17(right) as a function of threshold energies. As can be observed, the difference is less than 1%.

The Δ as a function of time for different threshold energies is shown in Fig. 2.19. Above a threshold energy of $\log_{10}(E_{\rm thr}/{\rm eV}) = 19.1$, the number of events to perform this study is not very large, and the statistical uncertainty of Δ is about 5%. To establish the growth rate of Δ per year for each threshold energy, a linear fit is performed for the evolution of Δ over time. We assume that Δ is 0 at the reference year[2], and thus, we have just one free parameter, p_1, describing the slope of the function.

The values obtained from the fit are shown in Fig. 2.20. The Δ variation per year at different threshold energies has an energy dependency ranging from $\sim 0.8\%$/year at low energies to $\sim 1.4\%$/year at the highest energies. As discussed earlier, we have observed a difference between 5T5 and 6T5 events, especially in the first years, and thus, one would expect this systematic effect to influence the p_1 value. Indeed, the influence is observed and is at the level of 0.1%/year. The same trend with energy is observed independently of the trigger conditions.

2.3.3 Interpretation

The decrease of the Area over Peak with time is related to the number of candidate stations as the station T2 triggers depend on this variable. In [87], it has been shown that the event rate and the Area over Peak are directly correlated, and it seems that the event rate has stabilized. We have shown, via a simple variable, the number of triggered stations per air-shower that the data are continuously affected by this loss. Even if the event rate is thought to have stabilized, the distributions of the number of stations continue to change, with a continuous loss in the number of stations per event for all energies.

By assuming a constant SD energy over time (that will be verified in Chapter 5), the loss of stations per event can be interpreted as a loss in resolution, since the resolution is directly dependent on the number of stations participating in the reconstruction. Using the parametrisation from [93], a maximum Δ of about 15% corresponds to maximum 5% loss in the resolution within 10 years. This prediction of the loss in resolution will be compared with the results obtained from a more detailed description of the time dependency of the detector in Chapter 5.

Moreover, a continuous decrease, with a larger decrease at the highest energies, has been observed, thus it needs to be monitored in the future years of operation.

[2] this hypothesis was also checked as a test of the method.

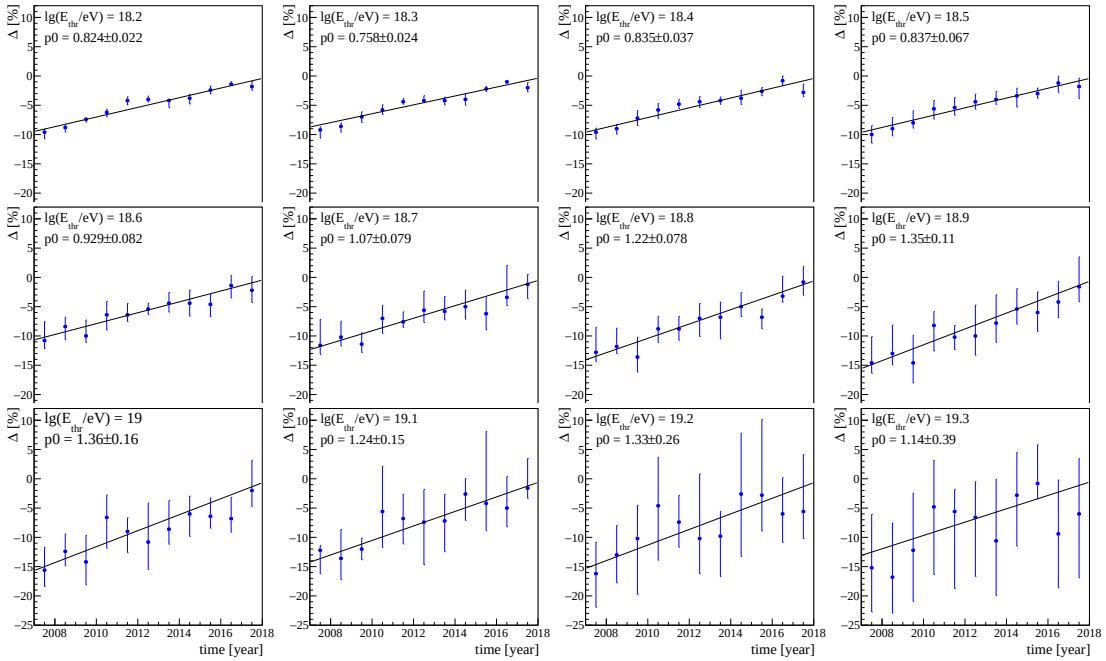

FIGURE 2.19: Δ as a function of time for different energies.

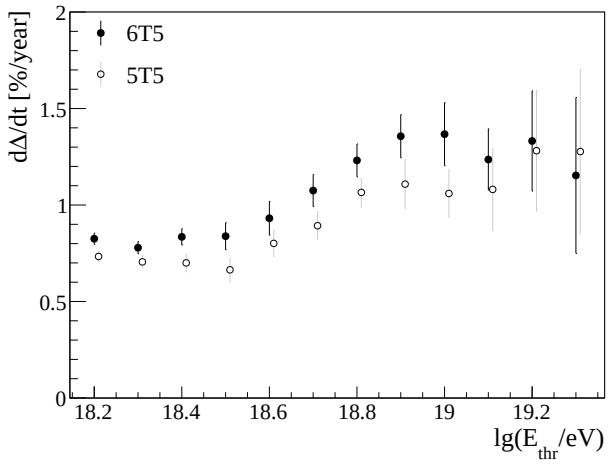

FIGURE 2.20: Yearly variation of Δ as a function of the threshold energy.

2.4 Risetime

The recorded trace in each triggered station contains information related to the mass of the primary particle that initiated the air-shower measured by the surface detector [94, 95]. Indeed, for the same energy, showers that penetrate deeper in the atmosphere (henceforth produced by lighter nuclei, as explained in Chapter 1) will produce signals with a larger time spread due to the different ratio between the electromagnetic and muonic contribution and the path length traversed by the secondary particles.

In order to exploit this feature of the EAS to perform composition studies with the surface array, a variable called *risetime* $t_{1/2}$ has been defined [95]: it represents the time needed by the total integrated signal to rise from 10% to 50% of its total value. In Fig. 2.21, an example of the method to obtain the risetime is shown. This variable

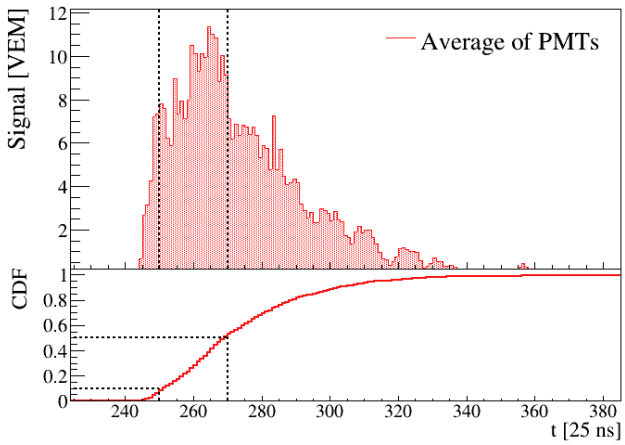

FIGURE 2.21: Top panel: example of a PMT-averaged station time trace. Bottom panel: Cum. Distr. Function of the signal. The dashed lines represent the time when the signal reaches 10% (t_{start}) and 50% (t_{stop}) of the total integrated charge.

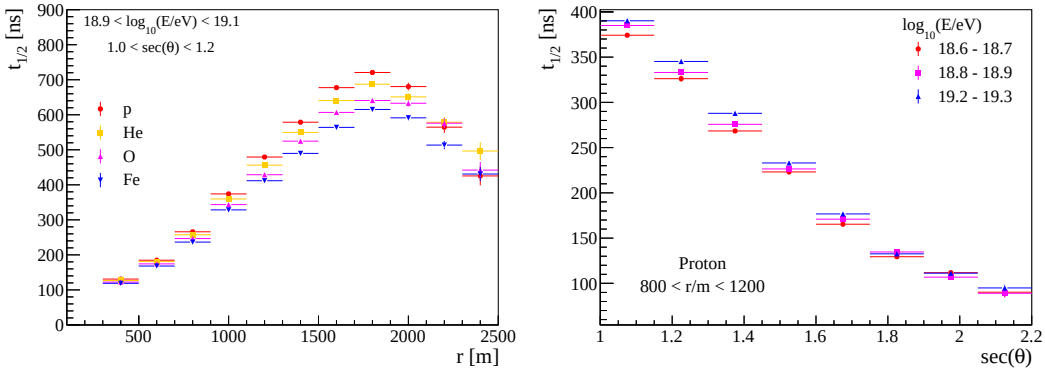

FIGURE 2.22: Risetime obtained from simulations. Left: Risetime as a function of the distance to the shower core for different primaries. The energy range is $18.9 < \log_{10}(E/\text{eV}) < 19.1$ and $\theta < 40°$. Right: Evolution of risetime as a function of the zenith angle of the incident primary particle (proton in this case) for different energy ranges. The distance to the shower core considered is between 800 m and 1200 m.

also maximizes the muon-to-electron ratio since muons are expected to arrive in the first time-bins being highly penetrating particles, traveling almost straight and unaffected by the atmosphere, while $e^{\pm}$ and γ experience attenuation and scattering in their path through the atmosphere. The risetime in a triggered station is computed individually for each PMT and then averaged between them.

In Fig. 2.22, left, it can be seen that the risetime is dependent on the distance in the shower axis, starting at ≈ 100 ns very close to the shower core and reaching values of almost 700 ns at 2000 m far from the core. The measured signals are very small for stations placed further than 2000 m, and the risetime measurement becomes more difficult, leading to a decrease in the risetime. It can also be noticed in the figure the separation between different primaries, confirming the risetime sensitivity to the mass of the primary particle. The risetime also shows a dependency on the zenith angle, as displayed in Fig. 2.22, right plot, in which the risetime of proton primaries for three different energy ranges decreases as θ increases. This dependency can be understood considering that particles arriving at the stations experience different atmosphere thicknesses proportional to secθ. Moreover, as the zenith increases, so

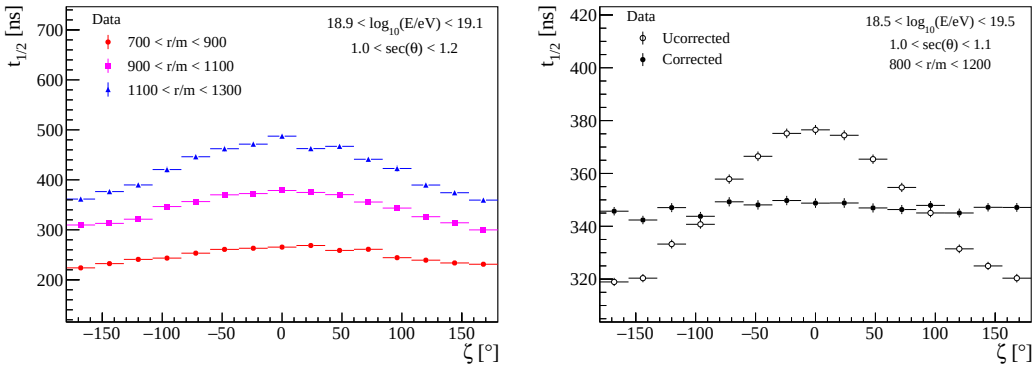

FIGURE 2.23: Left: Risetime as a function of the azimuth angle of the station (more details in text) for different distances to the shower core. The energy is between $10^{18.9}$ eV and $10^{19.1}$ eV, while θ is less than 40°. Right: Risetime before and after the azimuth correction. Energy range between $10^{18.5}$ eV and $10^{19.5}$ eV, θ less than 35° and the distance to the core is between 800 m and 1200 m.

does the amount the atmosphere traversed, reducing the electromagnetic component that is the main contributor to the spread of the signal.

2.4.1 Data selection and corrections

Data are selected to avoid a possible bias due to the reconstruction; thus, the maximum zenith angles used to study the risetime have been chosen to be less than 60°, while the minimum reconstructed energy needs to be larger than 3×10^{18} eV. We also selected stations that did not show signs of saturation in the low-gain channel since the computation of the risetime in these cases is unreliable. For traces with a saturated high-gain channel, the trace is obtained from the low-gain channel. The risetime of selected stations shows a dependency on the azimuth angle of the station with respect to the shower axis's projection onto the shower plane [96]. This behaviour is shown in Fig. 2.23 for different distances to the shower core and fixed energy and zenith angle ranges: this dependency arises from a combination of the effect of the atmosphere on the electromagnetic component (more affected for large azimuth angles) [97, 98] and of geometrical effects [99]. Indeed, it can be noticed that the asymmetry becomes stronger, moving further from the shower core.

A correction of this effect must be performed before comparing the risetimes of different stations. In this case, the applied correction is based on the work in [100], where the corrected risetime is obtained as:

$$t_{1/2}^{\text{corr}} = t_{1/2} - g(r)cos(\zeta) \tag{2.4}$$

where $g(r)$ is defined as a two-degree polynomial function of the distance to the core and is characterized by two parameters that depend on the zenith angle:

$$g(r) = A(\sec\theta) - B(\sec\theta)r^2 \tag{2.5}$$

A and B are parametrized as a third-degree polynomial function of the zenith angle:

$$A(\sec\theta) = p_0 + p_1 \times \sec(\theta) + p_2 \times (\sec(\theta))^2 + p_3 \times (\sec(\theta))^3 \tag{2.6}$$

$$B(\sec\theta) = p'_0 + p'_1 \times \sec(\theta) + p'_2 \times (\sec(\theta))^2 + p'_3 \times (\sec(\theta))^3 \tag{2.7}$$

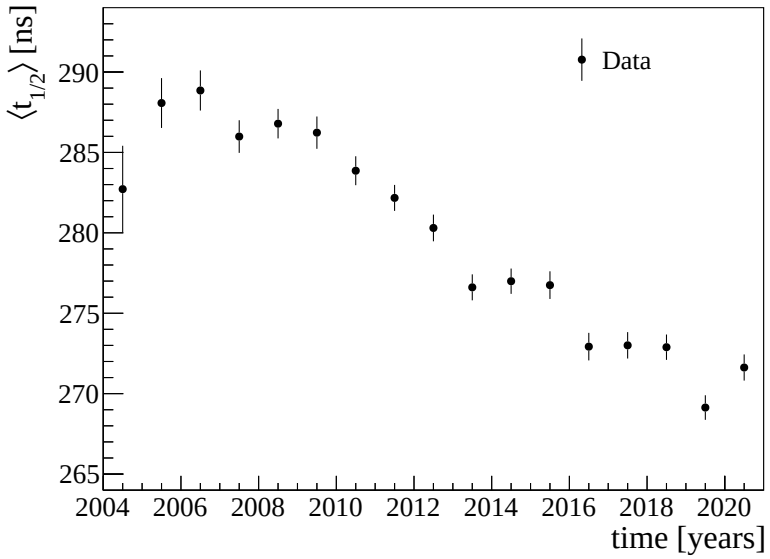

FIGURE 2.24: Mean value of the risetime as a function of time.

After applying this correction, the azimuth angle dependency is removed, as shown in the right plot of Fig. 2.23, where the corrected risetimes (black symbols) display a flat behavior as a function of ζ compared to the bell-shaped trend of the uncorrected ones (open symbols).

Traces are also corrected for the effect of the direct light on PMTs, which causes narrow spikes with a large signal on the recorded signal of a single PMT but not in the other two. The effect, however, does not strongly modify the mean values of risetime, with the correction being less than 1% [101].

2.4.2 Evolution over time

The evolution over time of the risetime can be studied after applying quality cuts and corrections on the data. In Figure Fig. 2.24, the mean value of the risetime as a function of the time is displayed. It can be clearly seen that the value of the risetime steadily decreases over time, being $\approx$ 287 ns just after the end of the deployment of the array in 2008 and dropping to $\approx$ 272 ns in the last years, with a decrease of $\approx$ 15 ns in 15 years. The error bars of each data point represents the error on the mean. The first years show larger uncertainties due to the completion of the deployment. A general decrease in the risetime is expected, considering that it is defined based on the shape of the traces, which, in turn, are affected by aging.

Chapter 3

Modeling the aging

The aging of the surface detector manifests itself as a decrease of A/P and τ of the VEM signal and reflects a decrease in the light collection efficiency; thus, it is induced by a change of the intrinsic properties of the tank. In particular liner reflectivity (s), water absorption length (w) and water level are a few of the properties previously investigated [102, 103, 104, 105]. A deterioration in the water quality or the Tyvek reflectivity will affect the calibration constants and long-term effects due to aging have an impact on high-level variables, as presented in the previous chapter.

A very comprehensive description of how aging effects on electronics and PMTs could be disentangled from the water absorption and liner reflectivity can be found in [106, 107]. The Area over Peak ratio and the time decay constants of VEM signals should be independent of the PMT individual characteristics or the electronics in the station, allowing the possibility of creating a general aging model based solely on the internal characteristics of the tank, regardless of the differences from station to station. However, Offline simulations of WCD assume that the internal properties of tanks are not changing over time. Thus a study of the influence of these parameters on the recorded signal is needed before implementing such a change in the software.

In this chapter, we present a model of the stations' evolution over time that takes into account only the intrinsic properties of the WCD, with the assumption that a change in the liner reflectivity and water absorption can reproduce the A/P behavior. We also assumed that the water level is not changing in time (unless a leak in the tank is present) because checks on the tanks were performed during the years, showing that the water level is constant. The time response of the tank is studied using the shape histograms [106, 107]. We simulated different station's internal conditions to study how the detector response evolves as a function of s and w. By matching the time decay of the signal for vertical muons (τ) between data and simulations, we obtained an estimation of the values for s and w that best describe shape histograms for different years. Finally, we simulated calibration histograms for the values of s and w obtained from our model to verify that we are able to reproduce the A/P evolution over time.

3.1 Simulations of shape and calibration histograms

This work aims to simulate shape and calibration histograms and study their evolution when liner reflectivity and water absorption change in the tank. Particles are injected using Offline r33544. SD simulations are performed using *FastMode* in the G4StationSim Module and following the prescriptions of the *Tutorial* for the SdSimulationCalibration. A custom version of the SdCalibrator was used to store the particle information and the corresponding signals produced in the tank.

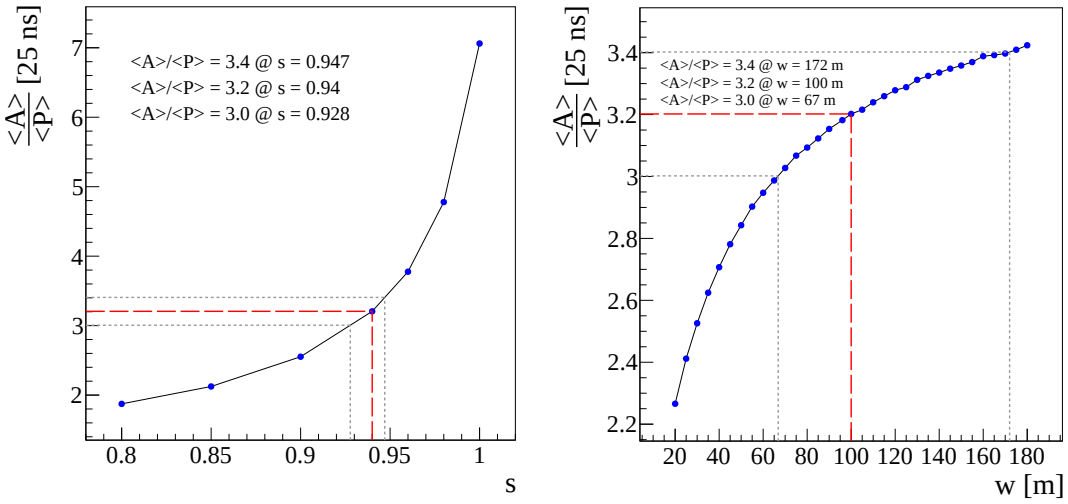

FIGURE 3.1: A/P for VCM. Left: Dependence on liner reflectivity, $w = 100\,\text{m}$. Right: Dependence on water absorption, $s = 0.94$.

The first studies were performed using vertically centered muons (VCM) injected in the center of the tank to investigate the influence of the tank properties on A/P. As can be seen in Fig. 3.1, A/P is more sensitive to the liner reflectivity. In particular, a change of reflectivity of ± 0.01 at $s = 0.94$ and fixed $w = 100\,\text{m}$ corresponds to a change of $\pm 0.2\,[25\,\text{ns}]$ for A/P; to obtain the same variation of the A/P at fixed $s = 0.94$, w has to be changed by $+72\,\text{m}$ and $-34\,\text{m}$, respectively. A decrease in s reduces the time decay constant of the photo-electrons trace (denoted here as τ_{PE}), as shown in Fig. 3.2 (right plot): a change for s of ± 0.01 corresponds to a change of $\pm 6\,\text{ns}$ for τ_{PE}. This change has a stronger influence on the Area since this variable is the integral of the signal over time and, as it can be observed in the left plot of Fig. 3.2, the signal becomes sharper as s decreases due to fewer photons being reflected. The Peak is less affected because it is the maximum value of the trace and is mainly determined by the first reflections, leading to a decrease of A/P. The first reflections at the liner can be seen in the middle plot of Fig. 3.2 that shows a zoom of the trace in the first 50 ns. Doing a rough estimation, the difference between the peaks is around $\Delta t = 5\,\text{ns}$, which corresponds to the time needed by photons to traverse the height of the tank from the bottom to the top. Indeed we can obtain $d = (c \cdot \Delta t)/n \approx 1.2\,\text{m}$, where n is the refractive index of water and c is the speed of light.

Taking into account the mild dependence of A/P on w, we explored the following phase space for s and w: s between 0.9 and 0.99, with steps of 0.01; w between 150 m and 50 m, with steps of 10 m. As a reference, standard values used in Offline for SD simulations are: $s = 0.94$ and $w = 100\,\text{m}$.

In order to reproduce the calibration histograms, we used simulations of low energy air showers. These are showers initiated by primaries with the rigidity (E/Z) distribution displayed in Fig. 3.3(a): the majority of primaries are light nuclei, accounting for 98% of all simulated primaries (88% protons and 10% ^{4}He). The rest are heavier nuclei: O, Si, Fe, and other nuclei (2%). All primary distributions were produced with a power law spectrum with a differential spectral index of 2.7. The distribution of secondary particles that reach the ground as a function of the total momentum of the particle can be seen in Fig. 3.3(b). These are the ones injected into the tank. The majority of highly energetic particles are muons around 1 GeV, while γ and $e^{\pm}$ contributions dominate the low energy range, around 100 MeV. We do not

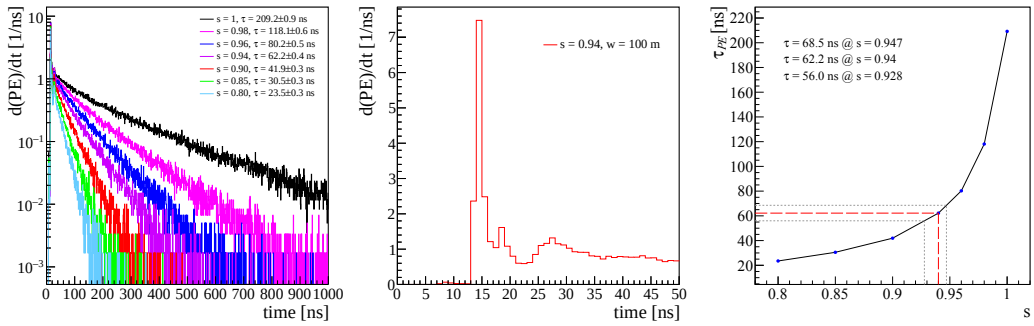

FIGURE 3.2: Left: Photo-electrons trace of a VCM with $E = 1\,\text{GeV}$. Middle: Multiple reflections are visible in the trace's first 50 ns. Right: Time decay constant dependency on liner reflectivity. The red dashed line is related to a simulation with $s = 0.94$ and $w = 100\,\text{m}$.

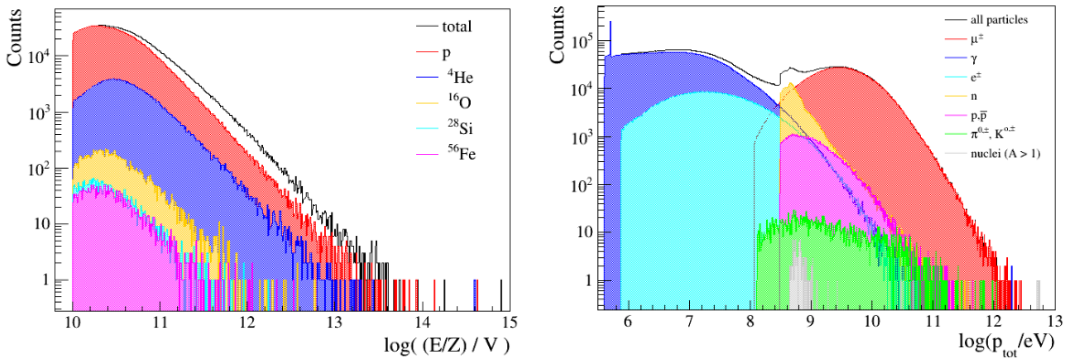

(a) (b)

FIGURE 3.3: (a) Energy distribution per nucleon for different primaries. (b) Total momentum distribution for secondary particles reaching the ground.

model the possible variation of the secondary particle flux along the year, due to the changes in the atmosphere; however, previous studies have shown that seasonal variations of A/P and τ are most probably related to the changes in electronics with temperature [108].

These secondary particles are randomly injected over a hemisphere with a 2.2 m radius that fully contains the tank. We injected 200 000 particles in the tank for each combination of s and w in the ranges mentioned above, for a total amount of $\approx$ 200 000 000 injected particles.

PMTs are simulated with identical properties (such as PMT gains, quantum efficiency and optical couplings) and their signals are combined to obtain an overall description of the tank response. In order to build shape histograms for each simulation, we selected and summed pulses with $0.9 \cdot Q_{\text{VEM}} \leq Q \leq 1.1 \cdot Q_{\text{VEM}}$, where Q is the integral of the trace and Q_{VEM} is obtained from the muon peak of simulated charge histograms multiplied by 0.96. The last condition is used to reproduce the same method used in the field [83] that is based on Q^{est}_{VEM}, an observable not simulated in the SdSimulationCalibration in Offline, since the Module does not reproduce the continuous on-line calibration of the stations in the field. An example of simulated shape histograms for standard values of s and w is shown in Fig. 3.4. These histograms are normalized to their peak. An exponential fit, using the same Eq. (2.1) employed for data, is performed to extract the time decay constant of the signals

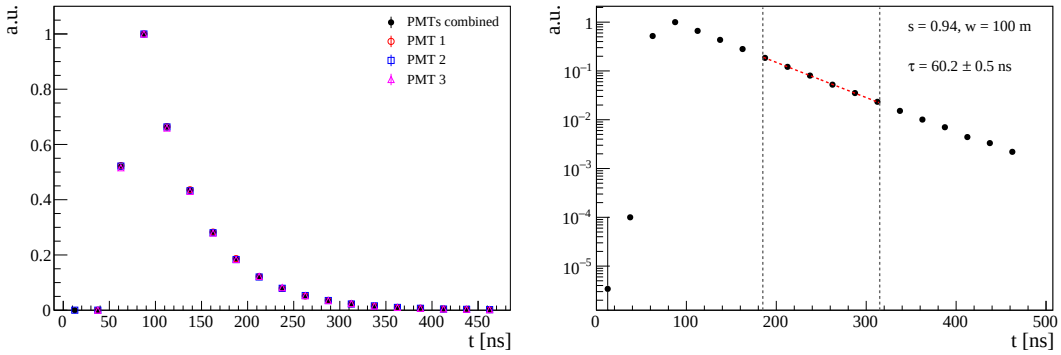

FIGURE 3.4: Shape histograms for different PMTs and their combined histogram (left). Fit on the combined histogram (right).

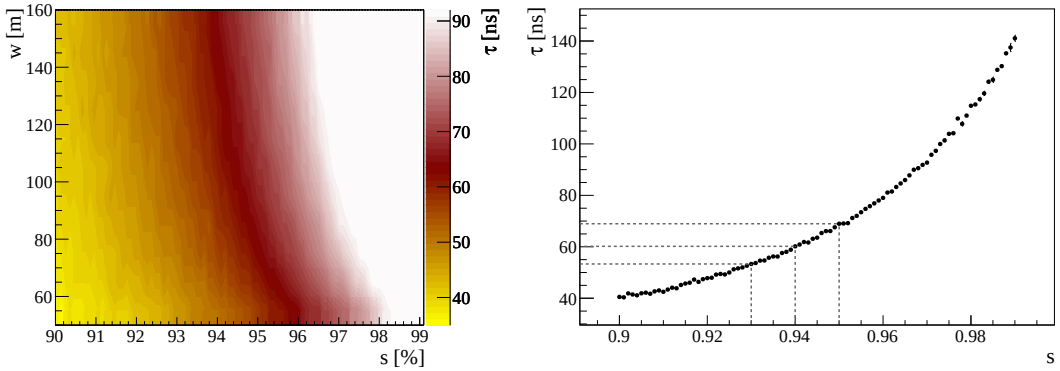

FIGURE 3.5: τ as a function of s and w for omnidirectional particles (left). The evolution of τ in terms of s for $w = 100\,\text{m}$ (right).

(τ). The fit range has been fixed at the same values as the one used for data in Section 2.2.1, [185, 315] ns, following the same reasoning applied in the case for data. To avoid any biases induced by arbitrary choices when comparing data and simulations, we applied the same selection criteria used for data and listed in Section 2.2.1. In this case, the criteria of a measured τ that differs by more than 10% between PMTs translates in $\Delta s = 0.01$ that is incompatible with the assumption of uniformity of tank parameters seen by each PMT.

The evolution of τ as a function of s and w is shown in Fig. 3.5, left. It can be noticed that the dependency on s is stronger than on w. On the right plot, the profile for $w = 100\,\text{m}$: τ ranges between 40 ns and 140 ns and it can be seen that a change in s of ± 0.01 from 0.94 can lead to a change of $\pm 8\,\text{ns}$ in τ.

To see the effect on calibration histograms also in the case of omnidirectional particles, we studied the dependency of A/P by varying s and w. The chosen threshold to produce these histograms is 3 [FADC bins/25 ns], lower than the standard value used in the SdCalibrator Module (15 [FADC bins/25 ns]), to avoid the trigger effects on the calibration histograms.

The simulated calibration histograms have been fitted with Eq. (2.2) to primarily extract the Area and Peak, which are defined based on the second derivative of the fit function, in the same way, used in data in Section 2.2.2. The fit to the combined PMTs distribution for standard values of s and w is shown in Fig. 3.6. The position of the muon hump can be seen at 181 [FADC bins] in the charge histogram and at

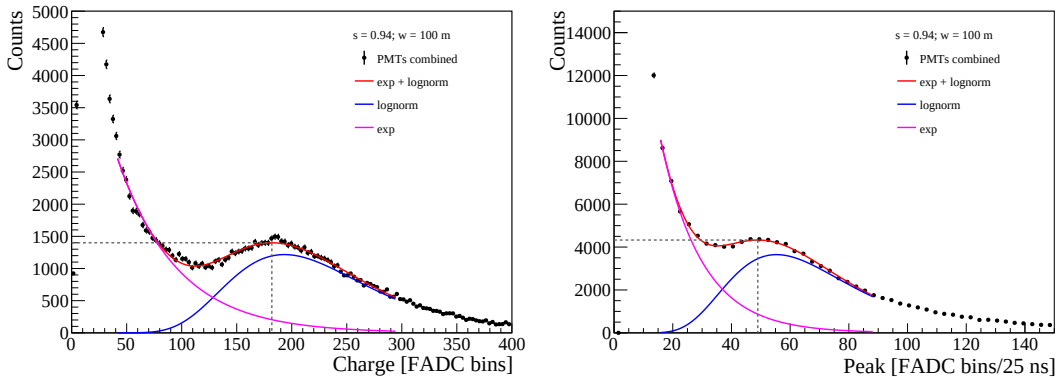

FIGURE 3.6: Charge (left), peak (right) distributions and their fits for the sum of PMTs.

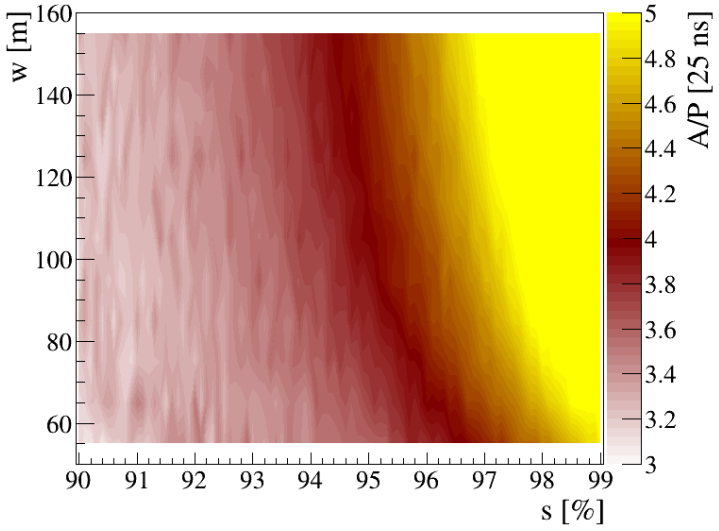

FIGURE 3.7: A/P as a function of s and w for omnidirectional particles.

49 [FADC bins/25 ns] in the peak histogram, giving $A/P \approx 3.7$ [25ns]. A valley between the first and second peak is also visible in both histograms. The evolution of A/P for values of s and w over the selected ranges show a strong dependency on s also in the case for omnidirectional particles, as shown in Fig. 3.7: at fixed $w = 100$ m, moving from $s = 0.94$ to $s = 0.93$ leads to a decrease for A/P of $\approx 5\%$, while a decrease of 10% in w (from 100 m to 90 m) at fixed $s = 0.94$ reduces A/P by only $\approx 0.7\%$.

The extracted values from the fit are used to normalize and rescale calibration charge histograms, as shown in Fig. 3.8 for different values of s and w: on the left varying s between 0.91 and 0.97 at fixed $w = 100$ m and on the right varying w between 50 m and 150 m at fixed $s = 0.94$. A decrease in liner reflectivity in simulations leads to a pronounced widening of the muon peak and an increase of the right tail of the first peak since the muon peak moves to lower values resulting also in a smaller *hump-to-valley* ratio. The fact that the increase in the right tail of the first peak is due to the muon peak is also suggested by the decrease of the exponential decay constant of the em part when s decrease. Simulations with different w show smaller differences between histograms, mostly seen for low-quality water, with similar behavior for s: an increase in the spread of the muon hump and the exponential tail of the first

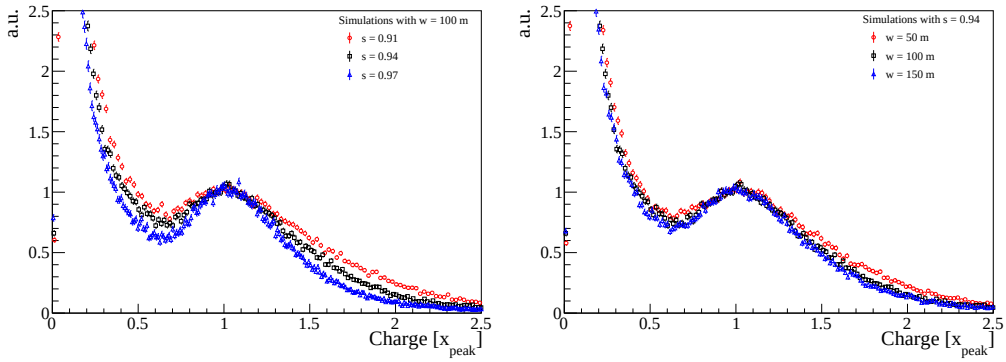

FIGURE 3.8: Comparing simulated charge histograms. Left: Varying liner reflectivity. Right: Varying water absorption.

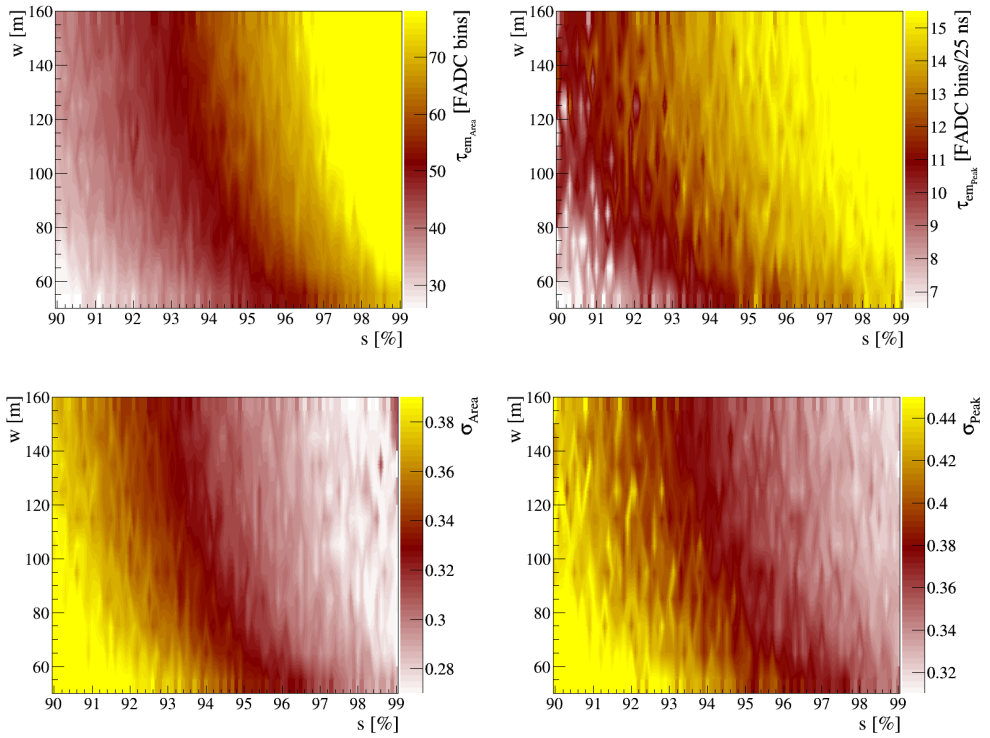

FIGURE 3.9: Exponential decay of the electromagnetic peak (τ_{em}) and width of the muon hump (σ) obtained from the fit as a function of s and w for charge (left), peak (right) histograms.

peak when w decreases. The dependency of the exponential decay of the em part (τ_{em}) and the width of the muon hump (σ) on s and w is shown in Fig. 3.9 for both charge and peak histograms.

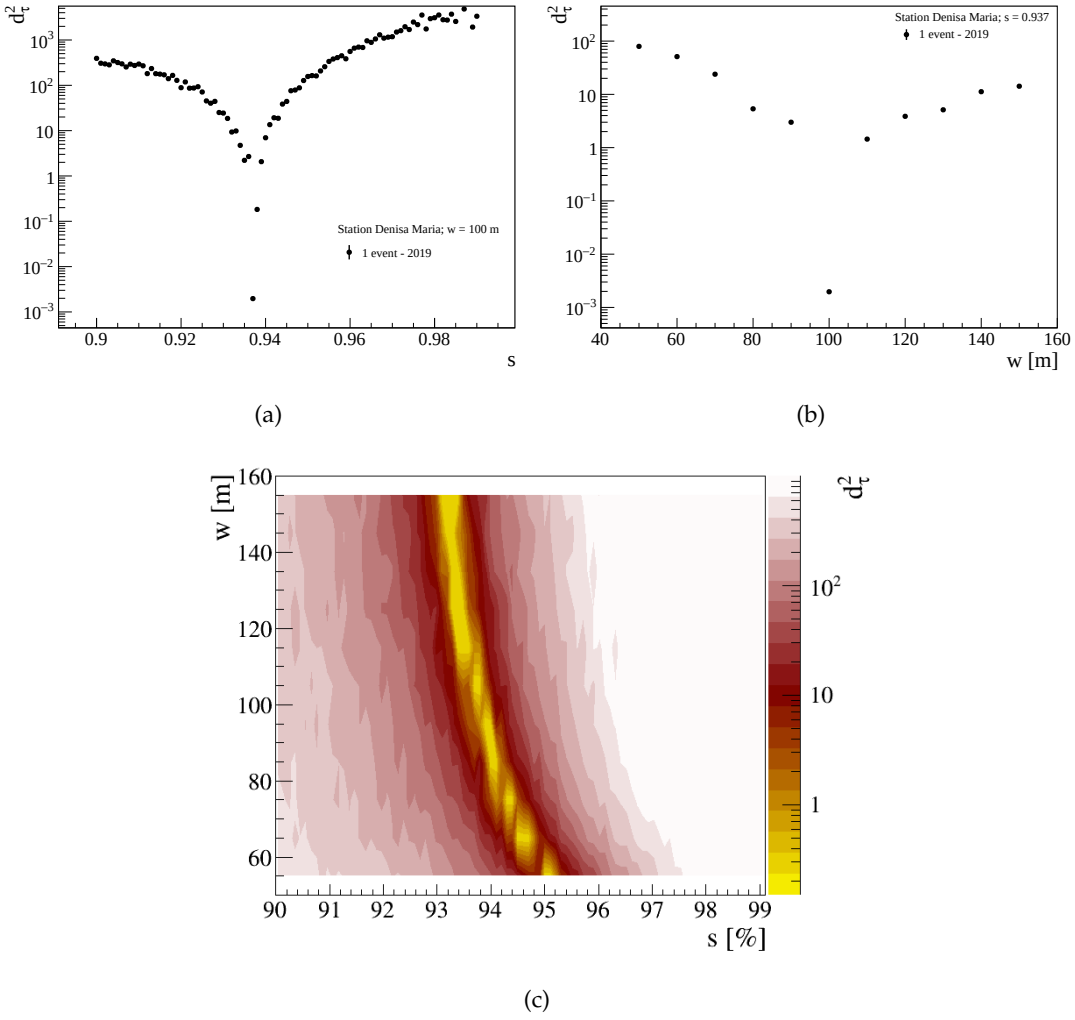

FIGURE 3.10: Distances between data and simulations. (c): d_τ^2 for one event in 2019. (b): Profile for $w = 100$ m. (a): Profile for $s = 0.937$, best matching liner value.

3.2 Matching data and simulations

To quantify the differences between data and simulated shape histograms, we defined a quadratic distance based on τ as follows:

$$d_\tau^2 = \frac{(\tau_{\text{data}} - \tau_{\text{sims}})^2}{\delta\tau_{\text{data}}^2 + \delta\tau_{\text{sims}}^2} \tag{3.1}$$

We scanned the parameter space of s and w, comparing each event from data with simulations and evaluating the distance between these histograms. The result of this method for one event of Denisa Maria in 2019 is shown in Fig. 3.10(c). A well-defined valley is visible in yellow, while white and reddish regions can be excluded; values of $w < 80$ m are unlikely since tanks in the field do not show a growth of bacteria inside the water [109], while for $w > 100$ m changes are not anymore visible when increasing w, as can be noticed from the plateau in the valley. There is also a degeneracy between s and w, and no well-defined minimum is observed. For this reason, we decided to fix the water absorption to the standard value of $w = 100$ m. The profile of the previous 2D scan for $w = 100$ m is shown in Fig. 3.10(a). The

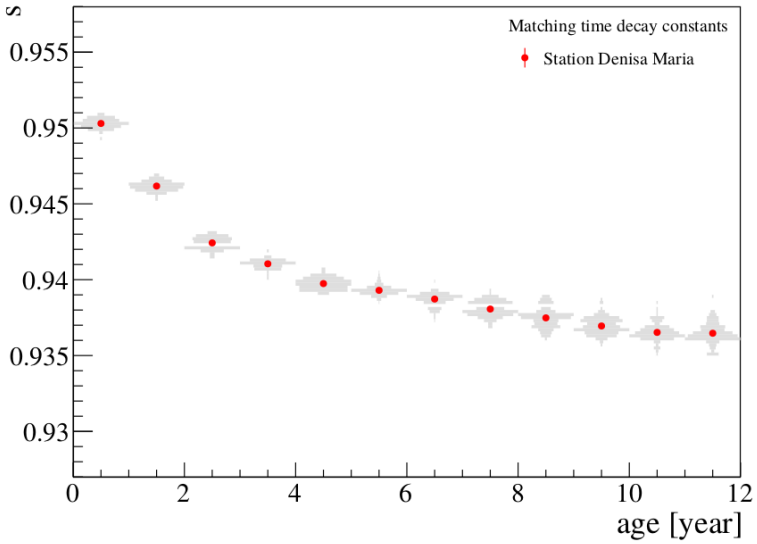

FIGURE 3.11: Liner reflectivity, s, over time for station Denisa Maria.

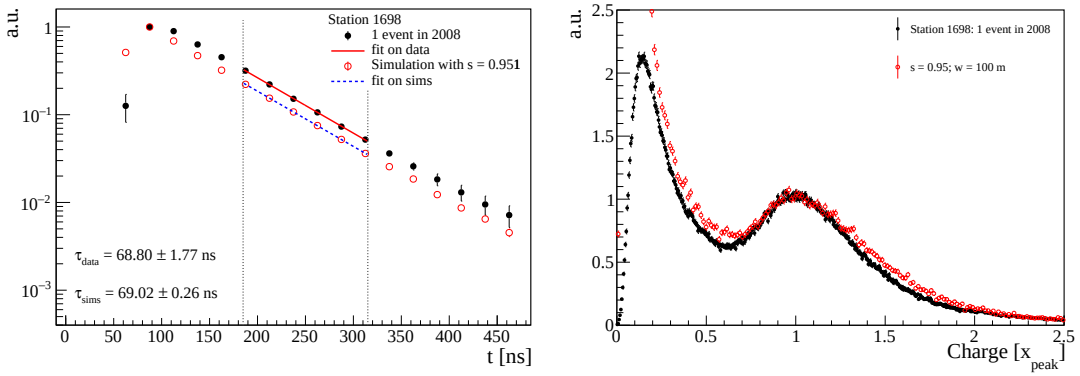

FIGURE 3.12: Comparison between simulations at best matching s and one event in 2008 for station Denisa Maria. Left: Shape histogram. Right: Calibration histograms.

minimum distance is found by fitting a 2nd-degree polynomial function around the minimum. In this particular case, it is located at $s = 0.937$.

Events are selected using the same criteria chosen in Section 2.2.1 and are the same ones used to produce Fig. 2.7. Each event is analyzed using this method, giving the evolution of the best matching liner reflectivity (called here s_{best}) over time. The result of the mean s for station Denisa Maria is shown in Fig. 3.11 (error bars represent the error on the mean). For station Denisa Maria we can describe the shape histograms evolution if the liner reflectivity has a decrease of $\approx 1.3\%$ over 11 years, from 0.95 to 0.937, as shown in Fig. 3.11, where s is represented as a function of the age of the tank.

While this method is able to reproduce the time decay constant of shape histograms, as shown in the left picture of Fig. 3.12, simulated calibration histograms at s_{best} obtained with the same method are not able to reproduce the calibration histograms extracted from data, Fig. 3.12 right plot. This difference is not well understood, but it could be related with a discrepancy in the flux of secondary particles experienced by the tanks in the Auger site compared to the one used to produce the simulations, since the real flux at the Auger site has never been measured, thus the

secondary particle distribution used in this study may not properly reproduce the one observed in the field. A variation of this flux should not affect shape histograms but could change the shape of charge and peak histograms. Another source for this discrepancy could be associated with a different PMT efficiency between data and simulations: in previous studies [107, 110] the efficiency of the PMT (including a possible variation of the transparency of the window) was simulated by using a constant factor on all photoelectrons. Thus, shape histograms are not affected by this effect, while calibration histograms show a dependency on this factor, especially for the *hump-to-valley* ratio.

3.3 Evolution over time

We extended the same analysis performed for station Denisa Maria to all the other stations of the array. As mentioned in Section 2.2.1, the events selection process concerned 1640 stations, for just 5 of which it was not possible to recover any information and an additional cut on the decay constant, requiring that $\tau < 100\,\text{ns}$, was used to remove outlier values due to bad-behaved stations.

The mean s, obtained as in the case of station Denisa Maria, as a function of age for all selected stations is illustrated in Fig. 3.13, left, in which it is possible to see a bimodal distribution during the years, as also previously observed for τ and A/P in Fig. 2.7 and Fig. 2.11. The mean s values for the two populations at each age are obtained by fitting a sum of two Gaussians for each age distribution, displayed in Appendix C.1, Fig. C.3. A general decrease over time with a difference in s between the two populations of $\approx$ 1% is observed. On average, s decreased by 1.7% in 15 years. In this case, the error on the mean is used as uncertainty. The distribution of s over the array for different ages is shown in Appendix C.1, Fig. C.5.

To obtain some more information, we classified the stations into three categories based on their s value: population 1, population 2, and mixed population. In order to do that, firstly, for each age, we separated them by choosing a 90% purity in each population from the total distribution. The double-gaussian fit was used to obtain the values where the contamination of the populations between them reaches the level of 10%. As an example, at age 6, in Fig. 3.13, right plot, the two dotted lines indicate the values obtained to separate the populations, with the color lines representing the corresponding population in which the purity cut was applied. The stations with an s value falling in the overlapping region were tagged as "mixed". For each year, then, each station was classified into one of the three categories and the general belonging of the station to one of the three categories was obtained by choosing the category which had the most tags during the years for that specific station. Then we looked at the positions of the tanks for these three subsamples. In Fig. 3.14, the spatial distributions of the liner populations can be seen: stations with lower values of s (population 1, blue dots) seem to be more located in the southern area of the array, while the second population (orange dots) appears more in the northern part, and the mixed population (smaller in absolute numbers compared to the others) is spread all over the array. The evolution of these three populations over the years can be seen in Appendix C.1, Fig. C.6.

Population 1 was deployed at the beginning, followed by population 2, that was completed during the years until 2008, when the array was finished. After that year, almost no changes appeared in the maps, as expected.

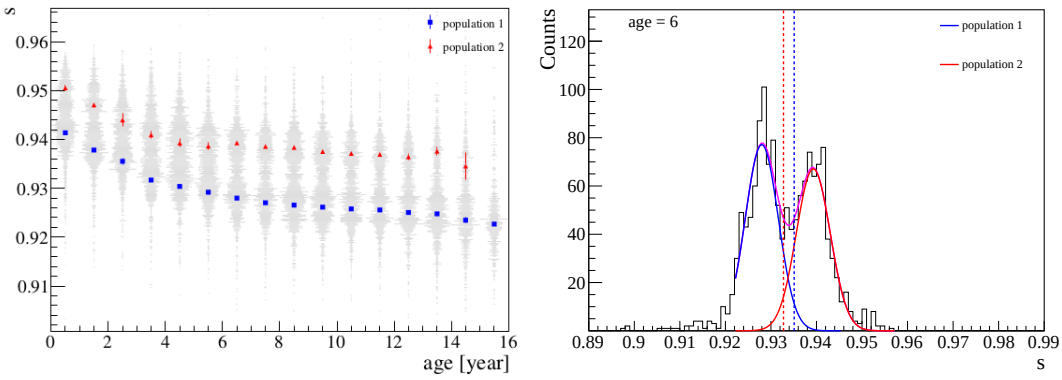

FIGURE 3.13: Left: s_{best} evolution over time for the full array. Right: Separating the two liner distributions at age 6 using a purity cut at 90%.

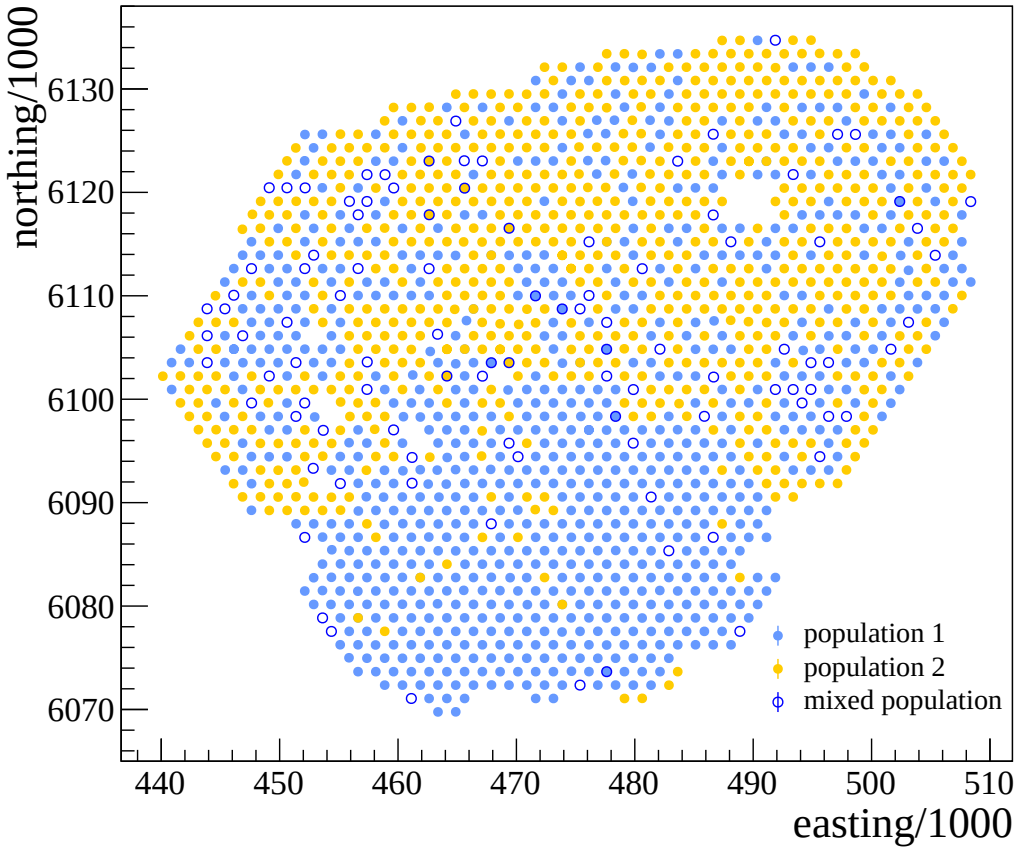

FIGURE 3.14: Map of the three station liner populations.

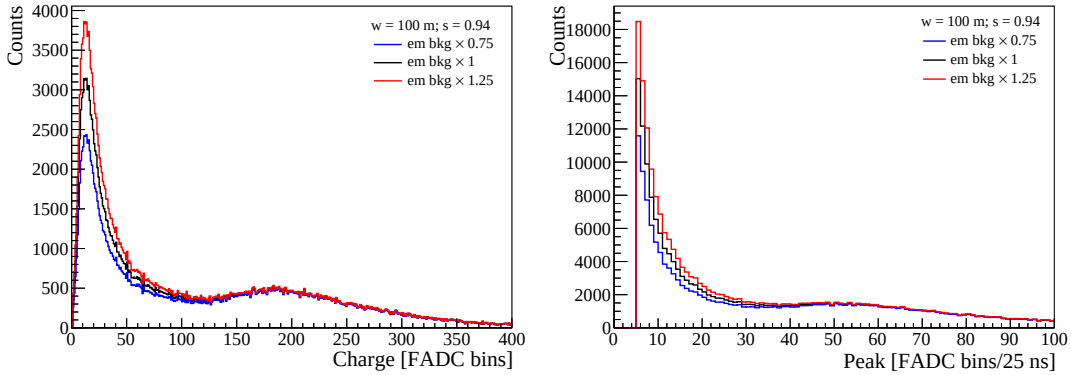

FIGURE 3.15: Calibration histograms (left: Charge, right: Peak) varying the contribution of the electromagnetic background.

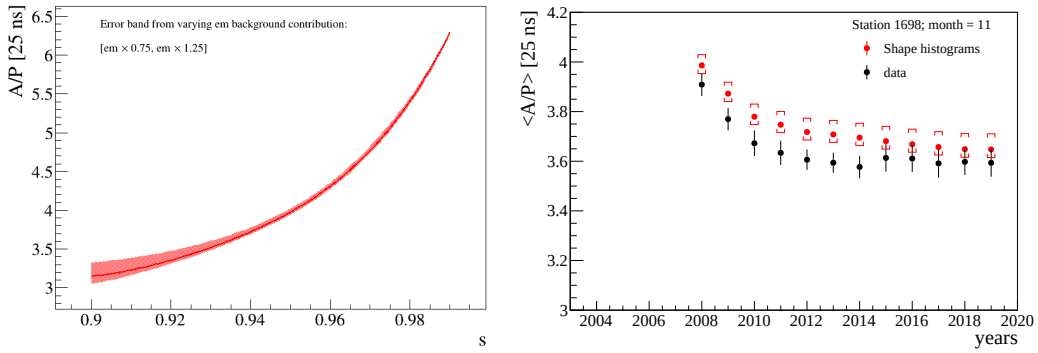

FIGURE 3.16: Left: A/P as a function of s. Right: Comparison between A/P over time for data calibration histograms and for converted s values obtained from matching data and simulations.

3.4 From τ to A/P

Values of liner reflectivity over time that were found by matching shape histograms between data and simulations can be translated into A/P values. In order to do this, we used the simulations to parametrize A/P as a function of s and fixed $w = 100\,\text{m}$ with a 4th degree polynomial function:

$$\begin{aligned} f(x) =& (3.724 \pm 0.008) + (22.5 \pm 0.4) \cdot (s - 0.94) \\ &+ (253.3 \pm 22.6) \cdot (s - 0.94)^2 + (3554.7 \pm 379.1) \cdot (s - 0.94)^3 \\ &+ (58902.8 \pm 13102.9) \cdot (s - 0.94)^4 \end{aligned} \tag{3.2}$$

A/P ranges between 3.1 [25 ns] for $s = 0.9$ and 6.2 [25 ns] for $s = 0.99$, as can be seen in Fig. 3.16, left plot, and the value for $s = 0.94$ is around 3.7 [25 ns].

The contribution of the electromagnetic background in calibration histograms has an effect on the determination of Area and Peak. Since we are not able to fully reproduce the exact electromagnetic background due to trigger effects and a lack of knowledge about the real flux in the Auger site, we simulated calibration histograms (charge and peak) with different electromagnetic components in order to

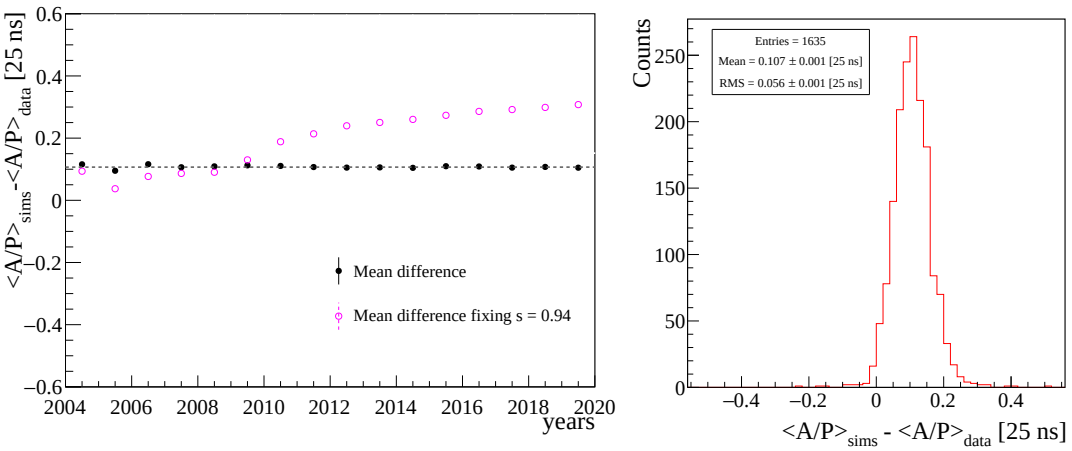

FIGURE 3.17: Left: Difference over time between A/P from data and from best matching simulations (filled symbols) for all considered stations. Open symbols show the bias when the aging model is not implemented in simulations. Right: Distribution of differences.

take into account this possible systematic in the parametrization of A/P as a function of s. The magnitude of the electromagnetic background obtained from injecting secondary particles inside the tank, as explained in the description of the method used to produce the calibration histograms, was modified by $\pm 25\%$, and the effect on calibration histograms can be seen in Fig. 3.15, for both charge and peak histograms: it is more evident for lower values of s, due to the merging of the muonic component with the electromagnetic component. The effect of this change is translated in the form of the error band showed in Fig. 3.16, left plot.

This model can reproduce the general decreasing trend of A/P for station Denisa Maria by only changing the liner reflectivity in the tank, as shown in Fig. 3.16. Systematic uncertainties are obtained from the error in the conversion from s values to A/P values. However, a small difference of 0.1 [25 ns] is observed between data and simulations. The same difference is observed for all stations over time, as shown in Fig. 3.17, left, where the dotted line represents the mean of the distribution of the average difference, obtained from the right plot, and the open symbols represents the difference over time when using the value of A/P when fixing s at the default value of 0.94. The mean average difference for all stations is 0.107 ± 0.001 [25 ns], with a spread of 0.056 ± 0.001 [25 ns] as shown in Fig. 3.17, right.

3.5 Discussion

τ is decreasing over time due to the aging of the SD, probably due to the deterioration of the characteristics of the tanks, such as liner reflectivity and water absorption. Simulations of different tanks conditions were performed, and a model to describe the A/P trend over time was implemented by matching data and simulations using shape histograms. We found that the shape histograms are mainly affected by the liner reflectivity, and we showed that by changing this parameter, we can describe the evolution of A/P. A decrease of 1.7% for s in 15 years is necessary to reproduce the aging of the tanks. A small A/P difference of 0.1 [25 ns] between data and simulations is present and cannot be reduced in this analysis. We also found that the stations distributions for τ, A/P and s show a bimodal behavior. In particular, when analyzing s over time and the array, the two observed populations are related to the deployment time. The effect of aging on air-shower measurements will be addressed in the next chapter.

Chapter 4

Aging effects on air-shower reconstruction

The loss over the years of the collected light in the WCDs has been shown to affect the shape histograms, the calibration histograms and the risetime. This effect is, therefore, also present in the recorded signal of air-showers in the tanks, possibly leading to an impact on the reconstruction of these air showers. Since standard Offline simulations do not take into account the time evolution of the SD, the effect of the aging in the showers reconstruction can not be quantified with the usual simulations chain.

In this chapter, the implementation in Offline of the aging model based on the decrease over time of the liner reflectivity of the tanks will be shown, and its effects on high-level and station-level variables will be studied. In order to precisely assess the changes due to aging in the EAS reconstruction, the first step consisted in modifying the liner reflectivity of all stations with the same value: first, with a high reflectivity (simulating young tanks just after their deployment) and then with a lower one (describing 15 years old tanks in the field). Each individual CORSIKA shower is then thrown in the array (fixing all the other properties) and reconstructed in these two different configurations, obtaining twin reconstructed showers, differing only by the internal reflectivity of the WCDs.

However, the surface array exhibits a complex behavior over time with two different stations populations, having different τ values that evolve in a similar way during the years, as shown in the previous chapters. A more realistic SD simulation is then performed, changing the properties of each tank according to its evolution over time as previously obtained by studying the shape histograms of the individual stations during the years. In this way, it is possible to realistically compare the results obtained from simulations with data.

4.1 Twin showers

The method used to study in detail what are the effects caused by aging on several observables consists of reconstructing the same shower twice using two different liner reflectivities in the definition of the properties of the tank in GEANT4 [111] detector simulations. All of the other parameters and event configurations are kept the same. This procedure allows us to selectively study the effect of aging in the reconstructed air showers, avoiding any other source of discrepancies.
The two reconstructed events are called *twin showers*, since they are obtained from the same primary CORSIKA shower and are used to asses how this single change can modify the air-shower reconstructed observables. To assess the maximum effect, two extreme values of liner reflectivity are used: 0.922 and 0.962, called respectively s_{min} and s_{max}.

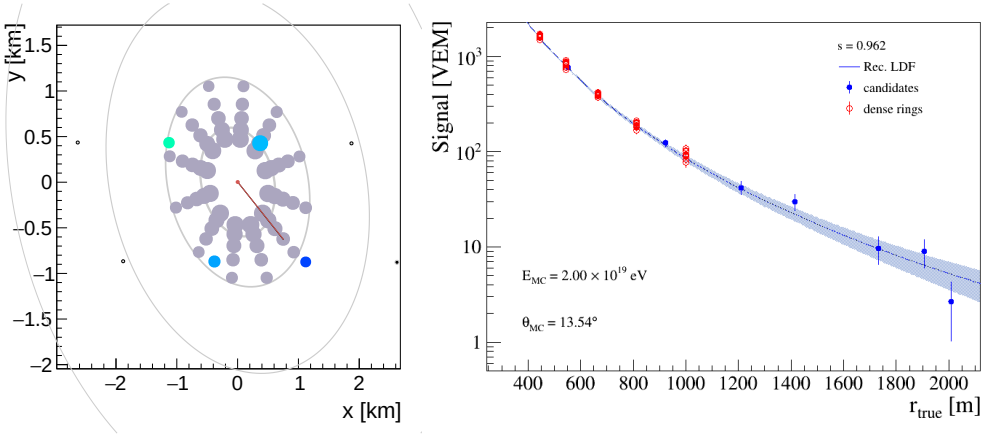

FIGURE 4.1: Example of a reconstructed shower with E = 2×10^{19}eV and $\theta = 13.54°$ for a young station. Left: Footprint on the ground, with the projections of the dense rings in grey. Right: Stations signals as a function of the distance to the true core location.

4.1.1 Simulations configurations

A sample of 1000 proton showers produced with CORSIKA 7.6400 and EPOS-LHC as hadronic model, was used to obtain the *twin showers*. The energy distribution of this sample is uniform in the energy range $19.0 < \log_{10}(E/\text{eV}) < 19.5$, as well the angular distribution in $\cos^2\theta$, for zenith angles between 0° and 65°.

Each shower has been fed to Offline v33544, and it is simulated and reconstructed two times, once using s_{min} and the other one using s_{max}. The reflectivity of all the stations in the array has been changed in the configuration file used for the reconstruction; an example of this *bootstrap* file can be seen in Appendix H. The calibration constants (Area and Peak of the calibration histograms) of the three PMTs were modified accordingly using the parametrization of Area and Peak as a function of the liner reflectivity obtained for vertically centered muons, as can be seen in Fig. 3.1, left. In setting the simulation parameters, the core location and the seeds for the detector and the shower simulations were fixed in order to have the same particles entering the tanks in the two different simulation configurations, using s_{min} and s_{max}, and thus avoiding any randomness in the reconstruction process. Each primary shower is thrown just once in the array for each of the two realizations.

To better understand how aging affects the shower reconstruction, a series of 5 artificial *dense rings* of stations were added around the shower core at different distances on the shower plane: 446, 545, 665, 812 and 1000 m. Each ring is composed of 12 stations. An example of the footprint of a shower can be seen in Fig. 4.1, left, where in gray the projections on the ground of the additional rings are visible.

The primary showers go through the full SD simulation chain, presented in the *Module Sequence* in Appendix H, where all the processes involved during the data acquisition on the field are reproduced, such as the detector response and the triggers. As for the data, the recorded signals are used to reconstruct the information about the primary particle initiating the shower. An example of the resulting lateral distribution function (LDF) for one shower, obtained by fitting the station signals over the distance to the shower axis on the shower plane, is shown in Fig. 4.1, right: the total signals of candidate stations are shown as blue dots, while the dense stations are represented with red open symbols.

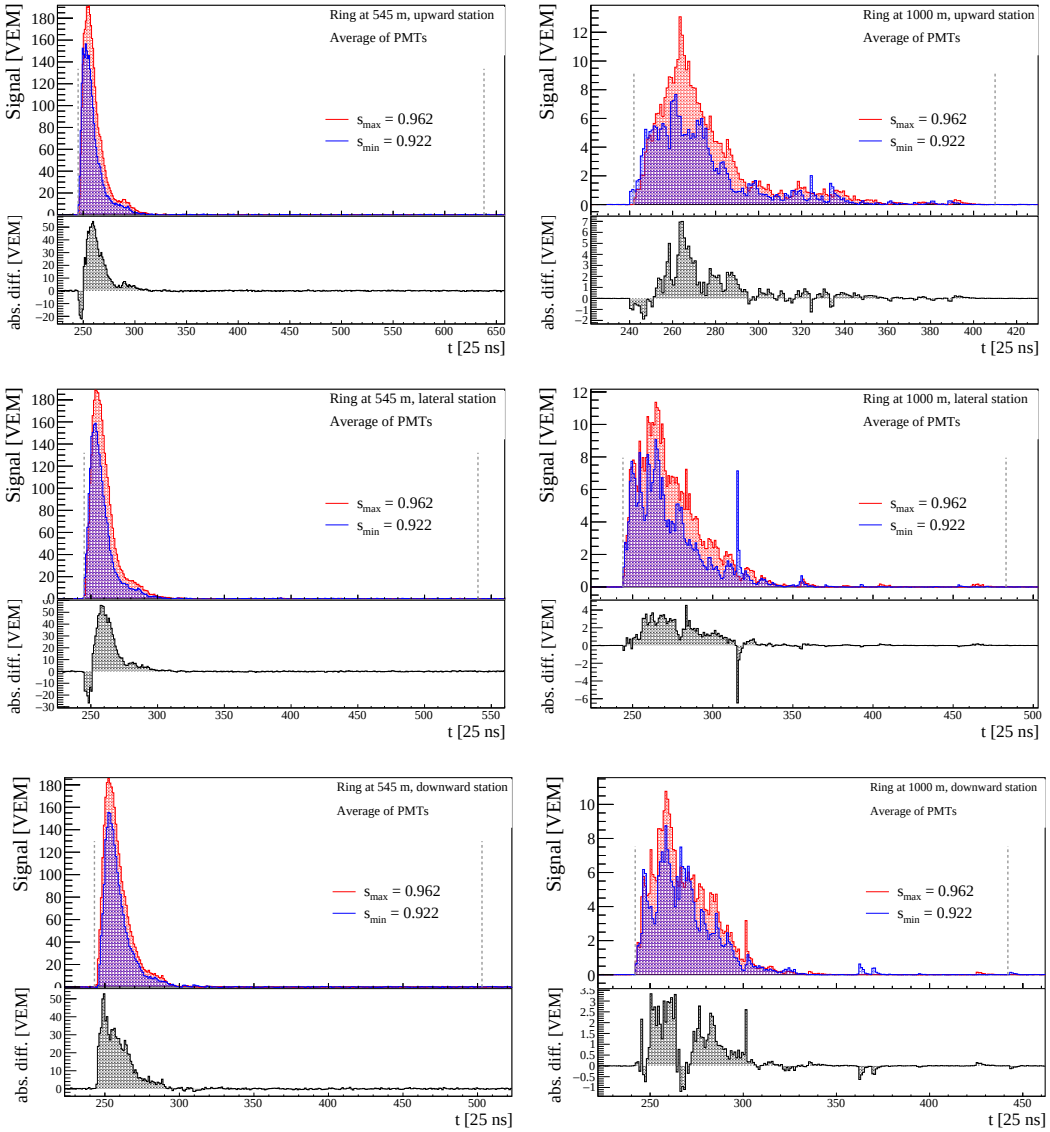

FIGURE 4.2: Signal traces of twin showers for several dense stations, in red young stations and, in blue, old stations. Left: Ring at 545 m. Right: Ring at 1000 m

4.1.2 Signal traces and risetime

The electronics samples the signals of the particles entering the tanks and the recorded traces are then calibrated using the values of the Area obtained from calibration histograms (or from the calibration constants defined in the configuration file, in the case of simulated events) and are expressed in units of VEM. For every event we average the traces from the three PMTs in a station to smooth their intrinsic fluctuations, thus better observing the trace shape. In Fig. 4.2, examples of simulated traces are shown: on the left, three stations (upward, lateral, and downward, defined as stations with azimuth angle on the shower plane of 0, 90 ° and 180 °, respectively) for the ring at a distance of 545 m and on the right for the ring at 1000 m. It can be noticed that the traces differ between the two different rings, being larger and narrower for the ring close to the shower core, with a peak up to 180 VEM. While the further from the core, the smaller and more spread the signals, as expected, with a peak of ∼10 VEM. The twin showers are displayed in two different colors: in red

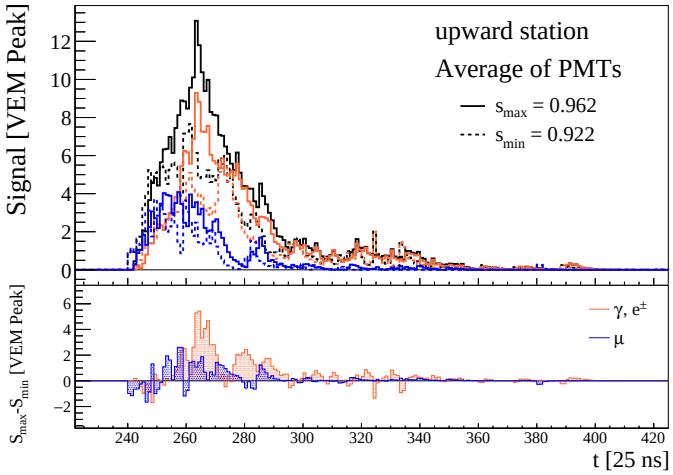

FIGURE 4.3: Same trace for the upward station showed in Fig. 4.2, split for the different signal components.

for the younger station (high reflectivity) and in blue for the older station (low reflectivity). The absolute difference between them can be seen in the lower part of each plot, in grey: the traces obtained with s_{max} are larger compared to the old ones, up to 50% in certain time bins. In both cases, 90% of the signals is contained in just 70 time bins, corresponding to 1.75 ms. Some traces in older stations, especially upward and lateral, appear to start earlier than their twin version, leading to a negative difference in the first time bins; this seems to be related to the trigger definition and the resulting time window in which the interesting part of the signal is defined. The start and stop times of this window is shown as grey dashed lines in Fig. 4.2, with a total time lenght that spans between 5 and 10 ms for different rings and stations.

The individual components of the total traces were extracted from simulated events. The electromagnetic and muonic contributions account for more than 99.5% of the total signal, thus they were the ones considered in this study. The electromagnetic component (orange line in Fig. 4.3) is more spread in time, around 100 time bins, while muons (blue line) cluster in $\approx$ 40 time bins. The older traces, shown with dashed lines in Fig. 4.3, top plot, are smaller than those produced in younger stations for both components. In particular, the time trace produced by γ and $e^{\pm}$ shows a larger difference than the muonic trace. Thus the light loss due to a decrease in the internal reflectivity of the tanks affects more the electromagnetic component. This is due to the fact that the VEM Peak is used to calibrate the traces and the geometry of the electromagnetic signal, that is produced at the top of the tank.

Such a decrease in the recorded light can affect the risetime of the signals, named as $t_{1/2}$ and defined as the time needed for the cumulative sum of the signal of a station to go from 10% to 50%, as defined in Chapter 2. Risetimes of PMTs-averaged signal traces and their components are computed for all stations. They are indicated as $t_{1/2,max}$ for showers reconstructed with s_{max} and $t_{1/2,min}$ when reconstructed with s_{min}. These risetimes are averaged for each ring, and then this average is compared for each twin version event-by-event: The distributions of the differences between them are shown in Fig. 4.4, left plot, for the ring at 812 m with a gaussian fit for all the different components. The mean electromagnetic $\Delta t_{1/2}$ is around 14 ns with a spread of almost 6 ns, while the mean $\Delta t_{1/2}$ of the total and muonic components is larger, around 18 ns, but narrower, with a standard deviation of 4-5 ns. In this case, the total risetime follows the muon risetime due to the fact that the ring is in a position away from the core, where the electromagnetic contribution has decreased. Hence the

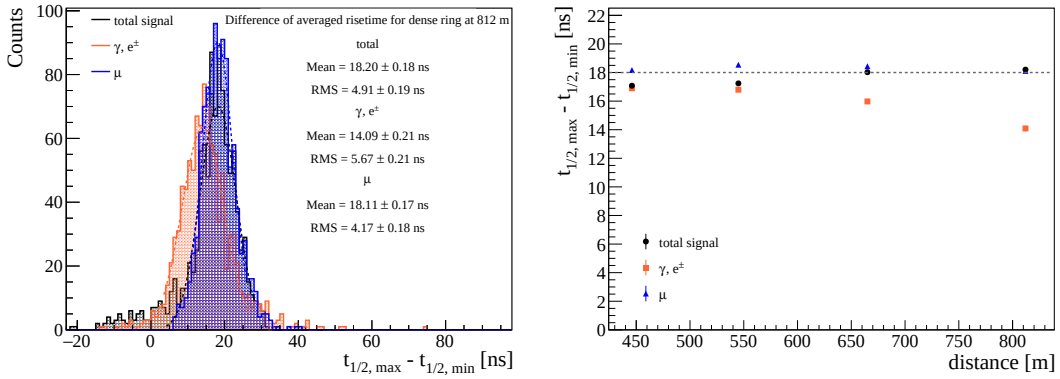

FIGURE 4.4: Difference between the averaged risetimes of twin showers. Left: $\Delta t_{1/2}$ distributions of the different components for the dense ring at 812 m. Right: mean of $\Delta t_{1/2}$ over distance to the shower axis.

total signal is dominated by the muonic signals. This is also visible in Fig. 4.4, right plot, where the mean $\Delta t_{1/2}$ as a function of the distance to the shower core is shown. Errors are defined as the error on the mean. It can be seen that $\Delta t_{1/2}$ of the total signal is closer to the electromagnetic one at short distances, while it approaches the muon one as the distance increase. The figure also shows that the mean $\Delta t_{1/2}$ for muons is constant at 18 ns over the distance, while the $\Delta t_{1/2}$ of γ and $e^{\pm}$ starts at 17 ns and drops at 14 ns at larger distances.

This difference of 18 ns in risetime between the twin showers is of the same order as what has been found in the risetime from data in Section 2.4.2, of ≈ 15 ns.

4.1.3 Station signals and energy estimation

The change in the shapes of time traces due to the less collected light affects the total signal recorded in each station. The individual PMT charge signals are obtained by integrating the traces in the time window identified as the part of interest, as explained in Chapter 1, and the resultant value is rescaled based on the calibration constants obtained from calibration. Finally, the total signal of a station is defined as the average of the signals from the working PMTs of the station.

To track the impact on the different components along the lateral profile of the shower, the average signal of individual components of each ring has been compared with its twin counterpart. The distribution of the relative difference between average signals for the ring at a distance of 445 m is displayed in Fig. 4.5, left. In this case, the mean difference of the total signal is $\sim -0.7\%$, in between the value obtained for the electromagnetic signal (-1.1%) and the muonic one ($\sim -0.2\%$). The mean values of ΔS as a function of the distance, right plot in Fig. 4.5, don't exceed the 1% difference. Moreover, it shows the same trend seen for the risetime in the previous paragraph: close to the shower, the contribution of the two components is similar, and the total signal is composed of a combination of the two; Moving away from the core, the electromagnetic component decreases, and the main contribution to the total signal comes from the muons.

The lateral distribution function for each shower is then obtained by fitting the total station signals as a function of the perpendicular distance to the shower axis. An example of twin showers' LDF can be seen in Fig. 4.6, left plot, where the logarithm of the signals as a function of the distance to the core is shown for an almost vertical proton: The dots represent the station signals, while the continuous line is

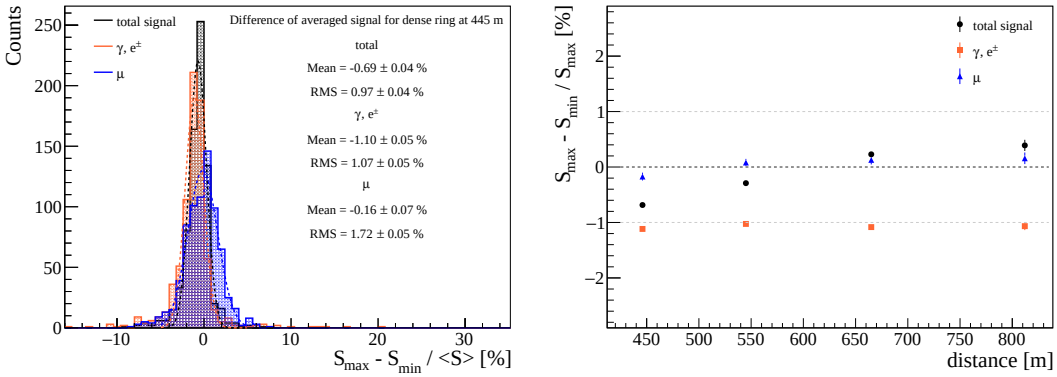

FIGURE 4.5: Relative difference of averaged signal for twin showers, for different components. Left: Distribution of the relative difference for the dense ring at 445 m. Right: Relative difference as a function of the distance to the shower core.

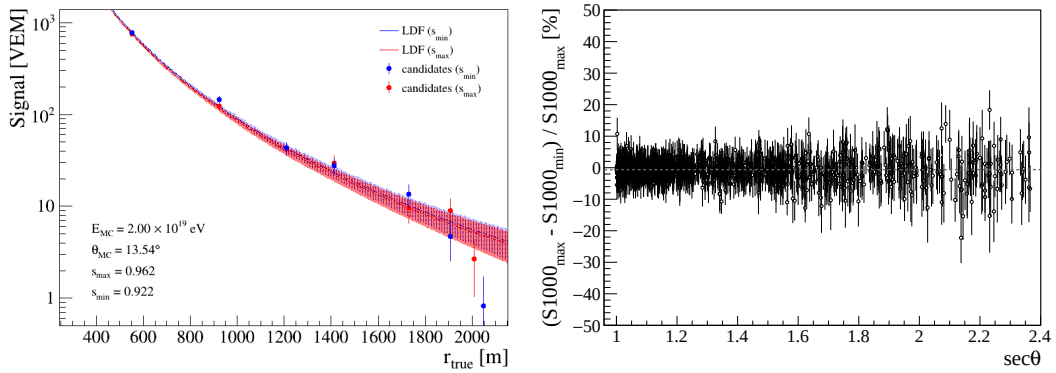

FIGURE 4.6: Left: Total signals vs distance to the shower axis and LDFs for an example of twin showers. Right: Relative difference of the shower size estimator as a function of the zenith angle.

the fitted LDF, with a shadow area displaying its uncertainties. The signals for the twin showers, in blue for the young event and red for the older event, slightly differ, and their reconstructed LDFs are in good agreement, overlapping almost perfectly.

The estimator of the shower size (S_{1000}) can be obtained from the LDF and compared between the twin showers. The evolution of the relative difference of S_{1000} as a function of the true zenith angle, Fig. 4.6, right plot, is less than 10% for the majority of the twin showers, with a slightly larger spread for the very inclined ones ($\theta > 60°$). The mean relative difference of the energy estimator between the simulations with different liner reflectivity is $-0.6 \pm 0.11\%$, with a spread of $\sim$ 3.4%, obtained from the distribution of the relative ΔS1000 in Fig. 4.7.

This result confirms the robustness of the Auger calibration using atmospheric muons, that can compensate even in the case of strong aging of the WCDs, with the energy estimator affected on average at the sub-percent level and an overcompensation for the electromagnetic component smaller than 1.5%.

This holds true if the calibration procedure on the field works properly and it is able to distinguish the muonic peak in the calibration histograms. For a few stations, this has proven to be difficult. Remediation of this problem has been found with a new calibration technique that requires a coincidence between the WCD and the SSD mounted on top [112, 113].

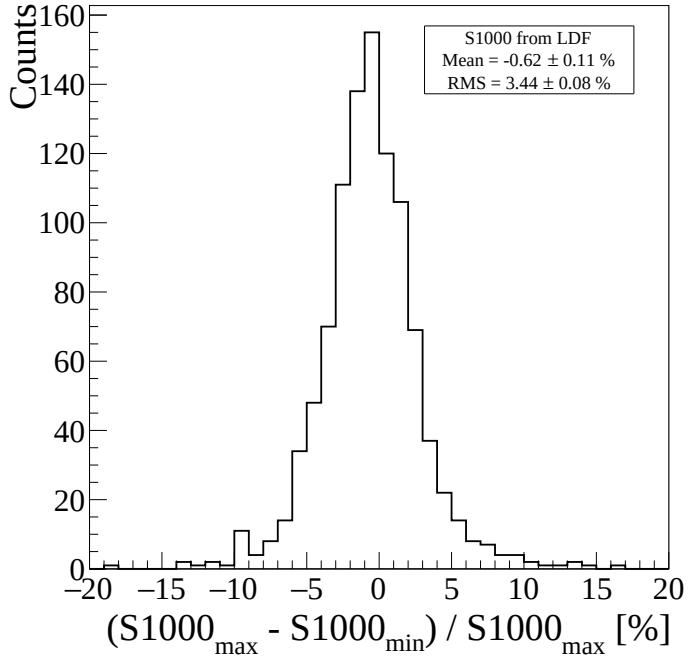

FIGURE 4.7: Distribution of the relative change on the shower size estimator due to the aging. The mean value of the distribution ($-0.62 \pm 0.11\%$) is the maximum difference expected due to aging.

4.2 Realistic time-dependent simulations: *SdEvolution*

As described in the previous chapter, the evolution of the signals recorded in the tanks over time shows the same behaviour, with each WCD aging in a similar way when we consider the time after its own deployment as a common reference (that we indicated as *age* of the tank). However, the time evolution of the array is more complex than the single station evolution, since the deployment lasted around 2 years, between 2004 and 2006. The time occured between the first and the last deployed station shifted the relative age between them, creating a multi-aged array at different snapshot in time. This age difference between the stations is not negligible, especially since in the first 4 years after the deployment the light collection in the tanks decreases faster than in the later years. Furthermore, the presence of two liner populations has been shown to be present in the array and to be related with the time of deployment, adding an extra layer of complexity.

Due to this, a time-dependent simulation of the full array was developed by creating and integrating a new StandardApplications in the Offline framework. The new application and the relative Module are called *SdEvolution*. The information on the status of each tank over time is taken into consideration by using the corresponding value of liner reflectivity obtained by the model of the aging built in the previous chapters thanks to the study of the time-decay of the light produced by vertical muons in the tanks.

In the next sections, the concept, design and use of the Application and the Module will be described, showing the full chain used to produce an event in a SD time-dependent simulation and focusing on the new changes implemented to achieve the desired result. In the section *Simulation library*, the details of the complete simulation library produced using this new feature will be presented and the effects of aging on simulations will be discussed.

4.2.1 SdEvolution Application

The new application follows the usual Auger structure: the first modules provide the simulation of the air-shower and the response of the array, while the second part handles the reconstruction as performed for data. The full bootstrap file and the *ModuleSequence* used can be found in Appendix I, together with other configuration files.

As a first step, a `CORSIKA` shower file is read and events are generated, accordingly with the user choices expressed in the bootstrap file of the *EventGeneratorOG* Module. After that, the new *SdEvolutionBLX* Module checks the presence and status of a file containing the information about the liner reflectivity of the stations. This file, called *sdEvolution.root*, contains the ID of the tank, the average liner reflectivity in several time intervals and the corresponding GPS times for all tanks analyzed. The file is shipped together with the Offline software and was produced in order to have a more accurate description of the time evolution of the SD, by analysing the time period between January 2005 and January 2020, with a more dense sampling compared to the analysis shown in the previous chapters: for each month, we required the same quality cuts used in the *shape analysis*, collecting at least 200 good events per month per station. From these events, the average liner reflectivity of the station for the corresponding month is obtained. An example for station Denisa Maria can be seen in Fig. 2.8. The GPS time of the first, *GPSStart*, and last analized event, *GPSEnd*, in each month is recorded and it is used by the Module to evaluate the reflectivity of the tank at every moment in time.

The Module allows in its bootstrap file (*SdEvolutionBXL.xml.in*) to indicate a different liner file, with an eye to future improvements or changes. After the first sanity checks, the Module retrieves the timestamp of the simulated event and the list of stations that are involved in the event. Using these information, the correct value of liner reflectivity for each station corresponding to the time of the event is obtained by linearly interpolating the braketing values contained in the *sdEvolution.root* file.

Since every simulated station is always initialized using the standard reflectivity of 0.94, the new Module takes care of changing this property in each station that is used for the reconstruction. Stations that show a value of liner reflectivity different than the default one are re-built using the proper value of liner reflectivity. Checks on the validity of the event date and on the presence of good reflectivity values in the file are also perfomed during the process.

By changing the response of the tank, a necessary step to correctly reproduce the behaviour of the stations consisted in updating, at the same time, the associated values of the calibration constants to convert the digital channels to units of VEM. As explained in the first chapters, these conversion factors, namely Area and Peak, are constantly evaluated on the field by the self-calibration of the stations, henceforth every change of the tank response it is reflected in these values. In simulations, instead, Area and Peak are tabulated and evaluated with vertical muons injected in ideal simulated tanks. When simulating the response of the array, tabulated values are retrieved by the *SdSimulationCalibrationFillerOG* module.

To select the proper values, accordingly with the status of the tank, the chosen approach consisted in parametrizing for each PMT the evolution of Area and Peak as a function of the liner reflectivity from the simulated charge and peak histograms for vertical muons, as described in Chapter 3. A 4^{th} degree polynomial function was

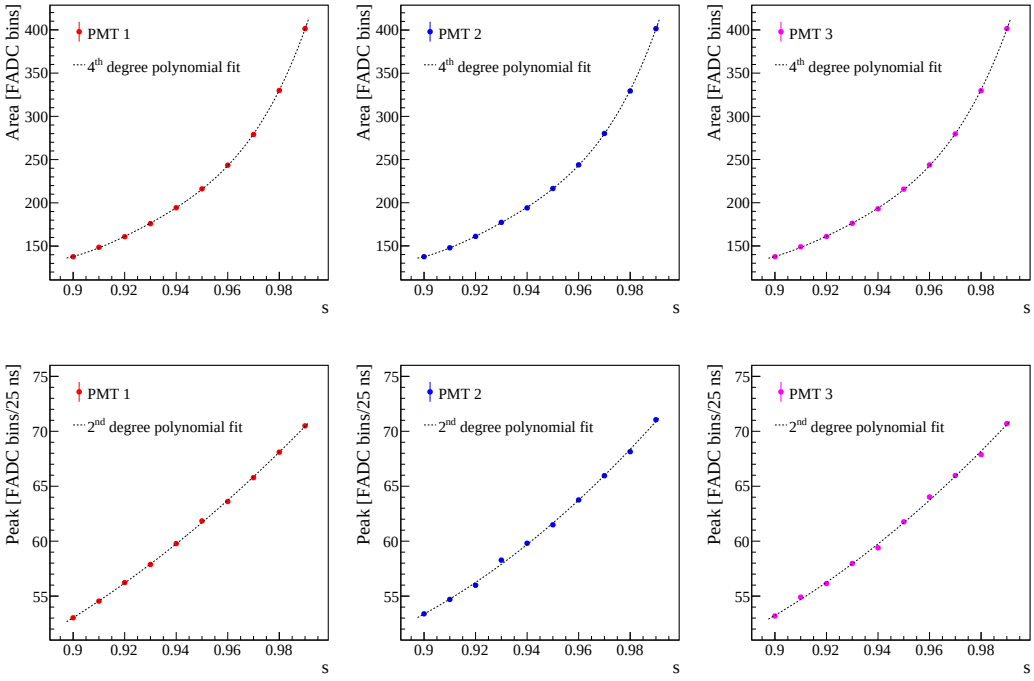

FIGURE 4.8: Area (top) and Peak (bottom) for vertical centered muons at different liner reflectivities. Polynomial functions are used to parametrize them (see text for more details).

chosen to describe the Area and a 2nd degree polynomial for the Peak, as follow:

$$\begin{aligned} A(s) =& a_0 + a_1 \cdot (s - 0.94) + a_2 \cdot (s - 0.94)^2 \\ &+ a_3 \cdot (s - 0.94)^3 + a_4 \cdot (s - 0.94)^4 \end{aligned} \tag{4.1}$$

$$P(s) = p_0 + p_1 \cdot (s - 0.94) + p_2 \cdot (s - 0.94)^2 \tag{4.2}$$

The coefficients a and p obtained from the fits for the three different PMTs can be found in Appendix I.7, while the results can be seen in Fig. 4.8.

Having obtained these values, we modified the structure of the module responsible to fill the calibration information for simulations: We added the option to obtain the values of Area and Peak from the two parametrization, Eqs. (4.1) and (4.2), with the possibility to also specify, in addition, the coefficients for each PMT. This last choice avoids any hard-coded value and open to further improvements or changes of the parametrization in the future.

The above mentioned modifications were the major ones introduced to implement the SD time evolution simulations. The next modules in the sequence follow the usual simulation chain by simulating the PMTs response, the FADC filters, the baseline and the triggers. The second part of the *ModuleSequence* takes care of the reconstruction of the event by applying the selection cuts and obtaining the shower information such as the shower plane, the curvature radius, the LDF and the energy. The reconstructed event information is then saved in the ADST format, the Auger standard for high level analysis, together with the simulated traces for the different components of the shower recorded by the stations involved in the event.

The surface array experiences other form of time instabilities during its operation, due to the status of the single stations: they could not be active in a specific

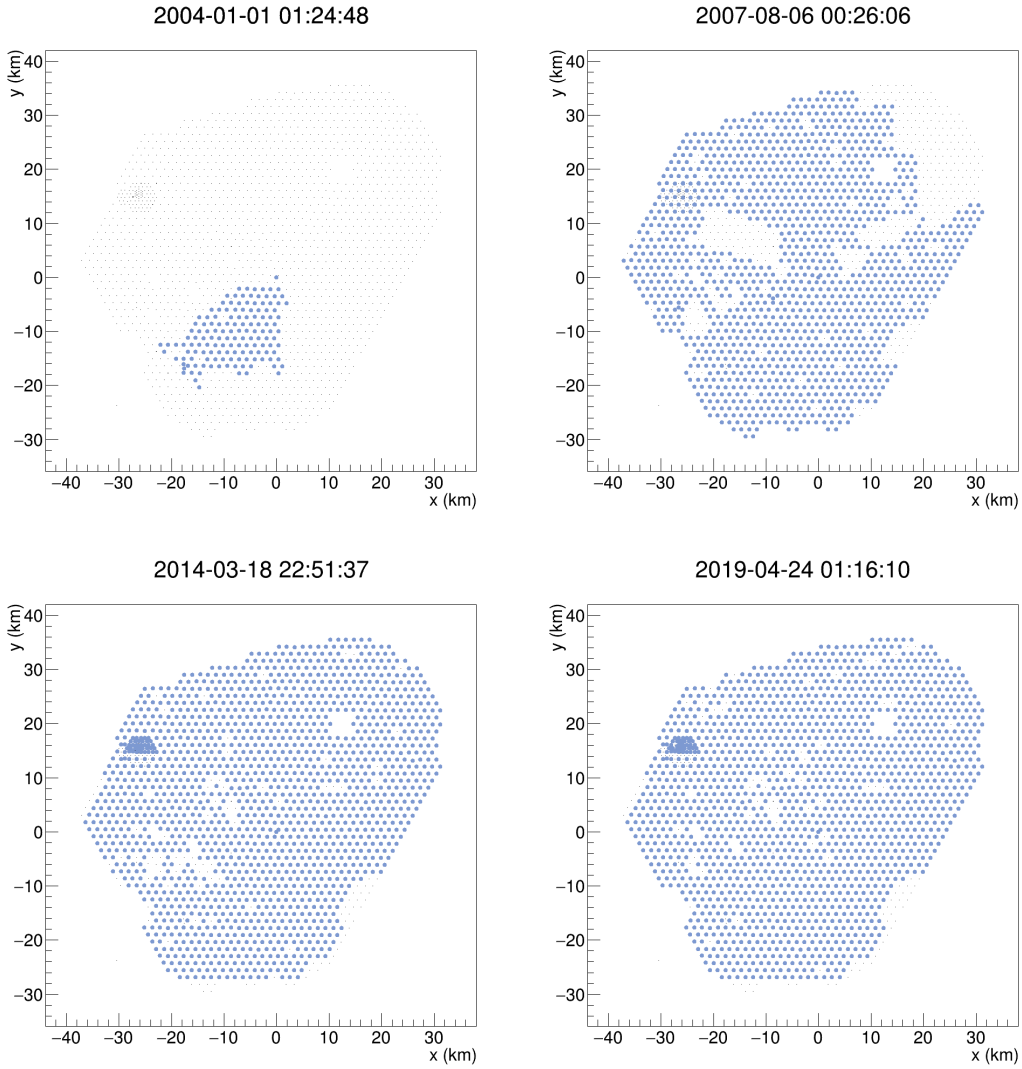

FIGURE 4.9: Array status at different times over the years. These maps are produced based on the T2Life information.

moment due to an energy power supply problem, they could be active but not sending signals because of a problem in the communication system or other unforeseen problems could be affecting the station. The criteria to establish if a tank is *alive* or not is defined based on the presence of T2 triggers sent by every station to the CDAS. The time information about the status of each tank is collected and saved in root files called T2Life that keep track of the activity of all the stations.

The current status of a station (in acquistion or not) during the event of a simulated air-shower is included in the detector simulations by using these files. A specific module and the relative Manager (*T2LifeROOTFileManager*) are used for this purpose and the latter is included in the higher-level manager, *SManagerRegisterConfig*, that collects and runs all the other detector description managers, such as the stations list, the model of the simulated station and the calibration manager. Thanks to the T2Life information, the roll-out of the deployment of the array is also included in simulations, as can be seen in the snapshot of the SD at different times in Fig. 4.9. To avoid others effects and isolate the time-dependent changes, the altitude of all the stations was fixed to 1400 m by creating a dedicated stations list.

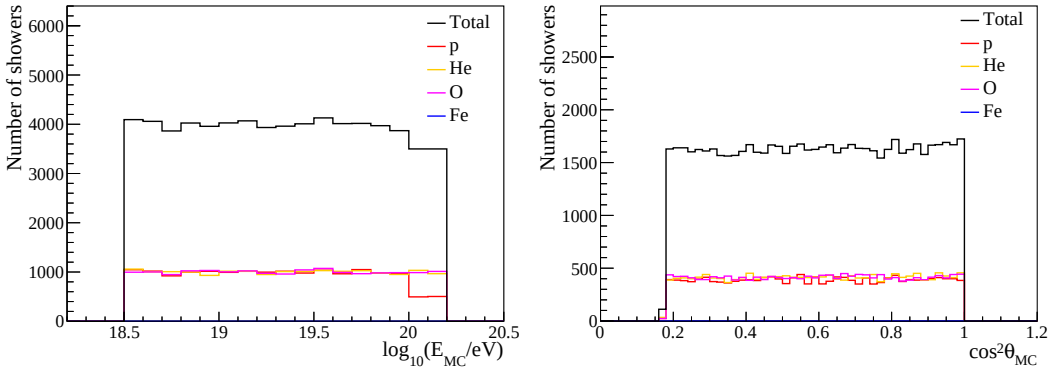

FIGURE 4.10: Distributions of the CORSIKA showers used as an input to produce the simulation library. Left: Energy distribution. Right: Zenith angle distribution.

CORSIKA showers						
$\log_{10}(E/\text{eV})$	**Primary**				**Realizations per shower**	
	Proton	Helium	Oxygen	Iron	**Standard**	**Aging SD**
18.5-19	5000	5000	5000	5000	5	10
19-19.5	5000	5000	5000	5000	5	10
19.5-20	5000	5000	5000	5000	4	8
20-20.2	998*	2000	2000	2000	3(*5)	6(*10)

TABLE 4.1: Number of CORSIKA showers for each energy bin and for each primary. The last two columns show the number of times each showers has been thrown in the array for the two modes. The '*' indicates that proton showers in the last energy bin had a different number of realizations (5 and 10, in the two modes, last two columns) compared to other primaries. See text for more details.

4.2.2 Simulation library

The application for the simulations of the aging array was then applied to produce a full library of reconstructed showers. In order to do that, a specific tag for Offline was created: *prod-20221010-test-sd-evolution*. As input files for the production, CORSIKA air-showers produced with CORSIKA 7.7420 and EPOS-LHC as hadronic model for four different primaries (p, He, O, Fe) were used. The energy range considered was $18.5 < \log_{10}(E/\text{eV}) < 20.2$, with a uniform angular distribution in $\cos^2\theta$ for $\theta < 65°$ and four different atmosphere. The total number of CORSIKA showers amounted to almost 67.000, coming from approximately 1000 showers every 0.1 steps in $\log_{10}(E/\text{eV})$, and were provided by the Monte Carlo Simulations task of the Collaboration [114]. Only the proton showers in $20 < \log_{10}(E/\text{eV}) < 20.2$ were slightly fewer (998, as shown in the last row of Table 4.1), due to a choice to reduce the production time. The energy and angular distributions of these showers can be seen in Fig. 4.10.

With this setup, each shower was then used as input for the application in two different modes: *standard* and *agingSD*. The first mode excluded the use of the Module *SdEvolutionBLX*, fixing in this way the liner reflectivity of all the stations to the standard value of 0.94 and it did not take into consideration the T2Life information

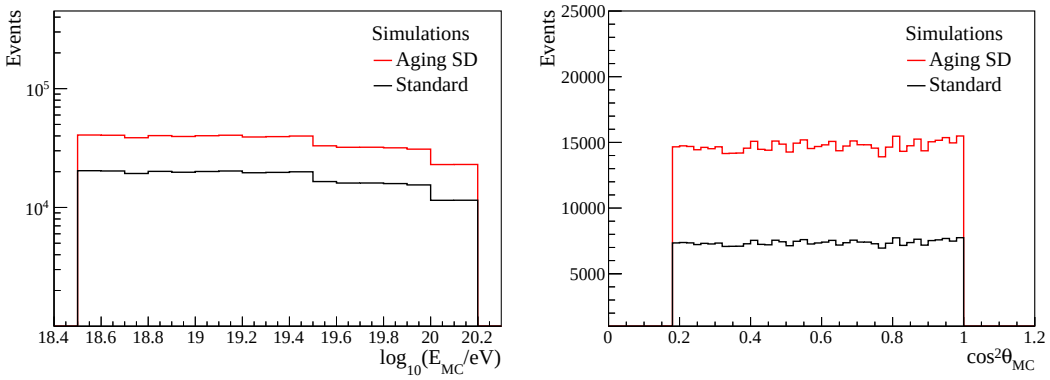

FIGURE 4.11: Distributions of the reconstructed showers. Only 6T5 events are selected. Left: Energy distribution. Right: Zenith angle distribution.

Reconstructed showers				
	Aging SD		**Standard SD**	
Quality cuts	Events	ϵ (%)	Events	ϵ (%)
Thrown showers	605 980	100.00	302 990	100.00
Successful jobs	604 932	99.83	302 507	99.84
6T5 trigger	601 275	99.22	301 045	99.36
$\log_{10}(E_{SD}/eV) \geq 18.5$	576 865	95.20	288 770	95.31
$\theta_{SD} < 60°$	527 669	87.08	264 106	87.17

TABLE 4.2: Number of reconstructed showers after each selection cut, together with the cut efficiency.

of the tanks, removing the temporal evolution of the array. For each run/shower, 5 events were generated at different random times between the 1st of January 2005 and the 1st of January 2020, to match the time frame contained in the liner reflectivity file and placing the core in random locations accross the array.

The *agingSD* mode, instead, included the liner information of all the stations and generated 10 events in a time period between 2005 and 2020, choosing random times uniformly distributed. The core of the shower was chosen randomly accross the array also in this case. The choice of doubling the number of events for this mode is motivated by the need of a bigger sample for events that included the liner variability to reduce statistical fluctuations and be able to observe small effects.
To reduce the computation time for more energetic events with $\log_{10}(E/eV) > 19.5$, the number of generated events from a single shower for the *standard* and *agingSD* modes was reduced to 4-8 and to 3-6 in the energy ranges $19.5 < \log_{10}(E/eV) < 20$ and $20 < \log_{10}(E/eV) < 20.2$, respectively. Table 4.1 summarizes these choices and the number of simulations used. All the runs used the *FastMode* option in the *G4StationSimulatorOG* module to further reduce the run-time of simulations; *FastMode* is, at the time of writing, the standard simulation procedure in Auger.

The two modes share the same detector seed used to initialize the detector simulations for each `CORSIKA` shower; In this way, another source of uncertainty was

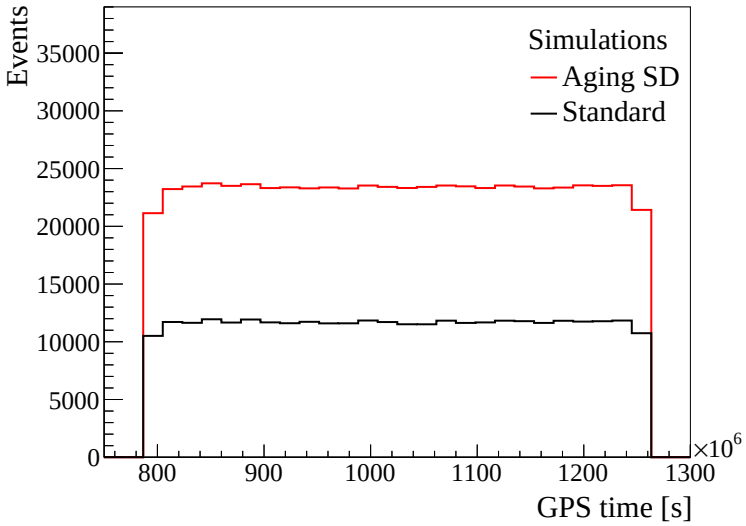

FIGURE 4.12: Time distribution of the reconstructed events. In red the *agingSD* mode and in black the *standard* one.

removed to compare more directly the two sets of simulation on a single shower basis, while from shower to shower the seeds has been changed, to reproduce a more realistic scenario. The physics seed, governing the choice of the secondary particles entering the tank, has been kept the same for all showers, instead. The massive production of this library was performed in the computing farm of the Praha group, that also took care of monitoring the jobs and verify their correct execution.

The final number of simulated events is above 600 000 for the *agingSD* mode and more than 300 000 for the *standard* mode. The Table 4.2 shows the number of generated events, the impact of failed jobs occured during the production of the library, and the effect of quality cuts. The energy and angular distribution of the reconstructed showers can be seen Fig. 4.11 for the two different modes, while Fig. 4.12 displays the events over time of the events: The distribution is flat over the years, confirming that the time range between 2005 and 2020 is sampled uniformly. In the case of the aging array, only 3657 events did not have a 6T5 trigger, accounting for the 0.6% of the total number of events, while events without a 6T5 trigger in *standard* mode are 1462, accounting for the 0.48%. The spatial distribution of the reconstructed core over the array is shown in Fig. 4.13: it can be noticed that the *standard* mode, Fig. 4.13(a), has reconstructed events distributed uniformly over the array while the *agingSD* set, Fig. 4.13(b), instead, shows a clear difference between the southern part and the northern part, with less events in the latter. This is due to the deployment of the array that is encoded in the T2Life file used to reproduce the evolution of the presence of the tanks in array over the years. The events that are not 6T5 can be placed on the core location maps discussed above, displayed in Fig. 4.13 as blue crosses, and show that these events occured mostly in the borders of the array or edges of empty areas, where no tanks are deployed, leading to missing triggered tanks needed to properly reconstruct the shower properties. It can be noticed that in the case of the aging detector that also contains T2Life information, these events appear more often, especially in the middle of the array, due to fact that the array had different borders while the deployment was in progress. This also explains the small difference in the ratio of not-6T5 events in the two different simulations sets.

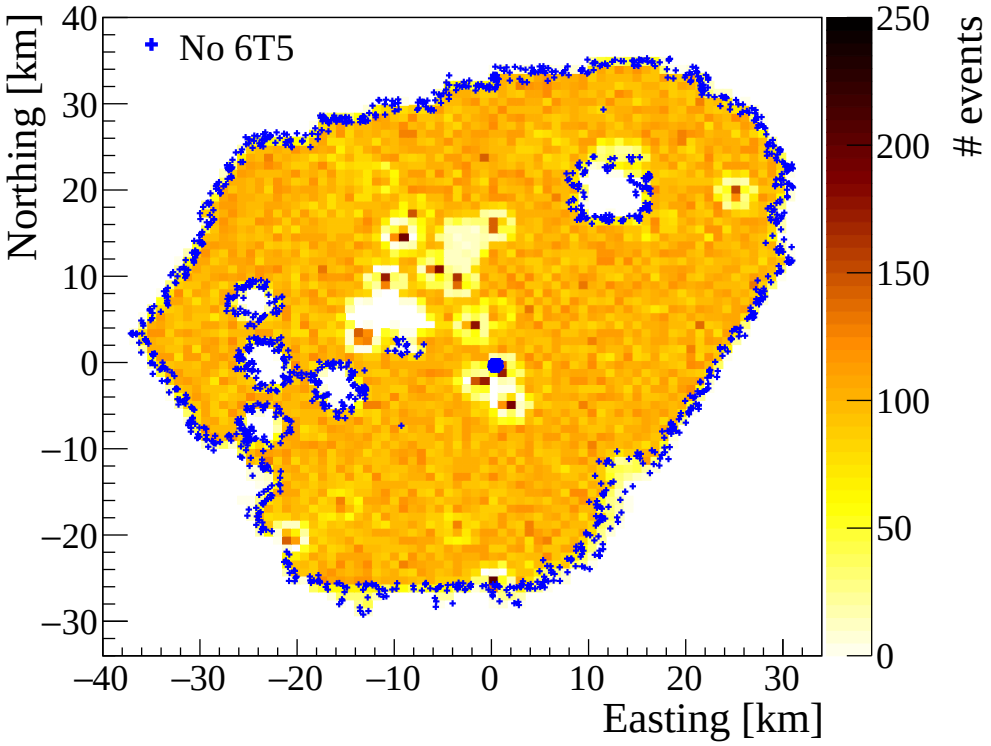

(a) Standard

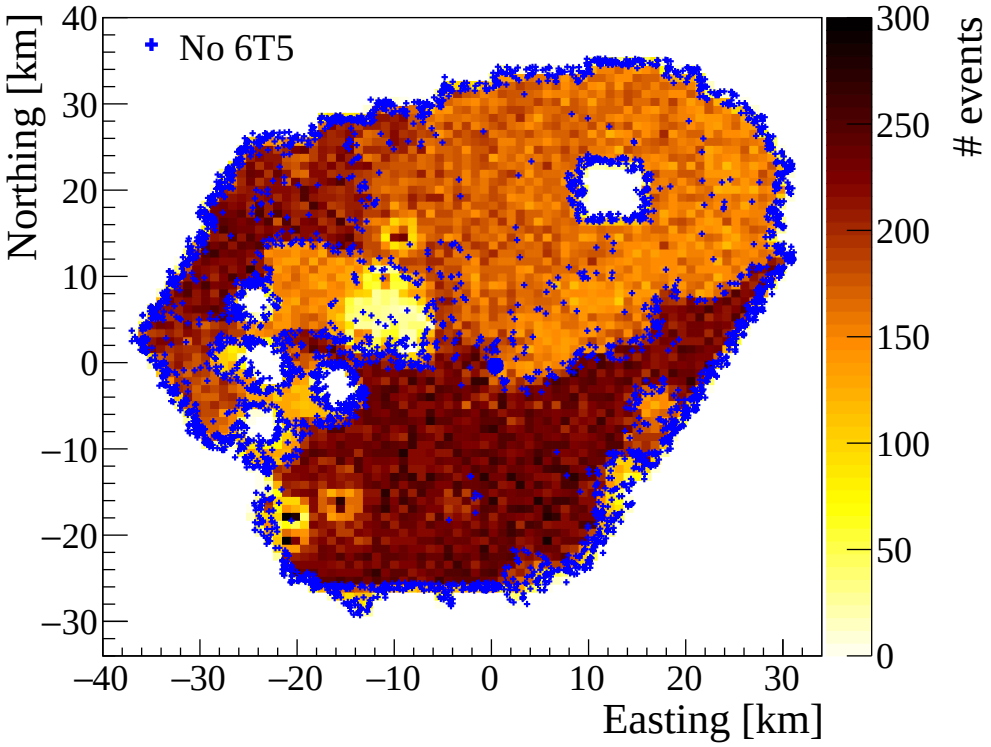

(b) Aging SD

FIGURE 4.13: Distribution over the array of reconstructed showers for the two different modes. Blue crosses show the location of events that are not 6T5. More details in the text.

SD data		
Quality cuts	Events	ϵ (%)
Total events	7 233 314	100.0
No lightning	7 232 796	99.99
LDF fit	7 232 796	99.99
$\theta_{SD} < 60°$	6 923 503	95.72
SD-triggered	6 921 886	95.69
6T5	5 642 072	78.00
$\log_{10}(E_{SD}/eV) \geq 18.5$	160 483	2.22
Bad periods	156 554	2.16

TABLE 4.3: Number of reconstructed showers after each selection cut, together with the efficiency of the cut.

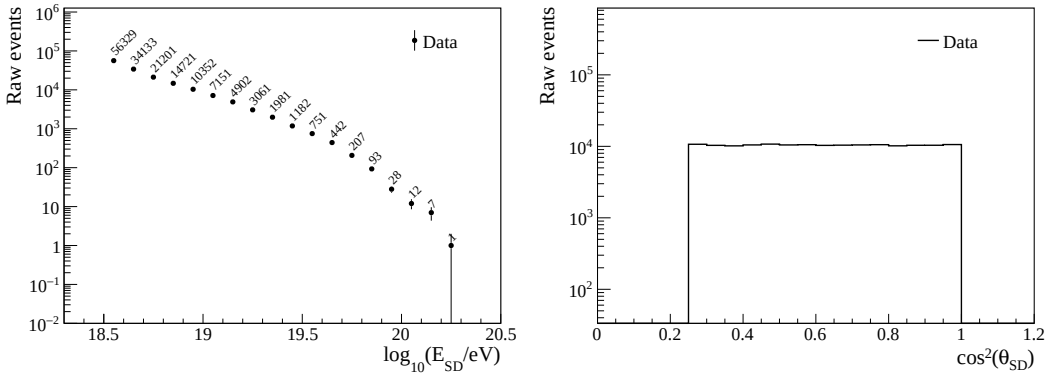

FIGURE 4.14: Distribution of selected data. Left: Energy distribution. Right: Zenith angle distribution.

4.3 Comparison with data

To assess the validity of the aging model and the *SdEvolution* simulations production, the change seen in data of several observables that are related to the light collection in the tank, as shown in Chapter 2, should be present and reproduced in simulations that contains the time evolution of the SD.

4.3.1 Data selection

In order to compare data and simulations, a selection of the recorded data by the surface detector is needed. The data set used is the ICRC2019, produced with Offline v3r99p2, that contains events from 2004 up to 2020 for a total number of events larger than 7 millions. From this dataset, events that survived the quality cuts shown in Table 4.3 were used. These cuts ensured the quality of the reconstruction to reject events due to lightning, or recorded in data taking periods where the performance of the array was not optimal. The largest effect on the number of events is the cut on the minimum reconstructed energy required for the events, that drives the total number of events down to $\approx$ 160 000, excluding events with an energy smaller than the energy for which the SD-1500 is fully efficient. This effect is expected due to the steep spectrum of cosmic rays. The other cut with a significant rejection (around

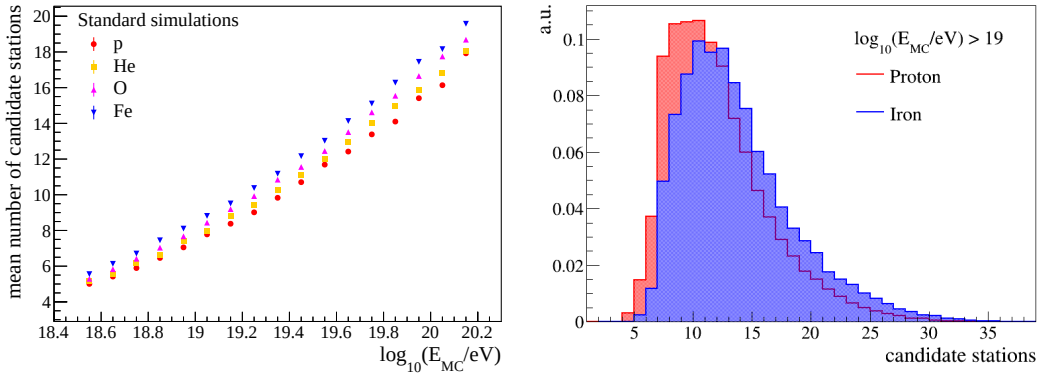

FIGURE 4.15: Mean number of candidates stations in simulations for different primaries. Left: Evolution in the number of triggered stations as a function of the energy of the primary particle for different nuclei. Right: Distribution of candidates for $\log_{10}(E/\text{eV}) > 19$ for proton (red) and iron (blue) primaries.

18%) is the 6T5 cut, the requirement that all the six stations around the detector with the highest signal are operational, in order to select only events that are fully contained in the array.

The energy distribution of the selected events is shown in Fig. 4.14, left, while on the right the angular distribution of the events is displayed. The latter shows a flat distribution as a function of the $\cos^2$ of the reconstructed zenith angle, similar to the angular distribution of simulations, seen in Fig. 4.11. The energy spectrum shows a step-wise power-law with different indexes, related with different physics explanations as described in Chapter 1, with few events at the highest energies.

4.3.2 Simulations reshaping

The energy distribution of simulations does not resemble the one observed in data, being uniform in the logarithm of energy. In order to compare the observables between data and simulations, such as the number of stations, the distribution of events needs to be re-weighted to follow the same distribution measured on data. This modification is of great importance; For example, events with a greater energy have a larger footprint at the ground, triggering more stations, as shown in Fig. 4.15, left figure, where the mean number of candidate stations as a function of the primary particle's energy is shown for different nuclei from simulations. It can be seen in this plot that candidates are between 5 and 6 for cosmic rays with energy of 3×10^{18} eV and they grow up to 17 and 22 for proton and iron, respectively, for energies above 150 EeV.

The energy distribution of SD events, shown in Fig. 4.14, is used to weight simulations, with each weight (in energy bins of size 0.1 decades) obtained as $w(E_i) = N_i/N_{\text{tot}}$, with N_i the number of events in the i-th energy bin and N_{tot} the total number of events. In order to maintain the total number of simulations after the weighting procedure, weights are renormalized as:

$$\hat{w}_i = w(E_i) \frac{N_{\text{sims}}}{\sum_{n=1}^{N_{\text{sims}}} w(E_n)} \tag{4.3}$$

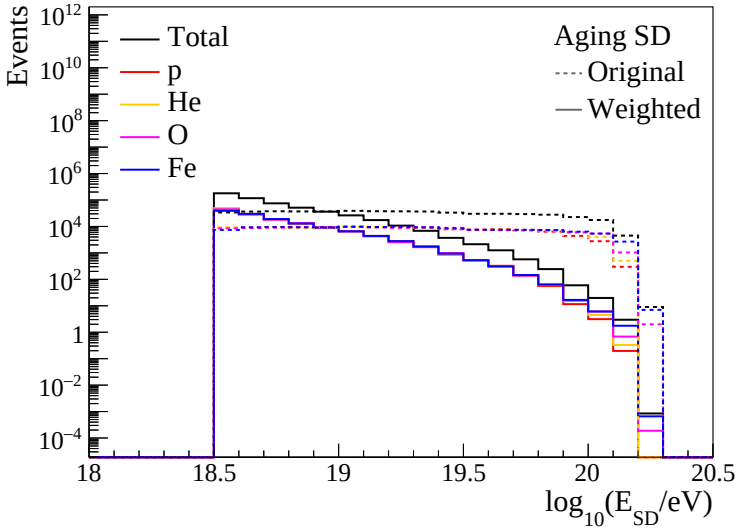

FIGURE 4.16: Energy distribution of simulations. Dashed lines represent the original spectrum. Different primaries are shown with different colors.

such as the total number of simulated events is preserved:

$$\sum_{n=1}^{N_{\text{sims}}} \hat{w}_i = N_{\text{sims}} \tag{4.4}$$

The resulting reshaped simulations energy distribution can be seen in Fig. 4.16 for the *agingSD* set of showers: Events with a larger energy are less occuring and the shape with different slopes, observed in data, is reproduced, while maintaining the total number of simulated events. The relative fractions of the different primaries in the total energy distribution has not been affected by the energy distribution rescaling.

The species of nuclei are not equally present in data as they are in simulations. This effect can alter the analysis of high-level observables when combining simulations for different primaries. Discrepancies can arise from the different contributions of the primary particles, as can be seen for example in the two distributions of candidates stations in Fig. 4.15, right plot. For $E > 10^{19}$ eV, protons (red) display a distribution of the number of candidates with a smaller mode, while iron nuclei have a distribution shifted towards larger numbers of candidate stations. The iron-initiated showers have a larger footprint and involve more stations than a proton-initiated shower. This can be understood considering that heavier nuclei develop higher in the atmosphere. The impact of different primaries on observables such as the number of triggered stations can be seen in Fig. 4.15, right plot. Due to this reasons, another rescaling is needed to properly reproduce the data, considering that the different species of primaries are present in different proportions at different energies.

The primaries fractions as a function of the primary particle energy have been estimated in Auger by fitting the X_{max} distributions, that are obtained through the air-shower measurement using the Fluorescence Telescopes [115], as explained in Chapter 1. The composition fractions are extrapolated by comparing the distributions with simulations. The energy range of FD starts from $\approx 10^{17.2}$ eV thanks to the HEAT telescope that observe the sky with an inclined field of view, towards the upper sky. In the case of the regular SD, the energy range of interest starts above $\approx 10^{18.5}$ eV,

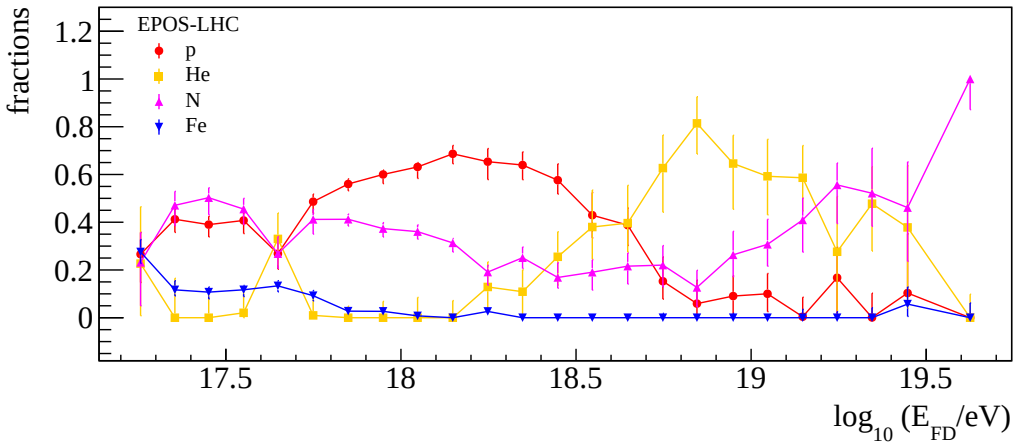

FIGURE 4.17: Composition fractions obtained when comparing simulations produced using EPOS-LHC with FD data [115].

where the regular array is fully efficient. The maximum energy measured by the FD, instead, goes up to $\approx 10^{19.6}$ eV due the design of the FD, while the SD can measure above 10^{20} eV. For this reason, when using the primaries fractions for the SD to re-scale simulations, we assumed that the ratios measured above $\approx 10^{19.5}$ eV are constant and equal to the value present in the last FD energy bin.

The evolution of the fractions is shown in Fig. 4.17: The fitted fractions for different kind of elements (light, medium and heavy) show that protons are the most abundant source of primaries ($\approx 60 - 70\%$) around 10^{18} eV and they fall below 10% above $10^{18.7}$ eV. Helium, instead, starts to increase at $10^{18.3}$ eV reaching its maximum value of 80% at $10^{18.5}$ eV and starts to decrease from that energy on and disappearing for energies higher than$10^{19.5}$ eV. Medium-weight elements, indicated here as Nitrogen-like, range between 50% and 10% and they become the dominant specie above $\approx 10^{19.2}$ eV, while iron is negligible above $\approx 10^{18}$ eV.

Using the composition information obtained from the X_{max} profile fitting, we assigned a weight equals to the relative fitted fraction to every reconstructed shower based on the specie and energy of the simulated primary. The choice to use the E_{MC} was dictated by the fact that the simulations library contains only the SD reconstruction, thus there is no information about the FD reconstruction. The two energies (FD and MC), however, are very close, with a small bias of less than $\approx$ 3% and a resolution better than 8% [66], allowing for the use of the Monte Carlo energy for the evaluation of the primary fraction of each shower. Since the composition fractions were obtained using Nitrogen simulations and the *SdEvolution* library contains Oxygen simulations, we assumed that the ratios are the same for the two elements.

The final energy distribution of the simulated events for the *agingSD* mode is shown in Fig. 4.18, left: The black full line represents the obtained distribution while the dotted line the original distribution. In the same figure the contributions of the fitted primaries are plotted with different colors: For the lower energy part of the distribution, the spectrum is given as a combination of light elements; at higher energies it becomes evident that the main contribution comes from Oxygen.

Having this final weighted distribution, it is possible to obtain again the fractions that were used as an input. The result, displayed in the right plot of Fig. 4.18, is slightly different from the FD values, since in this case the energy displayed is the SD one, thus different energy biases for each primary are involved, causing a shift

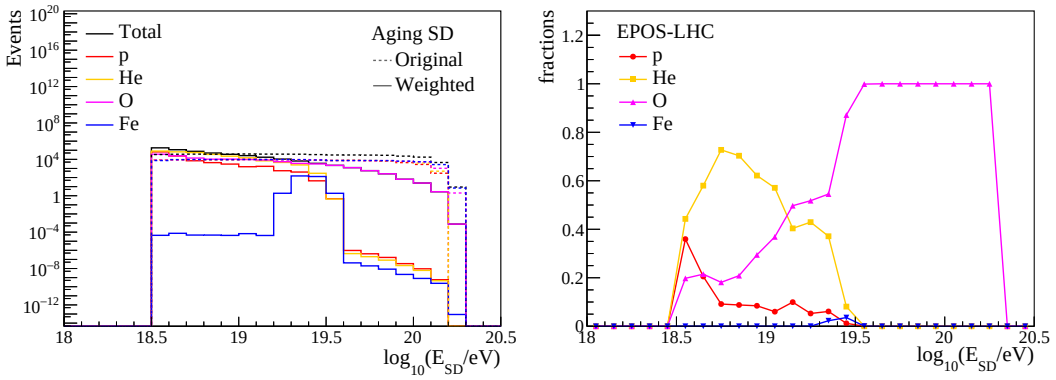

FIGURE 4.18: Left: Energy distribution of simulations after weighting the number of events and the species of primaries. Right: Primaries' fractions as a function of the SD reconstructed energy obtained from the comparison between the rescaled distributions of each primary to the total non-weighted reconstructed energy distribution.

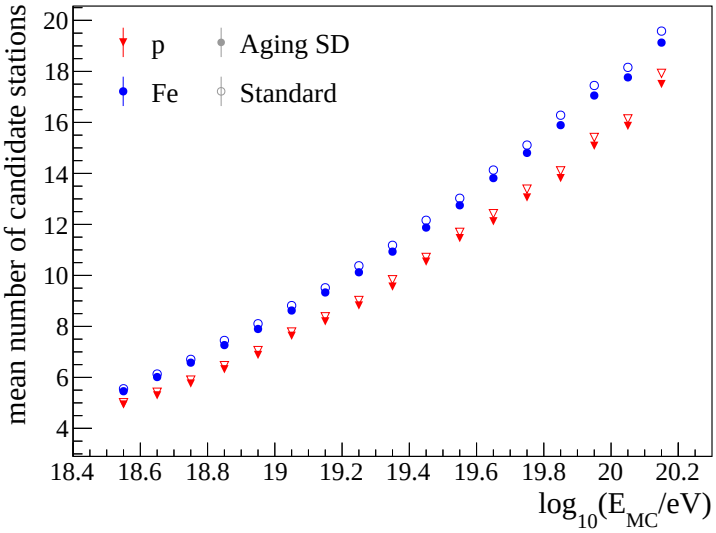

FIGURE 4.19: Mean number of candidate stations as a function of the primary energy for *standard* (open symbols) and *agingSD* (filled dots) mode. Protons are shown in red, iron nuclei in blue.

and a mix of different events in the same energy bin. Retrieving the distributions as a function of the Monte Carlo energy, instead, brings to a result compatible with the initial values of the primary fractions, confirming the correctness of the procedure.

4.3.3 Number of stations

One effect of the time evolution experienced by the SD, that has been shown in Chapter 2, is the decreasing number of triggered stations over time. The decrease of A/P, due to a loss of recorded light in the tank, can affect the station signal, reducing it to the point that it falls below the trigger threshold (especially for small signals) and the station would not be triggered during an event. Consequently, the trigger rate is affected and the mean number of candidate stations decreases over time.

The inclusion of the aging in simulations results in a decrease of the mean candidate stations along the entire energy range and for all the primaries, as displayed

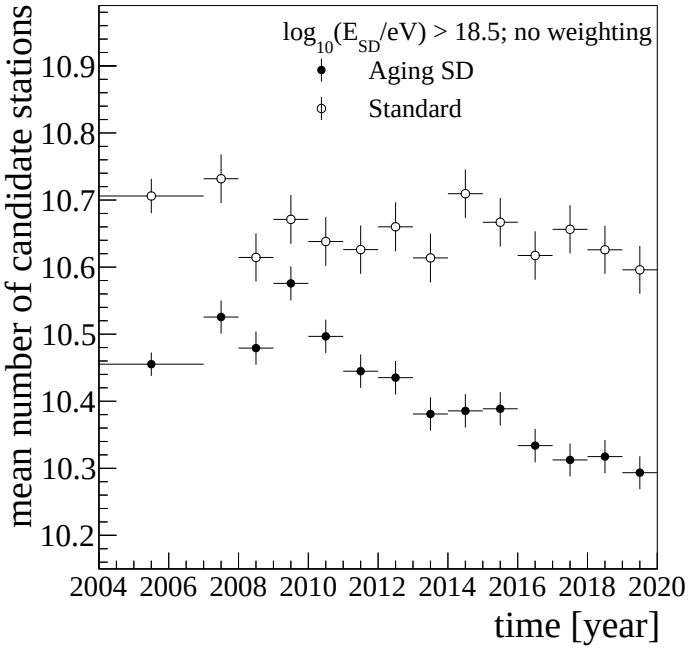

FIGURE 4.20: Evolution over time of the mean number of candidate stations of simulated air-showers with energy larger than 3×10^{18} eV.

in Fig. 4.19 for proton and iron for the two different modes. In order to verify that the new *SdEvolution* library is also able to reproduce the temporal trend observed in data, the average number of triggered stations as a function of time has been computed from the simulated events. It can be seen that the trend over time of the number of stations for the two modes for showers with $\log_{10}(E_{\rm SD}/{\rm eV}) > 18.5$, Fig. 4.20, is different, with the standard simulations showing a constant behaviour over time, with ≈ 10.6 candidates every year, while the aging simulations show a decrease over time of ≈ 0.3 candidate stations, starting at ≈ 10.6 in 2009 and reaching ≈ 10.3 in 2019. The latter can also reproduce the effect of the deployment on the mean number of stations, as can be seen in the first years, with a smaller value due to the fraction of the number of air-shower falling at the borders of the array, and thus not fully contained.

To adhere more to real conditions, each event has been weighted using the energy and primary fractions distributions, shown in Fig. 4.18. In Fig. 4.21, the mean number of stations over the years for aging simulations is shown for an energy threshold larger than 3×10^{18} eV: A decrease over time is present and, in particular, the absolute values are smaller, between ≈ 6.55 and ≈ 6.35, since events with a larger energy (and, thus, a larger footprint) are less occuring.

Simulations are then compared with data, looking at the time evolution of the number of triggered stations at different energy thresholds. It can be seen, in Fig. 4.22 for two energy thresholds ($\log_{10}(E_{\rm SD}/{\rm eV}) > 18.5$, left, and $\log_{10}(E_{\rm SD}/{\rm eV}) > 19$), right, that the decreasing trend observed in data is reproduced in simulations, especially until 2017. After that year, simulations show a plateau while data keep decreasing; this behaviour has still to be fully understood and it could be a sign of other aging effects not included in simulations. For both energy thresholds, the decrease of candidate stations in simulations between 2008 and 2017 amounts to ≈ 0.2.

However, simulations show smaller values of mean candidate stations compared to the events measured by the SD. A possible explanation could be related with the

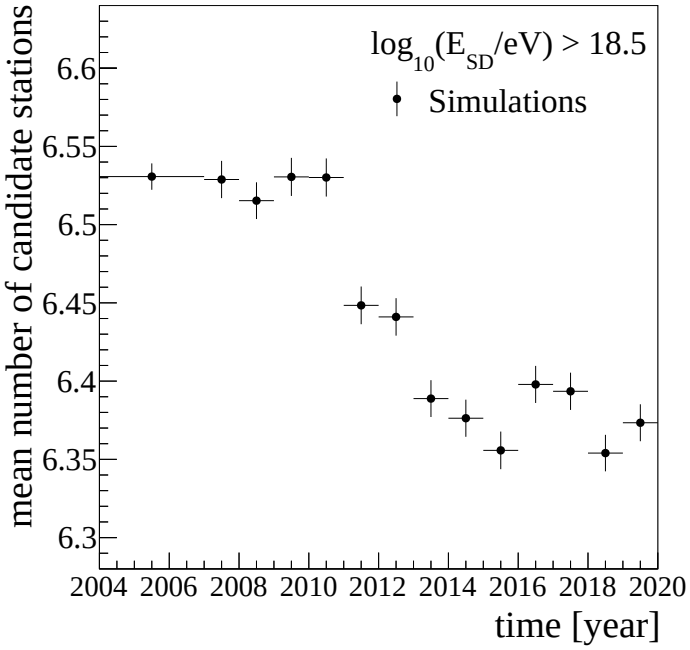

FIGURE 4.21: Weighted mean number of candidate stations over the years for *agingSD*.

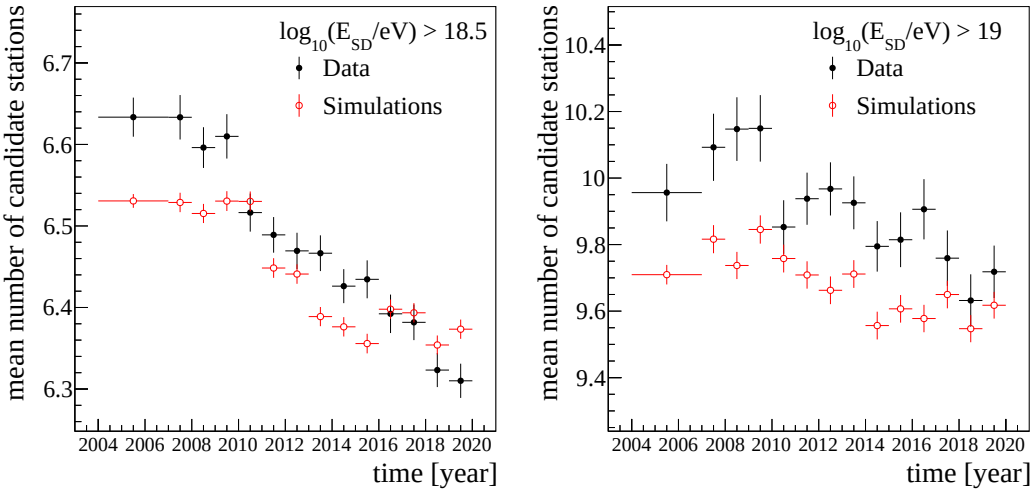

FIGURE 4.22: Mean number of candidate stations over the years for weighted *agingSD* simulations (open red symbols) and data (black dots). Two different energy thresholds are shown.

different trigger threshold implemented in simulations, based on a fixed value, as shown in Chapter 2, while in data it is adjusted through the on-line calibration. In this work, we did not change the value used for the trigger threshold definition in simulations, even if the aging showed to play a role in the conversion factor f_I between I_{VEM}^{peak} and I_{VEM}. Another explanation could be related to the fact that simulations predict less muons, thus the LDF extends further, triggering more stations. A further improvement of this work could take into account this change and verify if the discrepancy in the multiplicity is related to the software implementation of the trigger in simulations or the difference lies in the modeling of the air showers.

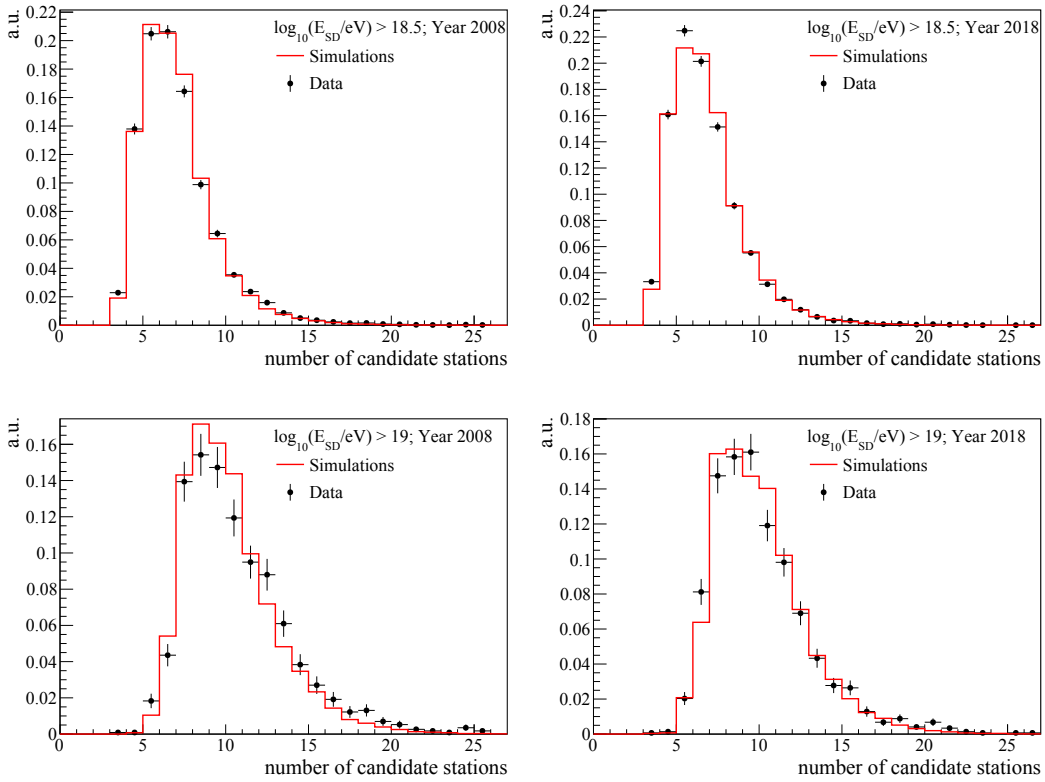

FIGURE 4.23: Distributions of candidate stations for data (black points) and simulations (red line) in 2008 (left) and in 2018 (right). Top: Events with $E_{SD} > 10^{18.5}$ eV. Bottom: Events with $E_{SD} > 10^{19}$ eV.

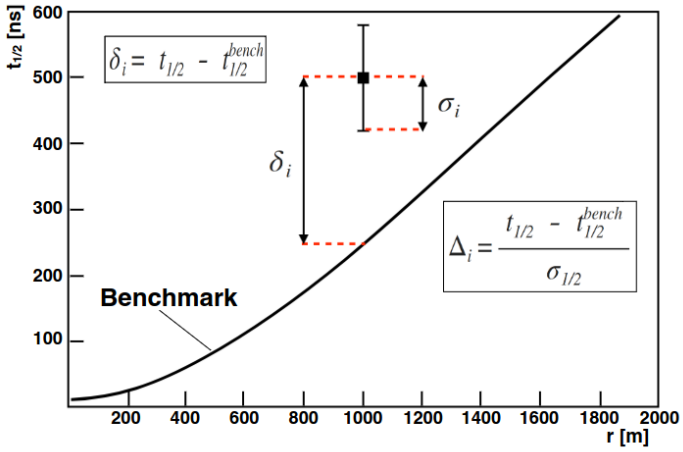

FIGURE 4.24: Schematic diagram to illustrate the Δ method. Taken from [51]

4.3.4 The risetime and Δ method

The measured risetime of the trace is related to the muon content of the recorded signal in the detector [51]. The total muon content of the stations involved in an event, in turn, contains information about the primary particle that generated the shower and, thus, it can be used to infer its mass. This property of the risetime (being sensitive to the mass composition of air-showers) has been used to infer the primary mass event-by-event with the "Δ method" [51, 101, 116]. This method combines the risetime information of all the stations triggered during an event into a single parameter called Δ and defined as follow:

$$\langle \Delta_S \rangle = \frac{1}{N} \sum_{i=1}^{N} \Delta_i = \frac{1}{N} \sum_{i=1}^{N} \frac{t_{1/2} - t_{1/2}^{bench}}{\sigma_{1/2}} \quad , \tag{4.5}$$

where $\langle \Delta_S \rangle$ is the average of Δ_i, that are defined as the deviation of the individual risetimes ($t_{1/2}$) of an event from a specific benchmark, weighted by their uncertainty $\sigma_{1/2}$, and N is the number of surface detectors triggered in the event. In Fig. 4.24, a schema illustrates in a clear way the definition of $\langle \Delta_S \rangle$. By definition, $\langle \Delta_S \rangle$ is a unitless observable. More details about the method, the benchmark definition and previous results can be found in [51, 101, 116].

As shown in Chapter 2, the risetime is affected by the decrease of recorded light in the tanks and this effect is propagated into the analysis that are built and designed based on this observable, such as the Δ method. Indeed, the time evolution of $\langle \Delta_S \rangle$ for the events recorded by the SD and selected using the quality cuts described in the previous paragraphs, shows a decrease over the years that resembles the same trend observed for the risetime, as can be seen in Fig. 4.25, in which the error bars represent the error on the mean of the value for each year. $\langle \Delta_S \rangle$ starts with a value of -0.18 in 2008 (end of deployment) and falls to -0.34 in 2020. The risetimes of each station have been selected and corrected using the same approach shown in Chapter 2.

This decrease over time has been also observed when data are split in different energy ranges. Since $\langle \Delta_S \rangle$ has an energy dependence (derived from the risetimes), to have a direct comparison between the chosen energy ranges, a normalization to the mean in each sub-sample is necessary, defined as $\langle \Delta_{norm} \rangle = \langle \Delta_S \rangle - \langle \Delta_{mean} \rangle$. The result is shown in Fig. 4.26, where it can be seen that the effect over time on $\langle \Delta_S \rangle$ is present for all the samples, with a relative decrease of $\approx 18\%$, showing that that the

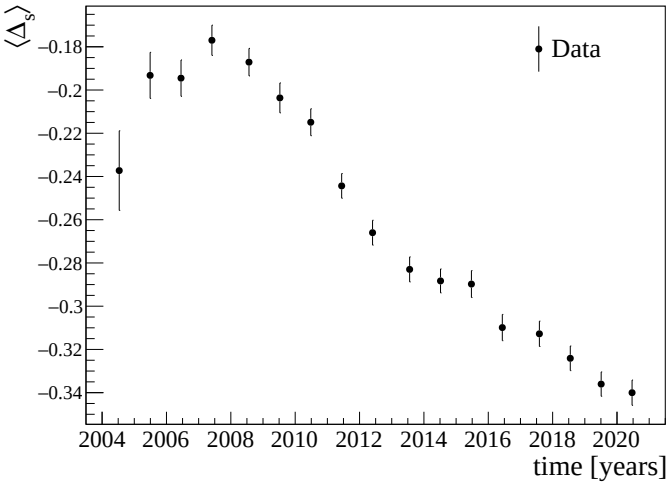

FIGURE 4.25: Evolution of $\langle\Delta_S\rangle$ as a function of time.

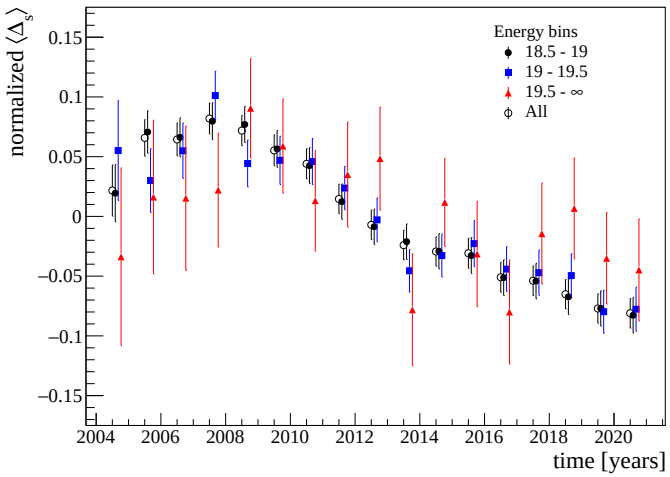

FIGURE 4.26: Evolution of $\langle\Delta_S\rangle$ as a function of time for different energy bins.

evolution over time is not energy dependent. Only for events with $\log_{10}(E_{SD}/eV) > 19.5$ the behaviour is less clear because of larger uncertainties due to less statistics; But the decrease is still visible and compatible with the average trend.

Simulated events are selected with the same criteria and the same method is performed usign the *SdEvolution* library. The evolution over time of $\langle\Delta_S\rangle$ for the two modes is shown in Fig. 4.27, left plot, where, in red, $\langle\Delta_S\rangle$ decreases over time of ≈ 0.1 when the aging of the array is taken into account, while, in open symbols, the standard simulations display a flat behaviour over time. In this case, simulated events are not reweighted following the energy distribution and all the primaries are represented equally.

In order to compare data and simulations, the latter needs to be rescaled following the energy distribution and the mass composition observed in data. In addition, due to the muon deficit in simulations with respect to data [55], a normalization to the mean is performed to obtain a direct comparison between the two. The result, illustrated in Fig. 4.27, right plot, shows that simulations that include the surface detector's evolution can reproduce the $\langle\Delta_S\rangle$ evolution over time observed in data. This decrease of $\langle\Delta_S\rangle$ over time is ≈ 0.1.

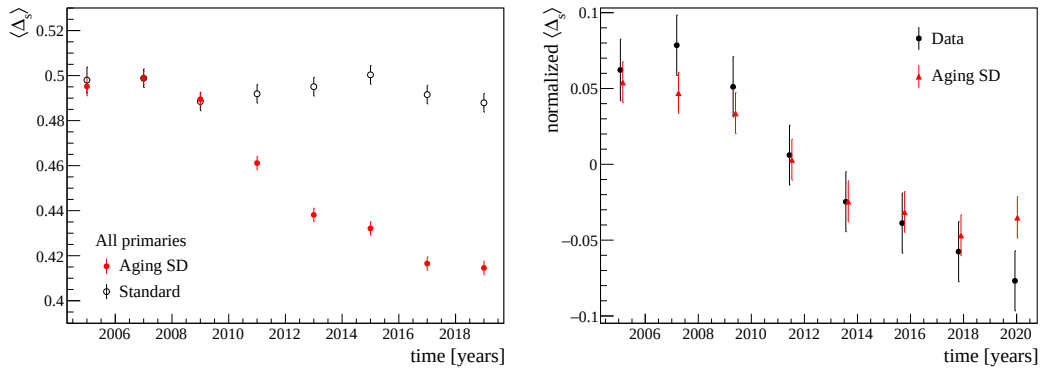

FIGURE 4.27: Evolution of $\langle \Delta_S \rangle$ as a function of time for data and simulations. Left: *standard* and *agingSD* simulations. Right: Data and aging simulations. In this case, $\langle \Delta_S \rangle$ is renormalized to its mean. Uncertainties are defined as the error on the mean for each time bin.

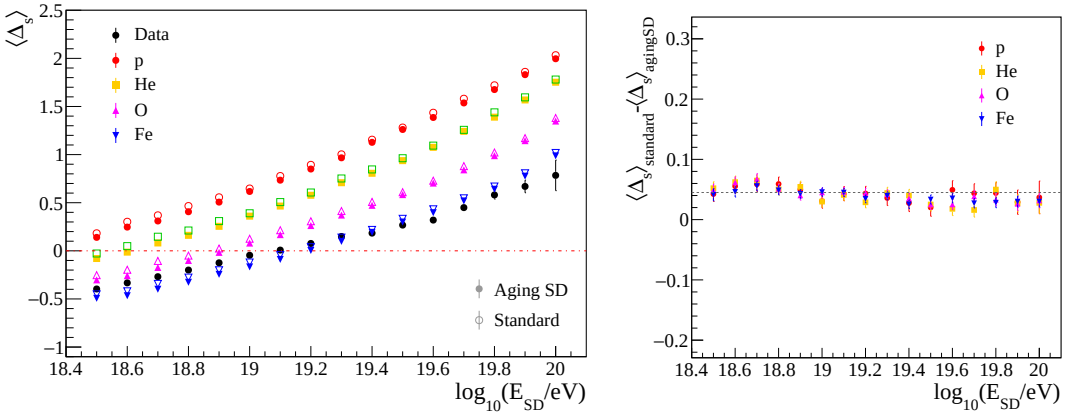

FIGURE 4.28: Left: Evolution of $\langle \Delta_S \rangle$ as a function of the reconstructed energy. Open symbols represent *standard* simulations, while filled symbols *agingSD* simulations. Data are shown as black dots. Right: Absolute difference between $\langle \Delta_S \rangle$ for *standard* and *agingSD*.

A decrease of the observed risetime, and consequently of $\langle \Delta_S \rangle$, would shift the event towards a heavier composition interpretation of the primary mass respect to the true atomic number, when compared to simulations. The effect of the aging on $\langle \Delta_S \rangle$ is assessed with the use of the *SdEvolution* library and it is visible in Fig. 4.28, left, in which open symbols display the mean value of $\langle \Delta_S \rangle$ as a function of the energy for different primaries using the standard simulations configuration, while the fill symbols show the same observable obtained using the simulations that include the time evolution of the surface detector. The black points represent, instead, the values of $\langle \Delta_S \rangle$ obtained for data. Events with $E_{SD} > 10^{20}$ eV are grouped together in the last energy bin, due to the small number of events in data at such energies. Error bars represent the error on the mean. The two simulations modes show an increasing trend for higher energies, as exepcted since the deposited signal increases (and the electromagnetic component with it), for larger energies. The difference between the two modes is small and constant over the energy. The general trend is similar for all the primaries, with an increase of $\langle \Delta_S \rangle$ of $\approx 1 - 1.5$ over the considered energy range.

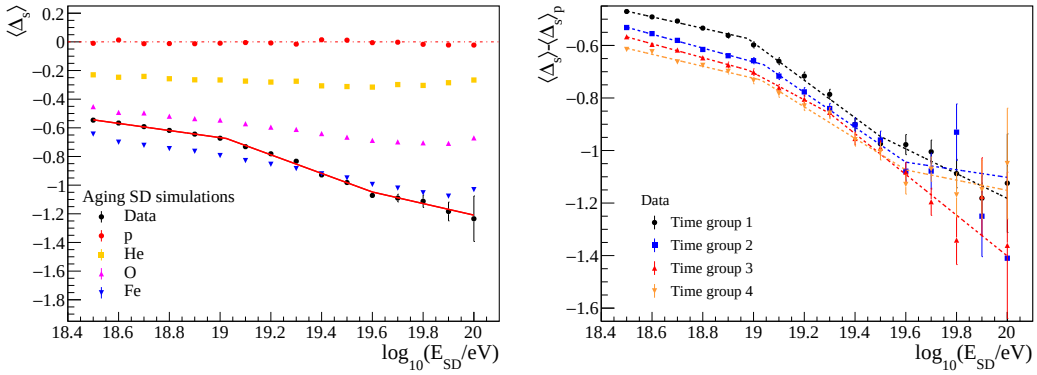

FIGURE 4.29: Normalized $\langle\Delta_S\rangle$ to proton simulations as a function of the reconstructed energy. Data are fitted using a broken linear function. Left: Data and simulations for all events. Right: Data split in different time groups.

In simulations, the slope of the evolution over the energy decreases as the primary mass increases. This is more evident when looking at $\langle\Delta_S\rangle$ after being renormalized to proton, as shown in Fig. 4.29, left plot, where only simulations in *agingSD* mode are displayed: Starting from a constant evolution for proton, the larger the primary mass the larger is the slope of the difference. The normalization to proton is obtained by subtracting a parabolic function fitted on proton.

The results for data show a different behaviour: $\langle\Delta_S\rangle$ starts at -0.55, between Oxygen and Iron and follow their trend as the energy increases, until E $\approx 10^{19}$ eV, where the slope changes and the data points get closer to Iron; from E $\approx 10^{19.6}$ eV the data follow the same trend of Iron. The trend of data has been studied in Fig. 4.29, by employing a broken linear fit, defined in Eq. (4.6) where x is the logarithm of the energy, and assuming two breaks, named x_0 and x_1, in which the data changes slope.

$$f = \begin{cases} A + s_0 \cdot \mathrm{x} & \text{for } x < x_0 \\ B + s_1 \cdot \mathrm{x} & \text{for } x_0 \leq x < x_1 \\ C + s_2 \cdot \mathrm{x} & \text{for } x \geq x_1 \end{cases} \tag{4.6}$$

The results for the two break points are $x_0 = 19.02 \pm 0.02$ and $x_1 = 19.6 \pm 0.19$, with the slope of the function changing from $s_0 = -0.25 \pm 0.01$ to $s_1 = -0.65 \pm 0.03$ after x_0, and becoming $s_2 = -0.40 \pm 0.27$ after x_1. This change in slope can be interpred as a change of mass composition in the data between x_0 and x_1, towards heavier nuclei or a change in the behaviour of hadronic interactions. Indeed, the evolution of $\langle\Delta_S\rangle$ with energy can be described by the combination of a polynomial and exponential function, two continuous and differentiable functions. A function obtained as the composition of these two functions is another continuous, differentiable function, while a piecewise function is continuous but not differentiable [117]. Effects due to detector or resolution effects were studied and seem to not be the cause of such breaks, as well as the aging presented in this work. Similar results have also been obtained in other studies [54].

Since the aging has a direct effect on the $\langle\Delta_S\rangle$ values, it is useful to verify the presence of the same features in different periods of time. In order to do that, the data set has been split in four different groups over time with a different time length, in order to have the same number of events in each group. The proton-renormalized $\langle\Delta_S\rangle$ as a function of the energy is shown in Fig. 4.29, right plot; in each subset the same behaviour is observed, with the most recent dataset (time group 4) not showing

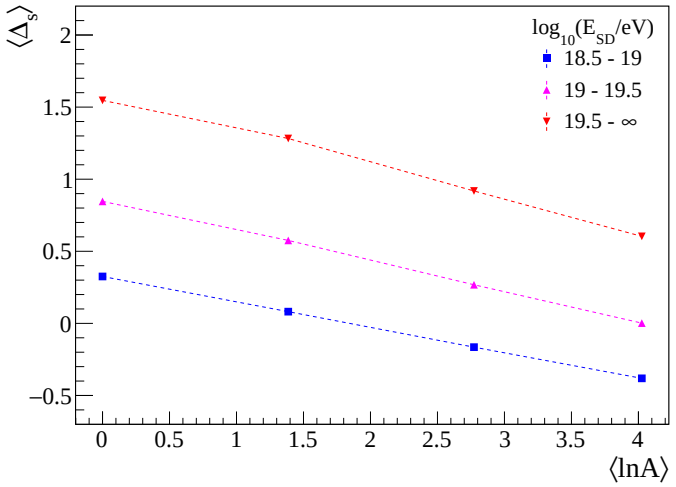

FIGURE 4.30: Δ as a function of the logarithm of the primary mass, obtained for simulations.

the second break due to a lack of statistics at higher energies. Another test to verify if these features are zenith dependent can be found in Appendix E, Fig. E.1, where a small bias for large zenith angles is visible.

The variation on $\langle \Delta_S \rangle$ due to the aging effect of the array is small but not negligible, especially when trying to infer the average primary mass composition and the observed trend of data using the $\langle \Delta_S \rangle$ method. The $\langle \Delta_S \rangle$ has a direct correlation with the primary specie, as shown previously. The relation between the two can be observed more clearly in Fig. 4.30, where the average value of $\langle \Delta_S \rangle$ from simulations is displayed as a function of the logarithm of the atomic number of the primary. The figure shows a linear relation between the two variables with $\langle \Delta_S \rangle$ decreasing as the mass of the primary increases, starting from ≈ 0.3 for proton to ≈ -0.4 for iron in the energy range $18.5 \leq \log_{10}(E/\mathrm{eV}) < 19$, represented with blue squares. The linearity is preserved for all energy ranges considered, as shown for the three different bins examined in Fig. 4.30, displayed with different shapes and colors: the absolute values of $\langle \Delta_S \rangle$ increase as the energy increases but the slope of the evolution as a function of the mass remains almost constant, with a similar decrease in $\langle \Delta_S \rangle$ of ≈ 0.7 from the lightest to the heaviest nuclei.

Having assessed the linear relation between $\langle \Delta_S \rangle$ and $\langle \ln \mathrm{A} \rangle$, it is possible to study the evolution of the mass composition of the events recorded by the surface detector array as a function of the reconstructed energy. The value of $\langle \ln \mathrm{A} \rangle$ from $\langle \Delta_S \rangle$ for simulations and data is obtained by the following relation

$$\langle \ln \mathrm{A} \rangle = \ln 56 \cdot \frac{\overline{\langle \Delta_S \rangle}_p - \overline{\langle \Delta_S \rangle}_x}{\overline{\langle \Delta_S \rangle}_p - \overline{\langle \Delta_S \rangle}_{Fe}} \quad , \tag{4.7}$$

where $\overline{\langle \Delta_S \rangle}$ indicates the average value of $\langle \Delta_S \rangle$ in the considered energy bin and $\overline{\langle \Delta_S \rangle}_x$ has been kept generic, since it is the average value of $\langle \Delta_S \rangle$ of the specific nucleus or of data for which the computation is performed.

Simulations of the aging detector of the different primaries in Fig. 4.31 show a constant behaviour as a function of the energy, as expected, besides some fluctuations at the highest energies. Data, instead, shown with black dots, display the

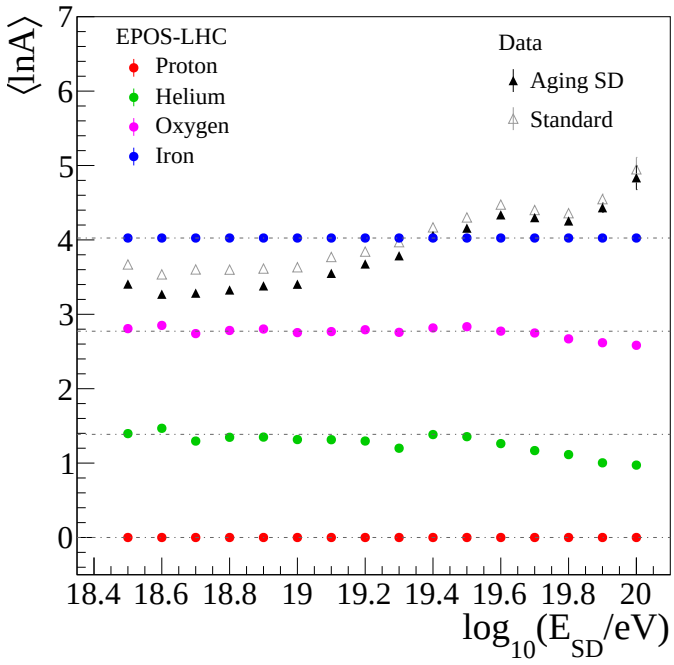

FIGURE 4.31: Computed mean value of the logarithm of the primary mass as a function of the reconstructed energy of the shower.

same trend observed when compared $\langle \Delta_S \rangle$ to simulations: the average mass composition of data is between oxygen and iron, with a value of $\langle \ln A \rangle$ of $\approx$ 3.2 at $E = 10^{18.5}$ eV, that grows as the energy increases towards iron to then flatten at around $E = 10^{19.5}$ eV, where $\langle \ln A \rangle \approx 4.2$. The open symbols represent the values that would have been obtained if $\langle \ln A \rangle$ would have been computed using the standard simulations. It can be seen that without the aging corrections, the method would have predicted an heavier composition compared to the one that considers the decrease of the risetime over the years, especially at lower energies.

It is not possible, however, to use these results to assess the correct mass composition of the data in absolute values. This is due to the well-known discrepancy between the hadronic models and the observed data regarding the muonic component of air-showers, the so-called *muon deficit* described in the first chapters. Since the simulations predict a fewer number of muons for air-showers, the results shown here are biased towards heavier elements, as it can also be noticed for the mass estimation of data that exceeds the iron mass. Indeed, the mass composition of UHECRs obtained with other methods used in the Pierre Auger Collaboration that are more sensitive to the electromagnetic component of the showers, such as the measurement of X_{max}, is predicted to be lighter than the one showed here. Nonetheless, the observed trend is similar.

In this study, the evaluation of the general trend has been studied to verify the effect of the aging in the $\langle \Delta_S \rangle$ method. It has been shown that the method is robust also in the case of a general loss of the collected light in the tanks, that in turn affects the risetime of the stations (the main observable used by the method). The aim of of this work was to reproduce the risetime behaviour, verify that the aging does not affect the main results of the study and assess the effect in the interpretation of the mass composition.

4.4 Summary

In this chapter, the aging model based on the evolution over time of the time-decay constant of pulses of vertical muons was applied to simulations by changing the liner reflectivity of the tanks in accordance with their behaviour over the years. The T2 trigger information sent by the stations during the operations in the field was also included in the simulations chain, to provide a better description of the whole array during the years. A complete library of reconstructed air showers for four different primaries at different energies and times has been produced, enabling a detailed study of the effect of the aging in several observables.

It has been shown that the decrease of the mean number of triggered stations over the years, observed in data, has been reproduced in simulations that take into account the aging. In that case, the energy distribution of the measured data and the inferred fractions of the primaries obtained by the Fluorescence Detector has been used to be able to compare data and simulations. As a further test, the time behaviour of $\langle \Delta_S \rangle$, an observable related to the risetime, has been has been reproduced in simulations and the impact of this change has been quantified.

The mentioned comparisons with data assess the goodness of the model and the capability of the method to describe in an accurate way the perfomances over time of the SD. This enables a deeper study of the impact of this long-term evolution on other high-level observables that are amongst the most important when reconstructing air-showers: the energy of the primary particle and its resolution as measured by the surface detector.

Chapter 5

Energy and energy resolution

In this chapter, real-time SD simulations will be used to assess the influence of the aging of the array in the energy reconstruction of the air-showers over the years and how this information can help to verify the hypothesis built in Chapter 2 when the decrease of the number of stations was studied. This will lead to an investigation in simulations of the change of the energy resolution of the surface detector over the years and a comparison with the predictions made by observing the trend of the mean number of stations in data.

Thanks to the design of the new simulation library, it is possible to disentangle between the intrinsic resolution of the array and the resolution loss due to the aging and access, in this way, the information regarding the shower-to-shower fluctuations.

5.1 Aging effects on the energy reconstruction

In the next paragraphs, the evolution over time of the reconstructed energy of air-showers and its resolution will be studied and the effect of the aging on these observables will be addressed. An estimation of this effect with the use of more realistic simulations of the SD response will improve the current and future systematic uncertainties in the interpretation of measurements.

5.1.1 Energy bias

Using simulated air-showers, it is possible to assess the bias present in the energy estimation by the surface detector reconstruction. The reconstructed energy of a shower, denoted here as E_{rec}, is compared with its true energy, E_{MC}. In Fig. 5.1, left, the relative biases for different primaries (displayed in different colors) are shown as a function of time: it can be seen that standard simulations, represented with open symbols, are in complete agreement with *agingSD* simulations (filled symbols), a sign that the aging does not affect the mean of the reconstructed energy. SD aging simulations show also a constant behaviour over time of the energy.

Simulated events were weighted following the measured energy distribution, shown in Chapter 4, since the energy bias in the reconstruction depends on the primary particle's energy, as visible in Fig. 5.1, right plot: the bias for iron, for example, is $\approx -1\%$ at $E = 10^{18.5}$ eV and becomes $\approx -10\%$ above $E = 10^{20}$ eV; the same trend is observed for the other primaries, with an increase of ΔE of $\approx 9\%$ in the energy range between $10^{18.5}$ eV and $10^{20.2}$ eV. Since the SD energy is obtained in a data-driven way, as shown in Section 1.3 with the use of the relation $E_{\text{FD}} = A(S_{38}/\text{VEM})^B$, the dependence of the energy bias on the true energy of the

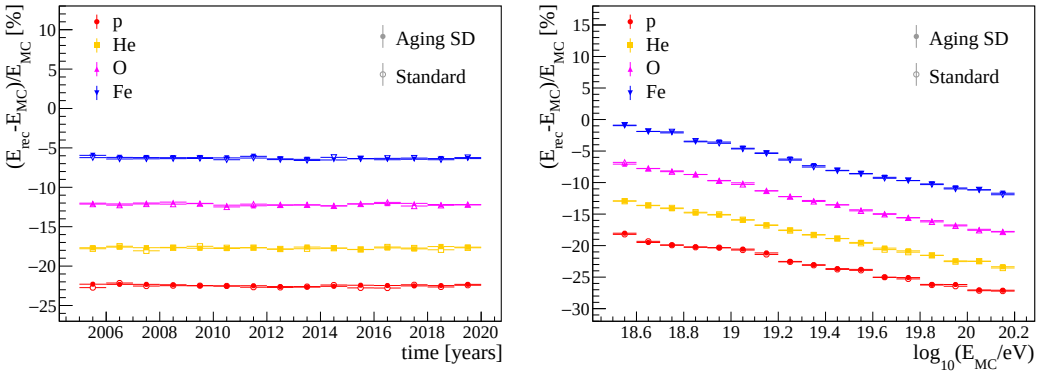

FIGURE 5.1: Left: Relative energy bias for all shower as a function of the time for different primaries. Open symbols: *standard* simulations. Filled symbols: *agingSD* simulations. Right: Relative energy bias for all shower as a function of the true energy for different primaries. Open symbols: *standard* simulations. Filled symbols: *agingSD* simulations. For both, uncertainties are defined as the error on the mean of the distributions in each year.

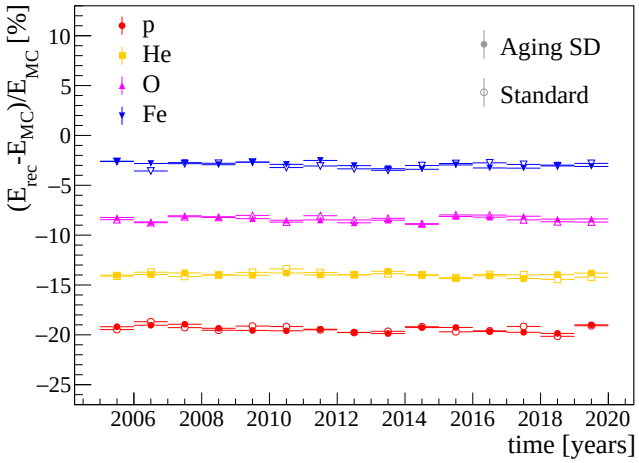

FIGURE 5.2: Energy bias between reconstructed energy and true Monte Carlo energy as a function of the years for different primaries, weighted by the energy spectrum. Open symbols: *standard* simulations. Filled symbols: *agingSD* simulations.

shower indicates that the value of the parameter B is different from data and simulations, as well as the A parameter. This is another indication of discrepancies between data and simulations, probably due to the lack of muons in simulations.

The energy bias between the two modes as a function of time, when the energy correction is included, is shown Fig. 5.2: it can be noticed that the behaviour over time remains constant for all primaries, while the absolute values of the bias changed, since now events with lower energies represent a larger contribution in the mean reconstructed energy. The difference in the energy bias between the two modes as a function of time is shown in Fig. 5.3: even in the case of a reduction of the signal due to the aging, it can be noticed that the reconstructed energy remains stable over the years, with variations at the sub-percent level. These results prove the robustness of the continuous calibration using atmospheric muons employed in Auger.

A similar result is obtained when looking at the energy estimator (S1000), see Appendix F.1, as a function of time for the two different sets of simulations. This result

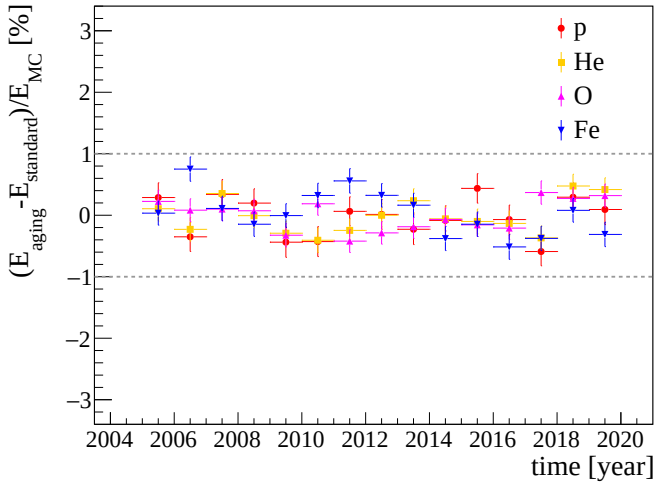

FIGURE 5.3: Change of the energy bias over time for the two different simulation configurations of the array: an ideal SD and a SD with a time-dependent behavior.

is compatible with the one obtained using *twin showers*. Even adding the complexity of multi-aged stations sparse all over the array and T2Life information, the energy estimator remains unaffected by detector changes during the years.

The constant SD energy over time observed in aging simulations confirms the assumption employed to obtain the effect produced on the energy resolution by the decrease of triggered stations, Section 2.3: The loss of stations per event with a constant SD energy with time will affect the resolution, since the latter is directly dependent on the number of stations participating in the reconstruction. The loss in resolution obtained in that case corresponded to a maximum 5% loss within 10 years. As a further crosscheck of the new *SdEvolution* model and simulation chain, this effect should be present with a similar magnitude when aging simulations are considered.

5.1.2 Detector resolution

The energy resolution, σ_E^{tot}, contains contributions from different sources, such as the detector resolution (in which we include in this case also the resolution due to the core location uncertainty) and the resolution due to physics effects (in this case mainly the shower-to-shower fluctuations), a way to isolate the detector contribution has been exploited, thanks to the setup used to produce the *SdEvolution* library. Showers stemming from the same `CORSIKA` parent, but generated at different times and at different locations over the array, are called *brother showers*. The detector energy resolution, σ_E^{det}, is obtained by computing the spread of the distribution of the reconstructed energy of each group of *brother showers*. In this way, the only effects considered when looking at the energy resolution are due to the detector and the core location, while the shower-to-shower fluctuations are avoided.

The σ_E^{det} dependence on the primary energy (E_{MC}) can be seen in the upper part of Fig. 5.4 for both *standard* and *agingSD* simulations, in open black and filled red symbols, respectively. In this case the figure shows the behaviour for proton only, with the uncertainties defined as the error on the mean of the distribution in each energy bin. The resolution is worse, in both cases, for lower energies (around 8.5 − 9.5% for $10^{18.5}$ eV) since showers with a lower energy will trigger less stations and this will affect the quality of the energy reconstruction, due to less data points used

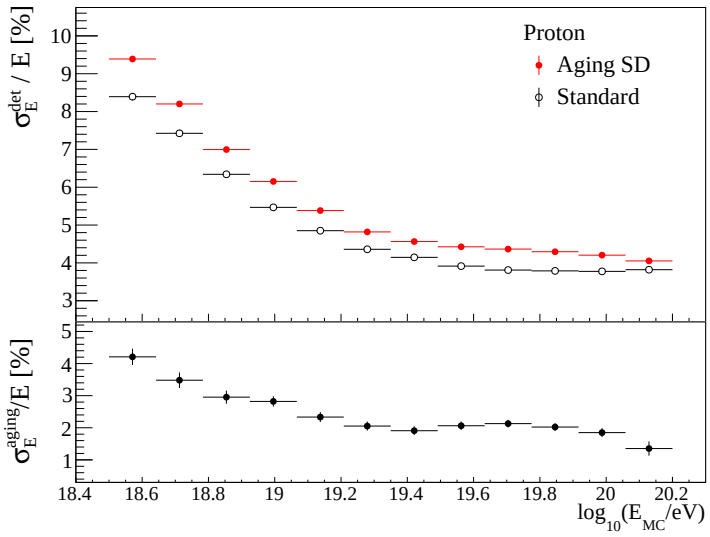

FIGURE 5.4: Top: Energy resolution due to detector effects; Open symbols: *standard* simulations; Filled symbols: *agingSD* simulations. Bottom: Energy resolution due to aging effects. See text for details.

for the fit of the LDF. The resolution as a function of the energy, going with $1/\sqrt{E}$, is $\approx 4\%$ at the highest energies.

It can be seen that there is a difference between the two simulations modes, with a worse resolution in the case of simulations including the aging. In order to quantify this difference, the contribution due to the aging (σ_E^{aging}) is obtained as the quadratic difference between the resolutions, as following:

$$\sigma_E^{\text{aging}} = \sqrt{(\sigma_E^{\text{evolution}})^2 - (\sigma_E^{\text{standard}})^2} \tag{5.1}$$

In Fig. 5.4, bottom panel, the evolution of σ_E^{aging} is shown, with the errors obtained from error propagation of the considered variables. Similarly to the case of the detector resolution, the lower the energy, the higher the effect, starting at $\approx 4\%$ and reaching the level of 2% for the highest energies. These findings are in agreement with what was predicted in Section 2.3 by studying the loss of candidate stations over the years. In that case the maximum loss in resolution in 10 years was estimated to be 5%.

The energy dependency of the contribution from the aging can be explained with similar considerations done for the detector resolution. The loss of recorded signal could move some stations under the trigger threshold, leading to a smaller number of stations involved in the reconstructions; this effect, in turn, will affect the energy reconstruction, as explained above, and events with a low number of stations would be more sensitive to such a change compared to high-energy events with a large number of stations. Another extra-effect, in this case, comes from the variety of stations as not all the stations have the same age.

When analysing the detector resolution for other primaries, Fig. 5.5 for *agingSD* simulations, it can be seen that they share the same behaviour and similar values. A slightly worse resolution at lower energies (iron being at $\approx 11.2\%$ at $10^{18.5}$ eV) and a sharper slope over the energy range for heavier nuclei is observed. The resolution due to the aging, instead, is compatible for all primaries and remains between 2 and 4%. A similar result has been obtained for the resolution of S1000 and can be observed in Appendix F.2.

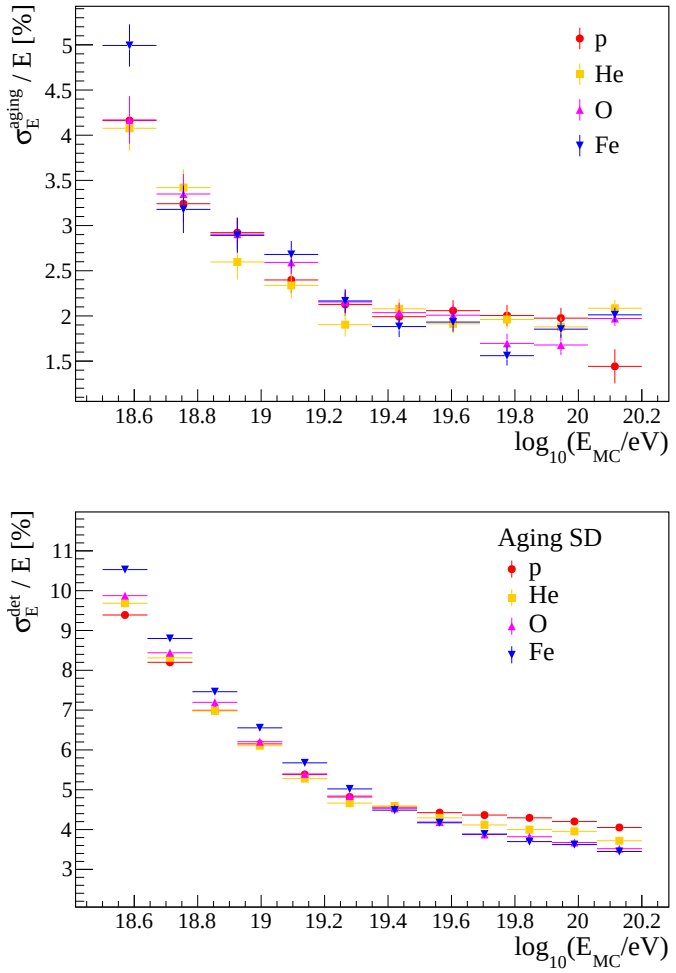

FIGURE 5.5: Energy resolution as a function of the Monte Carlo energy. Top: Contribution from the aging effect to the resolution. Bottom: Energy resolution due to detector effects.

5.1.3 Comparison with data

The results obtained for the detector resolution in simulations can be compared with data by looking at the energy error assigned to each reconstructed shower. This uncertainty derives from the statistical uncertainty of the reconstructed shower size $S(1000)$, $\sigma_{\text{stat}}(S(1000))$. The relation between E_{SD} and $S(1000)$ is based on the conversion of $S(1000)$ into S_{38} using the constant intensity cut (CIC) method and then calibrated with the energy measurement of the FD using hybrid events, as described in Chapter 1. For its part, $\sigma_{\text{stat}}(S(1000))$, estimated during the fitting procedure of the LDF [71], is directly related to the number of triggered stations and the uncertainties in their signals, thus describing the detector effects of the reconstruction on data.

The comparison between data and simulations is shown in Fig. 5.6, in which simulations for the two modes contain all the primaries weighted for the composition fractions, called AugerMix, to obtain a more realistic description. In grey, instead, σ_E^{det} for proton and iron in aging simulations are shown. Data agree better with *agingSD* simulations than with ideal simulations, varying from $\approx$ 10% at $10^{18.5}$ eV, down to $\approx$ 4% at $\approx 10^{19.4}$ eV where start to deviate. At that energy, simulations begin to show a flattening in the behaviour, while σ_E^{det} for data keeps decreasing. This discrepancy can be explained by the fact that the signal variance and LDF model

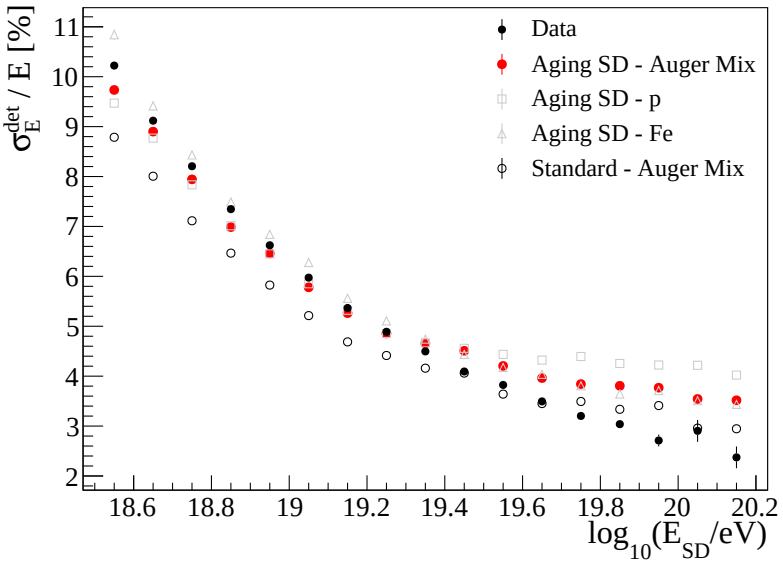

FIGURE 5.6: Energy resolution due to detector effects for data (black dots) and simulations (red for *agingSD* and open black symbols for *standard*). Primaries in simulations are weighted accordingly to the AugerMix. In grey, σ_E^{det} for proton and iron.

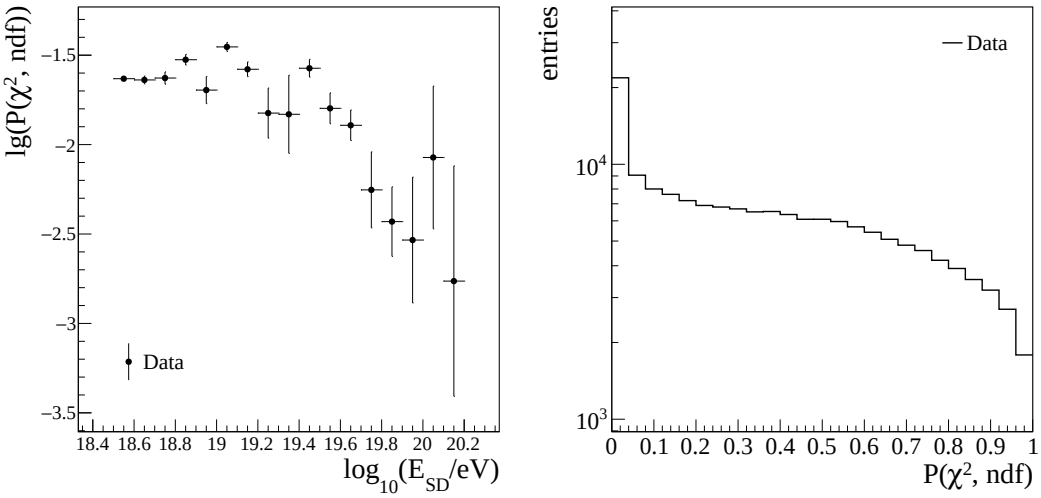

FIGURE 5.7: Left: Logarithm of the probabilities obtained from the reduced χ^2 of the LDF fit on data as a function of the reconstructed energy. Right: Distribution of the probabilities.

might not be properly determined. This is shown in Fig. 5.7, left, where the χ^2 probability decreases with increasing energy. This effect is not present in σ_E^{det} obtained in simulations, since it is derived from the *brother showers*.

The aging simulations reflect more the real values of the energy resolution observed in data, compared to the standard simulations. The use of this new library can improve the modeling of the uncertainties related to the energy, from which other studies could benefit.

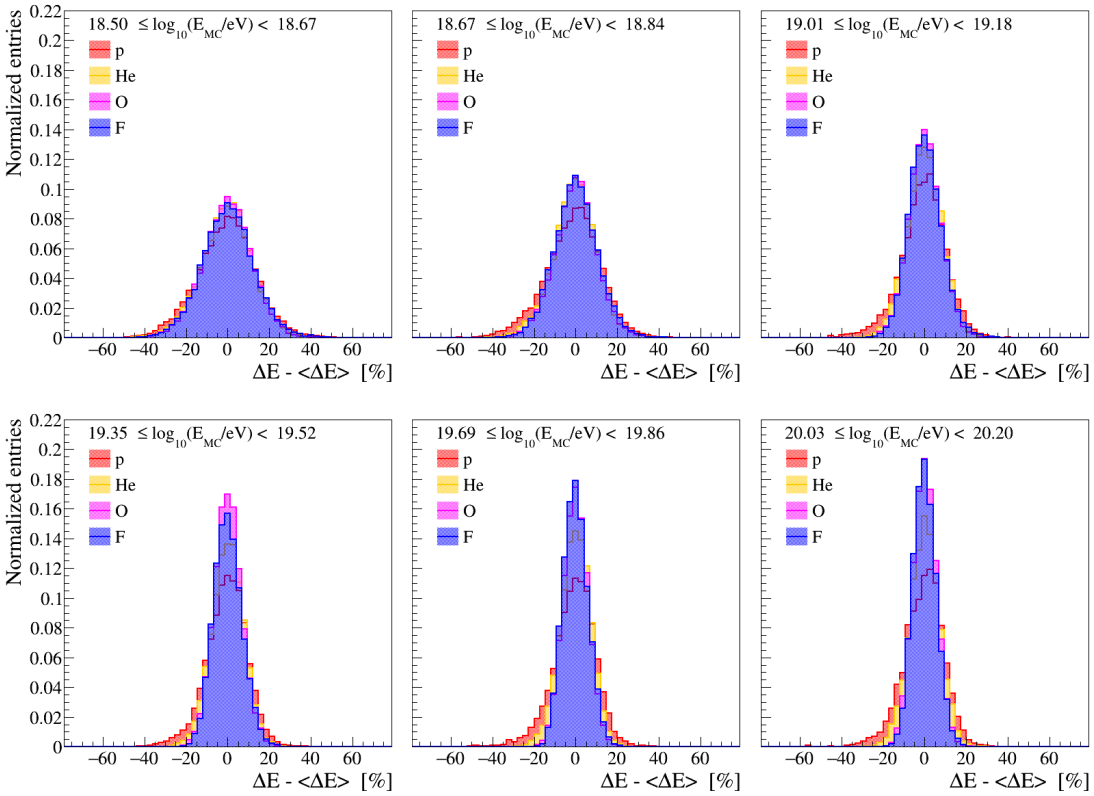

FIGURE 5.8: Distributions of ΔE renormalized to the mean for each primary in several energy bins. Aging simulations are shown.

5.1.4 Total resolution

From the reconstruction of the simulated air-showers, the total resolution, σ_E^{tot}, is obtained by measuring the spread of the distributions of the difference between the reconstructed energy of the events and their true energy, defined as $\Delta E = E_{\text{rec}} - E_{\text{MC}}$, without separating them based on the original shower. Events are just split in energy bins, to study the evolution of the total resolution as a function of the primary energy. These distributions are shown in Fig. 5.8 for several energy bins; All the primaries are displayed in each plot. To better appreciate the differences between primaries and compare them, the distributions are renormalized to the mean, visually enhancing their change of shape as the energy increases. It can be seen that, for greater energies, the distributions become narrower, producing a better σ_E^{tot}, as expected.

The total resolution for different primaries as a function of the true shower energy is displayed in Fig. 5.9. The spread of the energy distributions is between 12% and 14% at $10^{18.5}$ eV and it decreases to 10% for proton and between 5.5% and 7.5% at $10^{20.2}$ eV for the other primaries. The result is in agreement with the SD resolution obtained employing a data-driven method based on the FD measurement of the energy [1] and parametrized as:

$$\frac{\sigma_{\text{SD}}}{E} = \sigma_0 + \sigma_1 \exp\left(-\frac{E}{E_\sigma}\right) \tag{5.2}$$

where the values of the parameters are obtained from a fit to the data: $\sigma_0 = 0.078$, $\sigma_1 = 0.16$, and $E_\sigma = 6.6 \times 10^{18}$ eV. This method assesses the energy resolution by

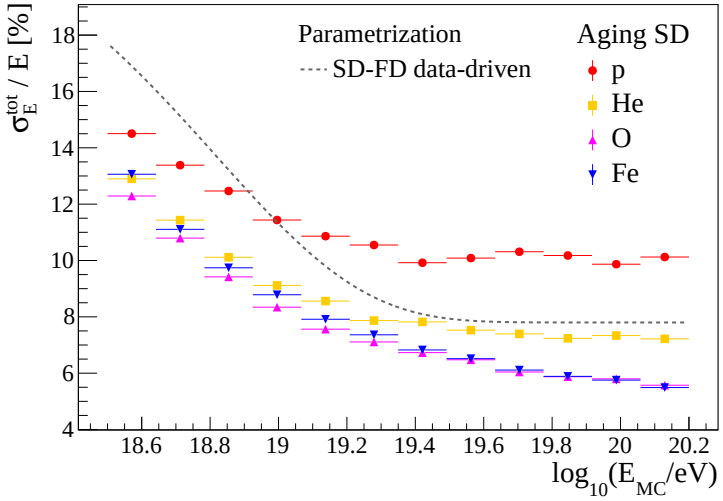

FIGURE 5.9: Total energy resolution as a function of the true energy of the showers for different primaries for *agingSD* simulations.

looking at the spread of the distributions of E_{SD}/E_{FD} of hybrid events, removing the need for any mass assumptions [1]. The resolution is $\approx 20\%$ at 2×10^{18} eV and tends smoothly to $\approx 8\%$ above 2×10^{19} eV.

5.2 Shower-to-shower fluctuations

Primary particles with identical characteristics (energy, mass and arrival direction) and propagating through the atmosphere, can produce different footprints on the ground. This is due to the fluctuations that occur in every particle interaction, in particular in the depth of the first interaction of the primary, producing secondary particles that have parameters that vary from shower to shower [11, 118]. The interactions of the secondaries have, as well, intrinsic fluctuations. The fluctuations due to physical processes in the shower are called *shower-to-shower fluctuations*, indicated as $\sigma_E^{\text{sh-sh}}$, and are difficult to estimate.

The capability to obtain and study the detector resolution, opens the possibility to tackle and describe the shower-to-shower fluctuations by subtracting the contribution of the detector resolution from the total resolution. The shower-to-shower contribution can be obtained as the quadratic difference between the total resolution and the detector one:

$$\sigma_E^{\text{sh-sh}} = \sqrt{(\sigma_E^{\text{tot}})^2 - (\sigma_E^{\text{det}})^2} \tag{5.3}$$

The results for oxygen *agingSD* simulations, for example, is shown in Fig. 5.10(c). In the top panel, the total resolution for oxygen as a function of the primary energy, represented with black dots, ranges between $\approx 12\%$ and $\approx 6\%$ while the red points show the detector resolution, shown previously in Fig. 5.5, top plot. In the bottom panel, the extracted shower-to-shower fluctuations are displayed. Their trend shows a decrease from $\approx 7.2\%$ for lower energies, to $\approx 4.2\%$ at the highest energies. The same procedure is applied to the other primaries and the fluctuations obtained are shown in Fig. 5.11. They are energy-dependent, with a decrease for different primaries between 1% and 3% over 1.5 decades in energy. It can also be observed that the absolute values are different based on the atomic number of the primary, with lighter elements having larger fluctuations compared to heavier ones.

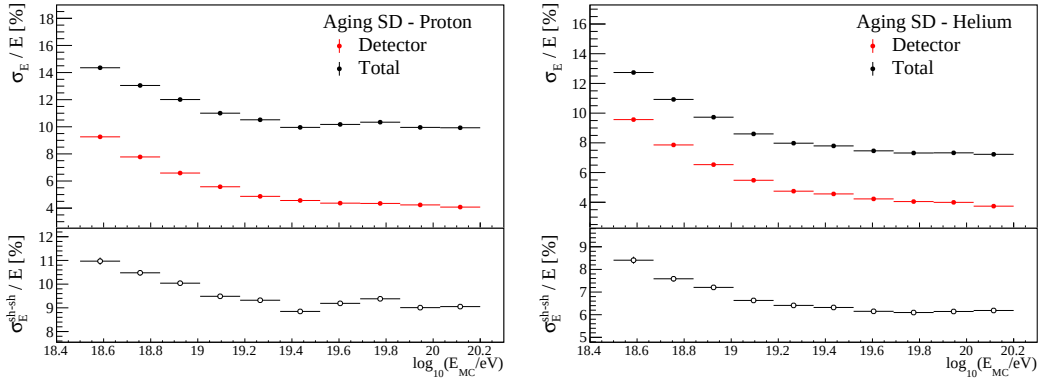

(a) Proton

(b) Helium

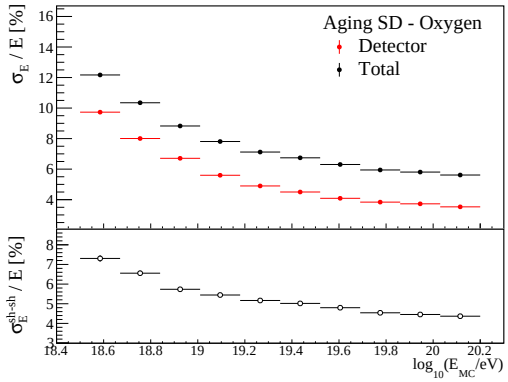

(c) Oxygen

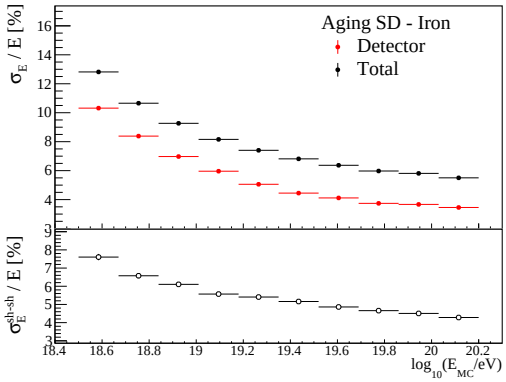

(d) Iron

FIGURE 5.10: Energy resolution and shower-to-shower fluctuations for different primaries. Top panel for each plot: Total energy resolution and detector resolution as a function of the Monte Carlo energy. Bottom panel for each plot: Contribution from shower-to-shower fluctuations to the energy resolution.

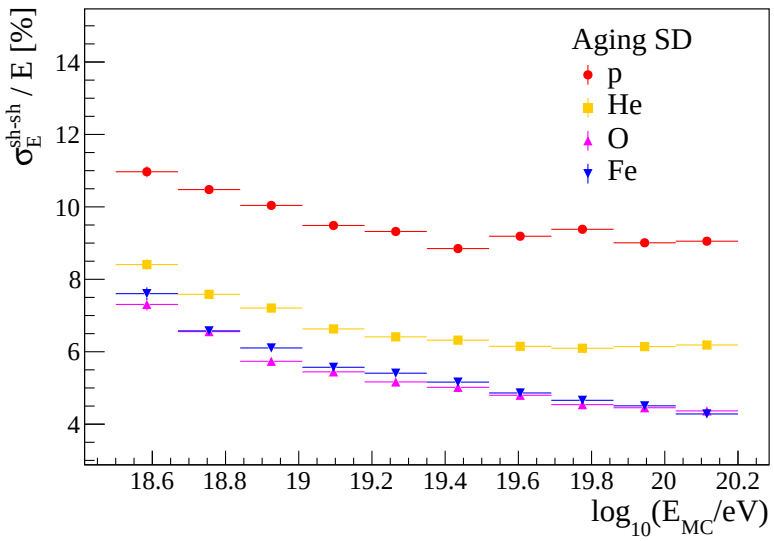

FIGURE 5.11: Contribution from shower-to-shower fluctuations to the energy resolution for different primaries.

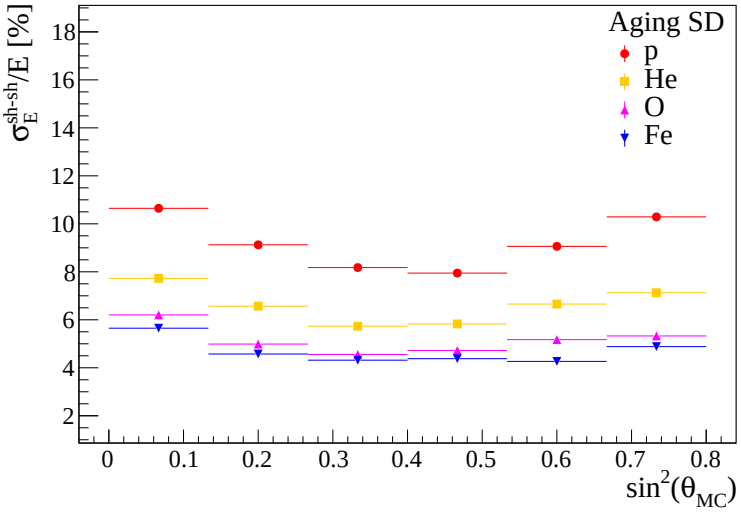

FIGURE 5.12: Contribution to the resolution of shower-to-shower fluctuations for *agingSD* mode as a function of the arrival direction for different primaries.

The behaviour of these fluctuations can also be studied as a function of the zenith angle of the incident primary particle, to understand the effect due to the arrival direction of the cosmic-ray in the observed fluctuations. The spread in energy due to shower-to-shower fluctuations in the case of *agingSD* simulations as a function of θ_{MC} has a parabolic behaviour for all primaries, shown in Fig. 5.12, at the level of $\approx$ 10% for very vertical and inclined proton showers and $\approx$ 6% for iron showers. It decreases down to $\approx 8(6)\%$ for proton (iron) showers arriving with a zenith angle around 36° ($\sin^2(\theta_{\rm MC}) = 0.35$), where it shows a minimum. This behaviour can be explained considering that fluctuations are mostly driven by the electromagnetic component, a more stochastic process, compared to the muon content of a shower that has a direct correlation with the primary mass. More vertical showers encounter less atmosphere and, thus, $e^{\pm}, \gamma$ are less absorbed, enhancing the fluctuations of shower to shower. The more inclined is the shower, the less the electromagnetic component, being attenuated, plays a role in the recorded signal at the ground. This effect starts to invert when showers are very inclined and the probability of muons decaying increase, producing the so-called *muon halo*, an additional electromagnetic contribution that, in turn, increases the shower-to-shower fluctuations. Another effect could be related to the spectrum of the muons reaching the ground, which might be different at different zenith angles. The detector resolution, shown with red point in the top panels of each plot in Fig. 5.13, appears to be constant over the zenith range. Only showers with energies greater than 10^{19} eV have been considered, to avoid that the worse energy resolution at small energies could distort the results by dominating the evolution over θ.

The same trend can be noticed in *standard* simulations, Fig. 5.13, right column, and when compared with the results obtained for simulations in *agingSD* mode, it can be seen that the shower-to-shower fluctuations are compatible, with a difference in resolution less than 0.5%, as displayed in Fig. 5.14 for single primaries. In Fig. 5.15, these differences are displayed for all the primaries. Fluctuations agree at the sub-percent level between the two different simulation configurations, for all the nuclei. This confirms that the inclusion of the aging in simulations is not introducing any bias in the physical properties of the showers and the observed effects on high-level variables are ascribable to the loss of signal in the tanks.

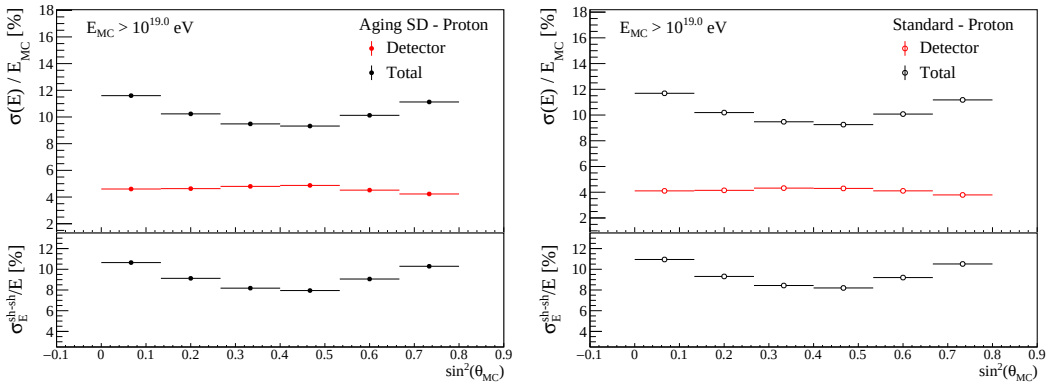

(a) Proton

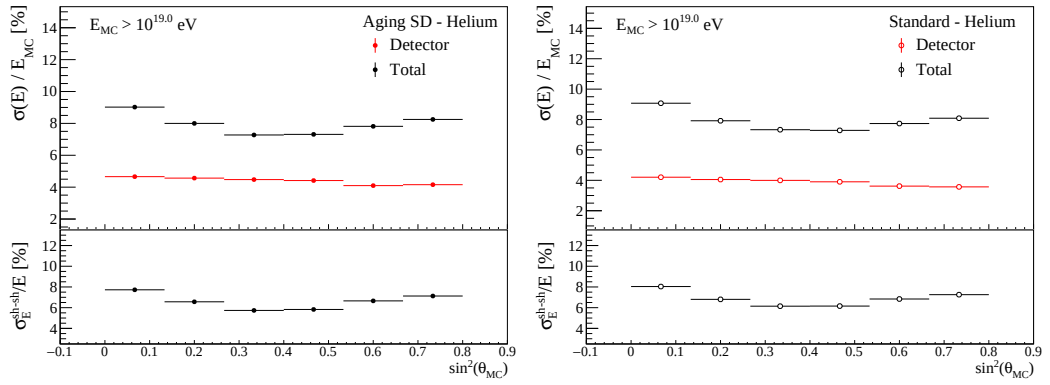

(b) Helium

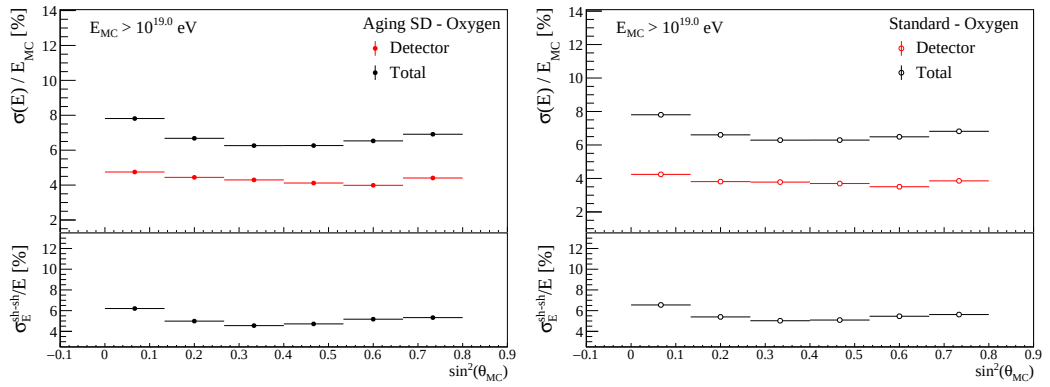

(c) Oxygen

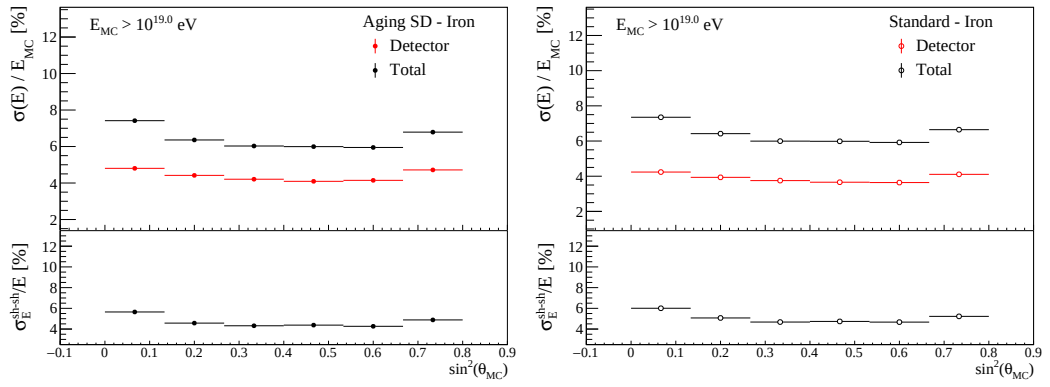

(d) Iron

FIGURE 5.13: Shower-to-shower fluctuations as a function of the arrival direction of the showers for different nuclei. Left: *agingSD* simulations. Right: *standard* simulations.

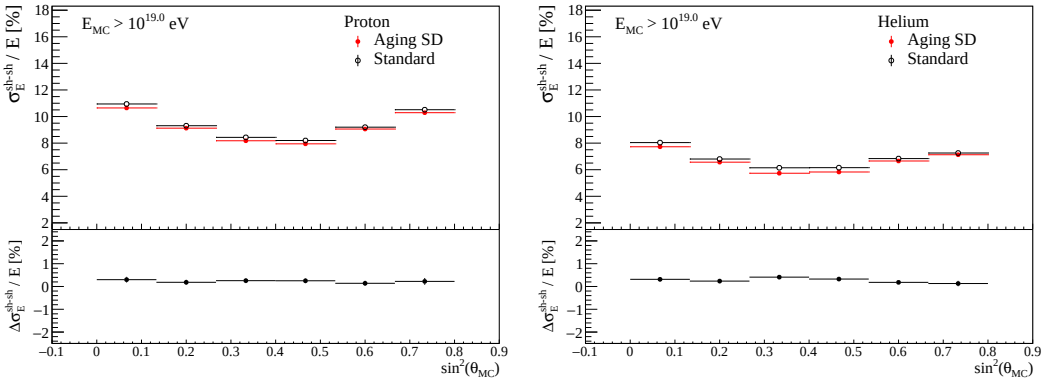

(a) Proton (b) Helium

(c) Oxygen (d) Iron

FIGURE 5.14: Comparison of shower-to-shower fluctuations between *agingSD* and *standard* mode as a function of the arrival direction for all primaries. Top panel for each plot: $\sigma_E^{\text{sh-sh}}$ for the two modes. Bottom panel for each plot: Difference of the fluctuations between the two modes.

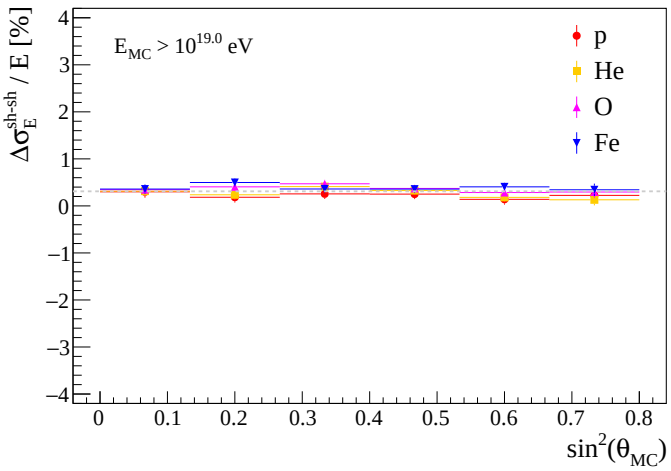

FIGURE 5.15: Change of the shower-to-shower fluctuations over the arrival direction for the two different simulation configurations of the array: an ideal SD and a SD with a time-dependent behavior.

Chapter 6

Muon signal using Deep Learning

In the previous chapters, the production and validation of a new simulations library to address and describe the aging effect has been described. The trend of several high-level observables has been reproduced and the effect on the reconstruction of air showers have been studied. Since these simulations are closer to what is seen in data, they could be very useful in studies that exploits the information contained in station-level observables, such as the time traces of the recorded signals.

In particular, the Pierre Auger Observatory has published innovative analysis in which Deep Learning algorithms have been used to infer and extract mass-sensitive observables from the SD recorded events. Since these algorithms are trained with simulations, an accurate description of the detector (and the shower physics as well) has become of great importance.

In this chapter, the field of Machine Learning will be briefly described, with a general explanation of one of its most used models: Neural Networks. These are the building blocks for the Deep Learnig models that will be discussed later in the chapter, with some of the architecture used in this work.

The second part of the chapter will describe the architecture used in order to extract the temporal signal of muons from the total signal measured in the WCDs. The method and its functioning will be shown, together with the results obtained when this Deep Neural Network is confronted with aging simulations.

6.1 Machine Learning

Machine learning (ML), a subset of artificial intelligence (AI), has transformed in recent years the landscape of technology, research, and industry. The definition of ML is teaching computers to autonomously learn from data without explicit programming. This process involves feeding the algorithm with a training dataset, enabling it to iteratively adjust its internal parameters and improve its performance based on examples provided in the form of training data. By enabling computers to learn patterns and relationships in data to make predictions, classifications, and informed decisions, machine learning has created new possibilities to solve complex problems.

Machine learning can be categorized into supervised, unsupervised, and reinforcement learning. In supervised learning, algorithms learn from labeled data, finding the relation between input and output variables. This type of learning enables the algorithm to generalize its understanding to new, unseen data. Unsupervised learning involves uncovering the underlying structure within data that lacks predefined labels. In this context, algorithms autonomously analyze patterns, clusters, and relationships, revealing insights without the need for explicit guidance. Reinforcement learning involves an agent learning to interact with an environment to maximize rewards. The agent navigates through a trial-and-error process, adapting

its actions based on feedback received from the environment. In the context of this work, we will primarly focus on supervised learning.
When designing and building an ML model, the following component are of primary importance:

- Data: High-quality, relevant data is the foundation. Clean, diverse, and representative data ensures accurate model training.
- Features: Observables extracted from the data that the algorithm uses for learning. The correct choice of such variables influences a model's performance.
- Model: The model embodies the algorithm's comprehension of the fundamental patterns within the data. This could be a decision tree, a neural network, or alternative structures, depending on the analysis.
- Training: During training, the model is fed with labeled data, adjusting its internal parameters iteratively to minimize the difference between predicted and actual outcomes.
- Testing and Validation: Once trained, the model is tested on new, unseen data to evaluate its performance and generalization capabilities. Validation ensures that the model is not overfitting the training data.
- Hyperparameters: These are parameters that are set before training begins and influence the learning process, such as the learning rate in neural networks.

In the field of physics, ML has emerged as a powerful tool for analyzing complex data, optimizing experiments and make accurate predictions [119, 120, 121, 122].

6.2 Neural Network

A neural network (NN) is a computational model inspired by the structure and function of the human brain's interconnected neurons. It is a fundamental component of machine learning, capable of learning complex patterns and relationships from data. Neural networks excel in tasks like image and speech recognition, natural language processing, and more [123].
A neural network consists of layers of interconnected nodes, known as neurons. These layers are categorized into three main types:

- Input Layer: This layer receives the raw data or features from the input dataset. Each neuron in the input layer corresponds to a specific observable of the data, x_i.
- Hidden Layers: These intermediate layers process and transform the input data through a series of mathematical operations, in which each neuron is associated with a weight, w_i, that is adjusted during the training. The number of hidden layers and the number of neurons in each layer can vary, depending on the complexity of the problem and the network's architecture. In the simplest architecture, only one hidden layer is present.
- Output Layer: The final layer produces the network's predictions or classifications. The number of neurons in the output layer is determined by the nature of the task. For instance, in a binary classification problem, there might be two output neurons representing two possible classes.

A visual representation of a NN is shown in Fig. 6.1.

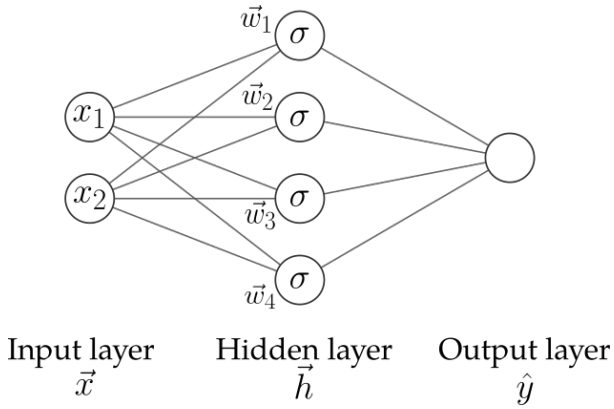

FIGURE 6.1: Simple neural network example. Input has 2 features, hidden layer has 4 neurons and the output is a single value. For clarity, the bias vector has not been included in the image. σ is the activation function. Image produced with [124].

6.2.1 Basic description of operation

The functioning of a neural network involves several key steps. Once the network's initial parameters are set, including weights and biases (an additional weight for the hidden layers), the data is fed into the input layer. The trasformation of inputs to outputs can be described through a mathematical representation, following the schema in Fig. 6.1. Given an input vector $\vec{x}$, containing the values of n observables for one realization, namely $(x_1, x_2, \cdots, x_n)$, and a weight matrix W with dimension (n, j), being j the number of neurons in the hidden layer, and column vector corresponding to the weights assigned to each neuron $\vec{w}_{i..j}$, with each vector having n components, $W = (\vec{w}_1, \vec{w}_2, \cdots, \vec{w}_j)$, the output $\hat{y}$ of a layer can be computed using the following equation:

$$\hat{y} = \sigma(W \cdot \vec{x} + \vec{b}) \tag{6.1}$$

where $\vec{b}$ is the bias vector. The activation function σ introduces non-linearity, enabling the neural network to capture complex relationships in data. A common choice for σ is the sigmoid function or the rectified linear unit (ReLU) [125], defined as $f(x) = \max(0, x)$. When using m training examples, the input becomes a matrix X of dimension (m, n). Due to this representation, this computational step, also known as "forward propagation", can exploit matrix algebra to perform calcutions between the layers and speed up the processes.

The next step is to assess the accuracy of the prediction. The difference between the predicted output and the actual target output from the training data, is quantified using a loss or cost function, J. The choice of a specific loss function depends on the nature of the problem and the characteristics of the data, with the Mean Squared Error (MSE) being the most widely used for regression problems. The aim is to minimize this loss, indicating how far off the predictions are from the actual values. Ultimately, through continuous adjustments over an interative procedure, called training and described in the next paragraph, a trained neural network can make accurate predictions or classifications when presented with new data. The network's ability to generalize from its training experiences is the result of finding the optimal set of parameters that minimize J. This process transforms the neural network into a powerful tool for complex pattern recognition.

6.2.2 Training

The core of neural network proficiency lies in their capacity to learn from data. This learning process entails the calibration of weights associated with connections between neurons, and this calibration is accomplished through a process known as training. An optimization algorithm, often gradient descent, is a core technique used to update the weights and biases in the direction that reduces the loss. Gradient descent involves iteratively adjusting network weights to minimize the error between predicted and actual outputs. The underlying principle revolves around finding the optimal configuration of weights that corresponds to the model's highest accuracy. The "gradient" signifies the rate of change of the error concerning each weight, providing directional guidance for weight updates. Mathematically, the weight and bias update step in gradient descent can be expressed as follows, in the case of the weight matrix:

$$W_{new} = W_{old} - \alpha \cdot \frac{\partial L}{\partial W_{old}} \tag{6.2}$$

where W_{new} represents the updated weights, W_{old} denotes the previous weights, α is the learning rate, controlling the step size and $\partial L/\partial W_{old}$ is the gradient of the loss function with respect to the weight. A similar formulation is used for the biases. The learning rate governs the size of each update, and plays an important role for the minimization process, since a value too large could cause the network to not reach the minimum, while a value too small can increase the training time significantly. The "backpropagation" algorithm [126, 127] is integral to the implementation of gradient descent in neural networks. It calculates the gradients of the loss function with respect to network weights through the chain rule of calculus. These gradients are then used to update the weights in a direction that reduces the loss, progressively steering the model toward optimal performance. Incorporating gradient descent and backpropagation, neural networks iteratively fine-tune their weights, gradually improving their ability to generalize patterns in the data.

These steps are repeated for a specific number of times known as "epochs." An epoch represents a complete pass through the entire training dataset. During each epoch, the network refines its predictions and minimizes the loss further. To manage large datasets efficiently, training data is often divided into smaller subsets known as "batches." Instead of updating the network's parameters after every individual data point, updates are made after processing each batch. This approach enhances training efficiency and allows the network to learn from patterns in smaller subsets, gradually improving its overall performance. This iterative process is repeated over numerous epochs until convergence, whereby the model achieves a satisfactory level of accuracy on the training data. The trained network can then be evaluated on unseen data to assess its ability to generalize.

The training of a neural network model requires a split of the dataset into three subsets: Training, validation, and test sets. The training set is the largest part and is used to teach the model. It learns patterns and adjusts parameters to minimize loss on this data. The validation set helps fine-tune hyperparameters and monitor performance during training, preventing overfitting. The test set is kept separate from training and validation. It serves to assess the model's performance after training and hyperparameter tuning. The separation of data points into the subsets must mantain the original distributions of the observables, in order to avoid any biases during the training and assessment of perfomance.

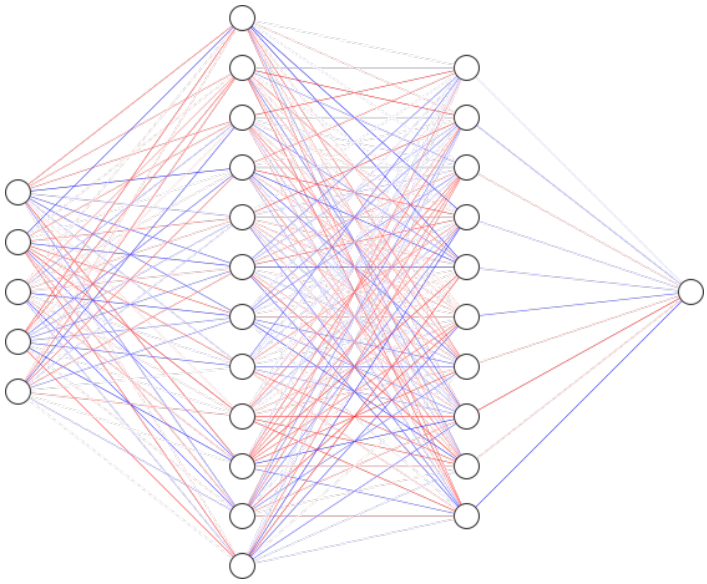

FIGURE 6.2: Deep neural network example of a fully connected layers model. The different colors represent positive (red) and negative (blue) weights, while the color intensity is proportional to the weight magnitude. Image produced with [124].

6.3 Deep Learning

Deep learning uses neural networks, but the main distinction to traditional networks comes from the presence of multiple hidden layers. The term "deep" refers to the multiple layers through which data is processed, allowing for the hierarchical extraction of features and representations as data moves deeper into the network. For this reason, a network of this type is also referred to as "Deep Neural Network" (DNN); An example of such a network is shown in Fig. 6.2.

The forward propagation, in the case of a DNN with n hidden layers, can be described as follow:

$$\begin{aligned} \vec{h}_1 &= \sigma(W_1 \cdot X + \vec{b}_1) \\ \vec{h}_2 &= \sigma(W_2 \cdot \vec{h}_1 + \vec{b}_2) \\ &\dots \\ \hat{y} &= \sigma(W_{out} \cdot \vec{h}_n + \vec{b}_{out}) \end{aligned} \tag{6.3}$$

where $\vec{h}_1$, $\vec{h}_2$, .., $\vec{h}_n$ are the hidden layers' outputs, each obtained from the previous layer's output. W_{out} and b_{out} correspond to the weight matrix and bias vector of the output layer.

Deep learning models require less feature engineering because they automatically extract features from raw input data [126]. For example, when presented with images for classification purposes, deep-learning systems can use convolutional neural networks (CNNs), specialized layers designed for image recognition, instead of manually extracting features from each image individually like one would have done using traditional methods such as Support Vector Machines or Random Forests [128].

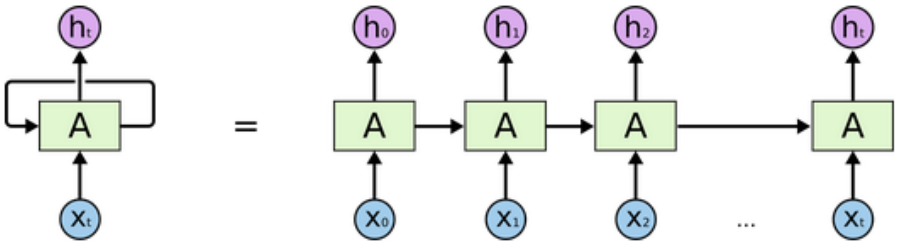

FIGURE 6.3: Schema of a recurrent neural network and the visual explanation of how the different elements of a sequence are connected to each other [130].

6.3.1 Fully Connected Layers

Fully connected layers, also known as dense layers, are a type of architecture used in deep learning models. Fully connected layers are used to connect all neurons from one layer to the next and allow for information flow between them. They have been found to be essential components of many deep neural networks (DNNs).

A fully connected layer is characterized by the presence of connections linking every neuron in the layer to every neuron in the subsequent layer, allowing the output from the previous step to be passed forward after being weighted in each connection according to an adjustable parameter associated with it; thus forming connections among all neurons across a DNN model architecture [129]. This allows for efficient data propagation throughout the entire network by allowing signals received at any given node on one layer being able to influence subsequent nodes down below without necessarily being explicitly connected together [126]. Furthermore, these types of architectures enable feature extraction capabilities by performing nonlinear transformations over the input data in each node, before applying additional convolutional or pooling operations to extract more complex features, if needed [128].

This type of networks offer several advantages when compared with other traditional architectures, including better scalability options, improved feature extraction abilities along with increased robustness against noise (due their ability to propagate information through multiple paths rather than having just a single path running through, which could potentially lead towards misclassification events).

6.3.2 Long Short-Term Memory

Recurrent Neural Networks (RNNs) are a class of neural network architectures that can process sequential and temporal data. In contrast to conventional feedforward neural networks, RNNs have a recurrent connection that allows them to maintain a memory of previous steps in the sequence. This intrinsic property makes RNNs very useful in tasks such as natural language processing, speech recognition, and temporal signal processing.

The distinguishing feature of RNNs is the feedback loop that connects the output of a neuron back to itself or other neurons in the same layer. This loop enables the network to consider previous steps in the sequence when making predictions at the current step. The core components of an RNN are recurrent neurons, which process input data and maintain an internal hidden state, called $\vec{h}$. This hidden state serves as memory and is updated at each time step as the network progresses through the

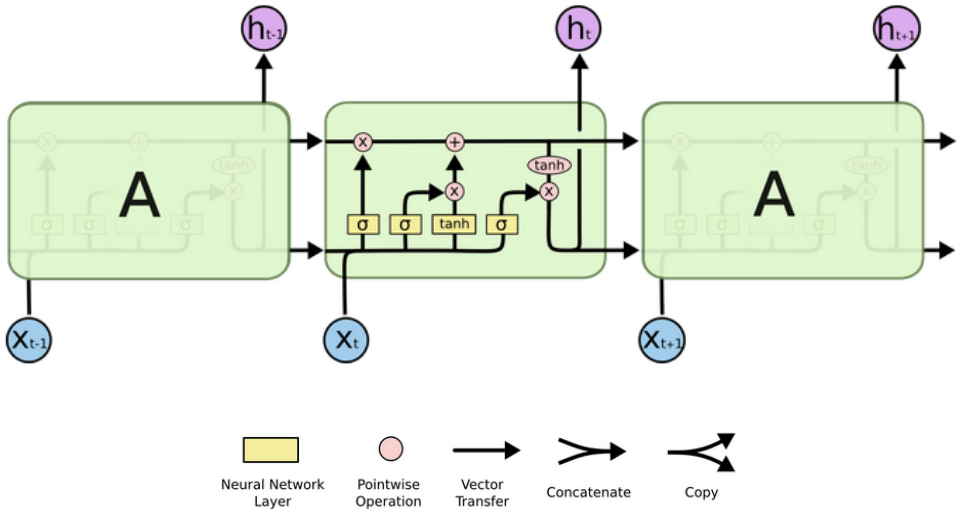

FIGURE 6.4: An LSTM module is composed of a repeating module (central block) that contains four interacting pieces associated with the cell state, input gate, forget gate and the output gate [130]. More details can be found in [130, 131].

sequence. The generated output at each time step is a result of both the current input and the hidden state. A visual representation of an RNN architecture is shown in Fig. 6.3, in which it can be seen that every element in the input $\vec{x}_t$ are processed individually and their outputs are connected, influencing each other.

One particular type of RNN is the Long Short-Term Memory (LSTM) network [132]. In Fig. 6.4 an LSTM layer and the schematic representation of its functioning is shown. The LSTM architecture was designed to overcome the vanishing gradient problem faced by traditional recurrent networks [133]. Traditional recurrent networks use backpropagation through time to learn from input sequences, meaning that the backpropagation is applied through all the time steps of the sequence (each one processed by a different layer) and the weights associated with all the layers are adjusted to minimize the cost function. This often leads to the gradients becoming very small or even zero when training over long sequences due to exponential decay caused by repeated multiplication performed using the chain rule during backpropagation in n sequential time steps, described by n layers.

LSTM are based on the concept of a cell state, C_t, that keeps some information and runs through the entire input sequence, facilitating the flow of information from one time step to the next. It enables the network to maintain and carry forward information over long stretches of time, allowing for the capture of patterns and context in the data. The distinguishing feature of LSTMs is the incorporation of gates, which are mechanisms that regulate the information flow within the cell state. These gates are designed to control what information is remembered, what new information is added, and what output is produced at each time step. The three types of gates in an LSTM: The forget gate, f_t, the input gate, i_t, and the output gate, o_t. The forget gate determines what not to retain from the previous cell state based on certain criteria, the input gate decides what new information should be added into memory cells, and the output gate generates the final output based on the updated cell state and hidden state. More details can be found in [130, 131]. This design allows LSTMs to better remember past events for longer periods than regular RNNs without suffering from vanishing gradients problems.

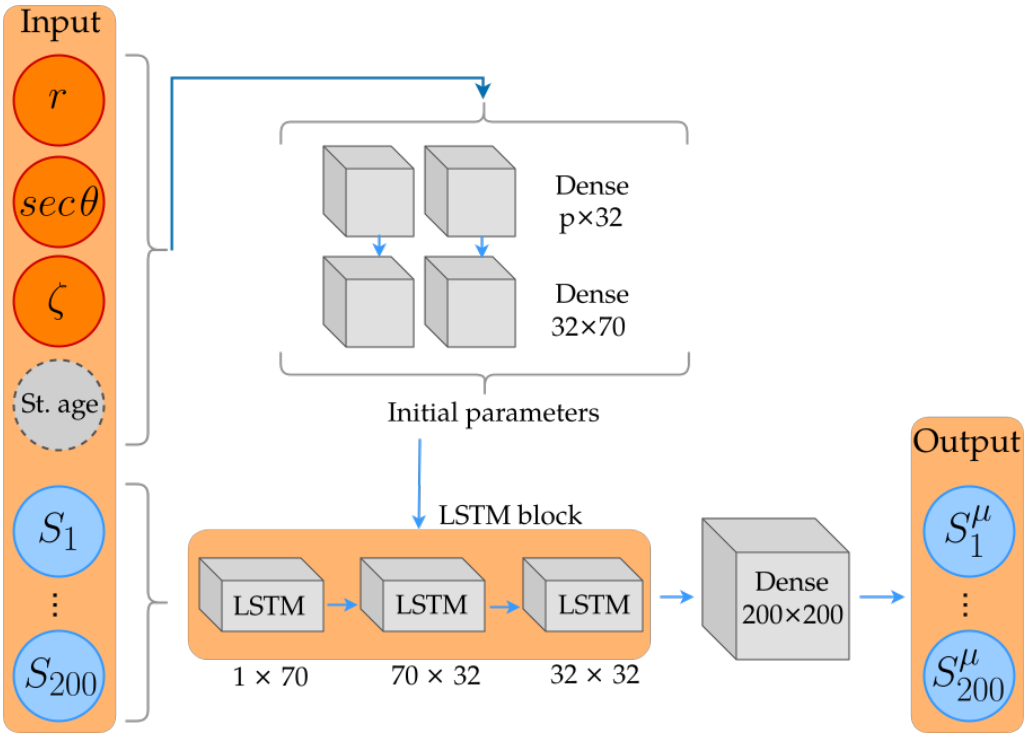

FIGURE 6.5: Schema of the network employed to extract the muonic signal. The different blocks, Dense and LSTM, can be observed, as well as the inputs and the output. In the Dense block, p represents the number of features used. See text for more details about the functioning of the model. Adapted from [131].

6.4 Temporal shape prediction of the muonic signal

ML methods, described in the previous paragraphs, have been employed in Auger to gain more knowledge and extract relevant information from the SD. The Collaboration published results [53, 134] on the capabilities of Deep Learning models to estimate X_{max} and N_{μ} from air shower events collected by the SD, allowing in this way the possibility to perform composition studies using the surface detector of Auger. The use of the SD could dramatically increase the statistics to perform mass composition analysis. In particular, the model presented in [131, 134] was designed to learn how to extract the time-trace of muons from the total signal recorded in each SD station, since the latter is the convolution of all the particles entering the station and, thus, it is not possible to directly obtain the number of muons at the ground using only WCDs.

These models are trained on simulations of air showers as well as of the detector. However, as seen in the previous chapters, the simulation framework does not take into account aging effects, that are directly affecting the signals time-trace in data. The datasets used to train the networks have a great importance, since these algorithms require a very good matching between data and simulations. In this work we used a similar approach of [131, 134], applying changes to the previous architecture, and we used the new SD time-dependent simulations to have a better description of the SD, assessing the impact and possible improvements to the models when the long term perfomances of the array are included.

6.4.1 Architecture

The architecture of the DNN designed for the extraction of the muon signal from the total one measured in each station, is based on two main components: An LSTM block and a Dense block. The first contains three LSTM networks connected to each other and used to learn the temporal pattern of the trace, while the latter is used to compute the parameters to initialize the LSTM with, based on the chosen observables related to the shower and the station. More specifically, the distance of the station to the reconstructed shower core, r, and the secant of the reconstructed arrival angle of the shower, $sec\theta$, are used to inform the network; These observables have been seen to improve the perfomance of the network [131], since they contain information about the attenuation in the atmosphere and this can help the network to predict better the muonic component. The architecture has been modified by adding the azimuth angle of the station on the shower plane, ζ, to the input observables of the Dense block. This choice of adding a new variable arises from the fact that signal shapes are influenced by the station's position on the shower plane, as seen for the risetime Chapter 2 and for the *twin showers* Chapter 4. Indeed, at different azimuth angles, the traversed atmosphere of the secondary particles is different, producing asymmetries in the traces.

The output of the Dense Block is used as one of the inputs of the LSTM block. The second, and main, input is the first 200 bins ($S_1, ..., S_{200}$) of the trace of the PMT-averaged signal recorded in the station. The lenght of the sequence has been chosen to reduce the input parameters and it contains the most relevant information of the signal. The vast majority of events contains 99% of their muonic signal in that timespan [131]. The LSTM block produces 70, 32 and 32 sequences of 200 elements each in the first, second and last layer, respectively. The last sequence is then passed through a final Dense layer, giving the final output that represents the 200 bins of the muonic time trace. The schema of the network is displayed in Fig. 6.5. The architecture's design was obtained through an optimization process based on the use of genetic algorithms by the work in [135].

An almost identical architecture has been used to train the model using aging simulations. In that case, in order to inform the network about this additional feature, we included the age of the station in the inputs fed to the Dense block, since this observable correlates with the loss of light in the tanks. For the two models, the number of trainable parameters amount to 87 276 and 87 340, for the standard network and the network including the station's age, respectively.

6.4.2 Data selection

The training of the network requires high-quality simulated traces, thus cuts were applied to simulations. The simulations library is the one described in Chapter 4, consisting of four different primaries with $\theta < 65^\circ$ and energies between $10^{18.5}$ eV and $10^{20.2}$ eV, reconstructed in two different simulations configurations (with and without the aging) for a total amount of $\approx$ 900000 reconstructed showers. Part of the selection is done at the event-level, by requiring a 6T5 trigger and a converged fit for the LDF. At the station-level, the signal obtained through the evaluation of the fitted LDF at the station distance must be greater than 5 VEM: $\mathrm{LDF}(r_{\mathrm{station}}) > 5$ VEM. Compared to the previous analysis [131], this cut excludes stations with upward fluctuations on their measured signal. In this work, stations with signs of High Gain (HG) channel saturation were also included in the selection, since in these cases

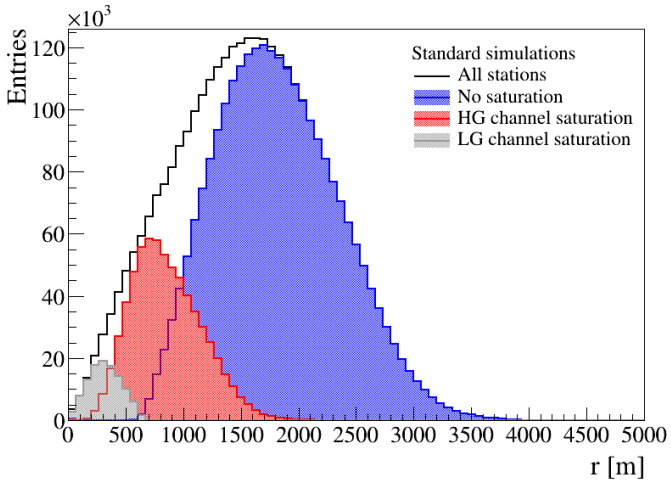

FIGURE 6.6: Stations distributions as a function of the distance to the shower core. Stations with different saturations are shown with different colors: No saturation (blue), HG sat. (red) and LG sat. (gray).

	Aging SD		**Standard SD**	
Quality cuts	Signals	ϵ (%)	Signals	ϵ (%)
Total traces	6 471 059	100.00	3 312 985	100.00
LDF fit	6 468 509	99.96	3 312 069	99.97
LDF(r_{station}) $>$ 5 VEM	5 686 455	87.88	2 883 164	87.02
No LG saturation	5 472 296	84.57	2 772 814	83.70
6T5 trigger	5 444 252	84.13	2 761 088	83.34

TABLE 6.1: Number of simulated traces after each selection cut, together with the cut efficiency.

the total trace is recovered from the Low Gain channel. The inclusion of HG saturated traces enables the analysis to explore a region closer to the shower core and increase significantly the statistics for $r < 1000$ m, as it can be seen in the distribution of the station as a function of the distance to the shower core, Fig. 6.6, for different types of saturation: Non-saturated traces' distribution (blue) peaks with 120 000 entries around 1700 m and the number decrease to ≈40 000 at 1000 m; traces with saturated high channel (red) show a bell-shaped distribution with mean around 600 m and represent the 20% of the total number of signals. Stations showing signals saturated in the Low-Gain channel (gray), being around ≈ 3% of the total number, are excluded from the selection.

The cuts affect differently the stations' distributions: For example, removing stations with LDF(r_{station}) $<$ 5 VEM impacts more stations that are far from the shower core, as expected, since their signals are smaller. This effect is shown in Fig. 6.7, where it can be seen that the LDF cut (displayed as a continuous line) reduces the selection efficiency after 1300 m, being in the range $90 - 70\%$ for 1500 m $< r <$ 2500 m and dropping steeply to 0 after that. It can also be noticed that this cut has a stronger effect on more inclined showers. In the same figure, the effect of the removal of LG saturated stations (displayed with filled symbols) is present uniquely below 500 m and affects in a similar way the showers with different zenith angles. The selection

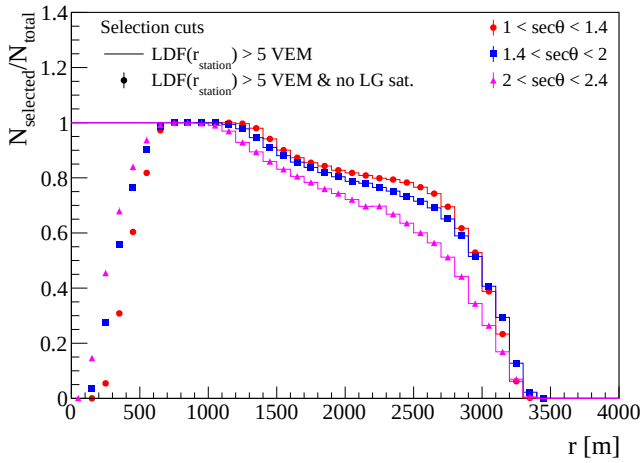

FIGURE 6.7: Selection efficiency for the signal-cut and the exclusion of LG saturated stations as a function of sec θ and distance to the shower core.

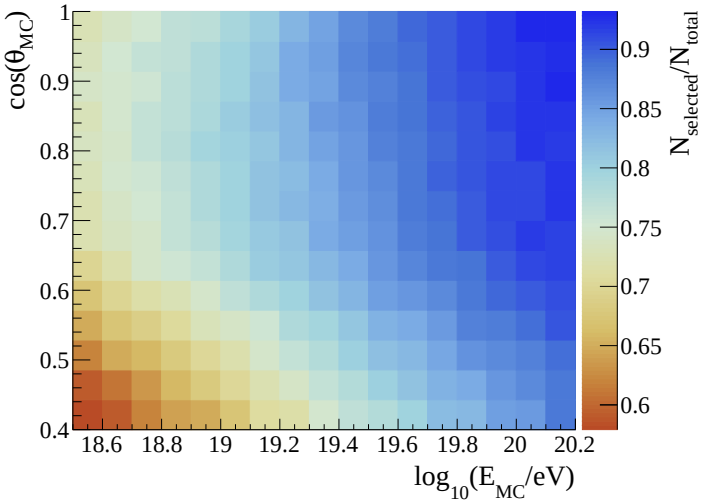

FIGURE 6.8: Selection efficiency as a function of the true zenith, θ_{MC}, angle and energy of primary particle, E_{MC}.

efficiency of the mentioned cuts and the absolute numbers of the traces are shown in Table 6.2, where it is shown that the available traces amount at ≈5.5 millions and 2.8 millions for *agingSD* and *standard* simulations.

When looking at the efficiency of all the cuts combined as a function of the features of the primary particle, Fig. 6.8, it can be noticed how the selection affects more showers with lower energies and larger zenith angles, with the number of survived traces being below $\approx$ 70% for $\theta_{MC} > 50^{\circ}$ and $E_{\mathrm{MC}} < 10\,\mathrm{EeV}$. In this work we extended the zenith angle range up to $\theta_{MC} = 65^{\circ}$.

6.4.3 Training

The selected simulated traces are split randomly in three datasets, in order to train the network and monitor the quality of the training process. The first split creates two subsamples, training-validation and test, with ratios $80\% - 20\%$ in order to have the majority of samples for the training. The first subsample is further divide, again with the $80\% - 20\%$ rule, in train and validation sets. When randomly separating

Simulations subsamples		
Dataset	Aging SD	Standard SD
Train	3 483 054	1 766 406
Validation	870 787	441 612
Test	1 090 411	553 070

TABLE 6.2: Number of simulated traces in each subsamples for the two simulation modes.

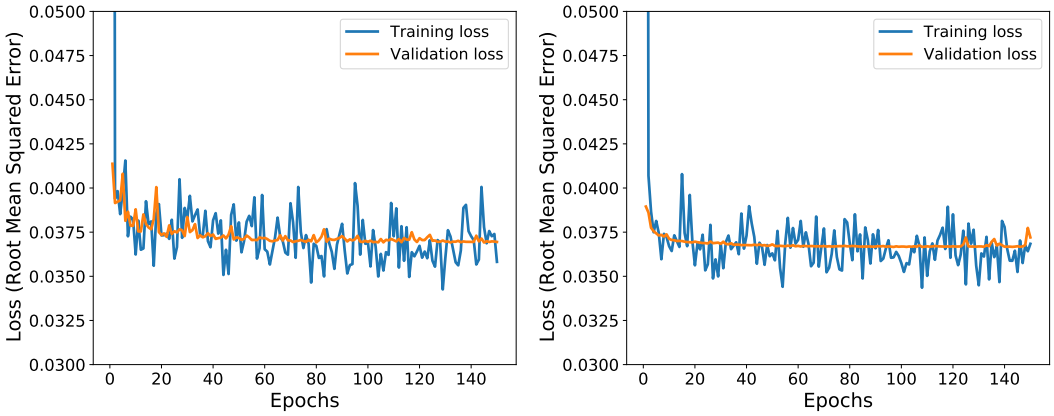

(a) Standard SD (b) Aging SD

FIGURE 6.9: Loss as a function of the number of epochs.

the stations in the samples, the split was performed at the event-level, avoiding that stations belonging to the same event were separated in the samples. In this way, in the test set after the training, events mantained their integrity, station-wise. While performing the split, specific attention has been given to avoid any distortion in the distribution of the traces between the samples. Each simulations dataset, *standard* and *agingSD*, have been separed in these way, as shown in Table 6.2: The training sets have, in total $\approx$ 3.5 millions aging traces and $\approx$ 1.8 millions standard traces, while the test sets range around 1 million and 550 000 traces in the two cases.

Before feeding the samples to the network, some preprocessing of the samples is necessary. To be more specific, all the observables used as inputs to the Dense block have been normalized in order to have, for each feature, a distribution with mean equals to 0 and standard deviation equals to 1. The traces have been rescaled too, with each trace divided by its maximum bin value and obtaining, in this way, traces comprised between 0 and 1. The scaling factor used for every single trace is then re-used to scale back their relative output, giving the predicted trace. This step helps the gradient descent algorithm to reach the minimum faster and can also help, when the network is applied to data, to minimize the differences between different calibrations.

The network is trained by comparing the predicted muon signal with the true one, present in simulations. The loss function for each trace is defined as the mean square error between the true bin values at time t, S_t^μ, and the predicted ones, represented with the symbol $\widehat{S_t^\mu}$, for the muon trace, as follows:

$$J = \frac{1}{200} \sum_{t=1}^{200} \left(\widehat{S_t^\mu} - S_t^\mu \right)^2 \tag{6.4}$$

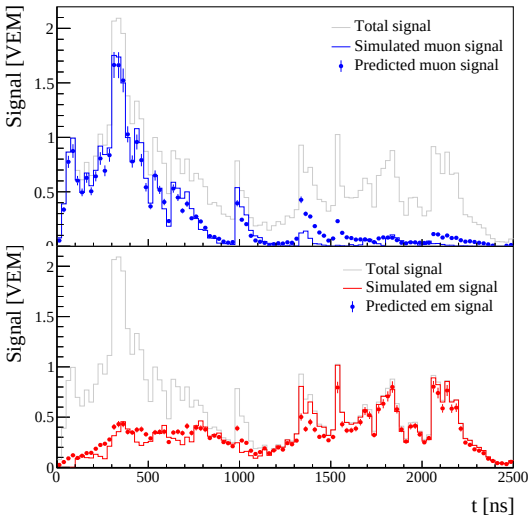

FIGURE 6.10: Top: Predicted muon signal trace (blue dots) from the total trace (gray line) and compared to the original muon trace (blue line). Bottom: Same comparison but for the electromagnetic component (red). The simulated trace is obtained from a station at $r = 1400\,\mathrm{m}$ from the core of a shower with $\log_{10}(E_{\mathrm{MC}}/\mathrm{eV}) = 19.95$ and $\theta_{MC} = 34°$.

The training has been performed thanks to CECI [136], on the cluster Dragon2, using a NVidia Tesla V100 GPU. We used 150 epochs with 512 batches; For the hyperparameters we chose a fixed learning rate of 10^{-3} and the ADAM optimizer. The *standard training* consisted in training the network using standard simulations and not including the stations' age in the input features and lasted around 2.6 h, while the *aging SD training*, including the stations' age and using the aging simulations, lasted around 6.8 h. The trend of the loss as a function of the epochs for the two trainings is displayed in Fig. 6.9, showing the loss decreasing as the number of epochs increases. The similar behaviour and absolute values of the training and validation loss confirm that the network does not show signs of over(under)fitting. The preprocessing of data was implemented in Python3.9 [137] (using the libraries numpy, scipy and pandas) and ROOT [138], while the network was built and trained using PyTorch1.13.1 [139].

6.5 Performance

An example of a predicted muon trace can be seen in Fig. 6.10, top panel: the continuous line shows the true muon trace, while the blue dots are the predictions in each time bin, while the total signal is displayed in light gray. Uncertainties are defined as the errors in the bin and the total lenght trace has been shortened to display better the results. It can be noticed that the trace is well reproduced, with the majority of the muon signal being properly reconstructed. Since the electromagnetic and the muonic components are the main contributions to the total signal, the electromagnetic trace can be obtained as a difference between the total and the muonic signal, shown in Fig. 6.10, bottom panel, in red.

To evaluate the perfomance of the network, the integrated muon signal, defined as $S^{\mu} = \sum_{t=1}^{200} S_t^{\mu}$, is used. This observables is related to the number of muons that reach the ground [11] and, because of this, convey a great importante for mass composition studies.

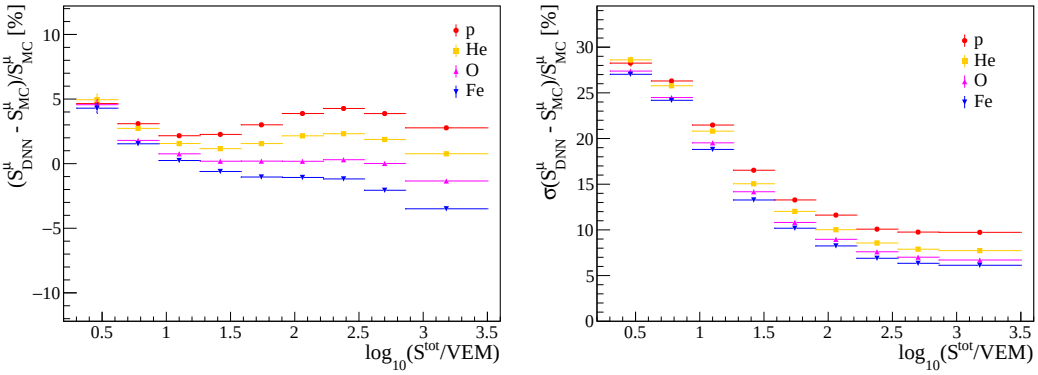

FIGURE 6.11: Perfomances of the standard training on the standard set. Bias (left) and resolution (right) of predicted muon signal as a function of the total signal for different primaries. Standard test set predicted with *standard training*.

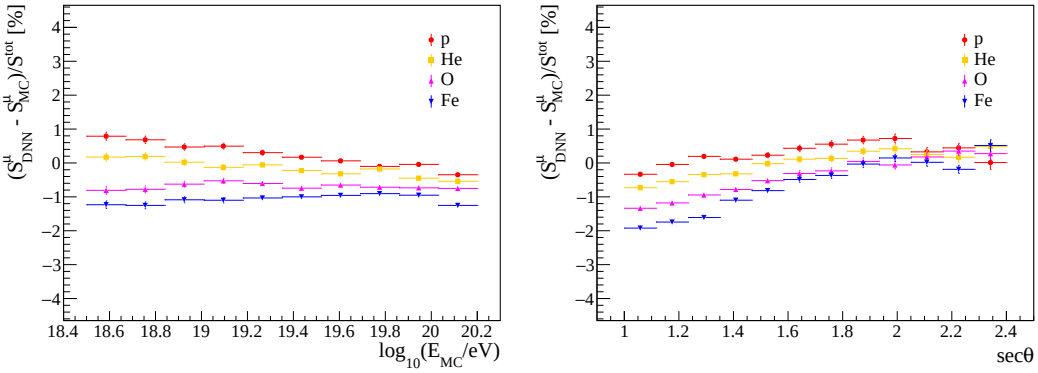

FIGURE 6.12: Bias of predicted muon signals as a function of the primary energy (left) and the zenith angle (right). Standard training on standard set.

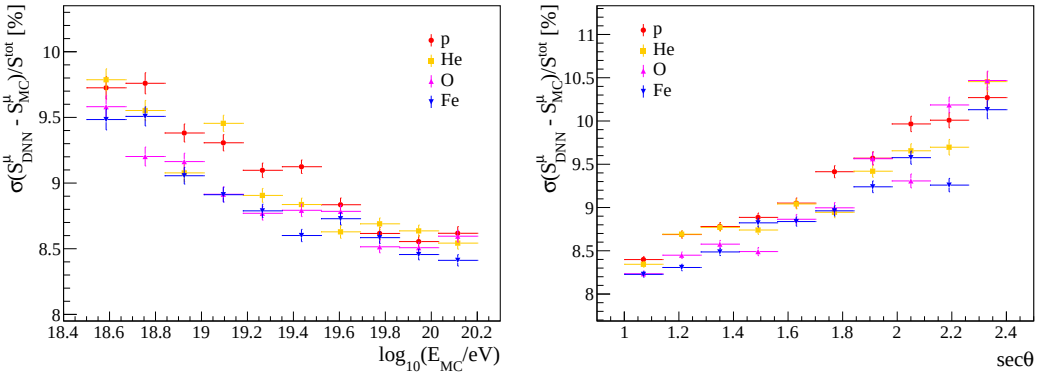

FIGURE 6.13: Resolution of predicted muon signals as a function of the primary energy (left) and the zenith angle (right). Standard training on standard set.

In this part of the study, we present the results obtained on the standard test set when the muon traces are reconstructed using the *standard training*. In the next paragraphs, the aging effect and the *aging SD training* will be discussed. The predicted, S^{μ}_{DNN}, and the true muon signal, S^{μ}_{MC}, are compared to evaluate the bias and resolution of the predictions. The results are shown in Fig. 6.11, where it can be seen

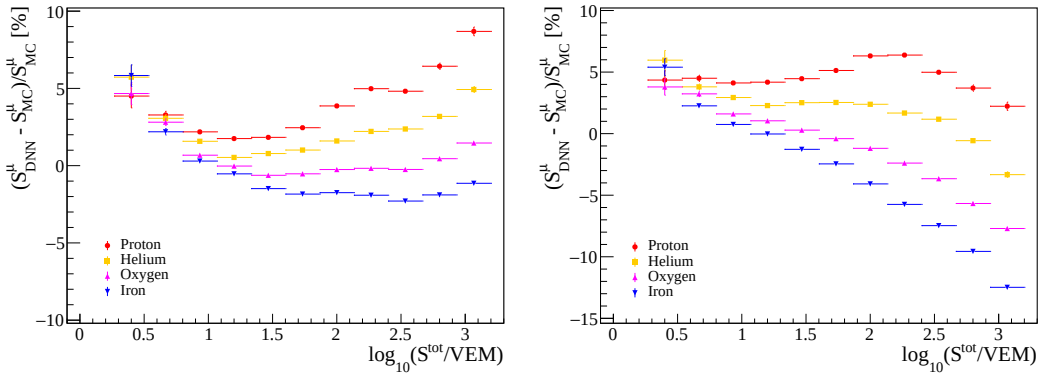

(a) DNN trained without ζ.

(b) DNN trained without ζ and r.

FIGURE 6.14: Bias of the standard set for two training configurations. More details in the text.

that the bias for all the primaries as a function of the total signal, left plot, is between -5% and 5%. The maximum difference between primaries is $\approx$ 6%, with heavier ones having a negative bias at larger energies, while the lighter ones having a positive one. It becomes smaller from small signals to higher signals, up to $\approx$ 10 VEM, where the biases for the primaries start to deviate between each other, with heavier elements being stable around 0 and -2% and lighter elements slightly increasing towards positive biases. The resolution, instead, show a similar trend for all the primaries, improving from $\approx$ 27% at 3 VEM to $\approx$ 6% at 100 VEM, with an almost constant difference of around 4% between light and heavy nuclei. These results are in agreement with the previous study [140], as it can be appreciated more from the figures in Figs. 6.12 and 6.13, where bias and resolution are analyzed as a function of the energy and arrival direction of the primary particle.

6.5.1 Tests on the capability of the model

To investigate further the possibilities offered by the DNN (comparing also the effect of the new changes) and test its limits, several crosschecks were performed.

Firstly, we removed the azimuth angle information during the training, to have a more direct comparison with previous results. As it can be seen in Fig. 6.14, left, the bias increases at the highest signals, especially for light nuclei. The stations with higher signals are the one closer to the shower core and that often show signs of saturation in the High Gain channel. This effect was not present in the previous analysis since these stations were excluded from the sample. The inclusion of the azimuth angle of the station in the shower plane, ζ, mitigates the increase in the bias, as shown in Fig. 6.11, left.

The network was then trained without the station's distance to the shower axis, r, and ζ, to verify the limits at which it is possible to extract a reliable muon trace. The results are shown in Fig. 6.14, right, in which the bias gets worse as the total signal increases, reaching the level of -13% in the case of iron. The exclusion of important information about the shower and the station leads to a difficulty for the network to predict in an accurate way the muonic time signal.

An additional test was performed to assess if the network is able to predict outside of the phase-space of the training dataset. In order to do that, the network was trained (this time including all the relevant station and shower information) only on protons and the predictions were performed on irons. The results are shown

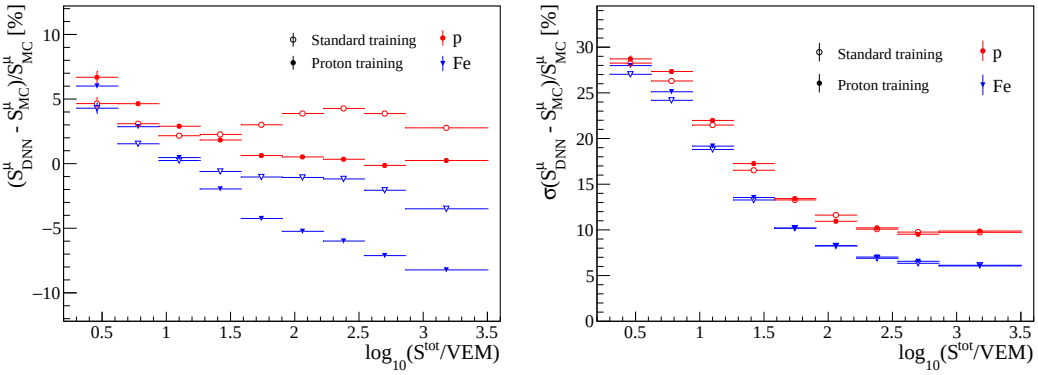

FIGURE 6.15: Perfomance of the DNN trained using only protons from the standard set. Left: Bias for proton and iron. Right: Resolution for proton and iron. More details in the text.

in Fig. 6.15: Left plot shows that irons can be reconstructed with a bias of $\approx -5\%$ up to signals of 100 VEM, while at the highest signals reaches level of -9%. The resolution, instead, shows no significant changes compared to the training using all the primaries. This last crosscheck were performed to verify that the network's predictions are not introducing extreme biases due to the training, since the application of the network to data will face the well-known discrepancy between data and simulations regarding the number of muons.

6.6 Aging effects

The loss of light in the WCDs can cause a change in the time trace of the signal over the years, as previously seen. Since the DNN is trained on simulated traces, when predicting the muon signal on data this effect could introduce a bias. Using the simulations library built on the aging model and validated on high-level observables, the network was trained with the two different modes, as explained before. For the predictions, three different datasets were obtained: Standard set and aging set when the DNN was trained on standard simulated traces and the *standard* and *agingSD* test sets were used for the predictions, named $standard_{\text{std}}$ and $agingSD_{\text{std}}$ respectively, an aging SD set when the training was perfomed using simulations including the aging and informing the network about the age of the station, named $agingSD_{age}$. The first set, $standard_{\text{std}}$, is used as a benchmark to assess the perfomance of the DNN in the case of no aging, the second one, $agingSD_{\text{std}}$, is utilized to study the bias introduce in the network when aging appears in the traces and the last one, $agingSD_{age}$, serves as a validation of the method.

While the bias displays a constant behaviour over the years for $standard_{\text{std}}$, grey filled point in Fig. 6.16(c) for both proton and iron, as expected, the $agingSD_{\text{std}}$ shows an increase of 2% bias over time, for proton (red) and iron (blue) represented with open symbols. The addition of the knowledge about the time spent on the field by the station, is able to remove this dependence, as observed for $agingSD_{age}$ (shown with filled red and blue points in Fig. 6.16(c)). However, a small worsening of the bias is observed for protons, coming especially from stations with signals lower than 30 VEM, Fig. 6.16(b), while for $S^{tot} > 100$ VEM, Fig. 6.16(b), the *aging training* mitigates well the aging effects. The cause of the observed worsening could be related to the added complexity of the array introduced in the model, but this is not yet

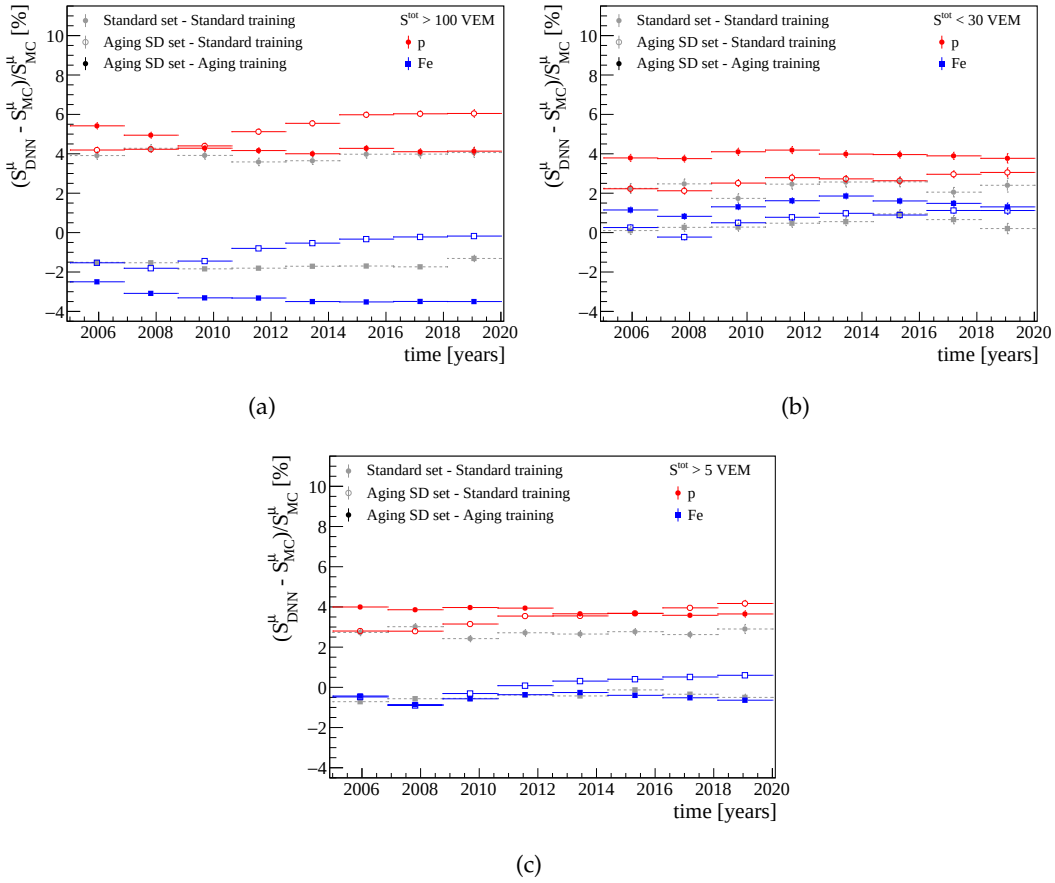

FIGURE 6.16: Bias of predicted muon signals for different total signal's thresholds as a function of time. Several samples and trainings are shown. See text for more details.

understood. The resolution of the predicted muon signals as a function of time is displayed in Fig. 6.17 and shows that the aging effects have a small impact (less than 1%), in both signal ranges (larger than 100 VEM and less than 30 VEM). The same behaviour of bias and resolution is observed when studying these two variables as a function of the stations' age, as shown in Appendix G.

The $agingSD_{age}$ bias and resolution as functions of the total signal are compatible with the ones obtained for the other two datasets, as shown in Fig. 6.18, with the additional property that the time-dependency has been removed. Thus, this model improve upon predicting the muon traces from data.

Another dependency that is also possible to study, is the behaviour of the bias in the muon signal prediction as a function of the distance to shower core, obtained by dividing the true muonic signal by the predicted one. For the small reconstructed energy bin considered in Fig. 6.19, $18.97 < \log_{10}(E/eV) < 19.15$, the bias is below 5% for $500\,m < r_{rec} < 1500\,m$ in the case of vertical (top left) and inclined shower (top right), where r_{rec} is the distance of the station to the reconstructed shower core. Stations at distances below 500 m are not considered, since that region is too close to the core and other effects could distort the prediction. The bottom left and right plots in Fig. 6.19 show the bias as a function of the distance for the electromagnetic signal, where the electromagnetic signal is calculated as the difference between the total and the muonic signals.

When considering the distance of the stations to the true shower axis, the effect of the core reconstruction uncertainty can be extracted. Comparing the trend of true

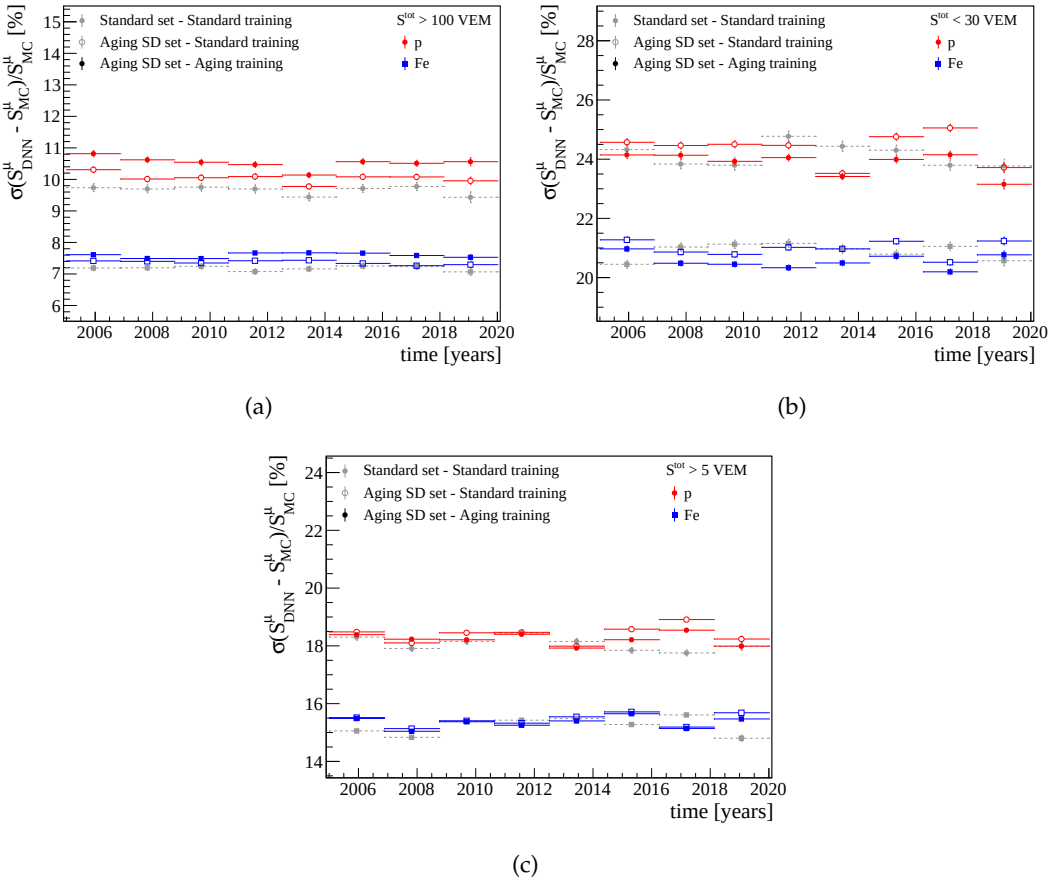

FIGURE 6.17: Resolution of predicted muon signals for different total signal's thresholds as a function of time. Several samples and trainings are shown. See text for more details.

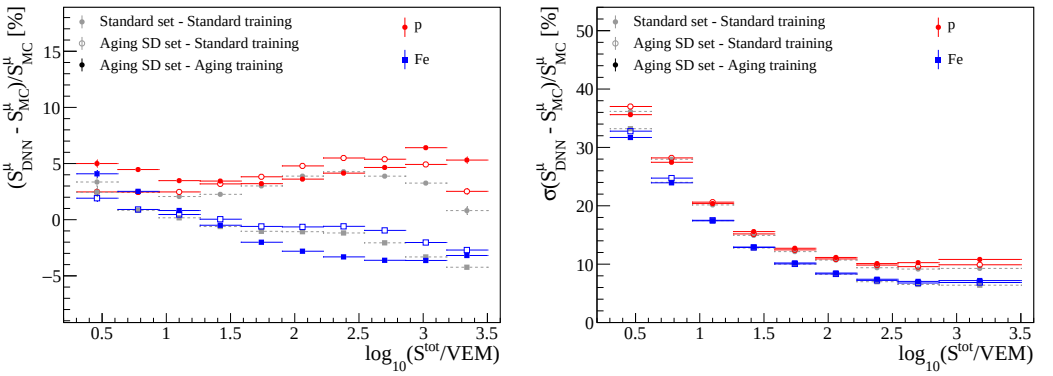

FIGURE 6.18: Bias and resolution of predicted muon signals as a function of the total signal for standard simulations, aging simulations and two different types of training. More details can be found in the text.

muon signal over the true distance ($S^{\mu}_{MC}(r_{MC})$) with the predicted one as a function of the reconstructed distance ($S^{\mu}_{DNN}(r_{rec})$), their ratio shows, in addition to the intrisic bias of the DNN model, the bias introduced by the core uncertainty. It can be observed, in Fig. 6.20, that the total bias as a function of the distance is less than 10% both for vertical and inclined events and for light and heavy nuclei.

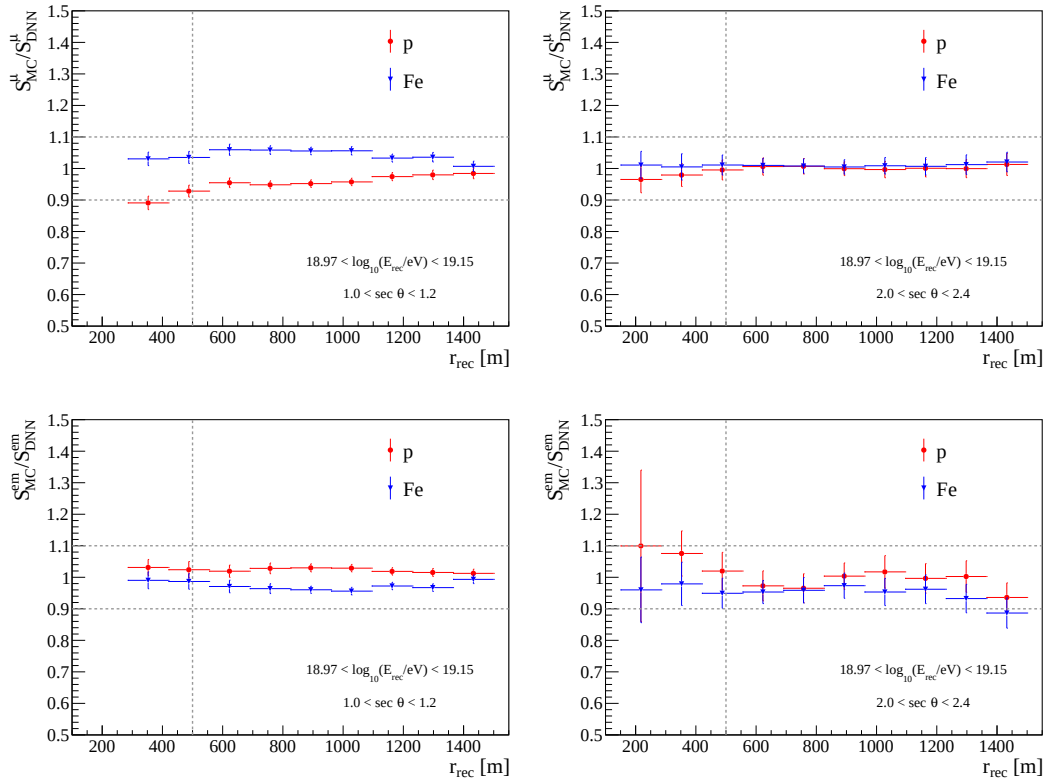

FIGURE 6.19: Bias as a function of the distance of the station to the reconstructed shower core.

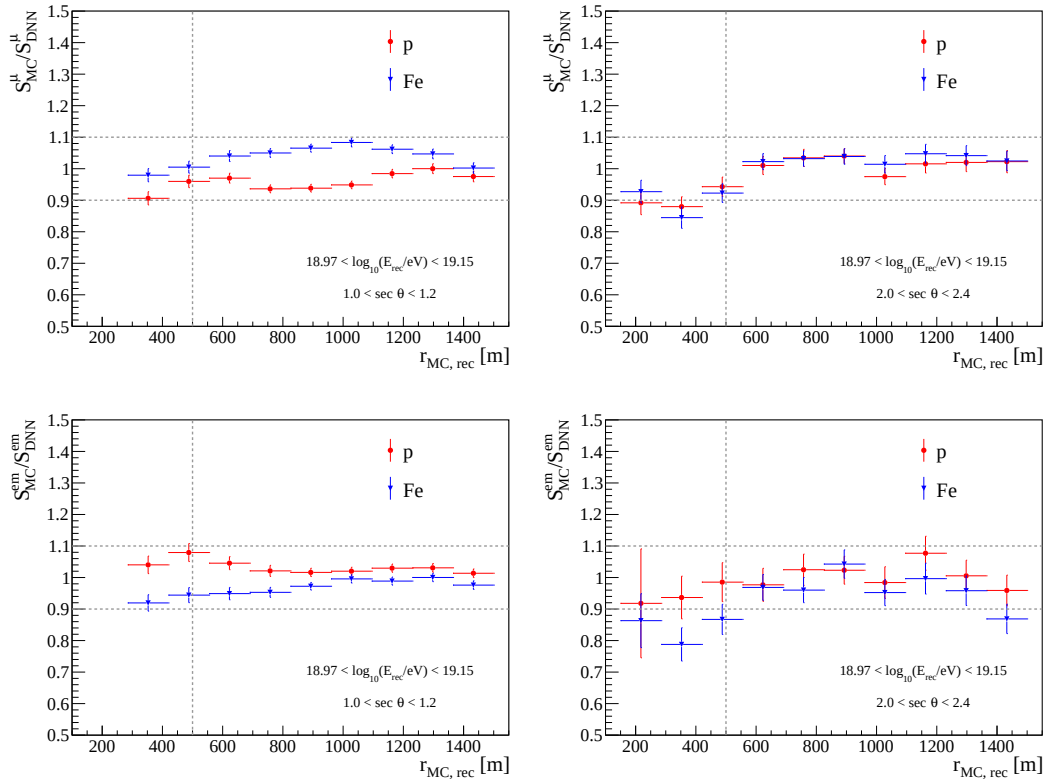

FIGURE 6.20: Bias as a function of the distance of the station to the reconstructed or true shower core.

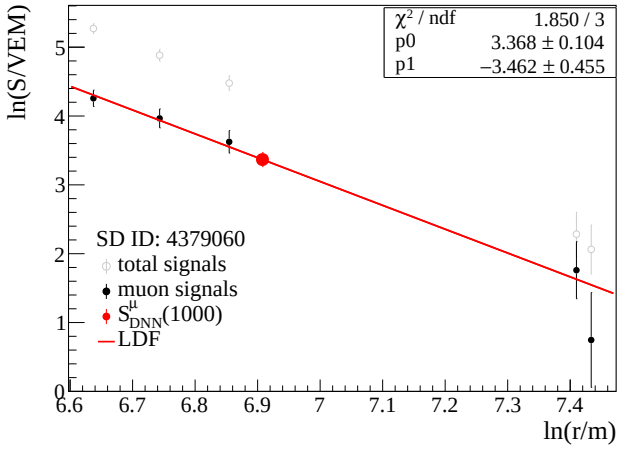

FIGURE 6.21: Muonic lateral distribution function for a specific event in the SD dataset. Black dots represent the muonic signals, while open light-gray symbols are the total signals. The red dot shows the muonic shower size estimator, $S_\mu(1000)$. The fit function is shown in red.

6.7 Reconstructing the muon signal from data

Having assessed the perfomances of the network and the effect caused in the reconstructed muon signal due to the aging, the DNN model was applied to data to extract the muonic contribution from the total measured signals. The ICRC2019 datasets, produced with Offline v3r99p2, for SD and golden hybrid events were used, to predict $S^\mu_{\rm DNN}$ for a total number of traces equals to 1284464 (SD) and 18683 (Hybrid). These traces were selected with the same selection criteria employed for simulations, as described in Section 6.4.2.

The muon lateral distribution for each event, i.e. the muon signals $S^\mu_{\rm DNN}$ of the candidate stations as a function of the distance to the shower axis r, was then obtained by grouping together the traces belonging to the same event. An example can be seen in Fig. 6.21 for an almost vertical shower ($\theta_{\rm SD} \approx 15^\circ$) with $E_{\rm SD} \approx 13$ EeV, where the black dots show the predicted muon signal for the candidate stations, while the gray open symbols represent the total signals measured with the SD, shown for comparison. The lateral distribution of muons for each event is fitted with a linear function in log-log scale, red line in Fig. 6.21, and, the muon signal, S^μ_{DNN} is obtained as a fitted parameter of the function:

$$S^\mu_r = S^\mu_{\rm ref}\left(\frac{r}{r_{\rm ref}}\right)^\alpha \tag{6.5}$$

The fit was perfomed at different distances, $r_{\rm ref}$, to obtain the muon signal for different r. The fit was performed on 283 036 SD events, with a $\approx$ 5% reduction to 268 293 events in the final stage, after applying quality cuts on the fit results: Minimum 3 stations have to be present in the reconstruction, the convergence of the fit is required and the parameter α must be negative and > -5. Fit results with negative or extremely high muon signals ($>$ 10000 VEM) were discarded. For the golden hybrid events, the reconstructed events amounted to 3175 after cuts (3262 before cuts, 2.7% rejection).

The same procedure has been applied to the predicted signals in the test sets of simulations. The precaution of performing the splitting in train-validation-test sets

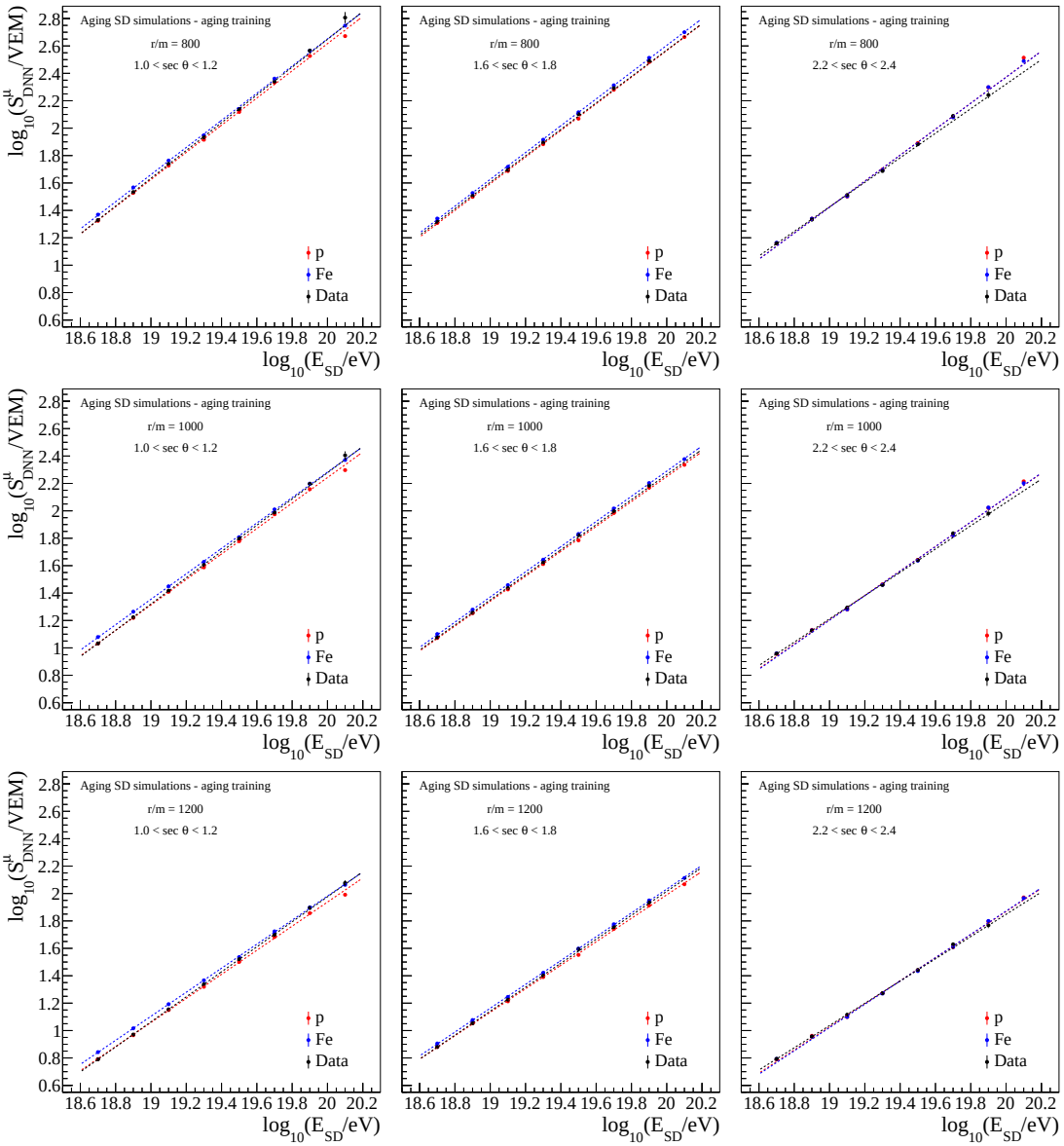

FIGURE 6.22: Muon signal as a function of the energy for different distances to the shower axis (800, 1000 and 1200 m), and different zenith ranges.

at the event level, indeed, allowed to preserve the integrity of the events and fit an LDF to the muon signals.

6.7.1 Energy dependence

The parametrization of the lateral profile provide a robust estimation of the muon signal for each event, allowing a more accurate study of the muon component in air showers. In this section, the analysis was performed using the SD dataset, in order to have a large statistics. The muon signal increases with the energy and with the mass of the primary particle, as modeled in Section 1.1.3, Eq. (1.7). This behaviour is reproduced in the results shown in Fig. 6.22, where the logarithm of S_μ is displayed as a function of the logarithm of the reconstructed energy E_{SD} for proton (red), iron (blue) and data (black) for different zenith angles (from vertical, left, to inclined,

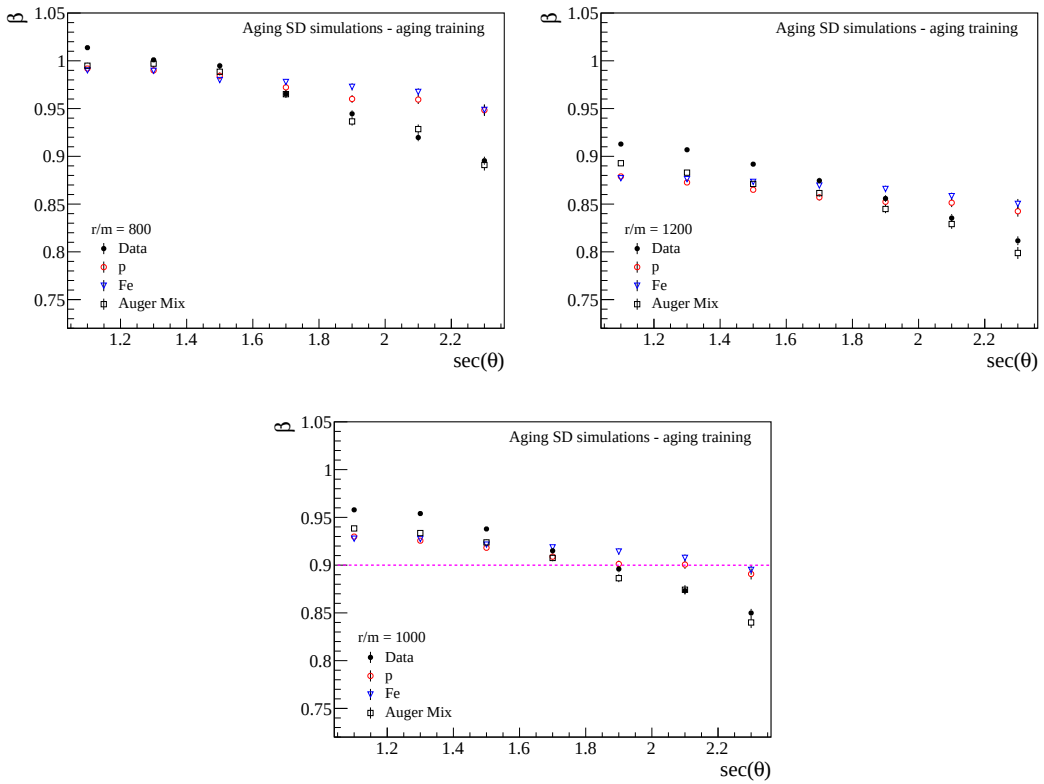

FIGURE 6.23: β parameter as a function of the zenith angle for data and simulations, including AugerMix; three different distances.

right) and different distances to the shower core (800, 1000, 1200 m from top to bottom). Distances closer or further from the core are avoided in this preliminary study, to avoid unwanted biases arising from the simplified LDF fit procedure and to allow that the obtained signals is between two candidate stations. The separation between proton and iron at higher zenith angles becomes smaller since, in this case, $S(1000)$ is mainly muonic, thus E_{SD} is based on S^{μ}, which creates a degeneracy. For vertical shower, E_{SD} is related to the sum of E_{em} and E_{μ} and thus depends more on E_{em}.

It can already be noticed in the figure, that in each distance ranges and for different showers' inclinations, the slope for data is different compared to simulations. The slope, β, is another important parameter in the description of the development of the hadronic shower, as explained in Section 1.1.3, as it relates with the fraction of charged pions over the total, or, more in general, the fraction of hadrons with a sufficient energy to re-interact rather than decay [141]. Due to this, it is sensitive to the hadronic interactions involved in the shower development. The trend of β as a function of the zenith angle, specifically secθ, Fig. 6.23, shows a dependency that is more prominent for data compared to simulations of pure primaries. When the information about the shower and the mass composition, AugerMix, are included in simulations, the slopes agree more at large zenith angles. For more vertical showers, however, β still shows a disagreement. The similar trend with the AugerMix and the difference with pure composition, is another indication through β of a mixed composition through the data. This zenith angle dependency is not expected, since the value of β for simulated muon signals as a function of the true energy of the primary is mostly constant over θ at ≈ 0.9, as shown by the magenta line in the case of β obtained at 1000 m. This points towards a bias that has to be investigated in

more details. The higher value of β for reconstructed proton and iron compared to pure simulations can also be associated with an energy bias of the SD energy, since it does not appear when S^{μ} is shown as a function of the true energy. As the E_{SD} is corrected for the zenith angle through the attenuation curve described in Section 1.3, a possible different attenuation in simulations with respect to data can also produce the described effect.

Another property of β that can be observed from this study is the dependence on the distance to the shower axis, with β decreasing further from the shower axis, due to the effect on muons at the different distances by the different phases of the shower development [141].

6.7.2 S^{μ} and X_{max}

The simultaneous study of the two mass sensitive variables [55, 60, 61], N^{μ} and X_{max}, has provided valuable information regarding the modeling of the shower development, in particular about the hadronic interactions, revealing a *muon deficit* in simulations, described in 1.1.3. The previous mentioned measurements were obtained with the use of very inclined showers, where the muonic component is dominant. Such a deficit has also been observed for the first time in vertical shower [131] by exploiting the capabilities of the DNN to extract the muon trace from the total trace and use S^{μ} as a proxy for the muon number. The DNN model that has been shown in this Chapter was based on a similar approach.

With the use of the golden hybrids events, the relation between S^{μ} and X_{max} can be studied, as it can be seen seen in the left plots of Fig. 6.24 and Fig. 6.25 (vertical, $\theta < 34^{\circ}$ and inclined, $54^{\circ} < \theta < 65^{\circ}$, respectively) at different distances for showers with energies $19 < \log_{10}(E/\mathrm{eV}) < 19.05$. In both figures, the statistical uncertainties are displayed as lines, while the errors represented by square brackets on the muon signal from data show the systematics due to the energy reconstruction, since a bias is present in the reconstructed SD energy, as shown in the previous chapter. In order to evaluate the systematics arising from the energy assignment, the uncertainties are estimated by evaluating the muon signals for energy ranges $\approx \pm 10\%$ around the energy bin under study: the upper error of the muon signal is obtained in the energy bin $19.05 < \log_{10}(E/\mathrm{eV}) < 19.1$, while the lower error by looking at the muon signal in the energy bin $18.95 < \log_{10}(E/\mathrm{eV}) < 19$. Systematic uncertainties on X_{max} are not shown, but are in the order of $\approx 6\,\mathrm{g\,cm^{-2}}$ [50]. However, systematic uncertainties on S_{μ} X_{max} need to be estimated in a more complete study.

The predictions for simulations are shown with filled colored symbols, while the AugerMix is represented with open symbols. The muon deficit has been verified, in particular for vertical showers, where is in agreement with the previous results [131]. It can be seen that the mean value of X_{max} is different between data and AugerMix. This could be due to a bias in the SD energy related to the muon deficit, since showers for data are selected in the chosen energy bin using their SD reconstructed energy, while simulations are selected based on their Monte Carlo energy.

Since the statistics of golden hybrids is limited, the dataset was enlarged with the values of the predicted X_{max} from SD events, obtained by another analysis, also based on Deep Learning [53], thus the observable is called here as $X_{\mathrm{max}}^{\mathrm{DNN}}$ [1]. In this way, the total dataset in which both $X_{\mathrm{max}}^{\mathrm{DNN}}$ and S_{DNN}^{μ} are present, contains 48 751 events, a factor larger than ten compared to the hybrid dataset. This increase strongly reduces the statistical uncertainties, as it can be noticed in both Fig. 6.24

[1] Courtesy of Jonas Glombitza

and Fig. 6.25, right plots. It also changes the mean value of the shower maximum for vertical event, shifting it by $\approx 20\,\mathrm{g/cm^2}$, from $\approx 747\,\mathrm{g/cm^2}$ to $\approx 767\,\mathrm{g/cm^2}$, for golden hybrid events and SD events, respectively. Also in this case, the muon deficit is present, confirming with a higher statistics what was previously found.

This difference of $\approx 20\,\mathrm{g/cm^2}$ in X_{max} between golden hybrid events and SD events in the case of vertical events provides a better agreement with the value obtained from the AugerMix, but the cause is not yet understood. A similar shift of $\approx 20\,\mathrm{g/cm^2}$ is observed between vertical and inclined golden hybrid events.

The results shown here are preliminary, assessing the capabilities of this study. Future studies could address the biases observed in this work and perform more detailed analysis using these new datasets enriched by two mass-sensitive observables. Moreover, a quantification of the observed discrepancy can be made.

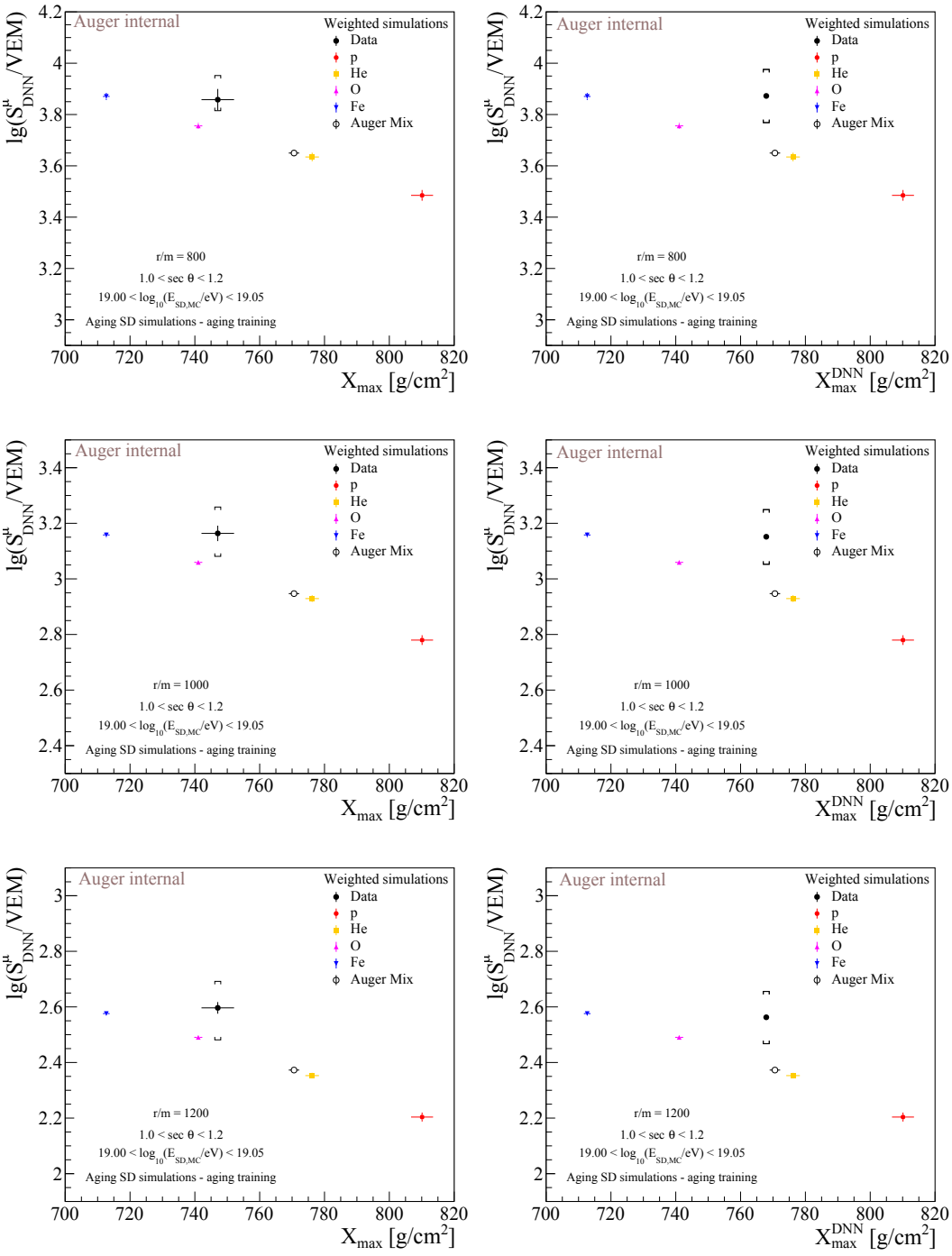

FIGURE 6.24: Vertical events. S^{μ} as a function of X_{max} for hybrid events (left) and SD events (right) at different distances (800, 1000, 1200 from top to bottom). Systematic uncertainties on X_{max} for the golden hybrid events are in the order of $\approx 6\,\mathrm{g\,cm^{-2}}$ [50]. Data are shown in black, AugerMix with open symbols and pure primaries simulations are colored. See text for more details.

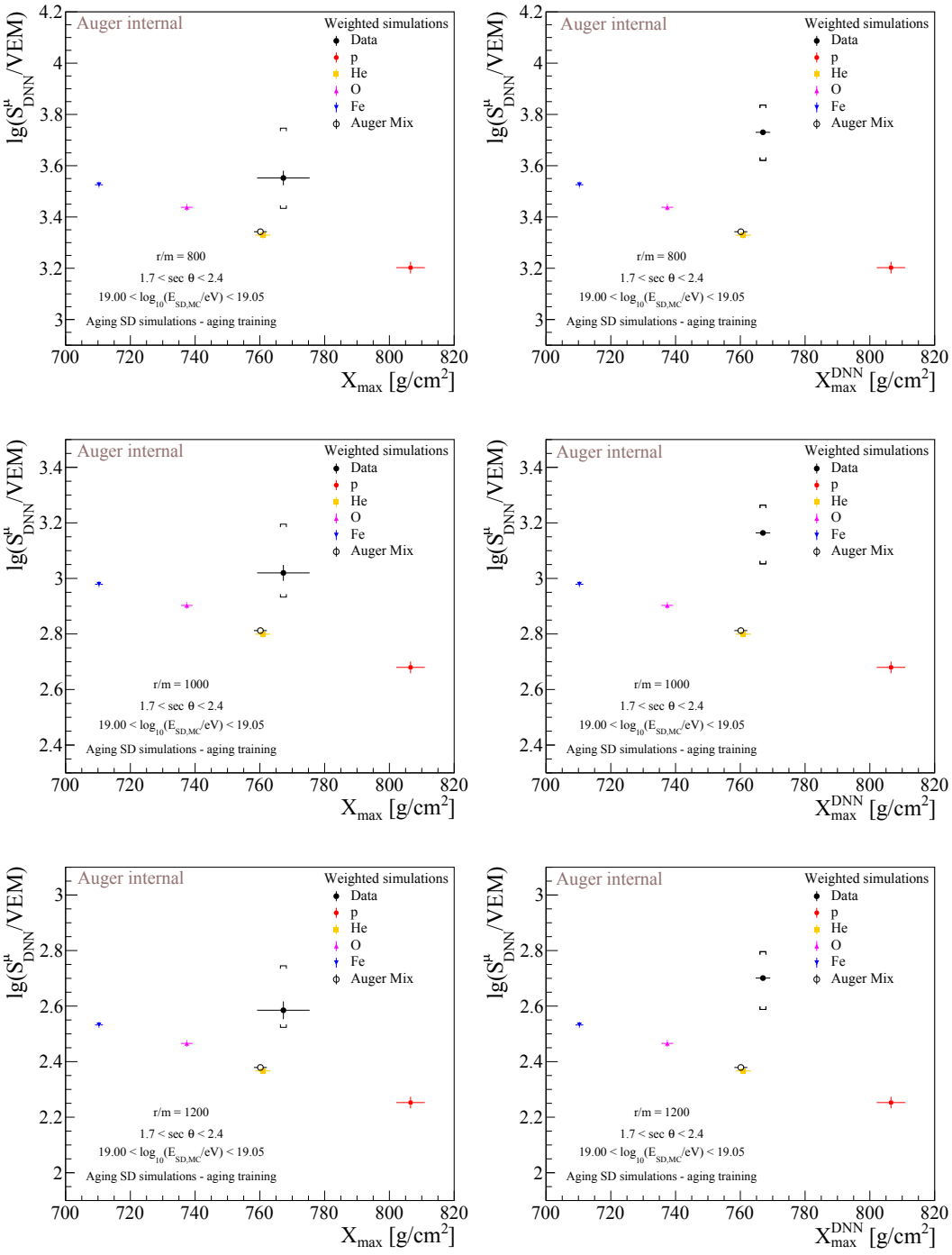

FIGURE 6.25: Inclined events. S^{μ} as a function of X_{max} for hybrid events (left) and SD events (right) at different distances (800, 1000, 1200 from top to bottom). Systematic uncertainties on X_{max} for the golden hybrid events are in the order of $\approx 6\,\mathrm{g\,cm^{-2}}$ [50]. Data are shown in black, AugerMix with open symbols and pure primaries simulations are colored. See text for more details.

Summary and conclusions

UHECRs are the most energetic particles known today in the Universe, and the study of their properties can shed light on some of the mysteries revolving around their sources, the production and acceleration mechanisms and the propagation through magnetic fields during their journey to Earth. The Pierre Auger Observatory is the largest cosmic ray observatory in the world and has been collecting data for the last 20 years.

Due to this long operation period, an important task consists of monitoring the array's performance to ensure high-quality data collection. Indeed, the measured signal in the tanks has been found to decrease over time. In this thesis, the long-term performance of the SD have been studied, observing that the light time-decay of the pulse shape histograms of vertical muons from low-energetic showers used to calibrate the stations, τ, decreases by about 11 ns in each station over 15 years, with the stations grouping in two different populations (Chapter 2). A similar result was obtained for the Area over Peak, a variable used to monitor the status of the stations and obtained from the calibration histograms, with a decrease of $\Delta A/P \approx 0.35$ [25 ns] over the same period.

With the use of dedicated `GEANT4` detector simulations, the cause of this decrease was investigated by varying the optical properties of the tanks, namely the water absorption and the liner reflectivity. A decrease of 1.7% over the years of the latter has been found to be able to describe the signal decrease, with the distribution of stations at each year being bimodal. The two populations of reflectivity observed over the array were found to be related to the time of deployment. A deeper study of the technical information of the liner producers could reveal some relations with this pattern. The reflectivities for all the stations over the years were modeled by matching simulated shape histograms with those obtained from data. As a blind test of the model, A/P was reproduced for all the stations, with a small A/P difference of 0.1 [25 ns] between data and simulations.

For the first time in Auger, a more realistic time-dependent simulation of the SD has been realized using the aging model. A new Module, called SdEvolution, was developed in $\overline{\text{Off}}\underline{\text{line}}$ to take into account the aging effects in simulations by modifying the reflectivity of the simulated tanks, accordingly with the time of the simulated events. The calibration constants used in simulations were also modified accordingly to reproduce the time response of the tanks correctly. A new simulations library, for four different primaries in $18.5 < \log_{10}(\text{E/eV}) < 20.2$ and with $\theta < 65°$, was produced. The roll-out of the deployment was also included as a temporal dependency. Simulations were obtained in two configurations, *standard* and *agingSD*, in order to assess the impact of the aging.

The signal loss affected the number of triggered stations in data, displaying a continuous decrease over the years and the same trend was reproduced in simulations that account for aging. A discrepancy in the absolute values was observed, and a deeper study of the trigger effects due to aging could shine some light on the matter. A worsening of the energy resolution by about 5% in 15 years was predicted as a consequence of the loss of triggered stations over the years in data. With the aging simulations, the aging effect on the detector resolution was independently assessed and found in agreement with the prediction, between 2 and 4%. The detector energy resolution in aging simulations itself was found to be in better agreement with the

measurement from data compared to the standard simulations, as well as the total resolution. The possibility to separately obtain the total and the detector resolution allowed the study of the shower-to-shower fluctuations in simulations. They show a decrease as a function of the primary energy between 1% and 3% per decade. The absence of significant differences in the shower-to-shower fluctuations between the two simulation configurations also proved the goodness of the procedure. While the resolution worsened due to the aging, the mean reconstructed energy showed sub-per cent changes over the years. This is another proof of the robustness of the Auger calibration using atmospheric muons.

The change of τ consequently also affects the risetime, the time for the measured PMT trace to go from 10 to 50% of its integrated charge, with an observed decrease by about 15 ns in 15 years for data. This observable is related to the muon content of the shower and thus is used to infer the primary mass event-by-event with the "Δ method". This method was applied to both data and simulations, showing that the decrease of Δ is reproduced with the aging simulations. The effect of the use of simulations describing the aging or not on the interpretation of Δ in terms of $\langle \ln A \rangle$ was studied, showing that without the aging corrections, the method would have predicted a heavier composition compared to the one that considers the decrease of the risetime over the years, especially at lower energies. It was also shown that the decrease is not energy-dependent. At the same time, a structure with breaks was observed for the evolution as a function of the energy, as reported in other analyses. These features are related to a change in the mass composition of data, going from Oxygen to Iron, with a transition region that starts at $\approx 10^{19}$ eV up to $\approx 10^{19.6}$ eV.

Having a set of simulations that describes better the detector, a Deep Learning model was developed based on previous works to extract the muon trace from the total trace in candidate stations. Modifications of the DNN were applied to improve the performance, including for example the azimuth angle of the stations, and inform the network regarding the signal's decrease over time, introducing the station's age as an input. The dataset was enlarged by including events with saturated high-gain channels. The performance agreed with previous works, showing, in addition, that a time-dependent bias can be removed with the age information. The extraction of the muon signal was then perfomed on data. The muon shower estimator at 1000 m was obtained event-by-event from the muons lateral distribution. This provided the possibility to study the evolution of the muon signal as a function of the energy, with the slope, β, of the trend pointing towards a mix composition. The study of β as a function of the zenith angle, indeed, confirmed an agreement with the AugerMix, but at the same time showed a bias for vertical showers, requiring a deeper study of the features underneath. The muon signal for each event was analyzed in conjunction with the shower maximum, $X_{\rm max}$, obtained from golden hybrid events and from another method that predicts $X_{\rm max}^{\rm DNN}$ from the SD signals using DNNs. The presence of the muon deficit has been observed with both dataset for vertical and inclined showers, with a 10-fold increase in statistics when the muons signals are combined with the $X_{\rm max}^{\rm DNN}$, strongly reducing the statistical uncertainties. This work open the possibility to combine $X_{\rm max}$ and the muon signal S_μ to perform composition studies with a significantly larger dataset.

The next step of this analysis will address in more details the systematic uncertainties of the muon signal predictions, also comparing the present results with simulations produced with different hadronic models. The systematics due to the DNN model would be addressed too.

The perfomance of the neural network could also be improved by including in the training of the DNN the information relative to the τ observed in each station

at each time, since this is directly related to the signal loss in the tank. The age of the station, indeed, provide information about the aging but does not distinguish between the two different tank populations observed in the field.

Future studies based on the work presented in this thesis could try to understand and explain the discrepancy observed in simulations between τ and A/P, with a focus on the effects of the electronics in calibration and shape histograms.

Last but not least, a measurement of the shower-to-shower fluctuations from data could be performed and compared to the results obtained in this work.

Appendix A

CIC fitted polynomial coefficients

	y_0	y_1	y_2
a	0.952	0.06	-0.37
b	-1.64	-0.42	0.09
c	-0.9	-0.04	1.3

TABLE A.1: Fitted parameters for the attenuation curve in three different energy ranges [1].

Appendix B

Example of a bad station with an erratic behaviour

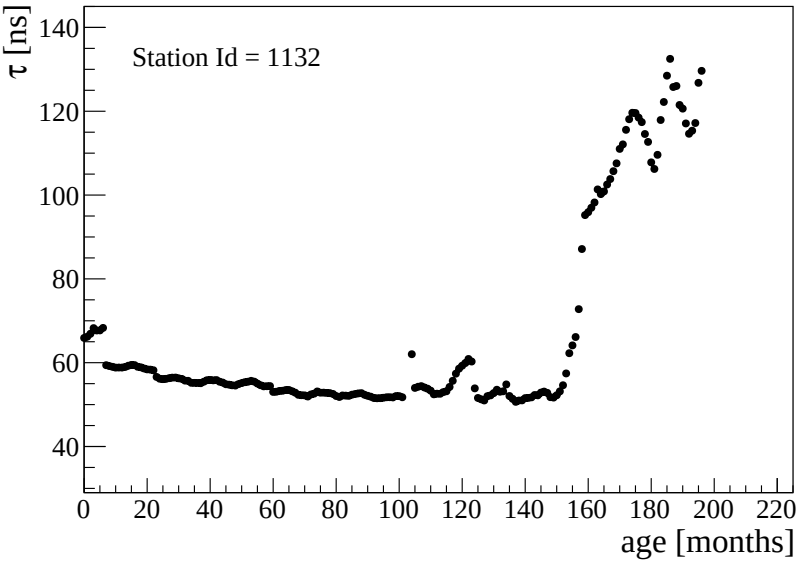

FIGURE B.1: τ over time for station with Id = 1132.

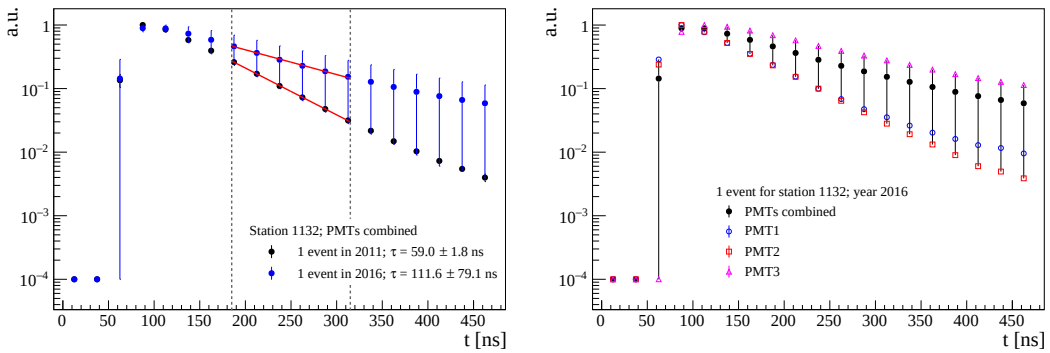

(a) Comparison of events in 2011 and 2016

(b) 1 event in 2016, all PMTs

FIGURE B.2: Examples of shapes histograms for station 1132.

Appendix C

Tank populations

C.1 Distributions of the two populations over time

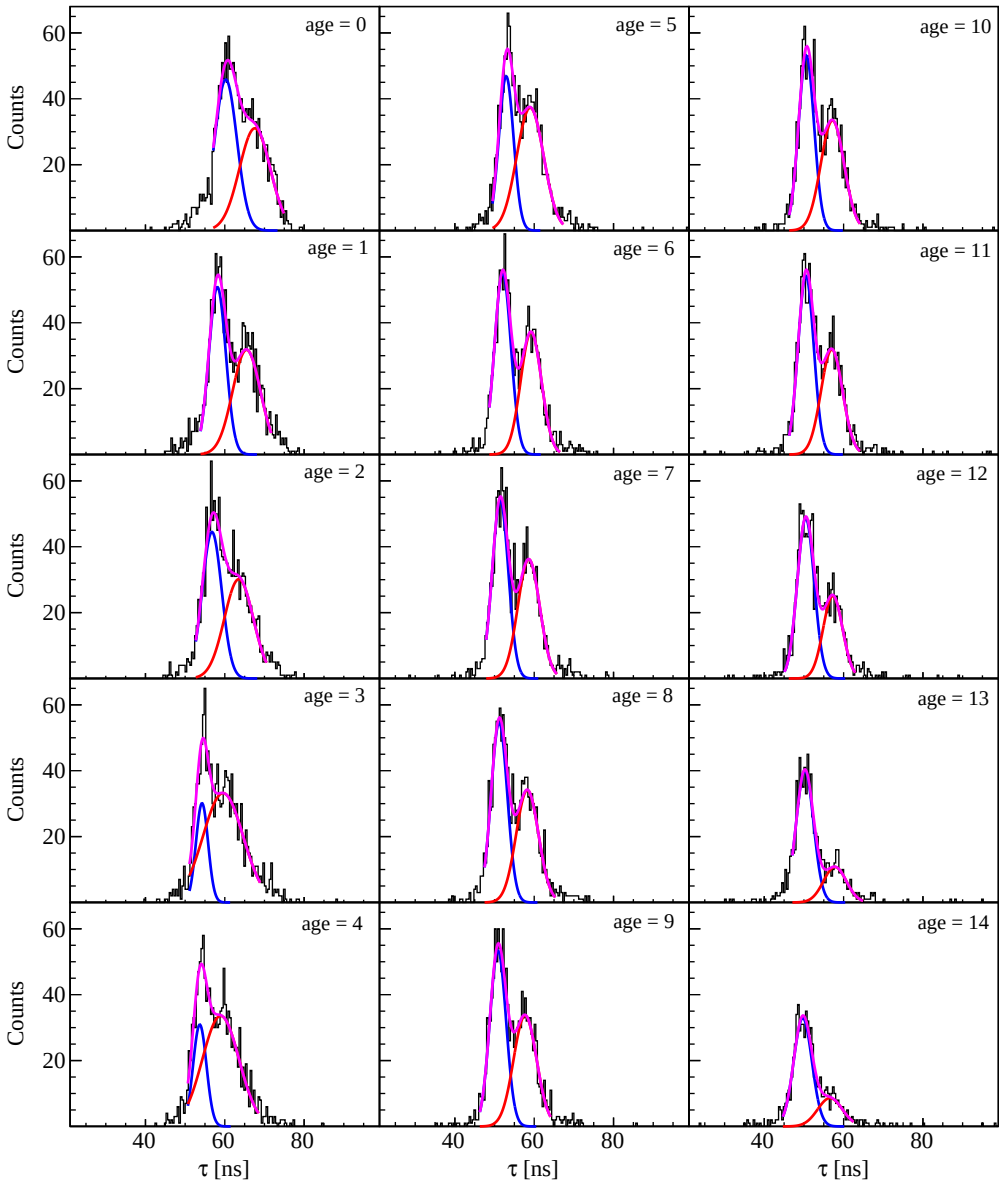

FIGURE C.1: Time decay constant distributions for different tank ages (year of deployment).

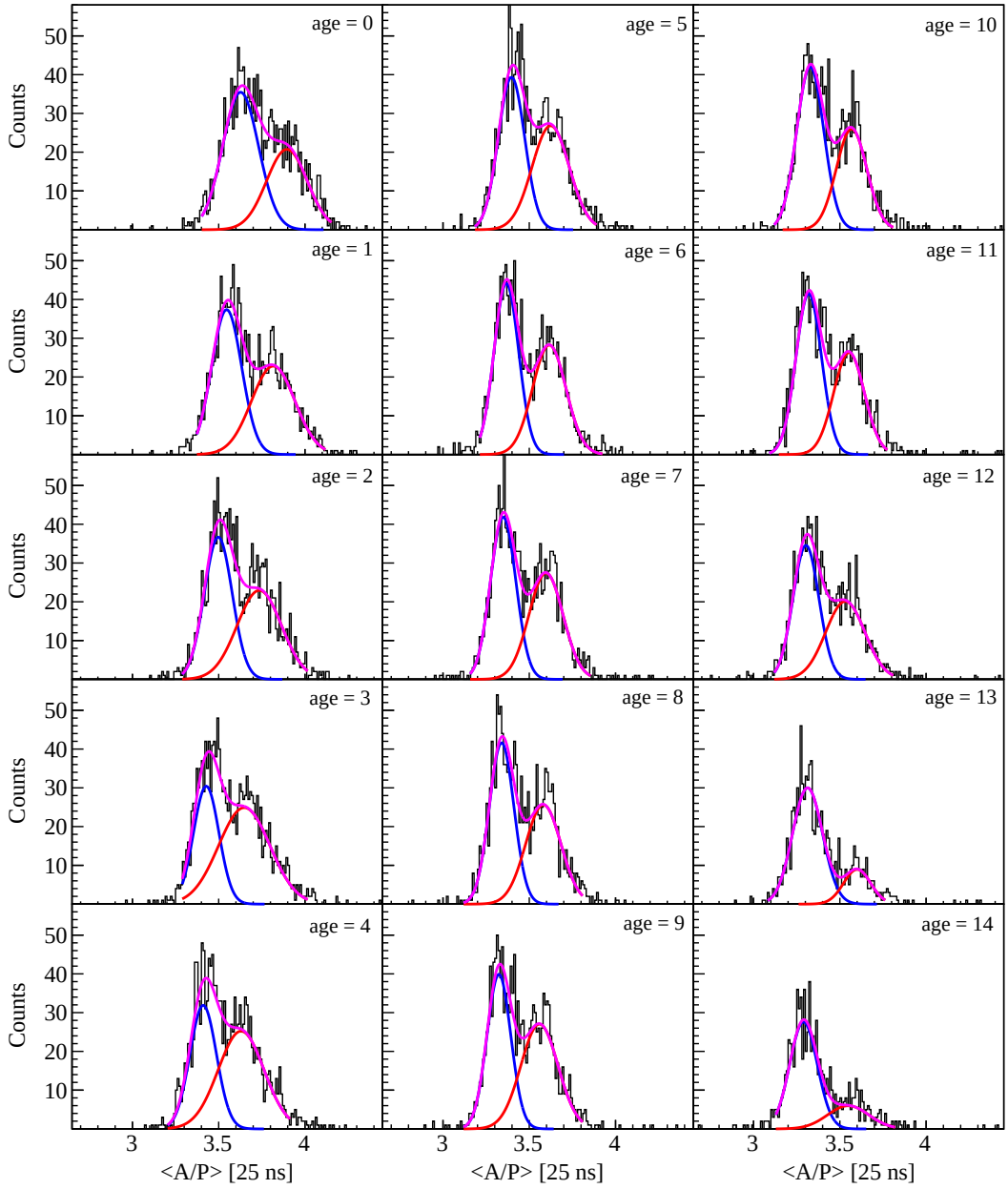

FIGURE C.2: A/P distributions for different tank ages (year of deployment).

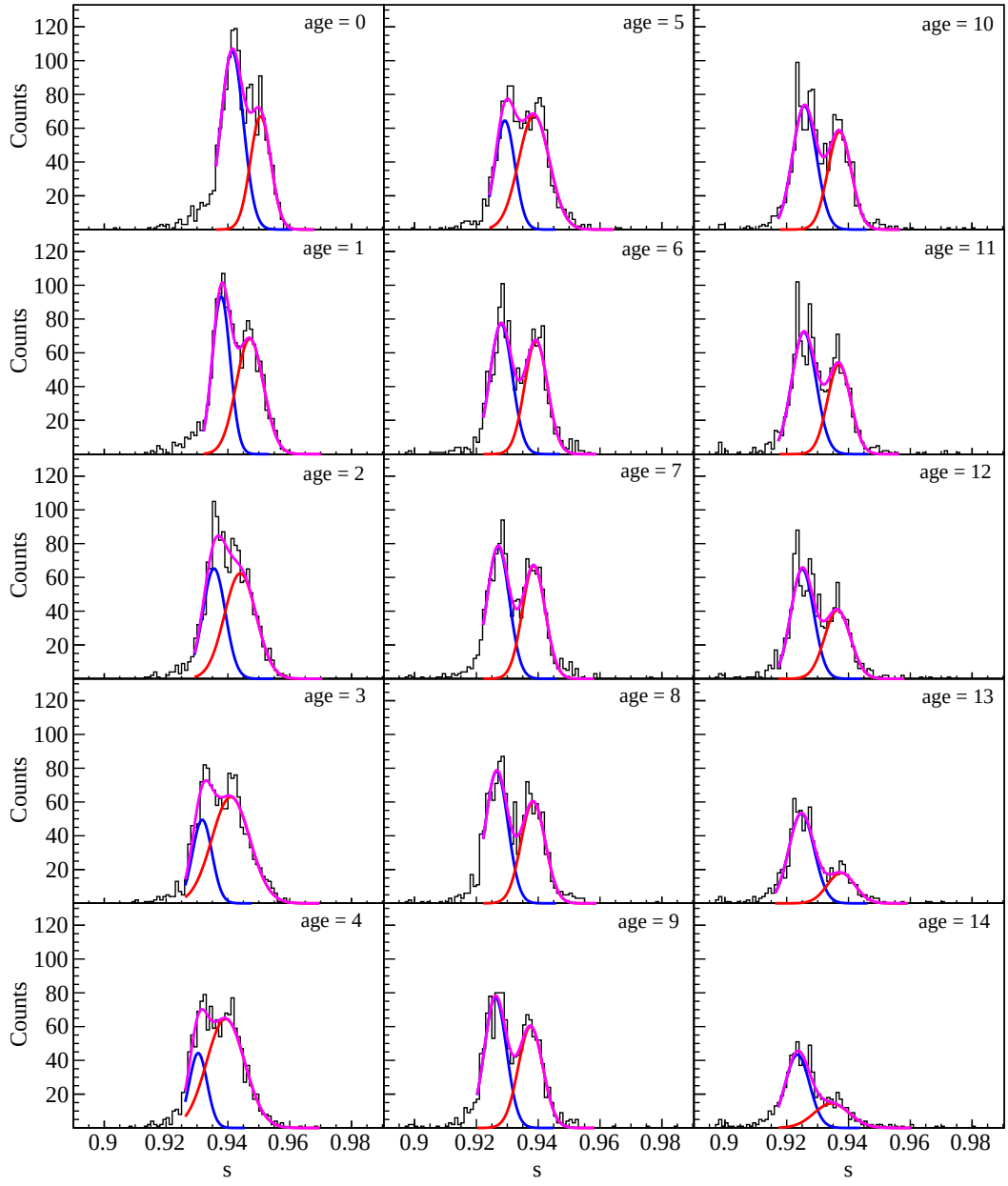

FIGURE C.3: Best match liner reflectivity distributions for different tank ages (year of deployment).

C.2 Distributions of the two populations

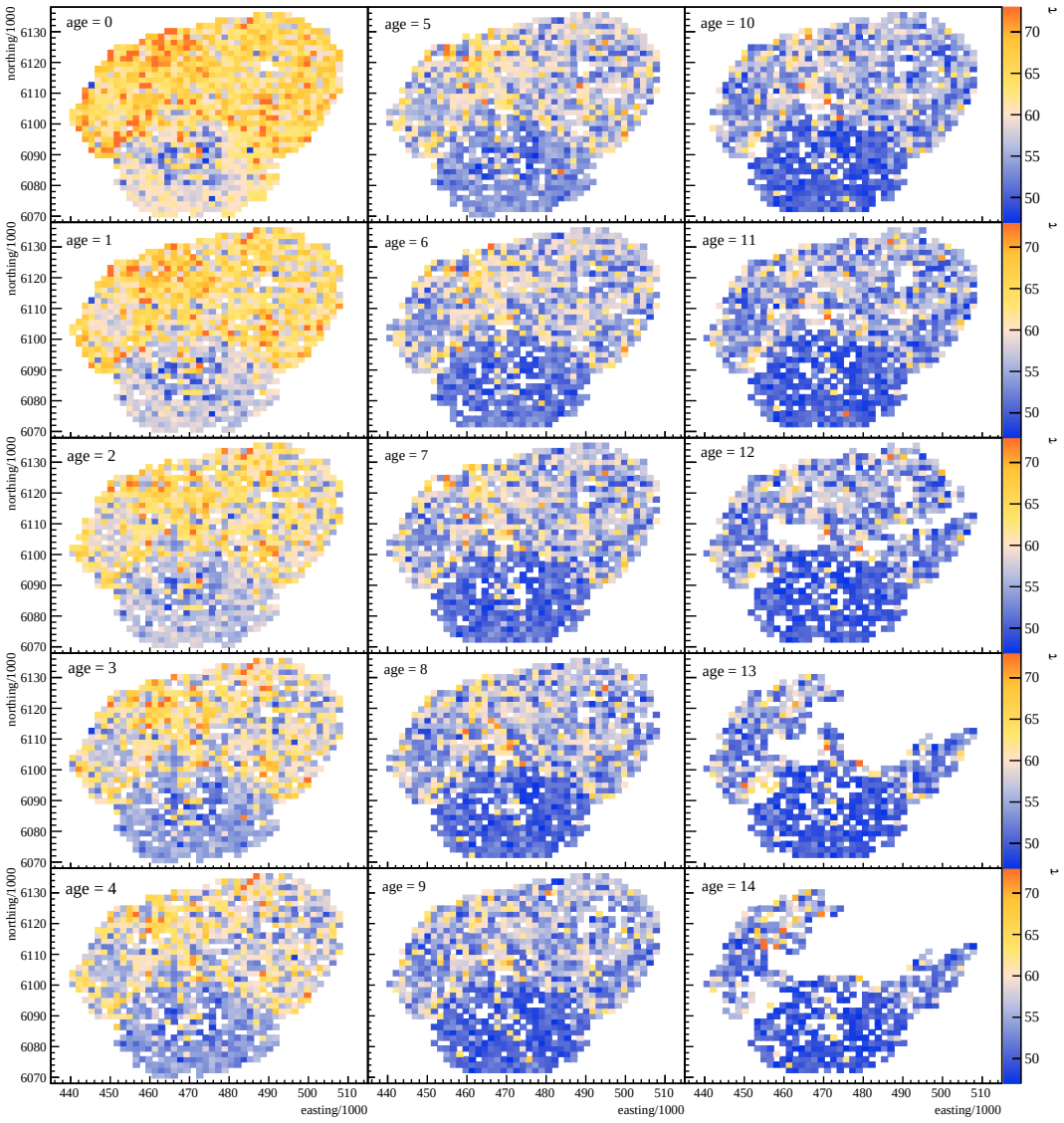

FIGURE C.4: Spatial distributions of the time decay constant for different ages of the tanks.

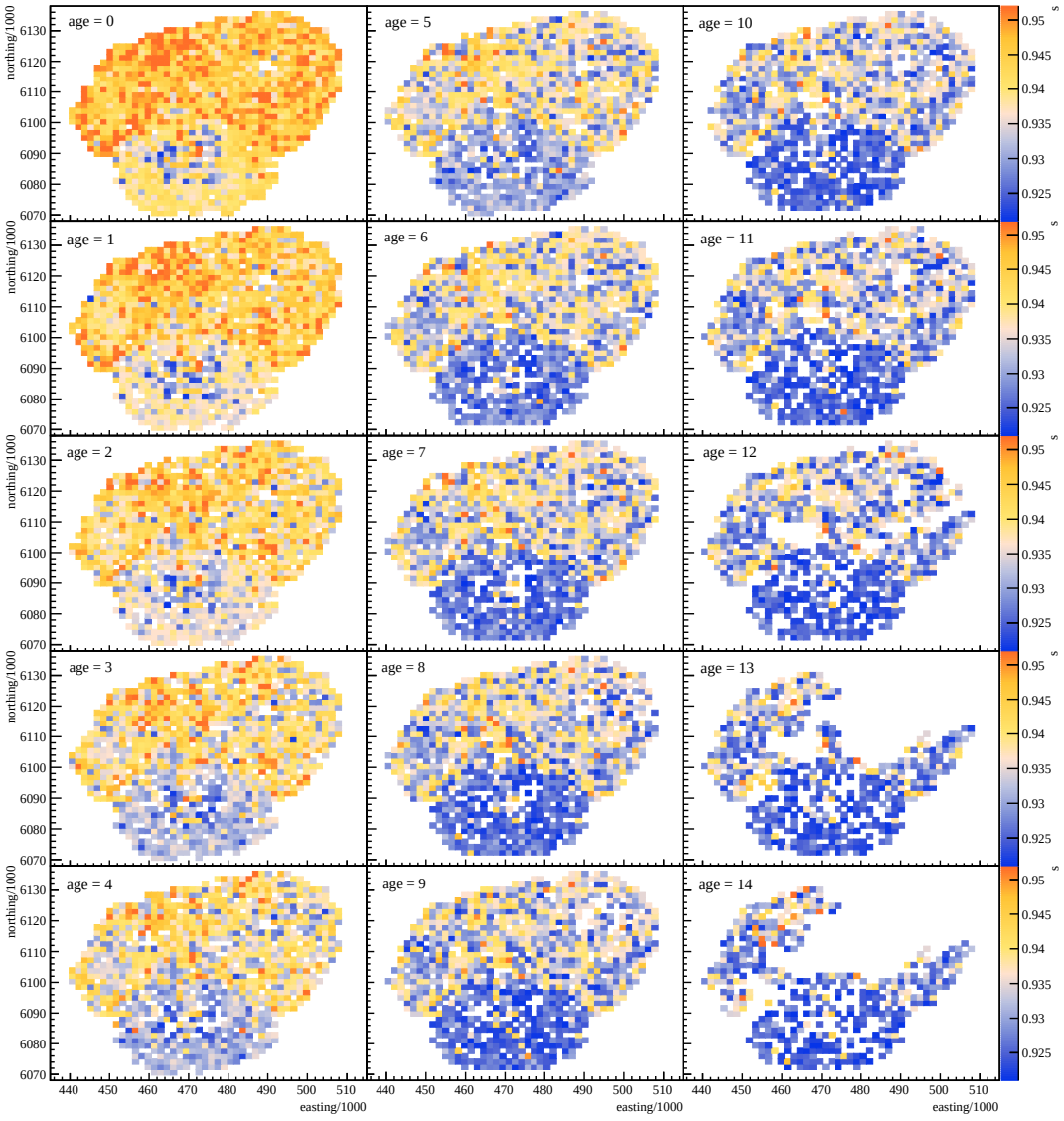

FIGURE C.5: Spatial distributions of the liner reflectivity for different ages of the tanks.

C.3 Evolution over time of the three liner categories

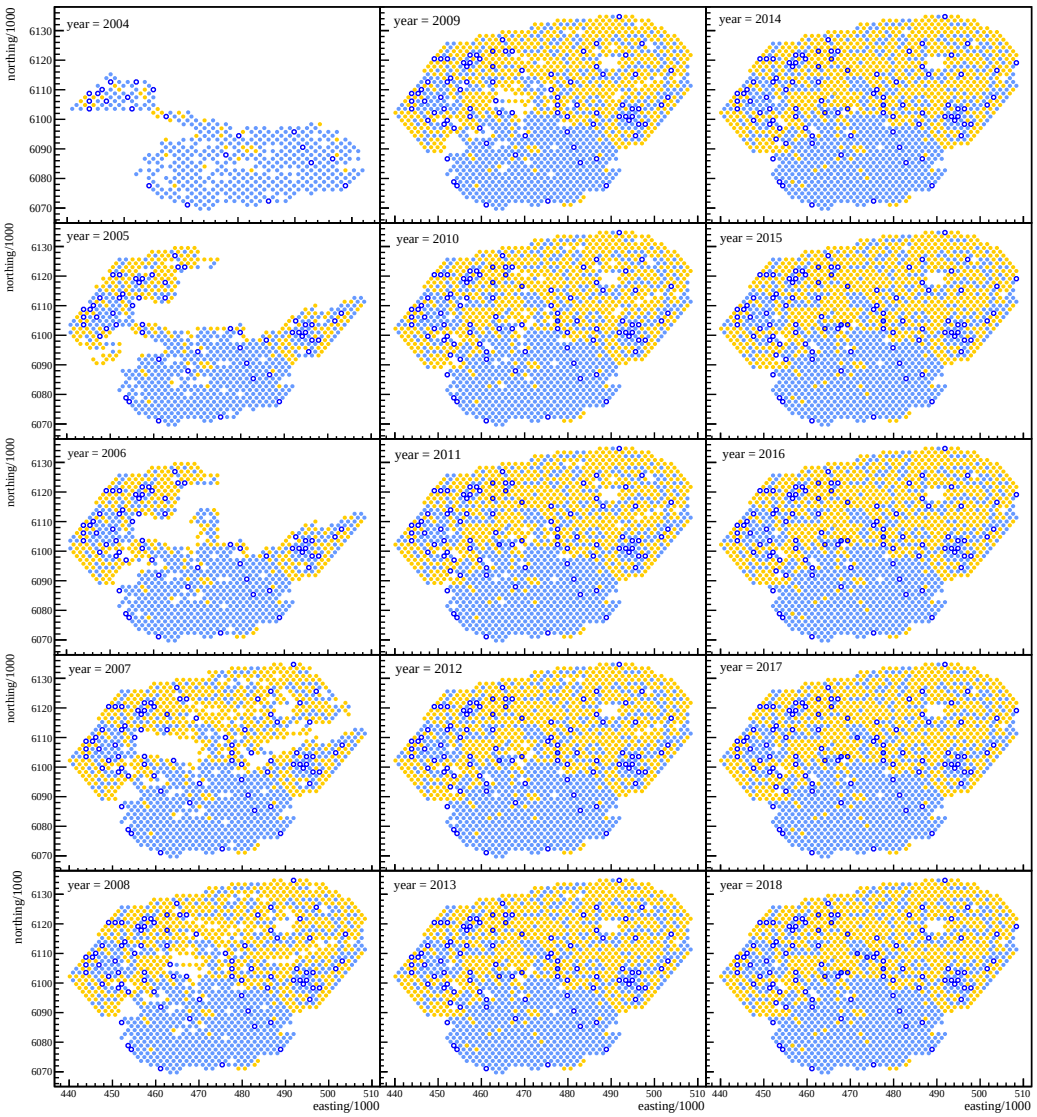

FIGURE C.6: Evolution in the array over the years for the three station liner populations.

Appendix D

Reconstructed fractions of primaries as a function of MC energy

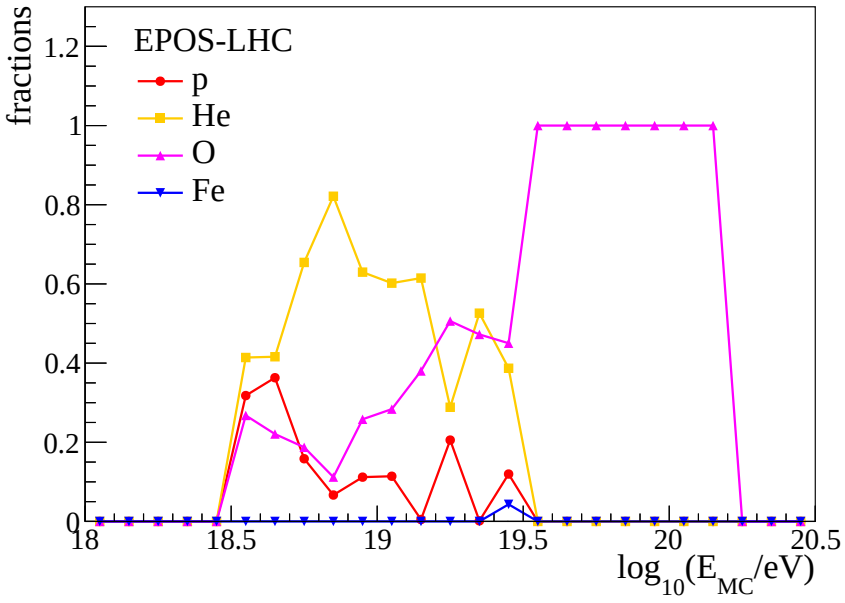

FIGURE D.1: Fractions of different nuclei as a function of the true Monte Carlo energy obtained from the comparison between the rescaled distributions of each primary to the total non-weighted reconstructed energy distribution.

Appendix E

Δ method: Zenith angle dependence of observed features

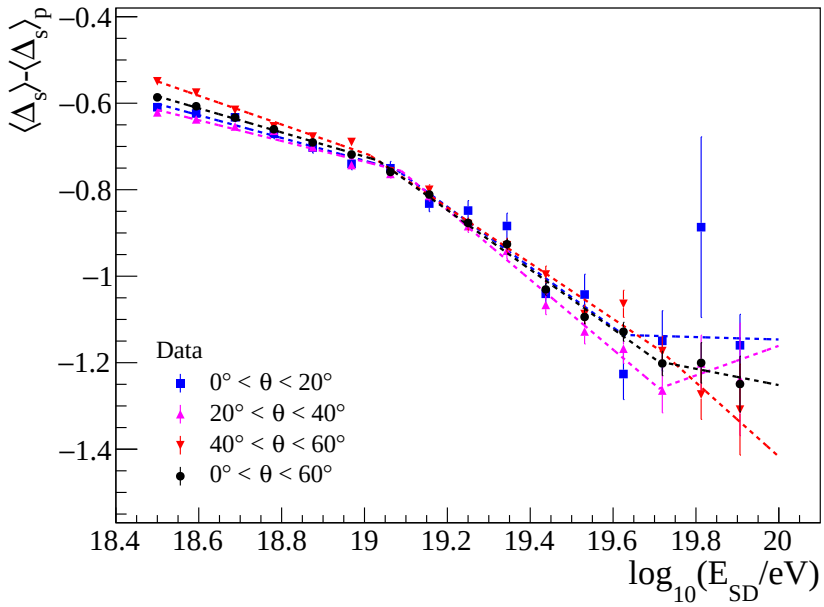

FIGURE E.1: Normalized Δ to proton simulations as a function of the reconstructed energy. Data are fitted using a broken linear function. Data is split in different zenith angle groups.

Appendix F

S1000 bias and resolution

F.1 S1000 bias over time

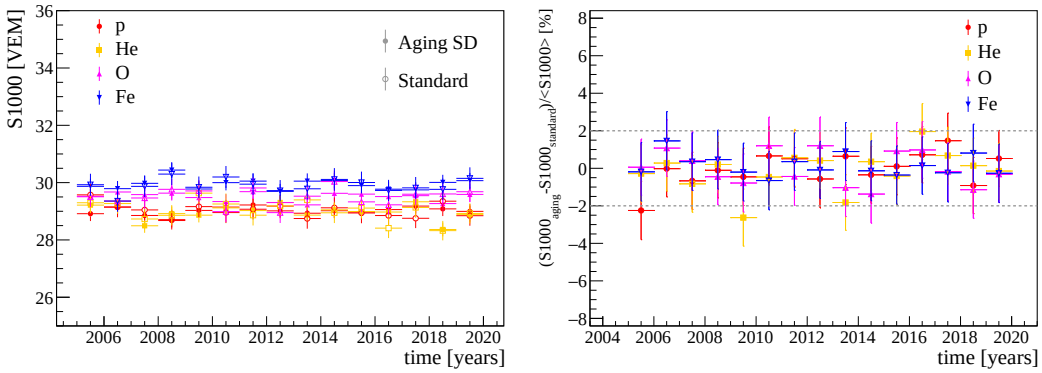

FIGURE F.1: Left: S1000 bias between reconstructed energy and true Monte Carlo energy as a function of the years for different primaries, weighted by the energy spectrum. Open symbols: *standard* simulations. Filled symbols: *agingSD* simulations. Right: Change of the S1000 bias over time for the two different simulation configurations of the array: an ideal SD and a SD with a time-dependent behavior.

F.2 S1000 resolution

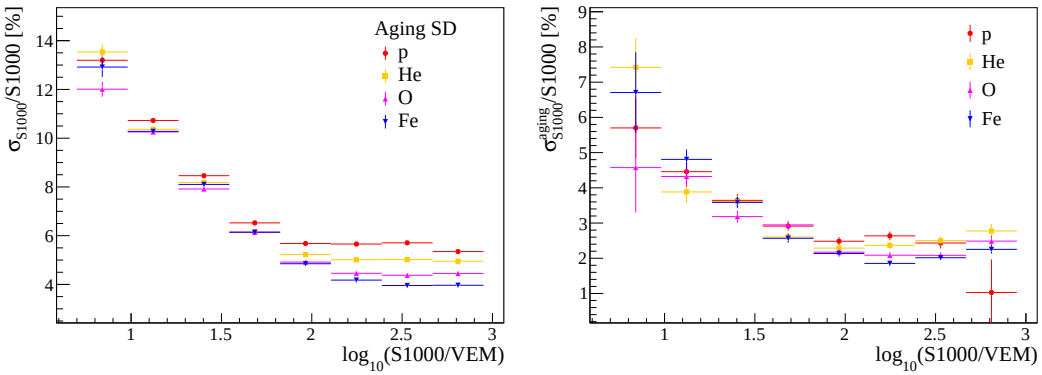

FIGURE F.2: Energy resolution as a function of the Monte Carlo energy of the showers. Left: Energy resolution due to detector effects. Right: Energy resolution due to aging effects.

Appendix G

DNN perfomance: Bias and resolution as a function of age

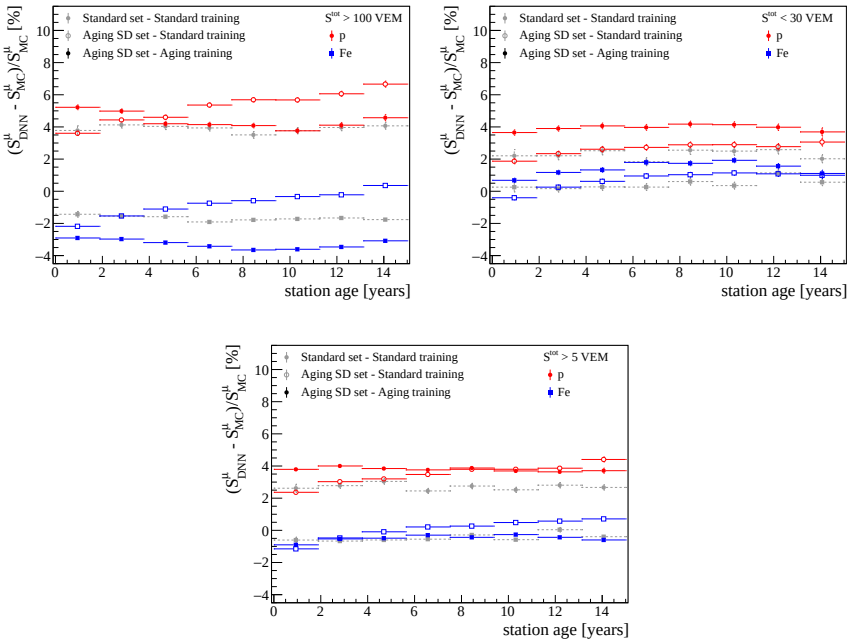

FIGURE G.1: Bias of predicted muon signals for different total signal's thresholds as a function of the station age. Several samples and trainings are shown. See text for more details.

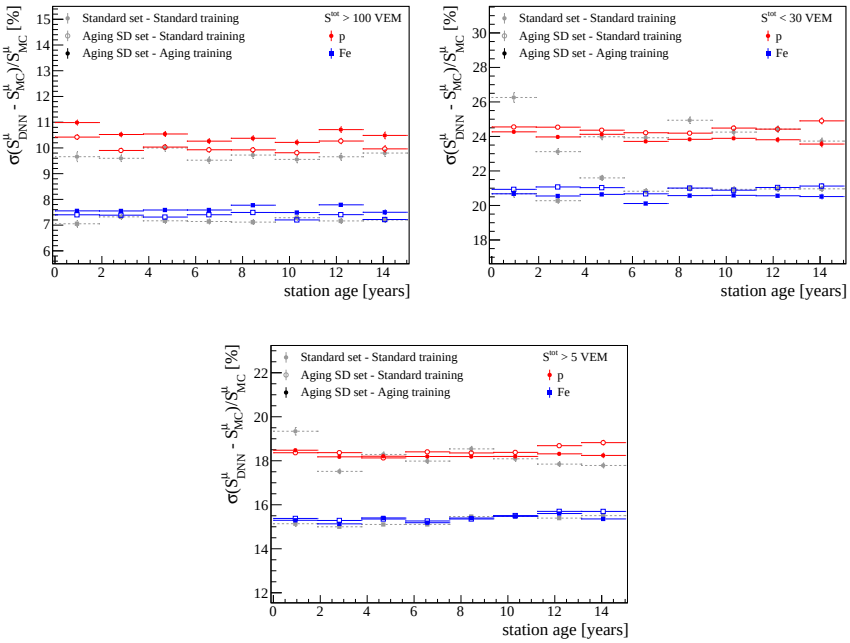

FIGURE G.2: Resolution of predicted muon signals for different total signal's thresholds as a function of the station age. Several samples and trainings are shown. See text for more details.

Appendix H

Twin showers

H.1 bootstrap.xml.in

```
<?xml version="1.0" encoding="iso-8859-1"?>

<!DOCTYPE bootstrap [
    <!ENTITY standardSdIdealDetConfig SYSTEM '@CONFIGDIR@/standardSdIdealDetConfig.xml'>
    <!ENTITY standardSdSimModuleConfig SYSTEM '@CONFIGDIR@/standardSdSimModuleConfig.xml'>
    <!ENTITY standardSdRecModuleConfig SYSTEM '@CONFIGDIR@/standardSdRecModuleConfig.xml'>
]>

<bootstrap
    xmlns:xsi="http://www.w3.org/2001/XMLSchema-instance"
    xsi:noNamespaceSchemaLocation='@SCHEMALOCATION@/bootstrap.xsd'
    xmlns:xlink="http://www.auger.org/schema/types">

    &standardSdIdealDetConfig;
    &standardSdSimModuleConfig;
    &standardSdRecModuleConfig;

    <centralConfig>

        <configLink
        id          = "ModuleSequence"
        type        = "XML"
        xlink:href = "./ModuleSequence.xml"/>

        <configLink
        id          = "EventFileReader"
        type        = "XML"
        xlink:href = "./EventFileReader.xml"/>

        <configLink
        id          = "EventGenerator"
        type        = "XML"
        xlink:href = "./EventGenerator.xml"/>

        <configLink
        id          = "SDenseStationListXMLManager"
        type        = "XML"
        xlink:href = "./SDenseStationMultipleRing.xml"/>

    </centralConfig>

    <parameterOverrides>
```

```
<configLink id="EventGenerator">
<EventGenerator>
    <eventIdentifier>
    <libraryIdentifier> s@LINER@ </libraryIdentifier>
    </eventIdentifier>
</EventGenerator>
</configLink>

<configLink id="EventFileReader">
<EventFileReader>
    <CORSIKA>
    <InputFilenames> @INPUT_FILE@ </InputFilenames>
    </CORSIKA>
</EventFileReader>
</configLink>

<configLink id="SModelsXMLManager">
<SModelsXMLManager>
    <stationModels>
    <liner id="1073B-tyvek">
        <reflectivity>
        <scaleY> @LINER@ </scaleY>
        </reflectivity>
    </liner>
    <water id="standard">
        <waterAbsorptionLength>
        <scaleY unit="m"> 100 </scaleY>
        </waterAbsorptionLength>
    </water>
    </stationModels>
</SModelsXMLManager>
</configLink>


<configLink id="SdSimCalibrationManager">
<SdSimCalibrationManager>
    <simModule name="G4StationSimulatorOG">
    <electronics isUUB="0">
        <PMT id='1'>
        <peak> @PEAK_PMT1@ </peak>
        <charge> @CHARGE_PMT1@ </charge>
        </PMT>
        <PMT id='2'>
        <peak> @PEAK_PMT2@ </peak>
        <charge> @CHARGE_PMT2@ </charge>
        </PMT>
        <PMT id='3'>
        <peak> @PEAK_PMT3@ </peak>
        <charge> @CHARGE_PMT3@ </charge>
        </PMT>

    </electronics>
    </simModule>
</SdSimCalibrationManager>
</configLink>
```

```
        <configLink id="RandomEngineRegistry">
        <RandomEngineRegistry>
            <!-- The initial seed for the eDetector random engine
                a seed of "0" means a random initialization -->
            <DetectorSeed> 2 </DetectorSeed>

            <!-- The initial seed for the ePhysics random engine
                a seed of "0" means a random initialization -->
            <PhysicsSeed> 2 </PhysicsSeed>

        </RandomEngineRegistry>
        </configLink>

        <configLink id="G4StationSimulator">
        <G4StationSimulator>
            <fastMode> 1 </fastMode>
            <fullTrackMode> 0 </fullTrackMode>
        </G4StationSimulator>
        </configLink>


        <configLink id="RecDataWriter">
        <RecDataWriter>

            <!-- Save SD FADC-Traces above this energy -->
            <minEnergyForTraces unit="EeV"> 0 </minEnergyForTraces>

            <saveSDTraces> 2 </saveSDTraces>
            <saveMCTraces> 1 </saveMCTraces>

            <savePETimeDistribution> 0 </savePETimeDistribution>

            <saveParticles> 1 </saveParticles>

            <asciiOutput>
            <outputFileMode> eNone </outputFileMode>
            </asciiOutput>

            <rootOutput>
            <outputFileName> @OUTPUT_DIR@/@OUTPUT_DAT@.root </outputFileName>
            <outputFileMode> eWrite </outputFileMode>
            </rootOutput>
        </RecDataWriter>
        </configLink>

        <configLink id="LDFFinderKG">
        <LDFFinderKG>
            <coreType> MC </coreType>
        </LDFFinderKG>
        </configLink>

    </parameterOverrides>


</bootstrap>
```

H.2 ModuleSequence.xml.in

```
<!DOCTYPE sequenceFile [
    <!ENTITY % sd SYSTEM "@CONFIGDIR@/standardSdSequences.dtd">
    %sd;
    ] >

<sequenceFile>

    <enableTiming/>

    <moduleControl>

        <loop numTimes="unbounded" pushEventToStack="yes">

            <module> EventFileReaderOG </module>

            <loop numTimes="1" pushEventToStack="yes">

                <module> EventGeneratorOG </module>

                <!-- simulation of muon background -->
                <module> SdAccidentalInjectorKG </module>
                <module> G4StationSimulatorOG </module>

                <!-- SdSimulation -->
                <loop numTimes="unbounded" pushEventToStack="no">
                    <module> CachedShowerRegeneratorOG </module>
                    <module> G4StationSimulatorOG </module>
                </loop>

                <module> SdSimulationCalibrationFillerOG </module>
                <module> SdPMTSimulatorOG </module>
                <module> SdFilterFADCSimulatorMTU </module>
                <module> SdBaselineSimulatorOG </module>
                <module> TankTriggerSimulatorOG </module>
                <module> TankGPSSimulatorOG </module>

                <module> CentralTriggerSimulatorXb </module>
                <module> CentralTriggerEventBuilderOG </module>
                <module> EventBuilderOG </module>

                <!-- SdSimReconstruction -->
                <module> EventCheckerOG </module>
                <module> SdCalibratorOG  </module>
                <module> SdSignalRecoveryKLT </module>
                <module> SdMonteCarloEventSelectorOG </module>
                <module> SdEventSelectorOG </module>
                <module> SdPlaneFitOG </module>
                <module> LDFFinderKG </module>
                <try>
                    <module> ScintillatorLDFFinderKG </module>
                </try>

                <module> SdEventPosteriorSelectorOG </module>

                <!-- export the ADST -->
```

```
                <module> RecDataWriterNG </module>

            </loop>
        </loop>
    </moduleControl>

</sequenceFile>
```

Appendix I

SdEvolution configuration files

I.1 bootstrap_evolution.xml.in

```
<?xml version="1.0" encoding="iso-8859-1"?>

<!DOCTYPE bootstrap [
    <!ENTITY standardSdRealDetConfig SYSTEM '@CONFIGDIR@/standardSdRealDetConfig.xml'>
    <!ENTITY standardSdSimModuleConfig SYSTEM '@CONFIGDIR@/standardSdSimModuleConfig.xml'>
    <!ENTITY standardSdRecModuleConfig SYSTEM '@CONFIGDIR@/standardSdRecModuleConfig.xml'>
]>

<bootstrap
    xmlns:xsi="http://www.w3.org/2001/XMLSchema-instance"
    xsi:noNamespaceSchemaLocation='@SCHEMALOCATION@/bootstrap.xsd'
    xmlns:xlink="http://www.auger.org/schema/types">

    &standardSdRealDetConfig;
    &standardSdSimModuleConfig;
    &standardSdRecModuleConfig;

    <centralConfig>

        <configLink
            id          = "ModuleSequence"
            type        = "XML"
            xlink:href = "ModuleSequence_evolution.xml"/>

        <configLink
            id          = "EventFileReader"
            type        = "XML"
            xlink:href = "EventFileReader.xml"/>

        <configLink
            id          = "EventGenerator"
            type        = "XML"
            xlink:href = "EventGenerator.xml"/>

        <!-- REAL Sd managers -->

        <configLink
            id          = "SManagerRegister"
            type        = "XML"
            xlink:href = "SManagerRegisterConfig_evolution.xml"/>

        <configLink
            id          = "T2LifeROOTFileManager"
```

```
        type       = "XML"
        xlink:href = "T2LifeROOTFileManagerConfig.xml"/>

    <configLink
        id         = "SStationListXMLManager"
        type       = "XML"
        xlink:href = "SStationListIdealAltitude_evolution.xml"/>

    <configLink
        id         = "SdEvolution"
        type       = "XML"
        xlink:href = "@CONFIGDIR@/SdEvolutionBXL.xml"/>

</centralConfig>


<parameterOverrides>

    <configLink id="EventFileReader">
        <EventFileReader>
        <CORSIKA>
            <InputFilenames>
                @INPUT_FILE@.part
            </InputFilenames>
        </CORSIKA>
        </EventFileReader>
    </configLink>

    <configLink id="SModelsXMLManager">
        <SModelsXMLManager>
        <stationModels>
            <liner id="1073B-tyvek">
            <reflectivity>
                <scaleY> 0.94 </scaleY>
            </reflectivity>
            </liner>
        </stationModels>
        </SModelsXMLManager>
    </configLink>

    <!-- for reproducibility -->
    <configLink id="RandomEngineRegistry">
        <RandomEngineRegistry>
        <DetectorSeed> @DETECTOR_SEED@ </DetectorSeed>
        <PhysicsSeed> 2000 </PhysicsSeed>
        </RandomEngineRegistry>
    </configLink>

    <configLink id="SdEvolution">
        <SdEvolution>
        <LinerFile> ./sdEvolution.root </LinerFile>
        </SdEvolution>
    </configLink>

    <configLink id="SdSimulationCalibrationFiller">
        <SdSimulationCalibrationFiller>
        <useParametrization> 1 </useParametrization>
```

```
            </SdSimulationCalibrationFiller>
        </configLink>

        <configLink id="EventGenerator">
            <EventGenerator>

            <coreRandomization>
                <useRandomStation> 1 </useRandomStation>
            </coreRandomization>

            <timeInterval>

                <timeOrdered>
                <nEvents> @NEVENTS@ </nEvents>
                <timeRandomized> 1 </timeRandomized>
                </timeOrdered>

                <startTime> 2005-01-01T00:00:00 </startTime>
                <endTime>   2020-01-01T00:00:00 </endTime>

            </timeInterval>

            </EventGenerator>
        </configLink>

        <configLink id="RecDataWriter">
            <RecDataWriter>
            <minEnergyForTraces unit="EeV"> 0 </minEnergyForTraces>
            <saveSDTraces> 2 </saveSDTraces>
            <saveMCTraces> 1 </saveMCTraces>
            <savePETimeDistribution> 1 </savePETimeDistribution>
            <saveParticles> 1 </saveParticles>

            <storeLidarData>  0  </storeLidarData>
            <storeAllPixels> 0 </storeAllPixels>
            <SaveRadio> 0 </SaveRadio>

            <useWeatherStations> 0 </useWeatherStations>
            <rootOutput>
                <outputFileName> @OUTPUT_FILE_ADST@ </outputFileName>
                <outputFileMode> eWrite </outputFileMode>
            </rootOutput>
            <asciiOutput>
                <outputFileMode> eNone </outputFileMode>
            </asciiOutput>
            </RecDataWriter>
        </configLink>

    </parameterOverrides>

</bootstrap>
```

I.2 bootstrap_standard.xml.in

```
<?xml version="1.0" encoding="iso-8859-1"?>

<!DOCTYPE bootstrap [
  <!ENTITY standardSdRealDetConfig SYSTEM '@CONFIGDIR@/standardSdRealDetConfig.xml'>
  <!ENTITY standardSdSimModuleConfig SYSTEM '@CONFIGDIR@/standardSdSimModuleConfig.xml'>
  <!ENTITY standardSdRecModuleConfig SYSTEM '@CONFIGDIR@/standardSdRecModuleConfig.xml'>
]>

<bootstrap
    xmlns:xsi="http://www.w3.org/2001/XMLSchema-instance"
    xsi:noNamespaceSchemaLocation='@SCHEMALOCATION@/bootstrap.xsd'
    xmlns:xlink="http://www.auger.org/schema/types">

    &standardSdRealDetConfig;
    &standardSdSimModuleConfig;
    &standardSdRecModuleConfig;

    <centralConfig>

        <configLink
            id          = "ModuleSequence"
            type        = "XML"
            xlink:href = "ModuleSequence_standard.xml"/>

        <configLink
            id          = "EventFileReader"
            type        = "XML"
            xlink:href = "EventFileReader.xml"/>

        <configLink
            id          = "EventGenerator"
            type        = "XML"
            xlink:href = "EventGenerator.xml"/>

            <!-- REAL Sd managers -->

        <configLink
            id          = "SManagerRegister"
            type        = "XML"
            xlink:href = "SManagerRegisterConfig_standard.xml"/>

        <configLink
            id          = "SStationListXMLManager"
            type        = "XML"
            xlink:href = "SStationListIdealAltitude_standard.xml"/>

    </centralConfig>


    <parameterOverrides>

        <configLink id="EventFileReader">
            <EventFileReader>
            <CORSIKA>
                <InputFilenames>
                    @INPUT_FILE@.part
                </InputFilenames>
```

```
    </CORSIKA>
    </EventFileReader>
</configLink>

<configLink id="SModelsXMLManager">
    <SModelsXMLManager>
    <stationModels>
        <liner id="1073B-tyvek">
        <reflectivity>
            <scaleY> 0.94 </scaleY>
        </reflectivity>
        </liner>
    </stationModels>
    </SModelsXMLManager>
</configLink>

<configLink id="G4StationSimulator">
    <G4StationSimulator>
    <fullTrackMode> 0 </fullTrackMode>
    <fastMode> 1 </fastMode>
    </G4StationSimulator>
</configLink>

<!-- for reproducibility -->
<configLink id="RandomEngineRegistry">
    <RandomEngineRegistry>
    <DetectorSeed> @DETECTOR_SEED@ </DetectorSeed>
    <PhysicsSeed> 2000 </PhysicsSeed>
    </RandomEngineRegistry>
</configLink>

<configLink id="SdSimulationCalibrationFiller">
    <SdSimulationCalibrationFiller>
    <useParametrization> 1 </useParametrization>
    </SdSimulationCalibrationFiller>
</configLink>

<configLink id="EventGenerator">
    <EventGenerator>

    <coreRandomization>
        <useRandomStation> 1 </useRandomStation>
    </coreRandomization>

    <timeInterval>

        <timeOrdered>
        <nEvents> @NEVENTS@ </nEvents>
        <timeRandomized> 1 </timeRandomized>
        </timeOrdered>

        <startTime> 2005-01-01T00:00:00 </startTime>
        <endTime>   2020-01-01T00:00:00 </endTime>

    </timeInterval>

    </EventGenerator>
```

```
        </configLink>

        <!-- to limit ADST size -->
        <configLink id="RecDataWriter">
            <RecDataWriter>
            <minEnergyForTraces unit="EeV"> 0 </minEnergyForTraces>
            <saveSDTraces> 2 </saveSDTraces>
            <saveMCTraces> 1 </saveMCTraces>
            <savePETimeDistribution> 1 </savePETimeDistribution>
            <saveParticles> 1 </saveParticles>

            <storeLidarData>  0  </storeLidarData>
            <storeAllPixels> 0 </storeAllPixels>
            <SaveRadio> 0 </SaveRadio>

            <useWeatherStations> 0 </useWeatherStations>
            <rootOutput>
                <outputFileName> @OUTPUT_FILE_ADST_STD@ </outputFileName>
                <outputFileMode> eWrite </outputFileMode>
            </rootOutput>
            <asciiOutput>
                <outputFileMode> eNone </outputFileMode>
            </asciiOutput>
            </RecDataWriter>
        </configLink>

    </parameterOverrides>

</bootstrap>
```

I.3 ModuleSequence_evolution.xml.in

```
<!DOCTYPE sequenceFile [
    <!ENTITY % sd SYSTEM "@CONFIGDIR@/standardSdSequences.dtd">
    %sd;
    ] >

<sequenceFile xmlns:xsi="http://www.w3.org/2001/XMLSchema-instance">

    <enableTiming/>

    <moduleControl>

        <loop numTimes="unbounded" pushEventToStack="yes">

        <module> EventFileReaderOG </module>
        <loop numTimes="unbounded" pushEventToStack="yes">
            <module> EventGeneratorOG </module>

            <try>
            <loop numTimes="unbounded" pushEventToStack="no">
                <module> CachedShowerRegeneratorOG </module>
                <module> SdEvolutionBXL </module>
                <module> G4StationSimulatorOG </module>
            </loop>
```

```
            <module> SdSimulationCalibrationFillerOG </module>
            <module> SdPMTSimulatorOG </module>
            <module> SdFilterFADCSimulatorMTU </module>
            <module> SdBaselineSimulatorOG </module>
            <module> TankTriggerSimulatorOG </module>
            <module> TankGPSSimulatorOG </module>

            <module> CentralTriggerSimulatorXb </module>
            <module> CentralTriggerEventBuilderOG </module>

            </try>

            <module> EventBuilderOG </module>
            <try>
            <module> SdCalibratorOG </module>
            <module> SdMonteCarloEventSelectorOG </module>
            <module> SdEventSelectorOG </module>
            <module> SdPlaneFitOG </module>
            <module> LDFFinderKG </module>
            <module> Risetime1000LLL </module>
            <module> EnergyCalculationPG </module>
            <module> SdEventPosteriorSelectorOG </module>
            </try>

            <module> RecDataWriterNG </module>

        </loop>

        </loop>
    </moduleControl>

</sequenceFile>
```

I.4 ModuleSequence_standard.xml.in

```
<!DOCTYPE sequenceFile [
    <!ENTITY % sd SYSTEM "@CONFIGDIR@/standardSdSequences.dtd">
    %sd;
    ] >

<sequenceFile xmlns:xsi="http://www.w3.org/2001/XMLSchema-instance">

    <enableTiming/>

    <moduleControl>

        <loop numTimes="unbounded" pushEventToStack="yes">

        <module> EventFileReaderOG </module>
        <loop numTimes="unbounded" pushEventToStack="yes">
            <module> EventGeneratorOG </module>

            <try>
            <loop numTimes="unbounded" pushEventToStack="no">
                <module> CachedShowerRegeneratorOG </module>
```

```
            <module> G4StationSimulatorOG </module>
        </loop>
        <module> SdSimulationCalibrationFillerOG </module>
        <module> SdPMTSimulatorOG </module>
        <module> SdFilterFADCSimulatorMTU </module>
        <module> SdBaselineSimulatorOG </module>
        <module> TankTriggerSimulatorOG </module>
        <module> TankGPSSimulatorOG </module>

        <module> CentralTriggerSimulatorXb </module>
        <module> CentralTriggerEventBuilderOG </module>

        </try>

        <module> EventBuilderOG </module>
        <try>
        <module> SdCalibratorOG </module>
        <module> SdMonteCarloEventSelectorOG </module>
        <module> SdEventSelectorOG </module>
        <module> SdPlaneFitOG </module>
        <module> LDFFinderKG </module>
        <module> Risetime1000LLL </module>
        <module> EnergyCalculationPG </module>
        <module> SdEventPosteriorSelectorOG </module>
        </try>

        <module> RecDataWriterNG </module>

    </loop>

    </loop>
  </moduleControl>

</sequenceFile>
```

I.5 SManagerRegisterConfig_evolution.xml.in

```
<?xml version="1.0" encoding="iso-8859-1"?>

<SDetectorManagerList
    xmlns:xsi="http://www.w3.org/2001/XMLSchema-instance"
    xsi:noNamespaceSchemaLocation='@SCHEMALOCATION@/SManagerRegisterConfig.xsd'>

    <manager> T2LifeROOTFileManager </manager>

    <!-- The SStationListXMLManager reads station positions from an XML file -->
    <manager> SStationListXMLManager </manager>

    <!-- The SModelsXMLManager reads static quantities describing the
                stations, like tank geometry, materials, etc -->
    <manager> SModelsXMLManager </manager>

    <!-- The SdSimCalibrationManager is used to read the calibration
                constants and histograms for simulated stations -->
    <manager> SdSimCalibrationManager </manager>
```

```
</SDetectorManagerList>
```

I.6 SManagerRegisterConfig_standard.xml.in

```
<?xml version="1.0" encoding="iso-8859-1"?>

<SDetectorManagerList
      xmlns:xsi="http://www.w3.org/2001/XMLSchema-instance"
      xsi:noNamespaceSchemaLocation='@SCHEMALOCATION@/SManagerRegisterConfig.xsd'>

      <!-- The SStationListXMLManager reads station positions from an XML file -->
      <manager> SStationListXMLManager </manager>

      <!-- The SModelsXMLManager reads static quantities describing the
                  stations, like tank geometry, materials, etc -->
      <manager> SModelsXMLManager </manager>

      <!-- The SdSimCalibrationManager is used to read the calibration
                  constants and histograms for simulated stations -->
      <manager> SdSimCalibrationManager </manager>

</SDetectorManagerList>
```

I.7 Area and Peak parametrization parameters

Area					
PMT	a_0	a_1	a_2	a_3	a_4
1	194.351	1923.57	17354	300731	4.71121e+06
2	194.858	1937.63	16556.8	296074	4.95229e+06
3	193.835	1912.93	18936.4	312170	3.9768e+06

Peak			
PMT	p_0	p_1	p_2
1	59.7545	188.378	508.687
2	59.6984	187.433	730.954
3	59.7489	186.893	608.274

List of Figures

List of Tables

Bibliography

[1] The Pierre Auger Coll. "A measurement of the cosmic-ray energy spectrum above 2.5×10^{18} eV using the Pierre Auger Observatory". In: *Phys. Rev. D* 102.062005 (2020).

[2] LHC Design Report. *The LHC Main Ring*. Tech. rep. 003. CERN, 2004.

[3] H. Becquerel. "Sur les radiations émises par phosphorescence". In: *Comptes rendus de l'Acad. des Sciences* 420 (1896).

[4] D. Pacini. "La radiazione penetrante alla superficie ed in seno alle acque". In: *Nuovo Cim.* VI/3 (1896). translated and commented by A. De Angelis, "Penetrating radiation at the surface of and in water", p. 93. URL: arXiv:1002.1810v1.

[5] V. F. Hess. "Über Beobachtungen der durchdringenden Strahlung bei sieben Freiballonfahrt". In: *Physik. Zeitschr.* 13 (1912), pp. 1084–1091.

[6] P. Auger et al. "Extensive Cosmic-Ray Showers". In: *Rev. Mod. Phys.* 11 (1939), pp. 288–291.

[7] W. Heitler. *The Quantum Theory of Radiation*. Oxford University Press, 1944.

[8] J. Linsley. "Evidence for a Primary Cosmic-Ray Particle with Energy 10^{20} eV". In: *Phys. Rev. Lett.* 10 (1963), pp. 146–148.

[9] T. Stanev A. Letessier-Selvon. "Ultrahigh Energy Cosmic Rays". In: *Rev. Mod. Phys.* 83 (2011), pp. 907–942.

[10] Karl-Heinz Kampert and Alan A. Watson. "Extensive air showers and ultra high-energy cosmic rays: a historical review". In: *Eur. Phys. J. H* 37 (2012), pp. 359–412.

[11] T. K. Gaisser, R.Engel, and E. Resconi. *Cosmic Rays and Particle Physics*. Ed. by Cambridge University Press. Cambridge University Press, 2016.

[12] E. Mayotte et. al A. Coleman J. Eser. "Ultra high energy cosmic rays: The intersection of the Cosmic and Energy Frontiers". In: *Elsevier BV* 149 (2023). DOI: 10.1016/j.astropartphys.2023.102819.

[13] The KASCADE Coll. "Kneelike structure in the spectrum of the heavy component of cosmic rays observed with KASCADE-Grande". In: *Phys. Rev. Lett.* 107 (2011), p. 171104.

[14] B. Peters. "Primary cosmic radiation and extensive air showers". In: *Il Nuovo Cimento* (1961).

[15] The Pierre Auger Coll. "Cosmic ray anisotropies in right ascension measured by the Pierre Auger Observatory". In: *Astrophys. J.* 891.142 (2020).

[16] The Pierre Auger Coll. "Observation of a large-scale anisotropy in the arrival directions of cosmic rays above 8×10^{18} eV". In: *Science* 357 (2017), pp. 1266–1270.

[17] The Pierre Auger Coll. "Features of the energy spectrum of cosmic rays above 2.5×10^{18} eV using the Pierre Auger Observatory". In: *Phys. Rev. Lett.* 125.121106 (2020).

[18] The Pierre Auger Coll. "Observation of the suppression of the flux of cosmic rays above 4×10^{19} eV". In: *Phys. Rev. Lett.* 101.061101 (2008).

[19] The Telescope Array Collaboration. "The Cosmic Ray Energy Spectrum Observed with the Surface Detector of the Telescope Array Experiment". In: *Astrophys. J. Lett.* 768 L1 (2013). DOI: https://doi.org/10.1088/2041-8205/768/1/L1.

[20] F. W. Stecker and M. H. Salamon. "Photodisintegration of Ultrahigh Energy Cosmic Rays: A New Determination". In: *Astrophys. J.* 512 (1999), pp. 521–526.

[21] K. Greisen. "End to the Cosmic-Ray Spectrum?" In: *Phys. Rev.Lett.* 16.748 (1966).

[22] G. Zatsepin and V. A. Kuzmin. "Upper limit of the spectrum of cosmic rays". In: *Pisma Zh. Eksp. Teor. Fiz.* 4 (1966), pp. 114–117.

[23] D. Harari. "The flux suppression at the highest energies". In: *Comptes Rendus Physique* 15.4 (2014), pp. 376–383. DOI: https://doi.org/10.1016\%2Fj.crhy.2014.02.011.

[24] J. L. Puget et al. "Photonuclear Interactions Of Ultrahigh-Energy Cosmic Rays And their Astrophysical Consequences". In: *Astrophys. J.* 205 (1976), pp. 638–654.

[25] The Pierre Auger Coll. "Combined fit of spectrum and composition data as measured by the Pierre Auger Observatory". In: *J. Cosmol. Astropart. Phys.* 04.038 (2017).

[26] W. Axford. "The acceleration of cosmic rays by shock waves". In: *Annals of the New York Academy of Sciences* 375.1 (1981), pp. 297–313.

[27] L. O'C Drury. "An introduction to the theory of diffusive shock acceleration of energetic particles in tenuous plasmas". In: *Rep. Prog. Phys.* 46.8 (1983), p. 973.

[28] A. M. Hillas. "The Origin of Ultra-High-Energy Cosmic Rays". In: *Ann. Rev. Astron. Astrophys.* 22 (1984), pp. 425–444.

[29] K. Kotera and A. Olinto. "The Astrophysics of Ultrahigh Energy Cosmic Rays". In: *Annual Review of Astronomy and Astrophysics* 49 (2011), pp. 119–153.

[30] E. Mayotte for the Pierre Auger Coll. "Measurement of the mass composition of ultra-high-energy cosmic rays at the Pierre Auger Observatory". In: 38^{th} *Int. Cosmic Ray Conf. (ICRC)*. Ed. by Proc. of Science. 365. 2023.

[31] T. Stanev. "Ultra high energy cosmic rays and the large scale structure of the galactic magnetic field". In: *Astrophys. J* 479 (1997), pp. 290–295. DOI: astro-ph/9607086.

[32] et al. H.P. Bretz M. Erdmann. "PARSEC: A Parametrized Simulation Engine for Ultra-High Energy Cosmic Ray Protons". In: *Astrophys. J* 54 (2014), pp. 110–117. URL: arXiv:1302.3761.

[33] The Pierre Auger Coll. "An Indication of Anisotropy in Arrival Directions of Ultra-high-energy Cosmic Rays through Comparison to the Flux Pattern of Extragalactic Gamma-Ray Sources". In: *Astrophys. J. Lett.* 853.L29 (2018).

[34] E. Mayotte for the Pierre Auger Coll. "Indication of a mass-dependent anisotropy above $10^{18.7}$ eV in the hybrid data of the Pierre Auger Observatory". In: 37^{th} *Int. Cosmic Ray Conf. (ICRC)*. Ed. by Proc. of Science. 321. 2021.

[35] J. Oehlschläger and R. Engel. *CORSIKA Shower Movies*. URL: https://web.ikp.kit.edu/corsika/movies/Movies.htm (visited on 07/30/2023).

[36] J. Matthews. "A Heitler model of extensive air showers". In: *Astropart. Phys.* 22.5-6 (2005), pp. 387–397.

[37] T. Stanev. *High Energy Cosmic Rays*. Second. 2366-0082. Springer-Verlag Berlin Heidelberg, 2010.

[38] S. Mollerach and E. Roulet. "Progress in high-energy cosmic ray physics". In: *Progress in Particle and Nuclear Physics* 98 (2018), pp. 85–118. DOI: 10.1016/j.ppnp.2017.10.002. URL: https://doi.org/10.1016%2Fj.ppnp.2017.10.002.

[39] J. Alvarez-Muńiz and et al. "Hybrid simulations of extensive air showers". In: *Phys. Rev. D* 66.3 (2002).

[40] D. Heck et al. "CORSIKA: A Monte Carlo Code to Simulate Extensive Air Showers". In: *Report FZKA* 6019 (1998).

[41] T. Pierog et al. "EPOS LHC: Test of collective hadronization with data measured at the CERN Large Hadron Collider". In: *Phys. Rev. C* 92.034906 (2015).

[42] R.S. Fletcher et al. "sibyll: An event generator for simulation of high energy cosmic ray cascades". In: *Phys. Rev. D.* 50 (1994), pp. 5710–5731.

[43] S. Ostapchenko. "QGSJET-II: towards reliable description of very high energy hadronic interactions". In: *Nucl. Phys. B* 151 (2006), pp. 143–146.

[44] Thomas Fitoussi for the Pierre Auger Coll. "Measurement of $X_{\max}$ and its mass Implications". In: 38^{th} *Int. Cosmic Ray Conf. (ICRC)*. Ed. by Proc. of Science. 319. 2023.

[45] JW Belz et al. "Measurement of pressure dependent fluorescence yield of air: Calibration factor for UHECR detectors". In: *Astroparticle Physics* 25.2 (2006), pp. 129–139.

[46] M. Bohacova. "Study of the air fluorescence by AIRFLY". In: *Nucl. Phys. B Proc. Suppl.* 190 (2009). Ed. by R. Caruso et al., pp. 266–271. DOI: 10.1016/j.nuclphysbps.2009.03.098.

[47] A. Yushkov for the Pierre Auger Coll. "Mass composition of cosmic rays with energies above $10^{17.2}$ eV from the hybrid data of the Pierre Auger Observatory". In: 36^{th} *Int. Cosmic Ray Conf.* Ed. by Proc. of Science. Vol. 358. 482. 2019.

[48] V. M. Harvey for the Pierre Auger Coll. "A new cross-check and review of aerosol attenuation measurements at the Pierre Auger Observatory". In: 38^{th} *Int. Cosmic Ray Conf. (ICRC)*. Ed. by Proc. of Science. 300. 2023.

[49] J. Bellido for the Pierre Auger Coll. "The Fitting Procedure for Longitudinal Shower Profiles Observed with the Fluorescence Detector of the Pierre Auger Observatory". In: 38^{th} *Int. Cosmic Ray Conf. (ICRC)*. Ed. by Proc. of Science. 211. 2023.

[50] The Pierre Auger Coll. "Depth of Maximum of Air-Shower Profiles at the Auger Observatory: Measurements at Energies above $10^{17.8}$ eV". In: *Phys. Rev. D* 90.122005 (2014).

[51] The Pierre Auger Coll. "Inferences on Mass Composition and Tests of Hadronic Interactions from 0.3 to 100 EeV using the water-Cherenkov Detectors of the Pierre Auger Observatory". In: *Phys. Rev. D* 96.122003 (2017).

[52] E. J. Ahn for the Pierre Auger Coll. "Inferences about the mass composition of cosmic rays from data on the depth of maximum at the Auger Observatory". In: 33^{th} *Int. Cosmic Ray Conf. (ICRC)*. Ed. by Proc. of Science. 2013.

[53] The Pierre Auger Coll. "Deep-learning based reconstruction of the shower maximum $X_{\max}$ using the water-Cherenkov detectors of the Pierre Auger Observatory". In: *Journal of Instrumentation* 16.07 (2021), P07019. DOI: 10.1088/1748-0221/16/07/p07019. URL: https://doi.org/10.1088%2F1748-0221%2F16%2F07%2Fp07019.

[54] Jonas Glombitza for the Pierre Auger Coll. "Mass Composition from 3 EeV to 100 EeV measured using the Surface Detector". In: 38^{th} *Int. Cosmic Ray Conf. (ICRC)*. Ed. by Proc. of Science. 278. 2023.

[55] The Pierre Auger Coll. "Muons in air showers at the Pierre Auger Observatory: Mean number in highly inclined events". In: *Phys. Rev. D* 91.032003 (2015).

[56] A. Etchegoyen for the Pierre Auger Coll. "AMIGA, Auger Muons and Infill for the Ground Array". In: *In Proc. 30^{th} International Cosmic Rays Conference*. Vol. 1307. 2007.

[57] The Pierre Auger Collaboration. *The Pierre Auger Observatory Upgrade - Preliminary Design Report*. 2016. arXiv: 1604.03637 [astro-ph.IM].

[58] The Pierre Auger Coll. "Direct measurement of the muonic content of extensive air showers between 2×10^{17} and 2×10^{18} eV at the Pierre Auger Observatory". In: *Eur. Phys. J. C* 80.751 (2020).

[59] The Telescope Array Coll. "Study of muons from ultrahigh energy cosmic ray air showers measured with the Telescope Array experiment". In: *Physical Review D* 98.2 (2018). DOI: 10.1103/physrevd.98.022002. URL: https://doi.org/10.1103%2Fphysrevd.98.022002.

[60] The Pierre Auger Coll. "Measurement of the fluctuations in the number of muons in extensive air showers with the Pierre Auger Observatory". In: *Phys. Rev. Lett.* 126.152002 (2021).

[61] The Pierre Auger Coll. "Testing Hadronic Interactions at Ultrahigh Energies with Air Showers Measured by the Pierre Auger Observatory". In: *Phys. Rev. Lett.* 117.192001 (2016).

[62] The Pierre Auger Coll. "The Pierre Auger Cosmic Ray Observatory". In: *Nucl. Instr. Meth.* 798 (2015), pp. 172–213.

[63] The Pierre Auger Coll. *The Pierre Auger Observatory Upgrade: AugerPrime*. arXiv: 1604.03637. 2016.

[64] The Pierre Auger Observatory. *Pierre Auger Observatory on flickr*. URL: https://www.flickr.com/people/134252569@N07/ (visited on 07/30/2023).

[65] T. Schmidt I. C. Mariş M. Roth. "A Phenomenological Method to Recover the Signal from Saturated Stations". GAP-Note 2006-012.

[66] I. C. Mariş. "Measurement of the Ultra High Energy Cosmic Ray Flux using Data of the Pierre Auger Observatory". PhD thesis. Karlsruher Institut für Technologie, 2008.

[67] The Pierre Auger Coll. "Trigger and aperture of the surface detector array of the Pierre Auger Observatory". In: *Nucl. Instrum. Meth.* A.613 (2010), pp. 29–39.

[68] P. Billoir. "Proposition to improve the local trigger of the Surface Detector for low energy showers". GAP-Note 2009-179.

[69] P. Billoir. "New proposal to improve the local trigger of the Surface Detector". GAP-Note 2011-089.

[70] The Pierre Auger Coll. "The fluorescence detector of the Pierre Auger Observatory". In: *Nucl. Instrum. Meth.* 620 (2010), pp. 227–251.

[71] The Pierre Auger Coll. "Reconstruction of Events Recorded by the Surface Detector of the Pierre Auger Observatory". In: *J. Instrum.* 15.P10021 (2020).

[72] S. Argiro et al. "The offline software framework of the Pierre Auger Observatory". In: *Nucl. Instr. and Meth. Phys. A* 580.3 (2007), pp. 1485–1496.

[73] K. Kamata and J. Nishimura. "The Lateral and the Angular Structure Functions of Electron Showers". In: *Progr. Theor. Phys. Suppl.* 6 (1958), pp. 93–155.

[74] K. Greisen. "Cosmic ray showers". In: *Ann. Rev. Nucl. Part. Sci.* 10 (1960), pp. 63–108. DOI: 10.1146/annurev.ns.10.120160.000431.

[75] D. Newton, J. Knapp, and A. A. Watson. "The Optimum Distance at which to Determine the Size of a Giant Air Shower". In: *Astropart. Phys.* 26.6 (2007), pp. 414–419.

[76] I. C. Mariş L. M. Bueno P. Billoir. "Signal variance for the TOTd and MoPS triggers". GAP Note 2014-035.

[77] T. K. Gaisser and A. M. Hillas. "Reliability of the method of constant intensity cuts for reconstructing the average development of vertical showers". In: 15^{th} *Int. Cosmic Ray Conf.* 1977.

[78] Hans Peter Dembinski et al. "A likelihood method to cross-calibrate air-shower detectors". In: *Astroparticle Physics* 73 (2016), pp. 44–51. DOI: 10.1016/j.astropartphys.2015.08.001. URL: https://doi.org/10.1016%2Fj.astropartphys.2015.08.001.

[79] P.D.J. Clark and D. Nitz for the Pierre Auger Coll. "Communications in the Auger Observatory". In: 27^{th} *Int. Cosmic Ray Conf. (ICRC)*. Ed. by Proc. of Science. Vol. 2. 2001, pp. 765–768.

[80] P. Bauleo et al. "A water tank Cherenkov detector for very high-energy astroparticles". In: *Nuclear Instruments and Methods in Physics Research Section A: Accelerators, Spectrometers, Detectors and Associated Equipment* 406.1 (1998), pp. 69–77. ISSN: 0168-9002. DOI: https://doi.org/10.1016/S0168-9002(97)01187-X.

[81] M. et al. for the Pierre Auger Coll. Aglietta. "Response of the Pierre Auger Observatory water Cherenkov detectors to muons". In: 29^{th} *Int. Cosmic Ray Conf. (ICRC)*. Ed. by Proc. of Science. 2005.

[82] The Pierre Auger Coll. "Studies on the response of a water-Cherenkov detector of the Pierre Auger Observatory to atmospheric muons using an RPC hodoscope". In: *JINST* 15.P09002 (2020).

[83] The Pierre Auger Coll. "Calibration of the surface array of the Pierre Auger Observatory". In: *Nucl. Instrum. Meth. A.* 568.2 (2006), pp. 839–846.

[84] P. Billoir P.N. Dong P.T. Nhung and I. Lhenry-Yvon. "Long term behaviour of well-behaved SD Cherenkov counters". GAP-Note 2010-048.

[85] H. Wahlberg C. Jarne. "Long Term Study of SD monitoring variables from 2004 to 2010". GAP-Note 2011-045.

[86] R. Sato for the Pierre Auger Coll. "Long Term Performance of the Surface Detectors of the Pierre Auger Observatory". In: 32^{th} *Int. Cosmic Ray Conf. (ICRC)*. Ed. by Proc. of Science. Vol. 3. 204. 2011. DOI: 10.7529/ICRC2011/V03/0952.

[87] I. Lhenry-Yvon. "Area over Peak ratio and event rate in SD Auger detectors". GAP-Note 2016-033.

[88] D. Mockler K. Choi I. C. Mariş. "Long Term Evolution of the Area to Peak ratio". GAP-Note 2019-028.

[89] I. Mariş. *Private communication*.

[90] R. Sato H. Wahlberg. "Description of the SD freezing events at winters of 2007 and 2010". GAP-Note 2013-041.

[91] Michael Schimp et al. "Presentations in the long term performance sessions https://indico.nucleares.unam.mx/category/58/".

[92] *Observer data production*. URL: https://web.ikp.kit.edu/observer/data.html (visited on 07/30/2023).

[93] V. Verzi O. Deligny P. Ghia. "SD resolution and bias parameterizations inferred from hybrid events". GAP-Note 2019-022.

[94] J. Linsley and L. Scarsi. "Arrival times of air shower particles at large distances from the axis". In: *Phys. Rev.* 128.2384 (1962).

[95] A. A. Watson and J. G. Wilson. "Fluctuation studies of large air showers: the composition of primary cosmic ray particles of energy $E_p \sim 10^{18}$ eV". In: *J. Phys.* A7.1199 (1974).

[96] The Pierre Auger Coll. "Azimuthal asymmetry in the risetime of the surface detector signals of the Pierre Auger Observatory". In: *Physical Review D* 93.7 (2016). DOI: 10.1103/physrevd.93.072006. URL: https://doi.org/10.1103%2Fphysrevd.93.072006.

[97] A. G. Mariazzi M. T. Dova L. N. Epele. "The effect of atmospheric attenuation on inclined cosmic ray air showers". In: *Astropart. Phys.* 18.351 (2003).

[98] M. T. Dova for the Pierre Auger Coll. "Asymmetries observed in giant air showers using water Cherenkov detectors". In: 28^{th} *Int. Cosmic Ray Conf. (ICRC)*. Ed. by Proc. of Science. 2003.

[99] X. Bertou and P. Billoir. "On the Origin of the Asymmetry of Ground Densities in Inclined Showers". GAP-Note 2000-017.

[100] C. Jarne et al. "An update to the asymmetry correction of risetime with data from 2004 to 2013". GAP-Note 2014-042.

[101] P. Sanchez Lucas. "The $\langle\Delta\rangle$ method: An estimator for the mass composition of ultra-high-energy cosmic rays". PhD thesis. Universidad de Granada, 2016.

[102] I. Lhenry-Yvon D. Dornic. "Analysis of CAPISA VEM water level data: Comparison with EasySim Simulations". GAP-Note 2007-80.

[103] M. C. Medina et al. "Sensitivity of muon data to the water level in a Water Cerenkov Detector". GAP-Note 2004-001.

[104] X. Bertou C. Medina. "Water Level experiment in Laura". GAP-Note 2003-091.

[105] P. Assis et al. "Measurements with the RPC Muon Hodoscope Installed at the Gianni Navarra Tank: First Results v1.1". GAP-Note 2015-033.

[106] P. Billoir. "What is ageing in the tanks of the Surface Detector?" GAP-Note 2014-038.

[107] P. Billoir. "Possible ageing effects on the VEM calibration and the attenuation curve". GAP-Note 2013-024.

[108] T. Suomijärvi S. Cometti. "EA current performances". GAP-Note 2016-038.

[109] I. Allekotte H. Wahlberg R. Sato. "Summary of Tests Towards Understanding the VEM Area over Peak Evolution". GAP-Note 2014-018.

[110] P. Billoir. "Ageing effects on the calibration of the Surface Detector through the Vertical Equivalent Muon". GAP-Note 2015-047.

[111] S. Agostinelli et al. "Geant4-a simulation toolkit". In: *Nuclear Instruments and Methods in Physics Research Section A: Accelerators, Spectrometers, Detectors and Associated Equipment* 506.3 (2003), pp. 250–303. ISSN: 0168-9002. DOI: https://doi.org/10.1016/S0168-9002(03)01368-8.

[112] I. Mariş R. Sato O. Zapparrata. "Using the AugerPrime scintillators for improving the calibration of the water Cherenkov detectors". GAP-Note 2021-046.

[113] Katarína Simkova. "The performance of a novel calibration method for the AugerPrime surface detector signals and the ultra-high-energetic cosmic-ray spectra on & off the galactic plane". MA thesis. VUB, IIHE, 2022.

[114] *Monte Carlo Simulations Task of the Auger Collaboration*. URL: https://www.auger.unam.mx/AugerWiki/Monte_Carlo_Simulations (visited on 07/30/2023).

[115] J. Bellido for the Pierre Auger Coll. "Depth of maximum of air-shower profiles at the Pierre Auger Observatory Measurements above $10^{17.2}$ eV and Composition Implications". In: 35^{th} *Int. Cosmic Ray Conf.* Ed. by Proc. of Science. Vol. 301. 506. 2017.

[116] A. Fedynitch F. Riehn R. Engel. "Estimating the Depth of Shower Maximum using the Surface Detectors of the Pierre Auger Observatory". In: 38^{th} *Int. Cosmic Ray Conf. (ICRC)*. Ed. by Proc. of Science. 429. 2023.

[117] A. A. Watson A. Bueno C. J. Todero Peixoto. "Correlation of Break Points in the Energy Spectrum with those found in the Elongation Rate measured using the Delta Technique". GAP-Note 2022-040.

[118] P.M. Hansen, J. Alvarez-Muñiz, and R.A. Vázquez. "A comprehensive study of shower to shower fluctuations". In: *Astroparticle Physics* 34.6 (2011), pp. 503–512. DOI: 10.1016/j.astropartphys.2010.11.001. URL: https://doi.org/10.1016%2Fj.astropartphys.2010.11.001.

[119] G. Carleo et al. "Machine learning and the physical sciences". In: *Reviews of Modern Physics* 91.4 (2019). DOI: 10.1103/revmodphys.91.045002. URL: https://doi.org/10.1103%2Frevmodphys.91.045002.

[120] G. Kasieczka M. Erdmann J. Glombitza and U. Klemradt. *Deep Learning for Physics Research*. WORLD SCIENTIFIC, 2021. DOI: 10.1142/12294. eprint: https://worldscientific.com/doi/pdf/10.1142/12294. URL: http://deeplearningphysics.org.

[121] Matthew Feickert and Benjamin Nachman. *A Living Review of Machine Learning for Particle Physics*. 2021. arXiv: 2102.02770 [hep-ph].

[122] K. Hashimoto A. Tanaka A. Tomiya. *Deep Learning and Physics*. Springer International Publishing, 2021. URL: https://doi.org/10.1007/978-981-33-6108-9.

[123] Hinton G. Y. LeCun Y. Bengio. "Deep learning". In: *Nature* 521 (2015), pp. 436–444. DOI: https://doi.org/10.1038/nature14539.

[124] Alexander Lenail. *NN-SVG*. URL: http://alexlenail.me/NN-SVG/index.html (visited on 07/30/2023).

[125] Vinod Nair and Geoffrey E. Hinton. "Rectified Linear Units Improve Restricted Boltzmann Machines". In: *Proceedings of the 27th International Conference on International Conference on Machine Learning*. ICML'10. Haifa, Israel: Omnipress, 2010, pp. 807–814.

[126] Ian Goodfellow, Yoshua Bengio, and Aaron Courville. *Deep Learning*. http://www.deeplearningbook.org. MIT Press, 2016.

[127] Hecht-Nielsen. "Theory of the backpropagation neural network". In: *International 1989 Joint Conference on Neural Networks*. 1989, 593–605 vol.1. DOI: 10.1109/IJCNN.1989.118638.

[128] Alex Krizhevsky, Ilya Sutskever, and Geoffrey E Hinton. "ImageNet Classification with Deep Convolutional Neural Networks". In: *Advances in Neural Information Processing Systems*. Ed. by F. Pereira et al. Vol. 25. Curran Associates, Inc., 2012. URL: https://proceedings.neurips.cc/paper_files/paper/2012/file/c399862d3b9d6b76c8436e924a68c45b-Paper.pdf.

[129] Li Deng and Dong Yu. "Deep Learning: Methods and Applications". In: *Found. Trends Signal Process.* 7.3-4 (2014), pp. 197–387. ISSN: 1932-8346. DOI: 10.1561/2000000039. URL: https://doi.org/10.1561/2000000039.

[130] Christopher Olah. *Understanding LSTM Networks*. URL: http://colah.github.io/posts/2015-08-Understanding-LSTMs/ (visited on 07/30/2023).

[131] J.M. Carceller López. "A study of the signals measured with the Water-Cherenkov detectors of the Pierre Auger observatory to infer the mass composition of ultra-high energy cosmic rays". PhD thesis. Universidad de Granada, 2020.

[132] S. Hochreiter and J. Schmidhuber. "Long Short-Term Memory". In: *Neural Computation* 9 (1997), pp. 1735–1780. DOI: https://doi.org/10.1162/neco.1997.9.8.1735.

[133] S. Hochreiter. "Untersuchungen zu dynamischen neuronalen Netzen". Diplom thesis. Institut f. Informatik, Technische Univ. Munich., 1991.

[134] The Pierre Auger Coll. "Extraction of the Muon Signals Recorded by the Surface Detector of the Pierre Auger Observatory Using Recurrent Neural Networks". In: *J. Instrum.* 16.P07016 (2021).

[135] A. Guillén et al. "Deep learning techniques applied to the physics of extensive air showers". In: *Astroparticle Physics* 111 (2019), pp. 12–22. ISSN: 0927-6505. DOI: https://doi.org/10.1016/j.astropartphys.2019.03.001. URL: https://www.sciencedirect.com/science/article/pii/S0927650518302871.

[136] Consortium des Équipements de Calcul Intensif - CECI. *High-performance computing centers*. Waloon Region. URL: https://www.ceci-hpc.be/.

[137] *Python*. URL: https://www.python.org/ (visited on 07/30/2023).

[138] *ROOT Data Analysis Framework*. URL: https://root.cern.ch/ (visited on 07/30/2023).

[139] *Pytorch*. URL: https://www.pytorch.org/ (visited on 07/30/2023).

[140] The Pierre Auger Coll. "A search for Ultra-High Energy neutrinos from TXS 0506+056 using the Pierre Auger Observatory". In: *Astrophys. J.* 902.105 (2020).

[141] A. Fedynitch F. Riehn R. Engel. "Sibyll*: ad-hoc modifications for an improved description of muon data in extensive air showers". In: 38^{th} *Int. Cosmic Ray Conf. (ICRC)*. Ed. by Proc. of Science. 429. 2023.